UNIVERSITY OF SOUTHAMPTON

INVESTIGATION OF THE VISCOUS RESISTANCE COMPONENTS OF CATAMARAN FORMS

I Ketut Aria Pria Utama

Thesis submitted for the degree of Doctor of Philosophy

DEPARTMENT OF SHIP SCIENCE
FACULTY OF ENGINEERING AND APPLIED SCIENCE

July 1999

UNIVERSITY OF SOUTHAMPTON

ABSTRACT

FACULTY OF ENGINEERING AND APPLIED SCIENCE
DEPARTMENT OF SHIP SCIENCE

Doctor of Philosophy

INVESTIGATION OF THE VISCOUS RESISTANCE COMPONENTS OF CATAMARAN FORMS

by I Ketut Aria Pria Utama

Research into the breakdown of resistance components of catamaran hull forms has been carried out over a number of years. The components consist of viscous and wave resistance as well as viscous and wave resistance interference. Significant investigation of wave resistance has been carried out. Less effort, however, has been dedicated to determining viscous resistance and viscous interference resistance, which can be important elements in the estimation of power for a new design.

Investigations into the components of viscous resistance have been carried out experimentally using a low-speed wind tunnel and numerically using a commercial CFD code (CFX). The investigations used representative reflex models of multihull ships and investigated the components of viscous resistance and viscous interaction effects between the hulls.

The experimental work was carried out on a single ellipsoid and a pair of ellipsoids in proximity and the CFD investigations were carried out on (1) a single ellipse and a pair of ellipses in proximity, (2) a single ellipsoid and a pair of ellipsoids in proximity and (3) single and twinhull configurations of round bilge/transom stern ship forms. In the experimental work, the tests were carried out without and with turbulence transition strip at separation to length (S/L) ratios of 0.27, 0.37, 0.47 and 0.57, and at Reynolds number values of 1.6×10^6, 2.4×10^6 and 3.2×10^6. In the numerical work, the investigations were conducted at the same S/L ratios, two- and three-dimensional, under turbulent flow condition and at a Reynolds number of 2.4×10^6. The CFD work was extended to a higher Reynolds number in order to investigate the scale effect.

The results of the experimental and CFD investigations are presented and discussed. Reasonable correlation between the approaches is achieved. Both approaches demonstrate form effect on the slender hull forms and the presence of viscous interaction in the catamaran mode.

The investigation has demonstrated the ability of the wind tunnel and CFD approaches employed to provide a better understanding of catamaran viscous resistance, including the influence of hull separation and length/displacement ratio. These methods also enable detailed investigations of the components of viscous resistance to be made, and can contribute to improving the prediction of viscous drag and interference effects, form factors and total ship resistance.

TABLE OF CONTENTS

LIST OF FIGURES

LIST OF TABLES

Dedicated to my late father (Ketut Wentra), my mother (Made Anom), my wife (Luh Mas Ariyati) and my daughter (Putu Audrina Utama)

ACKNOWLEDGEMENTS

The author wishes to acknowledge the support and assistance given by following:

Dr. A. F. Molland (Department of Ship Science), who supervised this project, for his continuous encouragement, advice, patience and friendship

Dr. J. F. Wellicome (Department of Ship Science) for his help in the theoretical field

Prof. W. G. Price (Head of Department) for his generous support and encouragement

Dr. R. J. Downes (Southampton University Computing Service) for his continuos help in computing facilities

AEA Technology Technical Support Department for their helps and discussions with the CFX code

Mr. D. J. Goldsworthy and Mr G. W. Baldwin (R. J. Mitchell Wind Tunnel) for their helps in the experimental work

Mr. W. W. Widayat (Director of Higher Education Project, ADB Loan No, 1253-INO, Ministry of Education and Culture, the Republic of Indonesia) for the financial support throughout the project

Dr. D. M. Rosyid (Director of Centre Grant Project, Sepuluh-Nopember Institute of Technology (ITS), the Republic of Indonesia) for the financial extension support

Prof. Soegiono (Rector, Sepuluh Nopember Institute of Technology (ITS), the Republic of Indonesia) for his continuous support

Finally, for my family for their patience, love and understanding

NOMENCLATURE

Demihull	One of the hulls which make up the catamaran
A	Cross-sectional area of body [m^2]
A_0	Maximum cross-sectional area of body [m^2]
a	Slope of curve
B	Body force
b_d	Breadth of wind tunnel [m]
C	Wind tunnel cross-sectional area [m^2]
c	Chord or length of the body [m]
C_B	Block coefficient
C_D, C_T	Coefficients of total resistance $\left[R_T / \left(0.5\rho(WSA)V^2\right)\right]$
C_F	Coefficient of frictional resistance
C_M	Midship coefficient
C_P	Prismatic coefficient or pressure coefficient
C_{P1}, C_{P2}	Empirical constants
C_S, C_{SF}	Coefficients of side-force
CSA	Cross-sectional area of body [m^2]
C_V	Coefficient of viscous resistance $\left[R_V / \left(0.5\rho(WSA)V^2\right)\right]$
C_W	Coefficient of wave resistance $\left[R_W / \left(0.5\rho(WSA)V^2\right)\right]$
C_{WP}	Coefficient of wave pattern resistance $\left[R_{WP} / \left(0.5\rho(WSA)V^2\right)\right]$
D	Maximum diameter of the model or hydraulic diameter [m]
E	Constant of shear stress
Fn	Froude number $\left[V / \sqrt{gL}\right]$
f	Fineness ratio [L/D]
G	Gap between catamaran demihulls measured at midships [m] or production due to body force

g	Acceleration due to gravity [ms^{-2}]
H	Betz manometer reading in metres of water or total enthalpy
H_d	Height of wind tunnel [m]
k	Turbulence kinetic energy
L	Length of the model from leading edge to trailing edge [m]
P	Inlet perimeter or shear production
p	Atmospheric pressure [Nm^{-2}]
R	Radius or gas constant
Rn	Reynolds number $[VL/v]$
R_T	Total resistance [N]
R_V	Viscous resistance [N]
R_W	Wave resistance [N]
R_{WP}	Wave pattern resistance [N]
S	Separation between centrelines of catamaran demihulls [m], or body maximum cross-sectional area [m^2]
T	Absolute temperature [°K]
t	Maximum diameter/thickness [m] or time
U	Undisturbed velocity [ms^{-1}]
u	Velocity in x-direction [ms^{-1}]
V	Undisturbed velocity in x-direction [ms^{-1}]
v	Velocity in y-direction [ms-1]
WSA	Wetted surface area [m^2]
w	Velocity in z-direction [ms^{-1}]
X_0	Length of plate where there is part laminar and part turbulent flow [m]
1+k	Form factor
β	Viscous resistance interference factor
∇	Volume of displacement [m^3]
Δy_p	Distance of the near wall to the solid surface [m]

ε	Turbulence dissipation rate
ϕ	Pressure field change around the demihull or gravitational quantity
κ	von Karman's constant
λ	Thermal conductivity
λ_3	Body shape factor
μ	Dynamic viscosity of fluid $[kg.m^{-1}s^{-1}]$
μ_{eff}	Effective viscosity of fluid $[kg.m^{-1}s^{-1}]$
μ_T	Turbulence viscosity of fluid $[kg.m^{-1}s^{-1}]$
ν	Kinematic viscosity of fluid $[m^2s^{-1}]$
ρ_a	Density of air $[kg.m^{-3}]$
ρ_w	Density of fresh water $[kg.m^{-3}]$
σ	Velocity augmentation between the hulls or stress tensor
τ	Wave resistance interference factor or tunnel shape factor or maximum thickness/length (D/L) ratio
ζ	Bulk viscosity $[kg.m^{-1}s^{-1}]$

1 INTRODUCTION

In the last few decades, there has been a significant growth of interest in multi-hulled ships for applications such as ferries, trawlers, and sporting craft as well as oceanographic survey vessels. The principal advantages claimed are a more convenient layout of accommodation, increased static stability and in some cases a reduction of installed power to achieve a given speed. Various hull forms have been developed to satisfy the design criteria of these vessels. Among them the catamaran concept has received considerable attention for such applications because it has large deck area, high transverse stability and unusual resistance characteristics. Designers and investors have shown commitment to the catamaran concept with investment in the latest generation of large catamarans of over 100m in length [1].

The estimation of power requirements for this type of vessel entails a thorough investigation into the resistance characteristics to achieve a feasible design. Catamaran resistance can present a complex phenomenon for ship designers as the interference effects between the hulls must be taken into consideration in addition to the resistance of the demihulls in isolation. There is a fundamental need for a correct breakdown and understanding of the resistance components for these vessels in order to allow satisfactory scaling from model to ship.

The dependency of the interference on speed, hull separation and hull form restricts the practical use of model series, as such series have to cover a wide range of parameters. Previous experimental studies of catamaran resistance have therefore tended to be confined to a small number of isolated resistance experiments. The data obtained from these tests, although useful, is not sufficient to establish a prediction method for the design stage. This confirms the need for further research into the resistance components of catamarans in order to establish a fundamental understanding of the interference phenomena. This better understanding will allow improved power predictions to be developed.

Two types of resistance interference with catamarans can be identified. Firstly, body or viscous resistance interference, which is caused by the asymmetric flow around the demihulls and its effects on viscous flow such as boundary layer formation and longitudinal vortices. Secondly, wave resistance interference, which originates from the interaction between the wave systems of the demihulls.

Although a number of experimental and theoretical investigations of catamaran resistance have been carried out in the past, there is a lack of understanding of the interference resistance components, especially at higher speeds. Also, less work has been dedicated to the determination of viscous resistance and viscous resistance interference. Further work on the components of viscous resistance was therefore considered to be necessary in order to identify the resistance components of catamarans in a more fundamental way.

A possible approach to investigating the viscous components and interference effects is to consider the case when the free surface is treated as a solid plane with wavemaking eliminated. In this case, a reflex body may be used to model the remaining resistance, which will then be solely of viscous origin. Such an approach allows the isolation of viscous resistance but does not take into account of any influences that surface waves may have on viscous resistance. Lackenby [2] carried out a number of detailed tests in a test tank and wind tunnel using a mathematical (Wigley) model in order to attempt to identify and improve the understanding of the components of ship resistance and their interdependence. The results of this work indicates that at lower speeds, up to Fn of about 0.3, there is close correspondence between the wind tunnel measurements and the total viscous drag by wake traverse measurements in the test tank. At a Fn of about 0.5 the measured wake traverse value was about 5% higher than that measured in the wind tunnel, indicating an increase in total viscous drag due to surface wave effects. This difference might be expected not to get any bigger at higher speeds when the proportion of wave resistance will decrease again relative to the total drag. The overall results of Lackenby's work would indicate that the influence of surface waves on viscous resistance is not large, and that it should be acceptable to treat the viscous resistance in isolation in order to investigate its properties and behaviour.

The current research project was therefore initiated which would consider the viscous components in isolation. Namely, reflex (or reflection plane) versions of the single or twin bodies are assumed to be travelling in air or deeply submerged in water. The free surface is then treated as a solid reflection plane. Such an approach would allow the use of Navier-Stokes solvers without the complications of a free surface and the use of direct measurements of total viscous drag from wind tunnel experiments.

The principal objectives of the work have been:

- To gain a better understanding of the viscous resistance components for high-speed displacement mono-hulls.
- To identify the viscous drag components and viscous interaction effects for high-speed displacement catamaran hull forms using experimental and numerical techniques.
- To propose improved methods for resistance scaling of high-speed displacement catamarans.

The work has been carried out using both CFD and experiments on single and twin bodies. The CFD approach was carried out using a commercial code (CFX) and the experimental work was conducted using a wind tunnel. Initially, numerical bodies of revolution were examined. The use of such mathematical forms would allow validation of the techniques by comparisons with analytical and other published results for a single body of revolution. This was followed by CFD investigations of round bilge transom hull catamaran forms.

A summary of the stages of the work programme is as follows:

- Background review and investigation; establish suitable range of bodies for investigation.
- Wind tunnel tests using single ellipsoid and twin ellipsoids of L/D=6.0. The chosen ratio is relatively small for fast craft but should ensure reasonable levels of interference in the case of twin bodies. It also allows comparisons to be made with published, analytical and experimental data for single bodies.

- CFD (CFX) investigation using single ellipse and twin ellipses of L/D=6.0. This was carried out in order to gain confidence in this approach before moving to three-dimensional cases.
- CFD (CFX) investigation using single ellipsoid and twin ellipsoids of L/D=6.0. Comparisons are made with published data (single hulls) and the wind tunnel data (twin hulls).
- CFD (CFX) investigation using single ellipsoid and twin ellipsoids of L/D=10.0. The L/D ratio was extended to make it more typical of fast craft.
- CFD (CFX) investigation using single reflex models of round bilge/transom stern hulls of $L/\nabla^{1/3}$=7.4 and 8.5 and extension to twin reflex catamaran hulls.
- Comparisons of CFD studies with tank test viscous drag data.
- Discussion of results with respect to improvements in the physical understanding of the viscous resistance components, levels of viscous resistance and viscous interference on catamaran forms.
- Proposals for practical applications of the outcome of the work.

An overall outline of the investigations is given in Figure 1.

A background to ship resistance components and their scaling is given in Chapter 2. Various possible methods are explained including experimental work using towing tanks and wind tunnels and the use of CFD approaches.

The wind tunnel investigation is described in Chapter 3. A description of the models, procedure of the tests and boundary corrections are given. The analysis and discussion covers the aspects of (total and skin friction) drag, side-force, pressure distribution, form factors, velocity distribution and induced drag. A comparative study with some published data is included.

An introduction into the use of CFD in ship design is described in Chapter 4. Outlines of CFD techniques and various commercial CFD codes are explained, including a brief description of the CFX code, which has been used for the current work.

Case studies using two-dimensional ellipses, three-dimensional ellipsoids and ship hull model forms are described in Chapter 5. The potential use of CFX is primarily compared with analytical solutions, covering two- and three-dimensional problems. The strategy to solve the problems (including grid generation and flow solver) is further discussed. Comparisons are made for the resistance components, interference effects and the derivation of suitable form factors.

An overall discussion, bringing together the results of the experimental and CFD investigations, is given in Chapter 6.

A summary of the outcomes and applications of the investigation and final conclusions are drawn in Chapter 7 together with recommendations for further possible work.

2 RESISTANCE COMPONENTS OF CATAMARANS

2.1 Introduction

The total resistance of a catamaran (which is composed of two bodies placed in close proximity) is generally different from the sum of the resistance of the two bodies when tested separately. This phenomenon is called *interference*, and it arises from the change in flow pattern that accompanies the placing of the two bodies in close proximity. The interference may be unfavourable or favourable. There are two types of interference resistance specific to catamarans, as reported by Pien [3]. These can be identified as (1) body or viscous resistance interference and (2) wave resistance interference.

Firstly, viscous resistance interference is caused by the asymmetric flow around the demihull and its effect on the viscous flow such as boundary layer formation and the development of vortices. It was assumed to exist even in the absence of free surface. Secondly, wave resistance interference resistance originates from the interaction between the wave systems of the demihulls. This interaction may be positive or negative depending on the hull form, speed and separation between the hulls. Interaction effects between the demihulls include changes in the boundary layer due to the modified pressure field around the demihulls and the influence on frictional resistance of the velocity augmentation between the demihulls. Also, there is the potential for induced drag to be generated due to the asymmetric flow over the individual demihulls.

2.2 Research Carried Out on Catamaran Resistance

Research studies into the breakdown of the resistance components of high-speed catamarans have been carried out world-wide. The studies cover theoretical and experimental work, being mainly carried out by use of the towing tanks. Between the wave and viscous drags, the wave resistance has probably been the most investigated feature of this craft type, as it is a major component which can be optimised by designers.

Catamaran hydrodynamics have been discussed in Ref. [3] to indicate the difficulties in predicting the resistance of a given catamaran hull form. These occur because the objective of a designer is to develop a catamaran hull form with favourable resistance performance, which cannot be approached without a reliable resistance prediction method. The difficulties have been overcome by using the concept of an effective hull form in which a catamaran hull form design procedure has been developed. This concept covers two parts. The first part entails designing an effective hull form, which is similar to a monohull design but different from the monohull design in the freedom of choice of beam, buoyancy distribution and after-body form. In the design, both good wave cancellation and high propulsive efficiency may be obtained by means of a suitable after-body form. The second task was the conversion of the effective hull to a demihull in order to prevent the asymmetric flow and induced drag. The method applies streamline tracing for the singularities in a free stream. The demihull obtained from this method is slightly asymmetric.

A study on the flow around a catamaran has been carried out by Miyazawa [4]. Velocity components around a symmetrical catamaran form were measured and compared with those around the demihull in order to understand the increase of the resistance. Analysis of wake traverse on a symmetrical catamaran was carried out on two separation ratios: 0.177 and infinity, and two Froude numbers: 0.156 and 0.319. The experiments showed that the viscous resistance of the catamaran was higher than twice the viscous resistance of the demihull, which is simply due to the increase of viscous resistance at low speed and due to wave-breaking at higher speed. This work indicated that unfavourable viscous resistance interference effects can occur.

In experimental and theoretical approaches to the wave resistance of catamarans, wave pattern measurement by the transverse cut method was carried out by Everest [5]. It was followed by the development of a prediction method for the wave resistance of catamarans i.e. by superimposing the wave patterns obtained from demihull wave pattern measurements in isolation. The purpose of this method was to understand the distribution of resistance across the wave spectrum. Although the predictions were similar to experimental results, a phase shift in Froude number base was observed similar to the one from theoretical calculation by use of thin ship theory. Experiments on mathematically defined models showed that a favourable interaction between the demihulls was possible in divergent waves, while the transverse wave system of each demihull reinforces the other causing adverse interactions. This interference resulted in resistance reduction in the range of 0.32 to 0.37 where divergent waves were significant and an increase in Fn range of 0.4 to 0.6 in which transverse wave were dominant. The experiments with a conventional catamaran supported the conclusions with a favourable resistance between Fn 0.30 and 0.34.

Some experiments on symmetric and asymmetric catamarans for trawlers were also carried out by Everest [6]. Experiments showed that the total resistance of the symmetric hull and the asymmetric hull were almost the same. It was also found that infinite separation had lower resistance than the other separation.

An analytical procedure to determine optimal hull spacing for minimum resistance of a catamaran form has been developed by Hsiung and carried out by the cubic search method [7]. Wave resistance of a catamaran was expressed in quadratic form in terms of hull offsets. The resistance was subjected to a number of geometric constraints such as C_B and waterline slopes. By solving the quadratic problem, the optimal form and separation for given constraints were obtained.

A study into the wave resistance of high-speed catamaran, to be operated in rivers, was carried out by Doctors et al. [8]. Initially, six different catamaran and eight different trimaran configurations were tested in towing tank under deep-water condition. All trimaran configurations generated larger waves than the catamaran configurations at corresponding displacements. This was thought to be due to the large interactions between the hulls, which are very close together in terms of length. A further catamaran design was developed. This design incorporated a minimum practical demihull beam, maximum separation and a large rocker, to give as small a transom area as possible. Comparison between the experimental results and the theoretical studies was included and it was generally true that the resistance correlates with the wave height. The final chosen design was a slim round-bilge catamaran form. It was selected for its better overall wave characteristics, compared with the other hulls and configurations tested and its ability to meet the practical needs of the State Transit Authority in running a ferry service on Sydney Harbour and the Parramatta River.

Experimental investigations on resistance (and seakeeping qualities) of high-speed catamarans in calm water condition have been carried out by Matsui et al [9]. Three catamaran models with different demihull forms were tested in order to investigate the influence of hull form on resistance. The three models were:

(1) A typical round bilge form selected from conventional high-speed displacement vessels.
(2) A mixed form with double chines. Particulars of this model were the same as those of model (1). The double chines were in the region of 20% model length forward the stern transom.
(3) A hard chine hull forms similar to that of a conventional planning hull.

Tests were carried out on the first model with three hull spacings at the same displacement. It was found that both total resistance and residuary resistance increase in the whole speed range when the spacing between demihulls is reduced.

The effect of length to displacement ratio $(L/\nabla^{1/3})$ was significant in affecting the resistance of high-speed displacement vessels in the speed range $Fn<1.0$. It was found that the resistance decreases as the value of $(L/\nabla^{1/3})$ increases and the amount of reduction is almost in proportion to the parameter $(L/\nabla^{1/3})$.

Test results for the same models, reported in [10], showed that hull form does have influence on the resistance and seakeeping qualities of high-speed displacement vessels. Total resistance of the model with mixed form was lower than that of the model with round bilge form at the same particulars and displacement. Its total resistance was 2.74% lower and the residual resistance about 7.5% lower at a speed of 3.0m/s (Fn 0.809).

Further work on reducing resistance and improving seakeeping qualities was carried out using a stern trim flap, bow anti-wave hydrofoils and bow spray strips. It was found that all the methods were quite effective in reducing resistance or improving waves and spray when they were properly used.

Final conclusions indicated that the spacing between the demihulls is an important parameter affecting hull resistance due to the interference of waves between demihulls and that a suitable gap ratio should be selected in practical applications. As a high-speed catamaran ($Fn<1.0$), the reduction in resistance and rolling, of afterbody with short hard chine as compared with round bilge form, could be expected. Also, a considerable reduction in resistance would be obtained by fitting a stern flap.

Incecik et al. [11] carried out an experimental investigation of resistance and seakeeping characteristics of a catamaran design. The work described a series of experiments carried out with a scale model of a new catamaran design to optimise the hull form, spacing between the hulls and position of longitudinal centre of gravity (LCG). Sinkage and trim in calm water, added resistance, heave, pitch, deck accelerations and loads on the cross-members of the catamaran in waves were measured. It was found that the design had good wave formation characteristics with insignificant re-attachment of water on the hull at the design speed and there was no water spray on deck at any tested speed. The increase in resistance due to wave interaction between the hulls was at maximum 6% of the total resistance. It was observed that the model trimmed by the stern by about 1.5^0 to 2.0^0 around the design speed. The results of the seakeeping experiments can be used (in conjunction with the wave spectra of a given area) to assess the operational characteristics of the catamaran in various sea states. The structural load measurements when combined with long-term wave statistics would aid the design of cross-members.

Experimental and theoretical investigations into the resistance components in calm water of high-speed displacement and semi-displacement catamarans with symmetric demihulls have been carried out in Southampton [12, 13, 14 and 15]. The investigations covered total resistance, running trim, sinkage experiments and wave pattern analysis based on multiple longitudinal cut techniques which were carried out for a mathematically defined hull form (Wigley hull) and three round bilge hulls derived from the NPL series [12 and 13]. A theoretical method based on linearised wave resistance theory was developed and examples of its application were compared with the experimental results. The results of the investigation provide a better understanding of the components of catamaran resistance including the influence of hull separation and length to beam ratio over a wide range of Froude numbers.

Predictions of catamaran total resistance based on single hull measurements and the assumption of zero viscous interaction were found to be only accurate over the higher band of speed under investigation [5]. It followed that at the lower speeds the assumption of zero viscous interactions was incorrect. Some viscous interaction had been expected, but the severity of the effect was greater than had been expected.

An approach to calculate the total resistance of a catamaran (which takes into account the wave interaction effect and viscous interaction effect) was introduced in [12 and 13]. The total resistance of a catamaran, in coefficient form, may be expressed as:

$$C_{T_{Total}} = (1 + \phi k)\sigma C_F + \tau C_W \qquad (2.1)$$

Where:

C_F is obtained from the ITTC-57 correlation line, i.e. $C_F = 0.075/(\log_{10} Rn - 2)^2$.

C_W is the wave resistance coefficient for the demihull in isolation.

$(1+k)$ is the form factor for the demihull in isolation.

ϕ is introduced to take account of the pressure field change around the demihull.

σ takes account of the velocity augmentation between the two hulls and would be calculated from an integration of local frictional resistance over the wetted surface.

τ is the wave resistance interference factor.

For practical purposes, ϕ and σ can be combined into a viscous resistance interference factor β, where $(1+\phi k)\sigma C_F$ is replaced by $(1+\beta k)C_F$.

Whence,

$$C_{T_{cat}} = (1 + \beta k)C_F + \tau C_W \tag{2.2}$$

Noting that for the demihull in isolation, $\beta = 1$ and $\tau = 1$.

Further investigations [14 and 15] strengthened the earlier results and provided further insight into the influence of hull parameters on the resistance components of high- speed displacement catamarans and offer a very useful extension to the available resistance data for this type of vessel. Study into the effect of B/T was also included although its effect on resistance was not large. Experimental procedures used to estimate the sideforce and induced drag were presented in [15]. It was shown that the induced drag generated by the demihull is negligible despite the generation of significant sideforce.

The results of work carried out by Couser et al [16] have further strengthened the understanding of the resistance components of high-speed catamarans and the appropriate form factors to be used for resistance scaling. Emphasis of the study was directed at developing a fundamental understanding of the resistance components of high-speed, transom stern vessels, with particular reference to catamarans. It was noted that for such vessels the total resistance is dominated by viscous resistance, particularly at higher speeds. The conclusions related to form effect on viscous resistance. Levels of catamaran viscous interaction were estimated which were aimed at providing practical guidance to the designers of such vessels.

A novel technique to predict the effects of demihull spacing on the wave-making resistance of a catamaran by testing one of its demihull in close proximity to a towing tank wall was conducted by Rovere [17]. The tank wall acted as the plane of symmetry of the catamaran, reflecting waves generated by the demihull, and thereby attempting to simulate the correct wave interference and blockage effects from the non-existent hull. A large number of experimental results and theoretical computations were made to examine the hypothesis and it is shown that the demihull approach can be used to predict the influence of the catamaran hull spacing with sufficient accuracy.

2.3 Resistance Components and Scaling

2.3.1 General

The resistance of a surface vessel may be broken down into components attributed to different physical processes, which scale according to different scaling laws. Such a breakdown is presented in Figure 2. The resistance of a vessel (neglecting air resistance) is due to shear stress and fluid normal forces acting on the vessel's underwater surface. The shear stress component is entirely due to the viscosity of the fluid. The normal force component may be separated into two major components: wave making, due to the generation of free surface gravity waves (inviscid) and a viscous pressure component caused by the pressure deficit at the stern due to the presence of the (viscous) boundary layer. The *transom stern presents a special case* and this has been included as a pressure drag component, as has induced drag for catamarans.

The standard ITTC practice is to break down the total resistance into viscous resistance (Reynolds number dependent) and wave resistance (Froude number dependent) components. This is described in equation (2.3):

$$R_T(F_n, R_n) = R_W(F_n) + R_V(R_n) = R_W(F_n) + (1+k)R_F(R_n) \qquad (2.3)$$

The wave resistance (R_W) contains the inviscid component and the viscous resistance (R_V) includes the resistance due to shear stress (friction drag) and the viscous pressure component. In practice, the viscous resistance is usually estimated using the ITTC-1957 correlation line (C_F) together with a suitable form factor (1+k). Here C_F is an approximation for the skin friction of a flat plate; the form factor is used to account for the three-dimensional nature of the ship hull. The form factor includes the effect of the hull shape on the boundary layer growth and the viscous pressure drag component. It should be noted that the ITTC-1957 correlation line is an empirical fit and that some form effect is included. The wave resistance component is usually derived from model tests or possibly from inviscid computational fluid dynamics (CFD) methods.

A particular problem for catamaran vessels at higher speeds ($F_n > 0.6$) is that, due to their slenderness, the total resistance is dominated by the viscous resistance components. This is unfortunate since the skin friction is calculated empirically based on the friction of a flat plate and is then modified, in a semi-empirical manner, to obtain the viscous resistance component. The relative magnitude of this resistance component can lead to a lack of precision in the final result.

It is therefore quite clear that the selection of a suitable form factor is critical to accurate extrapolation of model test results to full scale. Whilst it is possible to determine the form factor of a high-speed vessel by a number of alternative methods, it is not readily found during standard model testing procedures.

2.3.2 Direct Measurement of Resistance Components

A number of attempts have been made to measure the individual resistance components. Apart from total resistance, it is possible to measure pressure resistance using static pressure tappings and skin friction resistance using Preston tubes. It is also possible to measure the viscous resistance and the wave pattern resistance to a reasonable degree of accuracy. From these measurements, the form factor may be derived.

The viscous resistance component may be derived from measurements of the velocity field behind the hull. The transverse extent of the wake survey will determine how much of the viscous component is measured. For slow speed forms, a viscous debris may exist which is concentrated in the wake directly astern of the model. However, for high-speed vessels, viscous debris (probably originating from the spray sheet) may be observed to extend several times the model maximum beam either side of the model centre line and between the hulls in the case of multihulls. The viscous resistance components may also be investigated in a wind tunnel.

The wave resistance component may be derived from measurements of the wave pattern, for example using an Eggers type approach [18]. The total viscous resistance, hence form factor may then be deduced by subtracting the measured wave pattern resistance from the measured total resistance. However, the assumption implicit in this method is that any other non-viscous components of resistance such as wave breaking are negligible.

2.3.3 Geosim Series - A Series of Geometrically Similar Models of Increasing Length

Models are tested at different scales and hence Reynolds numbers. Since the viscous resistance is a function of Reynolds number the resistance breakdown may be derived from model tests at the same Froude number but different Reynolds number. This approach was first introduced by Telfer [19]. This method correlates the resistance of models tested at the same Froude number but different Reynolds number and leads the way to correlation with full-scale resistance predictions. The method does not, however, lead to a more detailed insight into the physical significance of the resistance components (and the mechanisms by which they are generated). It can be used to determine full-scale resistance, although the use of a large number of geosim models makes the approach expensive and usually confined to research investigations.

2.3.4 Practical Scaling and Estimates of Form Factors (1+k)

As mentioned earlier, a particular problem for high-speed craft (Fn>0.6) is that, due to their slenderness, the total resistance is dominated by the viscous resistance components. This increases the need for realistic and accurate estimates of form factors for such vessels.

A number of techniques for determining form factors, directly or indirectly, are available, including the use of low speed tests, measurement of total viscous drag and measurement of wave pattern resistance. Brief summaries of these techniques are as follows.

A Low Speed Tests

Hughes [20] initiated a 'new' method of scaling in the 1950s known as a form factor approach. He proposed the following method to determine the form factor:

(1) Model is tested at very low Froude number until C_T runs parallel with C_F hence $C_W \rightarrow 0$. In this case:

$$(1+k)=\frac{C_T}{C_F} \tag{2.4}$$

The results of this kind of test can be unsatisfactory due mainly to the difficulties in obtaining good low speed results as well as an insufficient knowledge of Froude number effects. Attention has been given by the Powering Performance Committee of the ITTC 1990 to the latter effect [21].

(2) C_W is extrapolated back at low speeds assuming $R_W \infty V^6$ or $C_W \infty R_W/V^2 \infty V^4$, i.e. $C_W \infty Fn^4$ or $C_W = aFn^4$ where a is a constant value. Hence from two measurements of C_T at relatively low speed:

$$(1+k)=\frac{C_{T1}-\left(\frac{F_{n1}}{F_{n2}}\right)^4 C_{T2}}{C_{F1}-\left(\frac{F_{n1}}{F_{n2}}\right)^4 C_{F2}} \tag{2.5}$$

and,

$$\frac{F_{n1}}{F_{n2}}=\frac{V_1}{V_2} \tag{2.6}$$

Where,

$$C_F = \frac{0.067}{(\log_{10} R_n - 2)^2} \tag{2.7}$$

Equation (2.7) is the simpler formula, which replaces the original proposal i.e. $C_F=0.066/(\log_{10}Rn-2.03)^2$. Subsequent and current practice is to derive (1+k) based on the ITTC formula, $C_F=0.075/(\log_{10}Rn-2)^2$.

Speeds as low as possible ($Fn \cong 0.10$ to 0.22) are necessary for this method [22]. However, it is generally difficult to achieve accurate resistance measurements at such low speeds. Problems almost always arise when a model is tested at very low speeds and one cause is attributed to laminar flow effect [23]. Therefore, great attention must be given to the determination of the true speed through the water. The presence of trip wire, studs or pins, or sand strip around the bow of a ship model therefore could have a marked effect upon the measured resistance [22].

Prohaska, in Hughes [24], used a similar technique to Hughes but applied more data points and formulated his equation as:

$$\frac{C_T}{C_F} = (1+k) + a\frac{F_n^{\,4}}{C_F} \tag{2.8}$$

Where (1+k) and a are the intercept and the slope, respectively.

For full form vessels, the points may not plot on a straight line and some other power of Fn between 4 and 6 may be more appropriate. Furthermore, a later ITTC recommendation as a modification to Prohaska's is:

$$\frac{C_T}{C_F} = (1+k) + a\frac{F_n^{\,n}}{C_F} \tag{2.9}$$

Where n, a and k are derived from a least square approximation.

This method is widely used for very low speed vessels, generally at $Fn \leq 0.1$ [25], without immersed transom. This is a drawback because unwanted Reynolds scale effects are then often introduced.

The application of low speed tests to transom stern vessels is questionable because of the different flow regime in the transom area (the flow does not separate from the transom at slow speed as it does at high speed). Furthermore, with slender hulls, the drag at slow speed is so small as to be difficult to measure accurately. Bow down low speed tests for fine transom stern forms have been reported by Molland and Couser [15] as a means of overcoming this problem and have had limited success. Dyne [26] reported that the pressure drag is low and its influence on k is practically negligible.

B Measurement of Total Viscous Resistance

Total viscous resistance (C_V) can be measured by a wake traverse. In this case, form factor is calculated as:

$$(1+k)=\frac{C_V}{C_F} \tag{2.10}$$

over the range of Froude number. In this case, C_V may include wave breaking which would lead to an overestimate of (1+k). This technique is satisfactory over a range of speeds but is very time consuming. It is, therefore, only applicable as a research tool and would not be recommended for routine commercial testing unless the system is automated [27].

Viscous resistance can be obtained by means of a wake traverse analysis such as that carried out by Insel and Molland [13]. The method used a wake traverse rig consisting of a rake with 24 pitot tubes, 12 2-way solenoid valves and 12 pressure transducers together with a micro computer based data acquisition system in order to survey the wake. This technique provided satisfactory results for obtaining the viscous drag of catamarans.

The viscous resistance measurement can also be carried out using a 3D Laser Doppler Velocimeter (LDV) such as that performed by Cordier and Dumez [28 and 29]. They also used a wake traverse and the two systems compared satisfactorily.

C Measurement of Wave Pattern Resistance

In this method the form factor is derived from the measurement of wave pattern resistance. Tanaka et al. [30] measured wave pattern resistance whilst Cordier and Dumez [28] and Insel and Molland [13] used direct measurement methods for wave pattern and wake analysis. In the case of wave analysis, form factor is determined as:

$$(1+k)=\frac{(C_T-C_{WP})}{C_F} \tag{2.11}$$

Wave breaking resistance is not included which may, if present, cause an overestimation of (1+k). The results are applicable over the range of higher speeds for vessels with transom sterns for which slow speed tests are not suitable. Fortunately, C_{WP} can be measured in a routine manner.

2.3.5 The Use of Wind Tunnels without the Presence of Wave Resistance

The testing of a reflex model in a wind tunnel enables direct measurement, and provides a convenient way of examining in detail, the viscous resistance and its components of skin friction and viscous pressure resistance in the absence of any wavemaking effects. However, some problems still remain, the largest of which is the uncertainty of there being turbulent flow over the model, that is, that the flow over the model provides a proper modelling of the flow over the full-scale ship hull. Because of the small size of a model, some form of turbulence stimulation is required to produce a rapid transition. Careful consideration of the flow around the transom of the model is also required. Furthermore, as the velocity and pressure distributions as well as resistance for a body moving in a tunnel are different from those of in unrestricted water, blockage effect must be taken into consideration.

In naval architecture, this method has for example been used by Lackenby [2] and by Joubert and Matheson [31] who used wind tunnel facilities to measure the resistance of two Lucy Ashton reflex geosims. The investigations have been extended to BSRA trawler series [32] and bodies of revolution [33]. Of major interest, the use of flat plate equations to determine the frictional resistance was not suggested because the effects of pressure gradient, surface curvature, lengthwise area variation and waves were omitted [31, 32 and 33].

As mentioned in Chapter 1, and referring also to Lackenby [2], the absence of surface waves should not significantly influence the findings of wind tunnel investigations. The results of this work indicates that at lower speeds, up to Fn of about 0.3, there is close correspondence between the wind tunnel measurements and the total viscous drag by wake traverse measurements in the test tank. At a Fn of about 0.5 the measured wake traverse value was about 5% higher than that measured in the wind tunnel, indicating an increase in total viscous drag due to surface wave effects. This difference might be expected not to get any bigger at higher speeds when the proportion of wave resistance will decrease again relative to the total drag.

2.3.6 Computational Fluid Dynamics (CFD) Methods

CFD technique, of varying degrees of complexity, may be used to predict various resistance components. Potential codes may be used to derive the pressure resistance due to inviscid flow characteristics (wave pattern resistance). The boundary layer integral method may be used to estimate the boundary layer growth in areas where separation and recirculation do not occur. This method would provide some insight into the pressure form drag. Full Reynolds averaged Navier-Stokes (RANS) codes may be used to predict the flow where separation and recirculation occur, thus potentially providing good estimates of form factor and possible scale effect; however these methods are extremely computationally intensive especially for the computation of high Reynolds number flow.

Computational fluid dynamics (CFD) is now being widely used as these advanced technologies take advantage of the increasing speed of computers. CFD is defined as a technique for making hydrodynamic calculations to predict the basic phenomena of specific flow problems [34]. CFD may also be defined as an analysis of systems involving fluid flow, heat transfer and associated phenomena such as chemical reactions by means of computer based simulation [35]. The technique is very powerful and spans a wide range of industrial and non-industrial application areas. These include mixing and separation in chemical process engineering, flows inside rotating passages in turbomachinery, calculation of lift and drag in aerodynamics of aircraft and vehicles and the hydrodynamics of ships.

The ultimate objective of CFD development is to provide a capability comparable to other CAE (Computer-Aided Engineering) tools such as stress analysis code. The main reason why CFD has lagged behind is the tremendous complexity of the underlying behaviour, which precludes a description of fluid flow that is at the same time economical and sufficiently complete. The availability of affordable high performance computing hardware and the introduction of user-friendly interfaces have led to an upsurge of interest and use of CFD.

CFD is popularly used because it provides several unique advantages such as a substantial reduction of lead time and costs of new designs, the ability to study systems where controlled experiments are difficult or impossible to perform and practically unlimited level of details of results [35]. The investment costs of a CFD capability are not small. However, the total expense is not normally as great as that of high quality experimental facilities such as towing tanks and wind tunnels. The major weakness of CFD techniques is that they are difficult to validate [35] and the validation process can be expensive [36 and 37].

The use of CFD in ship design is growing and this allows designers to investigate a full range of design options at the preliminary design stage, prior to full commitment in the build process or before choosing models and embarking on physical model experiments. One of the advantages of CFD is that the scale effects normally associated with model scale experiments can, in theory at least, be eliminated from the equations since CFD analysis is scale independent [37].

3 WIND TUNNEL INVESTIGATION

3.1 Introduction

As discussed earlier, in order to isolate the viscous component experimentally, a series of wind tunnel tests were carried out using the low-speed wind tunnel at the University of Southampton [39]. The models were a pair of ellipsoids with length to maximum diameter ratio (L/D) of 6.0. This ratio was selected as it was likely to provide an adequate velocity interaction between the bodies. An ellipsoid body of revolution was chosen because such a mathematical form would allow validation of the proposed experimental and numerical techniques to be made by comparisons with analytical and other published results for single bodies of revolution. The use of bodies of revolution for resistance investigations, especially in the field of aeronautics, have been widely carried out in the past including Young in the 1930s, Granville in the 1950s and Patel in the 1970s. In naval architecture, this was initiated by Joubert in the 1970s.

In order to express typical catamaran configurations, the models were tested with a number of separations to length (S/L) ratios: 0.27, 0.37, 0.47 and 0.57. The single hull configuration was also included to compare its resistance characteristics with those of the twinhull configuration. The measurements, analysis and discussions cover the aspects of drag and sideforce, pressure distribution, form factors, velocity distribution and the appearance of cross-flow and induced drag.

3.2 Description of Models

The models were built from fibreglass reinforced plastics (FRP) with an overall length of 1200 mm and diameter of 200 mm. These values were chosen as being appropriate to provide suitable S/L ratios to detect viscous interference, as well as the largest size commensurate with acceptable limits on corrections due to wall effects.

The models were constructed as hollow models in order to allow the insertion of pressure tappings. They were completed with internal stiffening, and seatings for the dynamometer and strut attachment.

The models each have a fineness ratio 6.0, which was chosen as the biggest ratio where the velocity interference is still sufficiently significant. Further information on the effect of varying fineness ratio against velocity interference can be found in Appendix A.

The principal particulars of the model, together with its coefficient in naval architectural terms, are as follows:

L	: 1200 mm	WSA	: 0.601 m^2	C_B	: 0.521	C_P	: 0.664
B	: 200 mm	∇	: 0.025 m^3	C_M	: 0.785	$L/\nabla^{1/3}$	: 5.17

Detailed calculation of the particulars can be found in Appendix B and it should be noted that the coefficients are based on one half of the reflex model, see Figure 3a.

The models were tested at four separations to length ratios (S/L): 0.27, 0.37, 0.47 and 0.57. In the terms of gap to length ratio, G/L will be 0.1, 0.2, 0.3 and 0.4 respectively. The single hull configuration was also tested.

The model set-up in the wind tunnel is shown in Figures 3b (schematic) and 3c (photograph). Further particulars of the models and the principal design characteristics of the four S/L ratios are given in Figures 4a to 4d.

Leading edge roughness (a turbulence stimulation strip) was applied to both ellipsoids, consisting of 0.15 mm diameter carborundum grit (No. 100) spread evenly over double-sided adhesive tape of 10 mm width; the leading edge of the roughness strip was located about 5% aft of the leading edge.

3.3 Apparatus and Tests

3.3.1 General

The tests were carried out in the 7ft x 5ft (2.13m x 1.52m) low-speed wind tunnel at Southampton University. Further details of the tunnel can be found in [40].

The upper ellipsoid was connected to the wind-tunnel dynamometer to measure total drag and sideforce. The lower ellipsoid could be adjusted to alter the separation between the two bodies. It was fitted with 109 pressure tappings connected to a pressure transducer to measure the pressure distribution over the body, see Figure 3b. The circumferential and longitudinal positions of pressure tappings are given in Figures 5a and 5b, respectively.

A pitot-static tube velocimeter was situated at approximately 0.25L behind the models, see Figure 3b. This was used for the measurement of (vertical and horizontal) velocity distributions.

3.3.2 Dynamometer

The existing three component dynamometer mounted above the wind tunnel was used for the tests. Further details can be found in [40].

3.3.3 Tests

The tests for each S/L ratio were carried out at three nominal speeds of 20, 30 and 40 m/s giving a range of Reynolds Number (Rn) based on model length: 1.6 to 3.2 x 10^6. In the context of aerodynamic wind-tunnel work [41], the models are in subsonic flow within the range of Mach Number: 0.06 to 0.12.

Since part laminar flow could occur over the smooth bodies at Rn up to 5 x 10^5 [42, 43 and 44] or even up to 3.2 x 10^6 [45], the tests were conducted with the models in two conditions. The first was without a transition strip. The second case was with a transition strip placed at about 0.05 L from the leading edge. Tests without transition strip for S/L = 0.57 were not carried out.

The tests were also extended to the single ellipsoid case to compare its drag, sideforce and form factors with those of the twin ellipsoids.

The investigation of the velocity distribution both vertically and horizontally about the model centre line was carried out at S/L=0.27 and 0.37 using the velocity measuring equipment situated at about 0.25L behind the model. This distance (0.25L downstream) was a typical measurement position for calculating wake traverse e.g. using Melvill Jones method [46].

Flow visualisation tests were also carried out in order to understand the flow characteristics over the body, especially about the trailing edge. Further details of the flow visualisation techniques can be found in [47]. In the current work, the flow visualisation (with transition strip) was carried out by applying red colour paint and then followed by a number of white-cotton threads situated close to the trailing edge. The tests were carried out at the nominal speeds of 20, 30 and 40 m/s.

3.3.4 Data Acquisition and Analysis

An automated computer based system for data acquisition was used. Data was recorded from the three-component dynamometer, which measured the forces acting on the model. Calibrations for drag and side-force were carried out, and the calibration constants included in the data acquisition and reduction system.

Drag and sideforce in Newtons were output from the acquisition system. These were subsequently non-dimensionalised using the free stream velocity (V_0) and wetted area (A) of the body as follows:

$$C_D = \frac{Drag}{0.5\rho A V_0^2} \tag{3.1}$$

and,

$$C_{SF} = \frac{Sideforce}{0.5 \rho A V_0^2} \tag{3.2}$$

Further details on the measurements of velocity are given in Appendix C.1.

Pressure measurements over the surface of the model were obtained using a Scanivalve system and pressure transducers. This allowed pressure data to be measured from the 109 individual pressure tubes and fed to the acquisition system.

For each local measurement of pressure (P_P), the non-dimensional pressure coefficient (C_P) was obtained directly as:

$$C_P = \frac{P_P - P_0}{0.5 \rho V_0^2} \tag{3.3}$$

where P_0 and V_0 are the reference free stream static pressure and velocity respectively. This expression does not require an explicit value for the calibration constant of the particular pressure transducer, since the transducer had a linear response.

The overall order of accuracy of the dynamometer force measurements and pressure measurements are within 1% [40].

3.4 Data Reduction and Corrections

The conditions under which a model is tested in a wind tunnel are not the same as those in free air and corrections must be carried out to account for the boundary effects. Many researchers in the past [48] have considered this problem, i.e. the interference of a wind tunnel on the drag of a body. The variation in drag arising from the restriction of the tunnel is not only affected by the blockage ratio but also by the length of the body, the velocity of the air and the geometries of the body and the wind tunnel [49].

The tunnel was run at constant pressure using a Betz manometer mounted upstream of the model. Changes in (atmospheric) pressure and temperature led to (small) changes in air density (ρ), dynamic viscosity (μ) and hence actual upstream velocity. The actual speed is used for the calculation of Reynolds number (Rn), drag coefficient (C_D) and sideforce coefficient (C_{SF}).

Boundary corrections consist of three major items: wake blockage, longitudinal buoyancy and solid-body blockage [50, 51 and 52]. The wake blockage for three-dimensional arrangements, e.g. the case of ellipsoid bodies of revolution, is very small and hence is usually neglected [50 and 52]. The longitudinal buoyancy correction is also insignificant [50]. It is indicated that wake blockage effects give rise to an additional effect on the drag force in which if C_D is about 0.004 the correction will be 0.0014% for single body and 0.003% for twin bodies [52]. This correction is also very small hence again is neglected.

The most recent reference [52] gives a formula for axisymmetric bodies for three-dimensional flow in rectangular wind tunnels. This formula indicates that the correction is 0.7% for the single body and 1.4% for the twin bodies. The proposals in [52] are applied for the blockage corrections because they are believed to be more reliable. Total drag and sideforce are corrected accordingly. Complete calculations of velocity, Reynolds number and boundary corrections can be found in Appendix C.

3.5 Presentation of Data

ITTC-1957 correlation line has been used to predict skin friction (C_F) hence a constant value of C_F was applied at the same speed (hence Reynolds number) for monohull and twinhull configurations. Normal drag or viscous pressure resistance (C_{VP}) is obtained from the integration of pressures over the body. The summation of (C_F+C_{VP}) can be compared with direct measurement of C_T from the wind tunnel tests. Furthermore, Equation (2.1), which contains viscous interference coefficients ϕ and σ is not convenient since σ could not be measured independently.

The results of the pressure measurements can be found in Appendix F and Figures 12 to 57. The pressure coefficient values were compared with other published data [55, 56 and 57] in Figure 58. Pressure drag was estimated by integrating the pressure coefficients over the body and, in addition to skin friction, will form the total drag. The comparison of total measured drag against calculated drag (skin friction plus pressure drags) can be found in Figure 59 and is further discussed in Appendix E.

The existence of sideforce and its variation with Reynolds number and S/L ratio was investigated, and the results are given in Tables 3 and 4. Sideforce may cause an additional drag, induced drag, which would influence the estimation of form factors. For example, if the induced drag was significant, the estimates of form factors would be less than when induced drag is not present or is neglected.

The distribution of velocity, indicating the velocity variation between and beyond the two bodies, for single horizontal and vertical cuts can be found in Figures 60 and 61. Flow visualisation studies are shown in Figures 62 and 63.

3.6 Discussion of Results

3.6.1 Force Distribution

Total drag and side-force are given in Tables 1 to 4 and are plotted in Figures 6 and 7. These results show the effects of transition strip, Reynolds number and variation of spacing between the hulls.

Some speed (Rn) effect is observed in the results. This may be partly due to the relatively low values of forces at the lower speeds, particularly at 20 m/s, and the possibility of extensive laminar flow in the case of the unstimulated models. It is considered that the results at 40 m/s were reliable and that these should be used for analysis and comparative purposes.

It can be seen from Tables 1 and 2 that drag coefficient without transition strip is about 0.0040 whilst that with transition strip is about 0.0047. In both cases it is clear that interference effects are present. There is an increase in drag for the two body case compared with the single body of the order of 2% to 3% without transition strip and 7% to 8% with transition strip. This level of interference remains effectively constant over the range of separations tested. See also Figure 10.

Form factor is defined as for marine applications as C_D/C_F. Values are shown in Figures 8 and 9 and are of the order 1.22 for the monohull and 1.30 to 1.36 for the twinhulls, remaining sensibly constant over the range of separations tested.

The results for sideforce shown in Tables 3 and 4 and Figure 11 indicate that the sideforce coefficient (attractive force between hulls) reduces rapidly with increase in separation and have broadly similar values for both without and with transition strip.

3.6.2 Prediction of Transition Point

Because of the lack of experimental data for the determination of transition point on smooth bodies, estimation has been carried out. A number of published data are available for this purpose [58 and 59] but none of them presented satisfactory results for the case of ellipsoid body of revolution. Ref. [58] provided an approximate formula, which is based on a correlation of transition-momentum-thickness Reynolds number, $R_{\theta tr}$, with transition x-Reynolds number, R_{xtr}. This formula if applied leads to a small proportion of turbulent flow, which is not in agreement with the current work. Ref. [59] introduced the use of a universal curve based on boundary layer Reynolds Number against pressure gradient parameter at transition, which can be applied to bodies of revolution but with great care. This also indicated a small proportion of turbulent flow and again, is not in agreement with the current work.

A parametric study was therefore carried out by assuming the transition point to occur between 0.05L and 0.50 L and examined for the nominal speeds: 20, 30 and 40m/s. This study, which can be found in Appendix D, indicates that the transition location is likely to be situated between 0.2L and 0.3 L. These results are in good agreement with other published data [60, 61 and 62]. These results are further applied to calculate skin friction drag of the models tested without transition strip.

Monohull Configuration

Drag coefficient for 40 m/s (Reynolds number: 3.2 x 10^6) is indicated to be about 0.0040 and the transition point is estimated at 0.2L. This result is in a good agreement with the result in [53] of fineness ratio 5.9 with a distance of transition point from leading edge of 0.257L. This gave a drag coefficient of 0.00405 with the same Reynolds number. Close agreement is also given by airship models A and B of fineness ratio 5.0 [55 and 56] at Reynolds number 3.16 x 10^6, transition point about 0.2L, which indicated drag coefficient values of 0.00405 and 0.00411.

The proportion of total drag to friction drag may be termed the form factor as applied in the marine field. The form factors obtained from the parametric study are 1.17 for 30 m/s and 1.23 for 40 m/s. They are in a good agreement with the fully turbulent results which respectively show the values of 1.22 and 1.23. These results, however, are higher than that in [53] which indicates a value of 1.07 and also in [54] which exhibits a value of 1.12 for fineness ratio 5 and C_B 0.6.

Twinhull Configuration

The introduction of the second body indicates an increase in C_D, particularly for the tests with transition strip, see Tables 1 and 2. This results from interference effects and causes the form factors to increase. The last results at S/L=0.57 should be treated with caution since the second body was relatively close to the tunnel floor.

These results indicate that the smallest separation ratio (S/L) has the largest interference and then reduces when the ratio increases, see Figure 10. This is in general agreement with [12, 15 and 63]. It is noted that the reduction is relatively small over the separations tested. However, the tests at S/L=0.57 indicate a further increase in interference at all speeds. This seems to be incorrect, possibly due to some wall effect at this large separation.

The measurement of forces also indicates the appearance of side-force or suction between the hulls and the results are given in Tables 3 and 4 and Figure 11. Side-force is seen to decrease rapidly as the separation increases.

The presence of side-force could lead to induced drag. However, since the side-force decreases rapidly with increasing separation whilst the drag remains approximately constant (see Figures 10 and 11), it may be inferred that the total drag does not contain a significant induced drag component.

3.6.3 Pressure Distribution

The distribution of pressure over the body is presented both circumferentially and longitudinally, see Figures 12 to 57. Pressure coefficient (C_P) values were recorded for each S/L ratio i.e. 0.27, 0.37 and 0.47 without transition strip and 0.27, 0.37, 0.47 and 0.57 with transition strip. Data for the single body, however, are not available because the single model case was not equipped with pressure tappings. It is however assumed that the largest spacings (S/L=0.47 and 0.57) will closely represent the single body case.

Circumferential Plots

Pressure plots at 0%L (leading edge) and 100%L (trailing edge) are excluded since they are both positive and constant, at approximately 1.02 and 0.2. The plots indicated that positive pressures also occur at places close to leading and trailing edges i.e. at 5%L and 95%L, see Figures 12 and 21. Between these, the pressures become negative. The maximum negative occurs at 50%L especially at position 0 and positions close to it (i.e. 1 and 11), at about -0.15. These results (which equate to the reflex waterline, Figures 4a and 4b) are relevant since those positions represent the closest gap, which show the lowest or the most negative pressures. This trend is the same in almost all the S/L ratios.

A contradiction is given by S/L = 0.57 (see Figure 21). The maximum negative pressures were also obtained at 50%L but the precise location changes to position 6 and any positions close to it. This is likely to arise because the second body is now very close to the tunnel floor hence the bottom wall effect may be significant.

It is seen in Figures 12 to 21 that the low speed (20 m/s) pressure data show some fluctuations and this may be due to the low values of actual pressures measured. The differences between the data at 30 m/s and 40 m/s are small and these data are considered to be reliable.

Longitudinal Plots

The longitudinal distributions indicated that positive pressures occur at both ends, at the leading and trailing edges, see Figures 22 to 57. Cp at the leading edge is about 1.02, which is close to the stagnation pressure. Cp at the trailing edge is about 0.2.

Almost all plots (i.e. without and with transition strip) indicated the same tendency. Smaller S/L ratios tend to show more positive pressures at the front and the rear parts but at the middle part they tend to exhibit more negative pressures. This is generally followed when S/L ratios change from 0.27 to 0.37 and 0.47. This would be expected since the middle part is the closest gap for each S/L ratio in which the pressure must be the smallest and conversely, the velocity must be the highest.

This trend, however, seems to be untrue for S/L=0.57. This ratio exhibits a more negative pressure at the middle part. This is believed to be due to the bottom wall effect at this largest separation, see Figure 4d.

An anomaly is shown when the nominal speed is 20 m/s and without transition strip (see Figures 22a to 33a) In this case, up to 10% L, the pressure decreases but then suddenly increases and from 20% L, it then returns to the expected levels. It is possible that this is due to transition and this information might be used to estimate the location of the transition point when sufficient experimental data are not available [57]. Further discussion of this can be found in Appendix D.

As mention earlier, some of the data at 20 m/s may be questionable due to the low values of actual pressures measured, whilst those at 30 m/s and 40 m/s are considered to be reliable.

Comparison with Published Data

A comparative study with previously published data [55, 56 and 57], based on the longitudinal pressure data, has been carried out. This can be seen graphically in Figures 58a to 58c. Figure 58a indicates that the pressure distribution over the fore end compares well with the front part of model A [55 and 56], which has a similar fore end shape to the current model.

In the case of model B [55 and 56], see Figure 58b, its front part is bluffer hence the pressure is more negative. However, the rear part is similar in shape to the current model and the pressure distribution becomes similar.

A similar effect is shown by the data in [57], see Figure 58c. This shows even more negative pressure at the front part. This is because the front part is much bluffer. However, the rear part is similar in shape to the current model and, again, the pressure distribution is similar.

The results of this study indicate that the pressure distributions of the current work compare well with previously published data for similar bodies of revolution.

Integration of Pressures

Pressure drag and sideforce can be calculated from the integration of the pressure distributions. This calculation can be found in Appendix E.

Pressure drag along with skin friction drag forms the total drag. The results indicate that total drag obtained from the summation of pressure drag and skin friction drag is higher than the measured total drag. This occurs at low speed tests (20 and 30 m/s), in which low measurements were recorded. The difference is about 10% to 40% at 20 m/s and about 2% to 8% at 30 m/s. At higher speed (40 m/s), the difference is not significant (less than 1%). The plot of total measured drag in comparison with the skin friction plus pressure drag can be seen in Figure 59.

The estimation of sideforce from the pressure distributions indicates that sideforce decreases as the separation increases. This is not the case for S/L=0.57, possibly due to the wall effect. The agreement with the measured data is very reasonable, particularly at the highest speed tested.

3.6.4 Form Factors

Form factors (1+k) for the monohulls and form factors for the twinhulls including viscous interference (1+βk) were obtained from Equation (3.1) The resulting values of (1+k) and (1+βk) for the various configurations are summarised in Tables 5 and 6. These factors may not necessarily be used directly for design or scaling purposes, but they do provide a broad indication of changes in viscous resistance and viscous interference due to changes in separation to length (S/L) ratio and speed (or Reynolds number).

For the monohulls, reference to Tables 5 and 6 indicate an increase in (1+k) with increasing speed and so as for twinhull configurations. This phenomenon would be expected physically.

For the twinhulls, reference to Tables 5 and 6 indicate (1+βk) values to be higher than the corresponding monohull (1+k) values indicating $\beta>1$ and suggesting some viscous interference between the hulls as well as the form effect of the demihulls. An exception was given to low speed tests (30 m/s) without transition strip, in which $\beta<1$ for two configurations (S/L=0.37 and 0.47). This is possibly due to low drag measurement.

3.6.5 Velocity Distributions

Single cut velocity distributions were measured at about 0.25L behind the model, both vertically and horizontally (see Figures 60 and 61).

The distributions were recorded at two configurations i.e. S/L = 0.27 and 0.37 at the nominal speed of 30 m/s. Figure 60 shows the velocity in the horizontal plane midway between hulls decreases between the hulls. Wider separation (S/L=0.37) shows that the velocity between -50 cm to 50 cm is slightly smaller than that of the smaller separation (S/L=0.27) (16.2 m/s compared with 17.8 m/s at the centre line position). Beyond that, they are nearly the same.

Figure 60 indicates that the velocity in the vertical centreline plane is smallest at 16.3 m/s at the centreline of each body. It then increases between the bodies and reaches the maximum at the centreline of the composition at about free stream velocity (30.3 m/s).

3.6.6 Flow Visualisation

Flow visualisation, with transition strip, was carried out using red paint (Figure 62) and followed by white cotton thread (Figure 63).

The tests provided a means of identifying flow separation with separation occurring at about 95% L from the leading edge (see Figure 62). This is in broad agreement with experimental work reported in [64] in which flow separation on ellipsoid body of revolution at zero incidence was found at a place close to the end of the body. This is also in agreement with [65], which concluded that the boundary layer separation takes place close to the end of the body.

Cross flow is apparent from the photograph, see Figure 62, although it is not clear in Figure 63. The presence of cross flow would correspond with the measurements of sideforce, and the possible presence of induced drag, discussed earlier.

3.7 General Discussion

3.7.1 The wind tunnel test results provide useful drag, sideforce and pressure data and contribute to understanding the behaviour of two bodies when in proximity, in this case representing reflex model for a catamaran. The results also provide detailed data for validation of the numerical CFD techniques, which would also be used to investigate interference effects.

3.7.2 The pressure distributions for the single body correspond satisfactorily with existing published data.

3.7.3 The detailed pressure measurements provide a good indication of flow and velocity change around the hull.

3.7.4 At the highest test speeds and high Reynolds number, integration of the pressures corresponded well with the direct drag and side-force measurements.

3.7.5 Drag of the twin bodies configuration was consistently higher than the corresponding monohull, confirming the presence of viscous interference between the hulls.

With increase in separation between the bodies, whilst the (attractive) side-force reduced rapidly, drag was seen to remain reasonably constant over the separations tested.

3.7.6 Flow visualisation studies clearly demonstrated the presence of cross flow over the hulls, arising from the velocity and pressure changes over the hulls. The rapid decrease in side-force with increase in separation, with the drag remaining sensibly constant, implies that the cross flow was not leading to induced drag of any significance.

4 THE USE OF CFD TECHNIQUES

4.1 CFD in Ship Design

The application of CFD to solve ship flow problems has grown significantly in recent years. It has been an integral part of the design spiral [38]. It is now possible to predict many complex flow phenomena linked with ship flows with varying levels of accuracy and associated confidence. This includes hull pressure distributions, total viscous resistance, flow visualisation and free surface effects.

Many commercial CFD codes are now available. In general, they are categorised into two solution types, i.e. panel methods and Navier-Stokes solutions [38]. Initially, computational restrictions have limited CFD development to surface panel based methods. Some panel codes to be mentioned are VSAERO/WHIP from the Analytic Method Inc. USA, DAWSON from MARIN the Netherlands and PALISUPAN from the University of Southampton UK. However, with recent increases in available computer power, applications are extended to the Navier-Stokes equations, commonly referred to as Navier-Stokes Solvers (NSS) or Reynolds Averaged Navier-Stokes (RANS). The use of NSS in ship resistance calculations is uncommon and a great deal of research in this field is still required. Further details about NSS can be found in [66]. Although limited to solving low Reynolds flows, NSS has played a major role in RANS code turbulence model development.

RANS code is the most widely used of CFD codes for solving ship flow problems at the present time. It takes the fundamental Navier-Stokes equations and averages them over a period of time. Furthermore, it introduces Reynolds stresses, which require closure for solution [35]. Closure is provided by way of turbulence model which predicts the Reynolds stresses, represented by the last term on the left-hand side of the steady state incompressible RANS Equation and calculated using the Boussinesq assumption. The equations are described in Appendix H.

The marine industry was slow at first to realise the advantages of CFD as a design tool, particularly as a result of high overhead costs and the inherent flow modelling problems linked with unsteadiness and free surface effects. CFD is, however, now considered as a leading edge enabling technology having a wide scope of applications, especially with direct relevance to ship resistance and flow, as identified by Bertram [67].

Currently, CFD solutions are limited to flows at Reynolds numbers much less than ship scale which is attributed to problems associated with grid resolution and turbulence modelling. Therefore, the use of CFD in ship flow studies is generally carried out at model scale only. With present technology, it was reported that the error of resistance calculations was about 3% compared with experiment [68]. Furthermore, Watson and Bull [69] reported that CFD is capable of predicting the fluid velocity distributions at model scale to an accuracy of around 5% of measured values.

The CFD approach has now evolved to a level of accuracy which allows it to be used during the design process. Significant progress has been made in predicting flow characteristics around a given ship hull. Ship designers can use this information to improve a ship's design. However, not much effort has been dedicated to determine viscous drag (both of monohull and multihull vessels) and viscous drag interaction of multihull vessels, important elements in the development of new designs of such vessel types.

4.2 Outline of CFD Methods

CFD codes are structured around the numerical algorithms that can tackle fluid flow problems. In order to provide easy access to their solving power, all commercial CFD packages include sophisticated user interfaces to input problem parameters and to examine the results. Therefore, all CFD codes consist of three main elements:

(1) Pre-processor.
(2) Flow Solver.
(3) Post-processor.

4.2.1 Pre-processor

Pre-processing consists of the input of a flow problem to a CFD program by means of an operator-friendly interface and the subsequent information of this input into a form suitable for use by the flow solver. The user activities at the pre-processing stage involve:

(1) Definition of the geometry of the region of interest (the computational domain).
(2) Grid generation.
(3) Selection of the physical and chemical phenomena.
(4) Definition of fluid properties.
(5) Specification of appropriates boundary conditions.

The solution to a flow problem (velocity, pressure, temperature etc.) is defined at nodes inside each cell. The number of cells in the grid governs the accuracy of a CFD solution. In general, the larger the number of cells the better the solution accuracy. The accuracy of a solution and its cost in terms of necessary computer hardware and calculation time are dependent on the fineness of the grid. Optimal meshes are often non-uniform: finer in areas where large variations occur from point to point and coarser in regions with relatively little change.

Efforts are under way to develop CFD codes with a self-adaptive meshing capability. Ultimately, such programs will automatically refine the grid in areas of rapid variations. A substantial amount of basic development work still needs to be done before these techniques are robust enough to be incorporated into commercial CFD codes. At present, it is still up to the skills of the CFD users to design a grid that is a suitable compromise between desired accuracy and solution cost.

The majority of the time spent in industry on a CFD project is devoted to the definition of the domain geometry and grid generation. In order to maximise productivity of CFD personnel, all the major CFD codes now include their own CAD-style interface and/or facilities to import data from proprietary surface modellers and mesh generators such as PATRAN, Pro-Engineer and I-DEAS. Recently pre-processors also give the user access to libraries of material properties for common fluids and a facility to invoke special physical and chemical process models (e.g. turbulence models) alongside the main fluid flow equations.

4.2.2 Flow Solver

The numerical methods generally used in CFD flow solvers can be classified as finite difference, finite element and spectral methods [35 and 70]. In outline, the numerical methods that form the basis of the solver perform the following steps:

(1) Approximation of the unknown flow variables by means of simple functions.
(2) Discretisation by substitution of the approximations into the governing flow equations and subsequent mathematical manipulations.
(3) Solution of the algebraic equations.

The main differences among the three separate streams are associated with the way in which the flow variables are approximated and with the discretisation processes.

The finite volume method was originally developed as a special finite difference formulation. This method has now widely been used by many commercial CFD codes including PHOENICS, FLUENT, CFX and STAR-CD. The numerical algorithm consists of the following steps:

(1) Formal integration of the governing equations of fluid flow over all the (finite) control volumes of the solution domain.
(2) Discretisation involves the substitution of a variety of finite difference type approximations for the terms in the integrated equation representing flow processess such as convection, diffusion and sources. This converts the integral equations into a system of algebraic equations.
(3) Solution of the algebraic equations by an iterative method.

The control volume integration distinguishes the finite volume method from all other CFD techniques. The resulting statements express the (exact) conservation of relevant properties for each finite size cell. The clear relationship between the numerical algorithm and the underlying physical conservation principle forms one of the main attractions of the finite volume method.

4.2.3 Post-processor

As in pre-processing, a huge amount of development work has recently taken place in the post-processing field. Owing to the increased popularity of engineering workstations, many of which have prominent graphics capabilities, the leading CFD packages are now equipped with versatile data manipulation tools. These include domain geometry and grid display, vector plots, line and shaded contour plots, 2D and 3D surface plots, particle tracking, view manipulation (translation, rotation, scaling etc.) and colour postscript output.

4.3 Mathematical Models

4.3.1 Governing Equations

The governing equations, which describe the motion of a viscous, incompressible fluid, are the Navier-Stokes equations and the equation of continuity. These are explained in Appendix H. These fundamental equations are averaged over a period of time to produce the Reynolds Averaged Navier-Stokes (RANS) equations. This averaging process introduces the Reynolds stresses, which require a turbulence model to provide closure.

A number of different turbulence models, with various levels of complexity, have been examined over recent years. Standard two-equation turbulence models, e.g. k-ε, have been widely used to examine the flow at model scale. Furthermore, the use of renormalisation group (RNG) k-ε model is now becoming more popular because of some advantages not given by the standard k-ε model.

The basic set of equations solved by the program for laminar flow consists of equations for the conservation of mass, momentum and, in a non-isothermal flow, energy. They are called the Navier-Stokes equations. It should be emphasised that the equations for 'laminar flow' are also valid for turbulent flow. Turbulent flows may be considered to be very unsteady laminar flows. Further details can be found in Appendix H.

4.3.2 Differencing Scheme

The calculated variables are velocity components in a fixed co-ordinate direction and pressure together with any scalar quantities such as enthalpy, density, turbulence kinetic energy, and turbulence energy dissipation. These allow the user to express the equations of conservation for mass, momentum and energy, as follows:

$$Convection - Diffusion = Source \qquad (4.1)$$

integrated over each control volume to give discrete equations, and also to conserve mass, momentum and energy within control volumes. The numerical treatment has therefore to represent the convective and the diffusive fluxes across the surface of each control volume, and to calculate the effects of sources and sinks.

Treatment of the advection terms determine the accuracy of the solutions of the model equations in CFX. The terms are difficult because the more accurate higher order schemes tend to be less robust and slower. There are a number of choices of discretisation methods available in the code, ranging from diffusive (simple upwind schemes) to bounded (quadratic upwind schemes), see [71] for the details. The available schemes are:

(1) Upwind differencing (UDS) which is first order accurate.
(2) Hybrid differencing (HDS), also first order accurate but slightly better than UDS because second order central differencing will be used across streams and in regions of low flow and this scheme is used as the default in the program.

(3) Central differencing (CDS) which is second order accurate but is rarely used because it is not robust, often requiring very small under relaxation factors or giving non-physical solutions.

(4) Higher-order upwind differencing (HUW), which is second order accurate.

(5) Quadratic upwind differencing (QUICK) which is third order accurate for the advection and other term such as diffusion remain only second order.

(6) Modified QUICK to eliminate non-physical overshoots (CCCT) which is third order accurate.

(7) Modified CDS to obtain diagonally dominant matrix (CONDIF) and modified HUW for higher Mach numbers (MUSCL).

4.3.3 Turbulence Models

A turbulence model is a computational procedure to close the system of mean flow equations so that a more or less wide variety of flow problems can be calculated. For most engineering purposes it is unnecessary to resolve the details of the turbulence fluctuations. Only the effects of the turbulence on the mean flow are usually sought. In particular, expressions for the Reynolds stresses and the turbulent scalar transport terms are always needed. For a turbulence model to be useful in a general purpose CFD code, it must have wide applicability, be accurate, simple and economical to run. There are two most common turbulence models. Firstly, classical models, which are based on time-averaged Reynolds equations and these include the k-ε model, Reynolds stress equation model and algebraic stress model. Secondly, there is the large eddy simulation (LES) model, which is based on space-filtered equations.

The classical models form the basis of turbulence calculations in currently available commercial CFD codes. LES are turbulence models where the time-dependent flow equations are solved for the mean flow and the largest eddies and where the effects of the smaller eddies are modelled. Although only the large scale eddies are resolved individually, this still requires the use of extremely fine grids hence causing solutions to be expensive and demanding on present computer resources. However, it is widely believed that LES will become the new standard in calculating turbulent flows with increasing computer power.

A number of classical turbulence models are available: the k-ε model, a low Reynolds number k-ε model, an RNG k-ε model, an algebraic Reynolds stress model, a differential Reynolds stress model and a differential Reynolds flux model. All these models are available for both incompressible and compressible flows.

Standard *k-ε* Model

The standard k-ε model uses an eddy-viscosity hypothesis for the turbulence where k is the turbulence kinetic energy and ε is the turbulence dissipation rate. It is the most popular turbulence model due to its wide degree of applicability and is the most widely used and validated model [35]. It is the simplest turbulence model for which only initial and/or boundary conditions need to be supplied, is well established, and is the default turbulence model in CFX. Further mathematical formulation can be found in Appendix H.

Low Reynolds Number *k-ε* Model

The low Reynolds number *k-ε* model is a modification of the standard *k-ε* model to allow calculation of turbulent flows at low Reynolds numbers, typically in the range 5,000 to 30,000. The model involves a damping of the eddy viscosity when the local turbulent Reynolds number is low, a modified definition of *ε* so that it goes to zero at the walls and modifications of the source terms in the ε equation.

RNG *k-ε* Model

The RNG *k-ε* model is an alternative to the standard *k-ε* model for high Reynolds number flows. The model, derived from a renormalisation group analysis of the Navier-Stokes equation, differs from the standard model only through a modification to the equation for ε except for using a different set of model constants. Further mathematical formulation can be found in Appendix H.

Reynolds Stress Turbulence Model

In the Reynolds stress turbulence model, the eddy-viscosity hypothesis is not invoked. Instead, equations are solved for the individual components of the Reynolds stress. In the algebraic stress model, these equations are solved algebraically whereas in the differential stress model transport equations are solved.

Reynolds Flux Model

The Reynolds flux model solves transport equations for the individual components of Reynolds stress, Reynolds flux and scalar fluctuation (in buoyant flows only).

The k-ε model is widely used due to its relative simplicity, robustness and fairly general applicability. However, this turbulence model suffers from several weaknesses e.g. unable to predict translational flows and relaminarisation accurately at high Reynolds number, tends to underpredict flow separation and have limited capability to predict flows with rapid strain and flows with streamline curvature, etc. [72].

In recent years, turbulence models, which are based on the statistical mechanics rather than the continuum mechanics approach such as the Renormalisation Group model (RNG) has begun to emerge [72]. The RNG k-ε model has been found to have better performance than the standard k-ε model [72 and 73]. Direct benefits of the RNG model e.g. [72] are:

(1) At high Reynolds number, the constants in the RNG k-ε model are evaluated by theory. Low Reynolds number functional relationship are also derived by theory (and not by empiricism).

(2) New terms appear in the ε transport equation, notably the rate of strain term, which are important for treatment of non-equilibrium effects and flows in the rapid distortion limit.

Prediction of k and ε Initial Values

The most accurate simulations can only be achieved by supplying measured values of turbulence kinetic energy (k) and dissipation rate (ε). However, if an outline design calculation is performed such data are often not available. An empirical method to derive the turbulence quantities at the inlet is proposed in the flow solver manual [71], formulated as follows:

$$k_{inl} = C_{P1}.u_{inl}^{\,2} \tag{4.2}$$

and,

$$\varepsilon_{inl} = \frac{k_{inl}^{\,1.5}}{C_{P2}.D} \tag{4.3}$$

where u_{inl} is mean inlet velocity, C_{P1} and C_{P2} are empirical constants (respectively 0.002 and 0.3) and D is hydraulic diameter ($D = 4A/P$, A is inlet area and P is inlet perimeter).

4.3.4 Pressure Correction

Unlike inviscid and incompressible flow, which is governed by elliptic partial differential equations and the relaxation technique (which is essentially an iterative process), viscous and incompressible flow is governed by the incompressible Navier-Stokes equations, which exhibit a mixed parabolic behaviour. Therefore, the standard relaxation technique for inviscid and incompressible flow is not particularly helpful in this case. Such an iterative process, called the pressure correction technique, is further introduced and currently widely applied in the numerical solutions of the incompressible Navier-Stokes equations.

The pressure correction technique is basically an iteration approach, where some innovative physical reasoning is used to construct the next iteration from the results of the previous iteration. This technique is embodied in an algorithm called SIMPLE (semi-implicit method for pressure-linked equations), pioneered and developed for practical engineering solutions by Patankar and Spalding [74].

A number of variants have been developed and included SIMPLER, SIMPLEC and PISO. Refinements to SIMPLE (e.g. SIMPLER) have produced more economical and stable iteration methods. The number of calculation involved in a SIMPLER algorithm is about 30% larger than that for SIMPLE, but CPU time is reduced by 30%-50% [35]. SIMPLEC and PISO have been found to be as efficient as SIMPLER in certain types of flows but it is not clear whether they can be stated to be better than SIMPLER [35]. The PISO algorithm, which stands for Pressure Implicit with Splitting of Operators is a pressure-velocity calculation procedure developed originally for the non-iterative computation of unsteady incompressible flows. However, it has been adopted successfully for the iterative solution of steady state problems. PISO involves one predictor step and two corrector steps and may be seen as an extension of SIMPLE, with a further corrector step to enhance it. Consequently, PISO provides quicker solution than SIMPLE and this was found to be very useful by Watson and Bull [69].

4.4 Validation of the Results

The wide spread application of CFD in the maritime industry has raised the question of code validation. This has brought into question the development of a quality standard in an attempt to improve confidence within the industry and to satisfy the requirements of regulatory bodies. The major emphasis of such standards is to ensure that flow solvers achieve a known level of accuracy.

In terms of validation, it is impossible to assess the prediction performance of a complex CFD code by any means other than by comparison with experimental work. Therefore, ship model data and full-size ship trial data are commonly used as benchmarks for assessing the validity of CFD solutions. However, such an approach will usually restrict the range of geometric/conditions for which the model can be used. This can be dangerous if these restrictions are not appreciated or understood by an end used who could see the code for a completely different geometry and base design decisions on what is a fundamentally flawed analysis. Closed form analytical solutions are also used, but are restricted in their application to practical flow problems.

The process of code validation can be seen as a series of stages involving:

(1) *Verification* of the code implementation against the underlying mathematical formulation. This is to ensure the code is free of error due to mistakes in expressing the mathematics in the particular computer language applied. Ideally the comparison should be made against an analytic solution although often the comparison can only be made with other numerical codes.

(2) Investigation of the *independence* of the solution from numerical parameters. The most common form of dependence is on the density of the grid points at which the governing equations are solved. Normally, the number of grid points is increased until the solution does not change. For iterative techniques, which use a convergence criterion, the dependence of solution on its value has also to be investigated.

    As far as the CFD approach is concerned, the results must be of grid independence [66]. This condition occurs when the increase of grid numbers no longer affects the results, such as total drag. The need to press the matter of grid independence in a very detailed fashion depends on the accuracy of the results expected by the user. If, for example, a less numerical precision (say less than 5%) is required the user can slightly relax the criterion for extreme grid independence and use fewer grid points. This certainly saves computing time which frequently means saving money.

(3) *Comparison* of numerical and experimental data. This is the most crucial area of code validation. As the majority of CFD codes are an approximation to the actual physics of the flow, there will be differences between the experimental and numerical results. Experimental data should have a specified accuracy. This should then allow the difference between experiment and theory to be quantified. However, in many codes a degree of empiricism is used to adjust the numerical

model to fit specific experimental data. The extent to which such an empirically adjusted model can be said to be valid for cases run at different conditions requires careful consideration.

Furthermore, recognising the need for validation in the maritime CFD sector, the American Society of Mechanical Engineers (ASME) has been at the forefront in establishing guidelines and standards. The proposed standards address all aspects of CFD and not just the accuracy of solutions. A detailed resume of the proposed guidelines can be found in the 1996 ITTC Proceedings [68]. The ITTC guidelines for validation of code solutions are based on those detailed in the policy statement of the ASME. Although general validation of a code is still the responsibility of fluid dynamists or computer programmers, the final user must appreciate the need for careful studies in order to assess the validity of a model and its solutions.

4.5 The Use of CFX in the Current Investigation

In order to extend the range of the current investigation, a numerical study was carried out, with the wind tunnel results providing basic data for the cases tested. The numerical work was carried out using the commercial code CFX. It is a Navier-Stokes code, originally developed under the title CFDS-FLOW3D at AEA Harwell [75]. Another example of the use of the commercial code in a similar field is given in [76] where the code FLUENT was used to model and investigate the resistance of a reflex catamaran model.

Among others, the use of CFX has become popular at the present time. The current work was carried out using CFX 4.2. The code consists of two interactive grid generators (CFX-MESHBUILD and CFX-BUILD), two flow solvers (CFX-F3D and ASTEC) and a radiation solver (CFX-RADIATION), two interactive graphics packages (CFX-VIEW and CFX-VISUALISE). Further details can be found in the manuals [71, 77 and 78].

The CFX investigation basically consisted of two stages. Firstly, a geometry model (e.g. ellipsoids or shiphulls) was developed and then the meshes gridded. This was done using CFX-MESHBUILD and the entire explanations can be found in [77]. Secondly, a command file containing information such as types of flow (laminar or turbulent, steady state or transient flow) and input data was created. The two files (geometry and command files) are then run under flow solver solution using CFX Flow Solver. User Fortran files (containing the detailed boundary conditions) and linked to command files may also be applied if necessary. The complete description of the second part can be found in [71].

An output file is finally produced, which stores all the relevant information of each run i.e.:

(1) Type of flow and solution procedures options as in the command file
(2) Topology structure i.e. a list of block names and sizes followed by a list of the patches and their locations
(3) Each wall and conducting boundary listed together with real information of the patches unless it has a default boundary conditions
(4) Grid vertex co-ordinates for each block
(5) Residual and monitoring values for each iteration
(6) Values of relevant variables at cell centres at the end of the run
(7) The list of the walls and conducting boundaries with the integration results over each surface, which gives the force on it.

Further details of output data to be printed can be found in [78].

The correct results are obviously the convergence results. These results will be obtained only if all the problems (including geometry and command files) have been set correctly. The convergence results will be the case if the mass inflow equals the mass outflow. This occurs when the mass source residual has fallen below some tolerance set by the user. Good convergence is illustrated by large values of the ratios: values less than one may indicate divergence. However, convergence difficulties are common if the problems have not been set up as intended (this is discussed further in Appendix G).

The dump file contains the results of the following variables: velocity components, pressure, turbulence kinetic energy (k) and turbulence dissipation rate (ε) which allows the post-processor program (CFX-VIEW) to plot different pictures such as vector, contour and shaded contours for each variable. See also Figure 64 for further details.

4.5.1 Grid Generation

The interactive grid generator is an interface to assist the user to create the geometry of the model. In CFX, the generation of the grid can be done in two ways, (1) by use of CFX-MESHBUILD and (2) by use of CFX-BUILD. In the current investigation, CFX-MESHBUILD was used for all geometry creation, as it was the only one available to the writer during the period of the research.

The interactive pre-processor (CFX-MESHBUILD) creates multi-block meshes to be used by CFX-F3D. Their vertices and edges define blocks, see Figure 65. The edges are subdivided before the grid generation is performed. Two or three-dimensional patches are created in CFX-MESHBUILD to specify the location of boundary conditions to the flow solvers, see Figure 66.

4.5.2 Boundary Conditions

Flows inside a CFD solution domain are driven by the boundary conditions. In a sense, the process of solving a field problem (e.g. a fluid flow) is nothing more than the extrapolation of a set of data defined on a boundary contour or surface into the domain interior. It is, therefore, of paramount importance that users supply physically realistic, well-posed boundary conditions, otherwise severe difficulties are encountered in obtaining solutions. The single most common cause of rapid divergence of CFD simulations is the inappropriate selection of boundary conditions. The best boundary conditions for viscous flow include the inlet, pressure, outlet (in CFX it is called mass-flow boundary) and wall boundary conditions [35].

A simple illustration of the poor selection of boundary conditions might be an attempt to generate a steady state solution in a domain with wall boundaries and a flow inlet but without an outlet boundary. It is obvious that mass cannot be conserved in the steady state and CFD calculations will blow up swiftly. The permissible combinations for the current work is (1) for bounded condition: inlet, wall and outlet, and (2) for unbounded condition: inlets and outlet. The first is called an internal flow problem and the second is called an external flow problem [35]. In the first case, normal velocity, turbulence kinetic energy (k) and turbulence dissipation rate (ε) must be given to the inflow boundary [35, 71 and 79]. In the second case, normal velocity, k and ε are given to the inflow boundary. The same data inputs must also be given to open boundaries, which are assumed as inflow boundary conditions. However, only the normal velocity is given and the rest are set as zero [35, 71 and 79]. Further details of flow types (internal and external flows) can be found in Figures 67 and 68.

Inlet Boundary Conditions

The distribution of all flow variables (including normal velocity, k and ε) needs to be specified at inlet boundaries. It is further recommended to give sufficient distance (i.e. more than or equal to the body length) to the upstream boundary. Patel et al [79] suggested at least one body length and Lin et al [80] also recommended one body length as the distance from the leading edge to the upstream boundary.

Outlet Boundary Condition

The boundary conditions required on the outlet boundary depend on the location of that boundary [79]. If outlet boundaries are placed too close to solid obstacles it is possible that the flow will not have reached a fully developed state (zero gradients in the flow direction) which may lead to sizeable errors. If the location of the outlet is selected far away from geometrical disturbances the flow often reaches a fully developed state where no change occurs in the flow direction. An outlet surface can be placed in such a region and then the gradients of all variables (except pressure) are zero in the flow direction far away from the obstacles. In order to give accurate results, it is imperative that the outlet boundary is placed much further downstream than 10 diameters of the solid body [35]. The solutions are found to be independent of the location of the outlet boundary when the distance is higher than one-half of the body length behind the stern [79]. Lin et al using ISFLOW code recommended that the minimum distance is twice the body length [80].

External Boundary Conditions

Patel et al [79] found that the solutions become independent of the location of the exterior boundary beyond a half body length, whilst Lin et al [80] proposed one body length to be the optimum distance.

Wall Boundary Conditions

The wall is the most common boundary encountered in confined fluid flow problems. The no-slip condition (u=v=0) is the appropriate condition for the velocity components at solid walls. Since the wall velocity is known, it is not necessary to perform pressure corrections to the wall. For the other variables, special sources are constructed, the precise form of which depends on whether the flow is laminar or turbulent. Immediately adjacent to the wall, an extremely thin viscous sub-layer exists and followed by the buffer layer and the turbulent core. The number of mesh points required to resolve all the details in a turbulent boundary layer would be prohibitively large and normally a wall function is employed to represent the effect of the wall boundaries.

In most CFD codes the wall boundary conditions are satisfied through a wall law [35 and 81]. This saves computing power since the innermost part of the boundary layer, where the gradients are largest, is not simulated but represented by the law of the wall. Currently, the most accurate way of solving turbulent flow in general purpose CFD code is to make use of empirical fits provided by the wall function approach.

The implementation of wall boundary conditions in turbulent flows starts with the evaluation of y^+, which is formulated as follows:

$$y^+ = \frac{\Delta y_p}{\nu}\sqrt{\frac{\tau_w}{\rho}} \tag{4.4}$$

Where Δy_p is the distance of the near wall to the solid surface. A near wall flow is taken to be laminar if $y^+ \leq 11.63$ [35]. The wall shear stress is assumed to be entirely viscous in origin. If $y^+ > 11.63$ the flow is turbulent and the wall function approach is used. The criterion places the changeover from laminar to turbulent near wall flow in the buffer layer between the linear and log-law regions of a turbulent wall layer.

The value of y+=11.63 is derived from the intersection of the linear profile and the log-law and is obtained from the solution of:

$$y^+ = \frac{1}{\kappa}\ln\left(Ey^+\right) \tag{4.5}$$

where κ is von Karman's constant (0.4187) and E is a shear stress constant dependent on wall roughness which for smooth walls is E = 9.8.

Using flat plate boundary layer theory [57 and 80], y^+ can also be defined as:

$$y^+ = 0.172\left(\frac{y}{L}\right)R_n^{\,0.9} \tag{4.6}$$

where L is body length and R_n is Reynolds number based on body length.

However, it should be noted that the y^+ value from Equation (4.6) is based on a turbulent boundary layer on a flat plate. It is therefore used only as an estimate in cases where the geometry is not actually a flat plate. Furthermore, y^+ is not a constant but varies over the wall surface according to the flow in the boundary layer.

To obtain the same accuracy by means of a simulation which includes points inside the (laminar) linear sublayer, the grid spacing must be so fine as to be uneconomical. The criterion that y^+ must be greater than 11.63 sets a lower limit to the distance from the wall Δy_p of the nearest grid point. The main mechanism for improving accuracy available to users is grid refinement, but in a turbulent flow simulation it must be ensured that, whilst refining the grid, the value of y^+ stays greater than 11.63 and is preferably between 30 and 500 [35].

In the wall function approach described above, the changeover from laminar to turbulent flow as the distance from the wall increases was assumed to occur at $y^+=11.63$ with log-layer constant (E) = 9.8 and this criterion applies to smooth walls. The current work is assumed as smooth walls. If the walls are not smooth, E should be adjusted accordingly and a new limiting value of y^+ would result. E may be estimated on the basis of measured absolute roughness values and among others, further details can be found in [57].

5 CFD INVESTIGATIONS

5.1 General

As mentioned earlier in Section 4.5, the CFD investigations were carried out using the commercial code CFX. The CFD work started with an investigation using two-dimensional ellipses. This was conducted in order to gain better confidence in the use of CFD and the use of this approach for three-dimensional cases. An elliptical form was chosen because, from two-dimensional point of view, it can represent a three-dimensional ellipsoid (and hence ship hull) form at a water line.

The CFD investigations then considered the cases of single and twin three-dimensional ellipsoids followed by ship hull models.

5.2 Investigations Using Two-dimensional Ellipses

5.2.1 Introduction

The investigations used two-dimensional grid models of twin ellipses representing a catamaran hull form. The models were built with S/L ratios of 0.27, 0.37, 0.47 and 0.57. The investigation was carried out under turbulent flow conditions and wall effect was not taken into account. A single ellipse form was also tested to compare its resistance characteristics with those of the twin ellipse form.

5.2.2 Boundary Conditions

All CFD problems are defined in terms of initial and boundary conditions. It is very important that the user specifies these correctly and understands their role in the numerical algorithm. Initial values of the flow variables must be specified at the flow entrance and this includes u and v velocities as well as k and ε values if using standard k-ε or RNG k-ε turbulence models.

The implementation of the most common boundary conditions in the discretised equations of the finite volume method includes inlet, outlet, wall, pressure and symmetry boundary conditions. They are the most commonly used boundary conditions applied for viscous and incompressible flows.

As the influence of wall is not taken into consideration, the external flow condition is applied [35]. The boundary conditions (for single ellipse case) are set as follows:

- The ellipse is set as rigid wall (wall patches).
- The entrance flow is set as inlet (inlet patches).
- The output flow is set as outlet (mass-flow boundary patches).
- The outer boundaries are set as inlets (inlet patches).

Furthermore, in order to save computing time, a half ellipse was developed and the boundary conditions along the ellipse's centre line were set as a symmetric plane (symmetry patches). It was found that this approach reduced the CPU time about a half without affecting the accuracy of the results. For example, when half body along with 4,200 cells is used, it takes 413 iterations and 338 seconds to converge. However, when full body along with 8,400 cells is applied, it takes 826 iterations and 676 seconds to converge. The final results for total drag and skin friction have similar values. The total drag and skin friction coefficients for 4,200 cells are respectively 0.0801 and 0.0572 and for 8,400 cells are 0.0800 and 0.0572.

Similarly, for two ellipses in close proximity, one ellipse is created and the boundary conditions between the two ellipsis are set as symmetric plane (symmetry patches) and the remaining (the outer boundaries) are set as inlet (inlet patches).

5.2.3 Investigation of Optimum Distance

As explained in Chapter 4, the optimum distance from obstacles in the flow to boundaries is of major importance i.e. to obtain minimum CPU time whilst, at the same time, the interior flow solution should not be affected by the location of the model boundaries.

In CFD flow solutions, the most important boundary location is the outlet, the mass-flow boundary. All outlets should be situated far enough downstream to ensure that the fluid flow is fully developed i.e. zero flow variable gradients in the direction of flow. If an outlet is placed too close to an area with a flow disturbance, it may result in solution errors because the assumed outlet condition of zero flow gradients is not held.

With regard to bluff body flows, it has been shown that there will also be an area of reversed flow downstream. This reversed flow would therefore contradict the outlet boundary condition of outward flow if the outlet were situated too close to the obstacle. It must also be remembered that it is not a good practice to place boundaries at excessive distance from the body. It may certainly waste valuable computational resources, which could be put to better use in resolving areas with high flow gradients.

Careful studies have been carried out on a half ellipse into the position needed in positioning the inlet, outlet and upper inlet boundaries. The positioning of the boundaries is based on the length of ellipse and each study is conducted until convergence is obtained. Firstly, upstream inlet and upper inlet distances were set fixed (1L) and downstream outlet distance was set as 1L, 1.5L, 2L and 3L. It was found that the result remains steady at 2L. Secondly, the upstream inlet was set at 1L, downstream at 2L and upper inlet at 0.5L, 1L, 1.5L and 2L. It was then found that the result was unchanged at 1L. Finally, downstream and upper inlets were respectively set as 2L and 1L and upstream set as 1L, 1.5L and 2L. It was finally found that the result remains steady at 1L. The entire results can be found in Table 7.

It can be seen from Table 7 that convergence criteria have been reached on all of the boundary condition positions. Comparing the results in Table 7, it is clear that the solution to the flow problems is more sensitive to the downstream outlet boundary condition than the upstream inlet boundary condition. The upstream inlet can be placed as close as one plate length upstream of the plate without affecting the flow solution, whereas the outlet mass-flow boundary must be placed at least two plate lengths downstream. The upper inlet needs to be situated at least one length above the obstacle before the solution becomes boundary independent. The current result is in agreement with the work done by Lin et al [80].

Based on the above results, it was decided that the inlet should be placed at a distance of 1L, outlet at 3L and upper inlet at 1L from the obstacle.

5.2.4 Grid Independence Study

Before a CFD solution can be regarded as accurate and valid, it has to be demonstrated that it is independent of the grid used for the solution. By virtue of the fact that the governing equations are approximated, and using a finite number of grid cells in the representation of a continuously varying flow field, it is not surprising that flow solutions are sensitive to the number of grid points. It was therefore necessary to demonstrate for a particular solution that grid independence is achieved. A grid independence study involves carrying out solutions on the CFD model, with successfully refined grids of reduced cell size, until the flow field variables become independent of the cell size, distribution and number. When an asymptotic limit is reached for a specific solution, the solution can be considered as grid independent, i.e. the solution is independent of the coarseness of the grid. The process of finding a grid independent solution can be a complex one, particularly when three-dimensional grids are considered, as the grid properties in each dimension are often interrelated with regard to the flow field variables.

The degree of grid independence for a particular model depends on the required accuracy in the final solution. If high accuracy is required, the user should press the matter of grid independence in a very detailed fashion which often means an increase in the number of cells and CPU time. If a little less precise accuracy (e.g. 1%-2%) can be accepted, the user can slightly relax the criterion for extreme grid independence and use fewer grid points thus saving computing time.

Grid independence case was investigated by applying various grid densities i.e. about 4,500, 7,000, 12,000 and 16,000 grid cells. It was shown that, as far as 2% order of accuracy on drag component is concerned, there is an insignificant discrepancy between 12,000 and 16,000 cells. The results for the single ellipse are respectively 0.073 and 0.072 and the error is about 1.4%. It can be said therefore that grid independence has been reached at about 12,000 cells and the results can be accepted. Further details can be seen in Table 8 and Figure 70.

5.2.5 Solution Strategy

Convergence of a steady state solution up to a third order of accuracy is taken into consideration, in order to achieve the most correct results and to relate to the experimental results. However, it is not easily achieved because the higher solution accuracy tends to be less robust and also slower. The strategy to solve this problem is taken as follows: firstly, the job is run with a first order of accuracy and the result is analysed. The same job is further run with a third order of accuracy and if successful the obtained result is analysed and compared with the first order result.

The most common first order schemes used for the investigation are the upwind differencing scheme (UDS) and the hybrid differencing scheme (HDS). UDS is based on the backward differencing formula hence the accuracy is only first order on the basis of Taylor series truncation error. UDS has been widely used because of its simplicity and can be easily extended to multi-dimensional problems. This scheme, however, produces erroneous results when the flow is not aligned with the grid lines. The resulting error has a diffusion-like appearance and is referred to as false diffusion, further discussed in [35].

HDS exploits the favourable properties of the upwind and central differencing schemes. The scheme is fully conservative and since the coefficients are always positive it is unconditionally bounded. The scheme produces physically realistic solutions and is highly stable. HDS has been widely used in various CFD procedures and has proved to be very useful for predicting practical flows. The disadvantage of HDS is that the accuracy in terms of Taylor series truncation error is only first order [35 and 71] but is slightly better than UDS because second-order central differencing will be used across the streams and in region of low flows [70]. HDS is used as the default in CFX.

For third order of accuracy, the quadratic upstream interpolation for convective kinetics (QUICK) scheme is commonly used. The QUICK scheme uses consistent quadratic profiles –the cell face values of fluxes are always calculated by quadratic interpolation between two bracketing nodes and an upstream node– and is therefore conservative. Since the scheme is based on a quadratic function, in terms of Taylor series truncation error, it is third order on a uniform mesh and is conditionally stable [35]. This scheme, however, is actually partly third order, i.e. third order for the advection and other terms e.g. diffusion remains only second order. This scheme is used for the current investigation and further details can be found in Appendix G.

QUICK schemes, however, can suffer from non-physical overshoot in their solution if the grid quality is not excellent. For instance, turbulence kinetic energy can become negative. CCCT is a modification of the QUICK scheme, which is bounded, eliminating these overshoots. Because this scheme is more accurate, it may take longer time to converge and a direct steady solution may sometimes not be the case. It has been found under the current investigation that (after several hundreds of iterations) the steady state is neither converging nor diverging, which indicates that a steady state solution does not exist. Therefore it is sensible to switch to a transient calculation. Further details of the CCCT scheme are given in [71].

5.2.6 Computational Efficiency

The jobs, consisting of a geometry file and a command file, were run with CFX flow-solver at Reynolds number of 2.4×10^6 as in the experimental investigation. The jobs were primarily run using the ASH machine and, as the time progressed, the use of a high performance computer (HPC) was introduced. ASH is a sun SPARC server with eight 60MHz processors (each with a floating-point unit) and 512 Mbytes of memory, running Solaris 2.6. Meanwhile, the HPC machine is a silicon graphics (SG) Octane, which has 2 processors running at 225 MHz; each processor is a MIPS R10000 Chip revision: 3.4 and the total memory size is 640 Mbytes.

For comparison, the ASH machine can solve the simple problem of 4,200 cells using third order scheme (QUICK) in 3,771 seconds whilst SG Octane solves it in 591 seconds. This is certainly a massive saving of computing time i.e. more than six times quicker.

5.2.7 Discussion of Results

First of all, a single ellipse along with 4,200 cells was investigated using the first order scheme (HDS) and then using the third order scheme (QUICK). Tests using HDS showed that total drag coefficient was about 0.112 whilst using QUICK was about 0.079. The first one seems to be overestimated compared to other data, which indicated that C_D is less than 0.1 [71], and QUICK has improved it significantly. The convergence solution using HDS lasted 338 seconds and 413 iterations, whereas using QUICK, finished in 591 seconds and 719 iterations. This occurs because QUICK is more accurate than HDS hence requiring more CPU time to converge. Further investigations were conducted using QUICK.

The usefulness of CFX was examined by comparing a CFX result (at inviscid condition) with the exact solution for the case of single ellipse. The exact solution is formulated as below:

$$C_P = 1 - \frac{(1+\tau)^2 \sin^2\theta}{\tau^2 \cos^2\theta + \sin^2\theta} \tag{5.1}$$

where τ is maximum thickness/length (D/L) and θ lies between -90° and +90°. The derivation of Equation (5.1) is given in Appendix J. To obtain the solution, the job is set as follows: the flow is set into laminar, the viscosity is set very small (up to 10^{-12}) and the wall is set as slip boundary condition. In this case, the Euler flow condition is applied.

In terms of pressure distribution, the CFX result is in a good agreement with the exact solution both at the leading and trailing edges, see Figure 71. The pressure distribution (C_P) at the leading edge is about 0.95 and at the trailing edge is about 0.93 which are both very close to 1.0, required as the stagnation pressure. The C_P

distributions between the leading and trailing edges are also comparable with the exact solution.

Comparison was also made with a constant pressure distribution given in [82]. In this case, constant pressure is formulated as:

$$C_p = -2t / c \qquad (5.2)$$

Where *t* is maximum diameter or thickness and *c* is chord or length of the body. This also shows a broad agreement at the centre part, as shown in Figure 71.

Furthermore, investigation into the turbulent flow condition was carried out as follows:

- Firstly, the job was run with the first order scheme (HDS) along with the standard k-ε model and SIMPLEC algorithm.
- Secondly, the job was run with the third order scheme (QUICK) along with the standard k-ε model and SIMPLEC algorithm.
- Thirdly, the job was run with the third order scheme (QUICK) along with the RNG k-ε model and SIMPLEC algorithm.

The results indicated that the third step provides the best result and was used for the whole investigation. The second step required more CPU time than the first one but it is more accurate than step two. The third step reduced the CPU time slightly in comparison with the second step and further improves the result by making it closer to the expected value. Initialisation into the flow input has reduced the CPU time about 10%. The use of the PISO algorithm has made further reduction on CPU time by about 5% without affecting the final results. It occurs because PISO adds an extra correction step to SIMPLE or SIMPLEC to enhance its performance per iteration.

The results are summarised in Table 9, which shows total drag, viscous pressure drag, skin friction drag, side-force and form factor. The results are presented in coefficient form as follows:

$$C_D = \frac{total\,drag}{0.5\rho V^2 A} \tag{5.3}$$

Where C_D is coefficient of total drag, ρ is air density, V is nominal speed and A is the projected area of the body in the direction of flow [71], for ellipse A is πLD/4.

Similar formulations are applied to calculate viscous pressure, skin friction and side-force coefficients:

$$C_{VP} = \frac{viscous\ pressure\ drag}{0.5\rho V^2 A} \tag{5.4}$$

$$C_F = \frac{skin\ friction\ drag}{0.5\rho V^2 A} \tag{5.5}$$

$$C_{SF} = \frac{side\ force\ drag}{0.5\rho V^2 A} \tag{5.6}$$

Where C_{VP}, C_F and C_{SF} are respectively the coefficients of viscous pressure drag, skin friction drag, and side-force drag. Total drag is referred to as the total force, viscous pressure drag is referred to as the force normal to the body, skin friction drag is referred to as the tangential force in the direction of flow and side-force drag is referred to as the total force between the bodies [41 and 71].

The ratio of C_D upon C_F is termed the form factor and the approximate value based on overall length and maximum breadth is given in [53]. In this case (when L/D=6.0), form factor for inviscid flow condition for a single body is about 1.20. The results of the current work using CFX leads to a form factor of 1.28, which is considered to be a satisfactory outcome.

It is shown that the effects of twin bodies on drag increase are apparent, as seen in Table 9. Total drag of the twin ellipses is higher than twice of the total drag of a single ellipse and this is in agreement with other data [4]. The total drag of the twin ellipses decreases as separation increases but the skin friction remains unchanged. Side-force, which does not exist in the one ellipse configuration, is clear with the two-ellipse configuration. This can lead to induced drag and, if this is significant, total drag and form factor would be less than previously estimated. Further details can be seen in Table 8. However, because the side-force decreases rapidly with the increase in S/L ratio, but the drag decreases much less rapidly, this indicates that total drag does not contain significant induced drag. Flow separation occurs approximately at the end of the body, Figure 73. This is in agreement with other data such as estimated in [65].

5.3 Investigations Using Three-dimensional Ellipsoids

5.3.1 Introduction

The investigations used a three-dimensional grid model of a pair of ellipsoids in close proximity, representing a catamaran hull form. The investigation was first carried out using ellipsoid body of revolution with L/D=6.0 ($L/\nabla^{1/3}=5.17$) at S/L ratios of 0.27 (G/L=0.103), 0.37, 0.47 and 0.57. The tests were extended to L/D=10.0 ($L/\nabla^{1/3}=7.26$) at S/L of 0.27 (G/L=0.170) and S/L=0.203 (G/L=0.103). All the tests were carried out under turbulent flow conditions. The wall effect was not taken into account. A single ellipsoid body was also tested in order to compare its resistance characteristics with those of the twin ellipsoids.

5.3.2 Boundary Conditions

The distance of the boundaries to the obstacles was made similar to that of two-dimensional cases. This has been proved already for the case of fully developed flow achievement as well as computing space and time efficiencies. The distance is made as follows, 1L for inlets, 3L for outlets, and 1L for outer boundaries. Patches similar to the two-dimensional cases were also applied for three-dimensional cases.

Unlike the two-dimensional cases, one ellipsoid (and not half ellipsoid) is built for the case of the single body, see Figure 74. This, of course, used more CPU time and space. However, this model can be easily reconfigured to represent two-body composition. The setting of boundary conditions were as follows, the ellipsoid was set as wall (wall patches), the flow entrance as inlet (inlet patches), the outer boundaries as inlet (inlet patches), and the outflow as outlet (mass-flow boundary patches). For two ellipsoids in close proximity, the boundary condition between the ellipsoids was set as symmetric plane (symmetry patches). The remaining boundary conditions (the outer boundaries) were set the same as those for the one ellipsoid configuration, i.e. as inlets (inlet patches).

5.3.3 Solution Strategy

The strategy to solve the current problems was the same as that for the two-dimensional cases. First of all, the job was run with the first order of accuracy and the result examined. The same job was further run with the third order of accuracy and the successful job analysed and compared with the first order result. HDS was used for the first order because of the default scheme and being better than UDS. QUICK was used for the third order because it could provide a direct steady state solution.

The jobs containing a geometry file and a command file were run using the CFX flow-solver at a Reynolds number of about 2.4 x 10^6. An example of the command file can be found in Appendix I.

5.3.4 Grid Independence Study

Grid independence was investigated by applying various grid densities i.e. about 50,000, 100,000, 200,000, 300,000, 400,000 and 600,000 cells. It was shown that (as far as the drag component and 2% order of accuracy was concerned) there was an insignificant change between 400,000 and 600,000 cells. The results for a single ellipsoid were respectively 0.00581 and 0.00576, the error being about 0.9%. Therefore it could be said that grid independence has been reached at 400,000 cells and the results could be accepted. The same strategy was applied for two ellipsoids in proximity. Further details can be seen in Table 10 and Figure 75.

5.3.5 Discussion of Results

Ellipsoid Body of Revolution, L/D=6.0 ($L/\nabla^{1/3}=5.17$)

First of all, a single ellipsoid along with 50,000 cells was investigated using the first order scheme (HDS) and then using the third order scheme (QUICK). Test using HDS showed that total drag coefficient was about 0.00960 whilst using QUICK was about 0.00658. The first seemed to be an overestimate compared with other data (e.g. wind tunnel work) and QUICK improved the solution significantly. The convergence solution using HDS lasted 93 minutes and 277 iterations whereas using QUICK finished in 135 minutes and 319 iterations. This occurred because QUICK is more accurate than HDS hence requiring more CPU time to converge. Further investigations were then conducted using QUICK.

As for two-dimensional cases, the feasibility of using CFX as a research tool for the proposed three-dimensional cases was examined by comparing a CFX result (in the inviscid condition) with available data such as (1) slender body theory and (2) an exact solution.

The pressure distributions in coefficient form (C_P) over the surface of a slender spheroid is given in [83]:

$$C_P = (t/c)^2\left[4x^2/(c^2-4x^2)+2-\log(4c^2/t^2)\right] \tag{5.7}$$

Where t is the maximum thickness and the longitudinal distance x is measured from the centre of the body, rather than from the nose.

The exact pressure distribution in coefficient form (C_P) for a prolate spheroid (i.e. including ellipsoid) can be found in [83]. For axisymmetric flow, the exact solution is formulated as below:

$$C_P = 1-(1+k_1{}^2)\left[1+(t/c)^2 4x^2/(c^2-4x^2)\right]^{-1} \tag{5.8}$$

where k_l is longitudinal coefficient of virtual mass.

The results are shown in Figure 76 and the CFX result is in a broad agreement with slender body theory and the exact solution. Pressure distributions (C_P) at the centre part are at similar level, although slightly underestimated compared with those of the slender-body theory and the analytical solution. C_P at the leading and trailing edges is less than 1.0, although at about 0.9, close enough to be acceptable. This is likely to be due to the end geometry itself, which is not built optimally using the available grid generator.

Investigation into turbulence flow condition was carried out as follows:

- Firstly, the job was run with the first order scheme (HDS) along with the standard k-ε model and SIMPLEC algorithm.
- Secondly, the job was run with the first order scheme (HDS) along with the RNG k–ε model and SIMPLEC algorithm.
- Thirdly, the job was run with the third order scheme (QUICK) along with the RNG k-ε model and SIMPLEC algorithm.

It was determined that the third step gave the best result and was applied for the entire three-dimensional investigations. It was also found that by initialising the inflow boundary condition, a saving of 10% on CPU time could be achieved and a further 5% saving was made when the PISO algorithm was applied, instead of SIMPLE or SIMPLEC. An example of a command file can be found in Appendix I.

A single ellipsoid and a pair of ellipsoids in proximity (S/L=0.27, 0.37, 0.47, and 0.57) were investigated. The models were run at Reynolds number of about 2.4×10^6. The results are presented in coefficient form as follows:

Drag coefficient:

$$C_D = \frac{total\ drag}{0.5\rho V^2 A} \tag{5.9}$$

Where C_D is coefficient of total drag, ρ is air density, V is nominal speed and A is wetted surface area (half of surface area of the ellipsoid), noting that the sum of the wetted area of both bodies is used in the twin body case.

Skin friction coefficient:

$$C_F = \frac{skin\ friction}{0.5\rho V^2 A} \tag{5.10}$$

The proportion of C_D upon C_F may be termed the form factor and an approximate value based on overall length and maximum diameter is given in [53]. In this case for single ellipsoid (when L/D=6.0), the form factor is about 1.07.

Side-force coefficient:

$$C_{SF} = \frac{side\,force}{0.5\rho V^2 A} \tag{5.11}$$

The effect of the second body on the increase of total drag is apparent as can be seen in Table 11. Total drag in the twin body configuration is significantly higher than that of the single body configuration. Total drag decreases as the separation increases. Skin friction also decreases when the separation increases as a consequence of changes in the velocity between the bodies. The proportion of total drag upon skin friction, the form factors, can be found in Table 11.

The accuracy of CFX in providing the total drag value as the sum of the friction and viscous pressure components was further investigated using velocities produced by CFX and the Melville-Jones wake traverse method [44]. The formula is as follows:

$$R_V = \rho U^2 \iint_w \left\{1 - \sqrt{g}\right\} \sqrt{g - p}\,.dy.dz \tag{5.12}$$

Where

$$P = \frac{P_B - P_0}{0.5\rho \overline{U}^2} \tag{5.13}$$

$$g = P + \left(\frac{\overline{U} + u}{\overline{U}} \right)^2 \tag{5.14}$$

The analysis of the wake traverse indicated that the coefficient of total viscous drag was about 0.00534, which was about 3% smaller than the CFX results. This would suggest that an adequate level of accuracy can be achieved by CFX using the sum of friction plus viscous pressure.

The skin friction results are in broad agreement with the ITTC correlation line, being within about 3.5%. For the case of one ellipsoid, C_F (from CFX) is about 0.004046 whereas C_F from the ITTC-1957 correlation line is about 0.003993. These results are deemed to be satisfactory, bearing in mind the ITTC line is a correlation line rather than a true three-dimensional friction line. However, total drag is higher than that of the experimental work. This is due to the viscous pressure drag given by CFX being higher than viscous pressure drag from the experimental investigation. This occurred due to the grid quality at the ends, which is not properly in square form as required, hence failing to capture the pressure changes with sufficient accuracy. Further results can be found in Table 11.

Side-force, which is not apparent in the single body configuration is present at the twin body configuration and this force could suggest the presence of induced drag. However, like the wind tunnel tests, a rapid drop in side-force whilst the total drag decreases gradually suggests that the level of induced drag is not significant. Further details can be found in Table 12.

The distribution of pressure over the body at the closest gap line is shown in Figure 77. This indicates the effect of two bodies placed in close proximity i.e. the pressure decreases or becomes more negative when the second body is introduced. Distributions of pressure at the centre part (especially for the two-body configuration) are close to the results of the experimental work. Pressure distributions (C_P) at leading edge are close to 1.0 and C_P at trailing edge is slightly higher than the wind tunnel results. This is likely to be the cause of the higher viscous pressure drag and hence total viscous drag by CFX. The difference, in total viscous drag is about 18% for the single-body case and also about 18% for the two-body case. Furthermore, the pressure distribution on the two-body configuration, taken at positions 0, 3, 6 and 9 as in the wind tunnel tests, clearly indicates the changes of pressure which will lead to a side-force and cross flow, as illustrated in Figure 78.

Horizontal velocity distributions given by CFX at S/L values of 0.27 and 0.37 are shown in Figures 79 and 80. These are seen to be in agreement with the experimental work.

Flow separation clearly occurs approximately at the end of the body, see Figure 81. This is in agreement with the experimental work [39] and other published data [64 and 65].

Ellipsoid Body of Revolution, L/D=10.0 ($L/\nabla^{1/3}=7.26$)

The investigation on ellipsoid bodies of revolution was extended to L/D=10.0. This was carried out in order to provide better comparisons with ship hull forms, since this ratio (L/D=10.0) is a more representative ratio for ships.

Two configurations were used, namely a single body and two bodies in proximity. Investigation on two bodies was conducted at S/L=0.27 and this has separation to gap (G/L) ratio of 0.170. The work was extended to G/L=0.103, which has the same G/L as the separation S/L=0.27 for L/D=6.0. This was done in order to determine the effect of gap ratio as well as S/L ratio on total viscous resistance and its interference. The tests were carried out at a Reynolds number of 2.4×10^6 and the results can be found in Table 13.

It was found that the total viscous drag of L/D=10.0 is of the order of 14% smaller than total viscous drag of L/D=6.0, indicating that the total drag is affected by the ratio of L/D. The pressure distributions can be found in Figure 77, which indicate that the values at the leading edge is the same as for L/D=6.0, but it is smaller at the trailing edge. This causes lower drag on this more slender body. Skin friction drag is in broad agreement with the ITTC-1957 correlation line being within about 2.6% for the single body configuration i.e. 0.004011 from CFX compared with 0.003909 from the ITTC correlation line. The total drag of the two bodies is slightly higher than total drag of one body i.e. less than 1%, whilst form factors remains unchanged. The difference of total drag between G/L=0.170 and 0.103 is not significant and this occurs because the body (L/D=10.0) is more slender. Side-force is also apparent in this case but quite small. It tends to decrease rapidly with increase in separation hence induced drag is not likely to be significant, see also Table 14.

5.4 Investigations Using Ship-hull Models

5.4.1 Introduction

Investigations were extended to round bilge/transom stern ship hull forms, Figure 82. Two models, derived from the NPL series and designated 4b and 5b, were used for the study. These are the same models as those used in the resistance investigations [12, 13, 14 and 15]. The particulars of the models are as follows:

Model 4b

L=1.6m L/B=9.0 B/T=2.0 $L/\nabla^{1/3}=7.41$ WSA=0.338m^2

Model 5b

L=1.6m L/B=11.0 B/T=2.0 $L/\nabla^{1/3}=8.50$ WSA=0.276m^2

A section through the models is shown in Figure 83.

Early CFX investigations indicated that the transom stern form could possibly cause problems, e.g. transom effect may not be solved properly. For instance, the transom effect is likely to be in error at low speed. It may, however, still be considered at higher speed (Figure 84) although, in reality e.g. from tank tests, the transom region is a free area and hence no backward flow will further increase the total drag. A cut stern form (without transom), which is used in [84] for the calculation of wave resistance, is also introduced for the current investigation. This approach was applied because the free surface is neglected. Another possible approach would be to model the transom in such a way that the flow detaches smoothly from the transom, such as a method developed by Nakos and Sclavounos [85].

5.4.2 Boundary Conditions

The distance of the boundaries to the obstacles was made as follows, 1L for inlets, 3L for outlets, and 1L for outer boundaries. Similar patches to the previous cases were also applied for the ship hull model cases.

A full ship hull model was built for the case of single body. This, of course, used more CPU time and space. However, this model could be easily reconfigured to represent the two-body case and hence save CPU time and space on the two-body configuration. The setting of boundary conditions were as follows: the hull was set as a rigid wall (wall patches), the flow entrance was set as inlet (inlet patches), the outer boundaries were set as inlet (inlet patches), and the outflow was set as outlet (mass-flow boundary patches). For two bodies in close proximity, the boundary conditions between the hulls were set as symmetric plane (symmetry patches). The remaining boundary conditions (the outer boundaries) were set the same as those for the one body configuration.

5.4.3 Solution Strategy

The strategy to solve the current problems was the same as the previous cases. However, only the third order scheme (QUICK) was used because it had been proved (from two-dimensional ellipse and three-dimensional ellipsoid tests) to give better results and could provide a direct steady state solution.

5.4.4 Grid Independence Study

Grid independence was investigated by applying various grid densities i.e. about 100,000, 200,000, 300,000, 400,000 and 600,000 cells (Figure 85). It was shown that (as far as the drag component is concerned and to be with 2% order of accuracy) there was an insignificant difference between 400,000 and 600,000 cells. The results for the single body model 4b were respectively 0.006101 and 0.006079 and the error was about 0.36%; for the single model 5b were respectively 0.005431 and 0.005407 and the error was about 0.44%. Therefore it can be said that grid independence has been reached at 400,000 cells and the results are acceptable. The same strategy was applied for two ellipsoids in proximity. Further details can be seen in Table 15.

5.4.5 Discussion of Results

The investigation began with the inclusion of the transom stern. The results for total drag, skin friction, viscous pressure and form factors are given in Table 16. The magnitude of transom drag (estimated from the difference between the with and without transom investigation) is presented in Table 17.

Further work was carried out with the exclusion of transom stern and this led to a reduction in the estimate of total drag and form factor. The results of the total drag, skin friction, viscous pressure drag and form factors were given in Table 18. The results shown in Tables 16, 17 and 18 indicate that the form factors predicted by CFX are the same order as those produced in tank tests for these models. Viscous interference is shown to be present for these hulls, the level being larger when the transom is included. These aspects, together with further comparisons with the wind tunnel and CFX ellipsoids and the tank test results, are discussed further in Sections 6.2 and 6.3.

Side-force is present with the twinhull configuration and shown in Table 19. For model 4b, it decreases as the separation increases. However, since it decreases rapidly it indicates that induced drag is not significant. For model 5b, side-force is small and remains steady although the separation increases. However, because the side-force is small (at about 1%-2% of drag) it also indicates the absence of any significant induced drag. Further discussion of side-force and induced drag, and comparisons with the wind tunnel results, are given in Section 6.4.

5.6 Effects of Higher Reynolds Number

Further tests with a higher Reynolds number were carried out on a single body configuration for models 4b and 5b. These were conducted at a Reynolds number of $1\text{x}10^8$, as compared with $2.4\text{x}10^6$ used in all the earlier investigations. The tests were conducted in order to find out the effects of the Reynolds number on the final results. A careful study on a two-dimensional flat plate was carried out and reported in [86] in relation to the transition from laminar to turbulent flow condition. Since the CFX code only models either fully laminar or fully turbulent flow, the transition point will not be detected. If laminar flow still exists although the problem has been set as turbulent flow, the final results will be in error and further correction would need to be made.

It was deduced for model 4b that the skin friction coefficient was about $2.240\text{x}10^{-3}$, which was comparable with the ITTC-1957 correlation line of $2.083\text{x}10^{-3}$. The viscous pressure drag was $1.069\text{x}10^{-3}$ and the total viscous drag $3.309\text{x}10^{-3}$. These then gave a form factor of 1.48 which is a similar value to the lower Reynolds number test ($2.4\text{x}10^6$) which was about 1.46.

The skin friction coefficient for model 5b was found to be $2.194\text{x}10^{-3}$ and comparable with the ITTC-1957 correlation line. The viscous pressure drag was $0.756\text{x}10^{-6}$ and the total viscous drag $2.950\text{x}10^{-3}$. These then gave a form factor of about 1.34 which is comparable with the lower Reynolds number test with the form factor of about 1.33.

The above results showed that the higher Reynolds number ($1\text{x}10^8$) tests produce almost the same result for form factor as the lower Reynolds number ($2.4\text{x}10^6$). This is an indication that fully turbulent flow has been modelled at the lower Reynolds number. The results also indicate that, based on the ITTC-1957 correlation line, CFX correctly predicts the influence of Reynolds number over the range tested.

This has a particular significance if CFD techniques (such as CFX) are to be used to investigate scale effects.

5.7 Use of a Different Fluid

It was considered useful, as a check, to carry out a test on a different type of fluid. A test with water was therefore carried out using the single ellipsoid body of revolution. It was found that, at the same Reynolds number (2.4×10^6), the total drag coefficient was 0.005617 which was within 0.64% of the test result with air (0.005581). The finding is correct theoretically for incompressible flow. The result confirms, as would be expected, that the drag coefficient in different fluids is the same when tested at the same Reynolds number.

6 OVERALL DISCUSSION

6.1 General

Investigations into the viscous resistance components for catamaran hull forms were carried out using wind tunnel tests and CFD (CFX) approach. This was carried out using a pair of ellipsoids of L/D=6.0 in proximity and represented a catamaran hull form. The investigations and discussions cover total viscous drag, skin friction, viscous pressure drag, side-force, flow separation and induced drag.

In the wind tunnel tests, skin friction was directly calculated using the ITTC-1957 correlation line, applied for the single and two-body configuration. Therefore, a constant skin friction coefficient was used regardless the effect of S/L ratios. Meanwhile, in the CFX tests, the values of skin friction were given by the code. Skin friction of two-body case was higher than that of single body case and this decreased as the separation increases. This indicated that the effect of the separation on velocity and pressure changes between the bodies was clear. In general, the skin friction given by CFX for single body case was in broad agreement with the ITTC-1957 correlation line, within about 5%. This would indicate that, as far as skin friction determination was considered, CFX should provide adequate accuracy for the investigation.

Viscous pressure drag coefficient, in the wind tunnel tests, was calculated using two methods i.e. (1) by using C_T-C_F and (2) by integrating the pressures over the body. The first method could possibly underestimate the viscous pressure drag because the effect of the S/L ratios was excluded from the calculation of skin friction hence viscous pressure drag. The second method provided satisfactory results for higher Reynolds numbers, i.e. for Rn of 2.4×10^6 within about 6% and for Rn of 3.2×10^6 within about 1%. Poor results at lower Rn were possibly due to lesser accuracy in the low speed tests. In CFX, the viscous pressure drag was calculated from the integration of normal forces over the body and this was directly provided by the code. The results, however, are about 15% higher than the experimental results. A comparison of the pressure distribution (C_P) between the wind tunnel and the CFX results, taken at the closest distance between the hulls, is given in Figures 86a to 86d. It is apparent that the C_P from CFX is slightly higher than the C_P from the wind tunnel tests. The reasons for this are possibly due to the geometry hence the grid quality, which is not optimally built by the available grid generator, particularly at the ends.

Total viscous drag was directly calculated from the wind tunnel tests. This was also directly determined by CFX, from the summation of skin friction and viscous pressure drag. Because the viscous pressure drag given by CFX was higher than that of the wind tunnel tests, whilst the skin friction remains similar, hence the total viscous drag from CFX was higher than that of the wind tunnel tests. The difference was about 18% and, as mentioned earlier, this is possibly due to the effect of geometry and grid quality.

Further investigation using more slender body (L/D=10.0) indicated the effect of length to maximum diameter ratio (L/D). It was found that the more slender body will provide less resistance and its effect due to S/L ratios is less pronounce than the bluffer body e.g. L/D=6.0.

Further tests using the CFD approach were conducted using ship hull models (4b and 5b). The investigations were treated in two ways i.e. with and without the effects of transom stern form. Tests without transom stern were also carried out because CFD failed to recognise the area behind the transom as a free region when tested at high Reynolds number. It was found that the increase on drag when the transom stern was included was likely to be due to viscous pressure drag.

6.2 Form Factors

The ratio of total viscous drag divided by skin friction may be termed the form factor. The form factors for single ellipsoid and twin ellipsoids (L/D=6.0 with equivalent to $L/\nabla^{1/3} = 5.17$), from the wind tunnel tests, were about 1.20 and 1.30. The form factors for the same case given by CFX were about 1.40. The difference was about 10% and this is possibly due to the geometry complexity derived from the available grid generator. Further CFX work using a more slender ellipsoid (L/D=10.0 with equivalent $L/\nabla^{1/3} = 7.26$), indicated smaller values of about 1.20. It is clear that L/D ($L/\nabla^{1/3}$) ratio does affect the drag composition and hence the form factors.

The CFX results for ship hull models 4b and 5b were compared with the previous tank test results, Refs. [14 and 15]. Tank test results on model 4b showed that the form factors were 1.30, 1.47 and 1.45 respectively for single hull, S/L=0.20 and S/L=0.40. Tests with the same models using CFX and with transom stern indicated that the form factors were 1.45, 1.56 and 1.49. The CFX results are higher than the tank test results by about 11%, 6% and 3% and this is possibly due to the geometry and the grid quality used. Tank test results on model 5b indicated that the form factors were 1.26, 1.41 and 1.40, whilst CFX showed that the form factors were 1.33, 1.40 and 1.37. The differences were about 5%, 1% and 2%. Further details can be seen in Figure 87.

These results are very promising in that changes in form factor between the monohull and catamaran, and for changes in $L/\nabla^{1/3}$ ratio, are predicted reasonably well by the CFX calculations. This offers future opportunities for developing and predicting ship viscous resistance components in more detail using CFD techniques.

6.3 Levels of Viscous Interference

Equations (2.2) and (2.3) in Chapter 2 showed that total viscous resistance can be expressed as $(1+\phi k)\sigma C_F$ or $(1+\beta k)C_F$. Unlike the wind tunnel investigation, the CFX investigation has allowed the prediction of levels of viscous interference due to separation to the change in the pressure field around the hull (ϕ), change in the skin friction (σ) or the combined effect (β).

The levels of viscous interference derived from the wind tunnel tests are given in Table 5 and 6 and from the CFX investigations given in Tables 20 to 23. These are presented in terms of the viscous pressure drag of two bodies upon the viscous pressure drag of one body (C_{VP2}/C_{VP1}), the skin friction of two bodies upon the skin friction of one body (C_{F2}/C_{F1}) and the viscous interaction factor (β).

It is seen from Tables 5 and 6 and 18 to 23 that in all cases the major change in resistance occurs due to a change in the viscous pressure drag, rather than the skin friction. As would be expected, the interference is larger for the lower $L/\nabla^{1/3}$ cases. The results would suggest that, from the point of view of total viscous drag, any development in minimum drag hull forms should concentrate on the reduction of form drag interaction rather than say wetted area and skin friction.

Total Viscous Interference

In terms of the twin body total viscous drag upon single body drag, the proportions of C_{V2}/C_{V1} for the wind tunnel and CFX investigations are shown in Table 24 and are plotted in Figure 88.

The total viscous interaction predicted by CFX is less than that derived from the wind tunnel tests, but the same trends of a decrease in interaction with an increase in separation are observed. It is also noted that the CFX results indicate that the interaction decreases as L/D ($L/\nabla^{1/3}$) increases.

Comparisons of the CFX results with tank test results for catamarans, from [14 and 15], are included in Table 24 and Figure 89, and are as follows:

- Tank test results on model 4b indicated that C_{V2}/C_{V1} was about 1.13 (S/L=0.20) and 1.11 (S/L=0.40), whilst tests using CFX and with transom stern showed that the ratios were about 1.15 (S/L=0.20) and 1.06 (S/L=0.40) and without transom were 1.06 (S/L=0.20) and 1.04 (S/L=0.40).
- Tank test results on model 5b indicated that C_{V2}/C_{V1} was about 1.12 (S/L=0.20) and 1.11 (S/L=0.40) whilst tests using CFX indicated that the ratios were about 1.09

(S/L=0.20) and 1.04 (S/L=0.40). Further tests on CFX without the effect of transom stern indicated the values of 1.05 (S/L=0.20) and 1.02 (S/L=0.40).

The above summaries indicate that the CFX results show broad agreement with the experimental tank test results.

6.4 Side-force and Induced Drag

The investigations indicated the appearance of cross-flow and the development of side-force with the two-body cases. This can lead to induced drag and, if this is significant, total drag and form factor would be less than previously estimated. The appearance of side-force and hence possible induced drag was discussed in the case of two ellipses (L/D=6.0), wind tunnel tests on the two ellipsoids (L/D=6.0) and CFX investigations of two ellipsoids (L/D=6.0 and 10.0) and two ship hulls in proximity (models 4b and 5b).

Side-force exists in the two-ellipse case and the details can be found in Table 10. Because the side-force decreases rapidly with the increase in S/L ratio, but the drag decreases much less rapidly, this indicates that total drag does not contain significant induced drag.

Side-force is present in the two-ellipsoid (L/D=6.0) case both from the wind tunnel and CFX investigations. In the wind tunnel tests it was of the order of 80% of drag at S/L=0.27 to 28% of drag at S/L=0.47 (Tables 3 and 4). CFX predictions for the same S/L values indicated side-force of the order of 54% and 16%, Table 12. At the same time it has already been noted that whilst the side-force drops relatively rapidly with increase in S/L, total drag decreases gradually which would suggest a low level of induced drag. Couser et al [87] investigated induced drag for catamaran hulls by testing a hull at incidence and deducing the induced drag resulting from the production of side-force. The results suggest that induced drag is very small.

Data given by Lin et al [80] can be applied to ellipsoids for this purpose. In that case, a body of revolution was tested at several angles of attack. These results are compared with those of the two-body configuration at zero incidence. It was found that, for L/D=6.0 the induced drag coefficient was about 2×10^{-5}. This is very small, being about 0.3% of the total drag and can be ignored.

Side-force is also apparent at L/D=10.0 but quite small. It tends to decrease rapidly with increase in separation, hence induced drag is not significant. An estimate was made using the data of Lin et al [80] and it was found that the induced drag was about 1×10^{-6}. This is only 0.02% of the total drag and hence is not of significance.

Side-force is present with two bodies for models 4b and 5b. For model 4b, it decreases as the separation increases. However, since it decreases rapidly it indicates that induced drag is not significant. For model 5b, side-force is small enough which indicates the absence of any significant induced drag.

The results for side-force with change in S/L from the wind tunnel and CFX investigations are summarised in Figures 90 and 91. It is noted that, for similar L/D (or $L/\nabla^{1/3}$), the levels and changes in side-force are broadly similar, and decrease fairly rapidly with increase in hull separation. As seen earlier, drag decreases less rapidly with increase in hull separation suggesting that the level of induced drag is not significant.

6.5 Future Applications of Developed Techniques

Two methods for the determination of ship viscous resistance have been developed and described, namely experimental investigation (using a wind tunnel) and numerical work (using CFX code). The results from the wind tunnel tests for one body are in agreement with previous published data for a single body of revolution, and the wind tunnel offers a reliable method of investigating viscous drag. The wind tunnel tests also indicated the presence of viscous interaction between the bodies. It is considered that the wind tunnel work could be usefully extended to consider reflex ship hulls. A parametric investigation of such hulls would allow a closer study of the influence of say $L/\nabla^{1/3}$ and S/L on viscous drag components, and the development of improved estimates of the viscous component for scaling purposes.

The total drag from the CFD investigation was higher than that given by the wind tunnel tests. The cause is believed to be due to the geometry and grid quality at the leading and trailing edges. The CFD work clearly indicated the existence of viscous interference and flow separation.

The changes in relative viscous effects due to change in S/L and $L/\nabla^{1/3}$ were predicted correctly by CFX. It also allowed a closer examination of the components of viscous drag (viscous pressure and friction). It is considered that such a code, like the wind tunnel tests, could be used to develop improved estimates of the viscous component for scaling purposes. The use of a better grid generator, and increase in computer power, are likely to improve the quality of the absolute levels of the predictions.

7 CONCLUSIONS AND RECOMMENDATIONS

7.1 General

7.1.1 The current investigations has demonstrated that the total viscous resistance of displacement catamarans can be treated as a summation of the principal resistance components analogous to monohull resistance, i.e. skin friction and viscous pressure resistance together with a viscous interference resistance. Experimental and numerical results have revealed characteristics of these viscous interference effects, particularly at high speeds, and have contributed to a better understanding of catamaran resistance.

7.1.2 The literature review indicated that two types of interaction, namely wave and viscous interactions, must be taken into consideration. Whilst a substantial amount of work into the wave resistance and its interference has been carried out, not much effort has been dedicated to determine viscous resistance and viscous interference resistance. It is also found that even extremely slender hull forms may have a viscous resistance component which is significantly greater than the frictional resistance of an equivalent flat plate based, say, on the ITTC-1957 correlation line. Form factors for slender forms are therefore normally greater than unity. This, points to the need for and the importance of the investigation described in the current work.

7.1.3 The current work has focused on the investigation of the viscous resistance and viscous interference effects using experimental investigation and numerical study. The experimental work was carried out using a low-speed wind tunnel, without and with turbulence transition strip and tested at varying speeds and Reynolds numbers up to $3.2x10^6$. A parametric study was carried out on tests without transition strip because of the mixing of laminar and turbulence flows. A comparative study was conducted using published data for single bodies of revolution. The numerical study was carried out using the commercial CFD code (CFX) and considerations were given to optimum distance from the obstacle, grid independence criteria, optimum CPU time, higher Reynolds number effects and the use of different types of fluid on the final results. A comparative study was carried out with analytical data for inviscid and incompressible flow cases and also with published data for viscous incompressible flows.

The principal findings and conclusions drawn from the investigations are outlined as follows.

7.2 Wind Tunnel Investigation

7.2.1 The wind tunnel tests indicated that the chosen model ratio was suitable for the current investigation and the blockage effects could be adequately taken into consideration. Comparative studies with existing published data for single bodies of revolution supported these findings and provided general agreement with the current work.

7.2.2 A parametric study, carried out to estimate the transition from laminar to turbulent flows on the models without the transition strip, indicated similar form factor values to the same models when tested with turbulence strip. This would indicate that the difference between the total drags of the two treatments is similar to the frictional deficit between the two.

7.2.3 The wind tunnel test results provide useful drag, side-force and pressure data and contribute to a better understanding of the behaviour of two bodies when in proximity, in this case representing a reflex model of a catamaran.

7.2.4 The pressure distributions for the single body correspond satisfactorily with existing published data. The detailed pressure measurements provide a good indication of flow and velocity change around the hull. At the highest test speeds and high Reynolds number, the integration of pressures corresponded well with the direct drag and side-force measurements.

7.2.5 The drag of the twin bodies configuration was consistently higher than the corresponding monohull, confirming the presence of viscous interference between the hulls. With increase in separation between the bodies, whilst the (attractive) side-force reduced rapidly, drag was seen to remain reasonably constant over the separations tested. The drag result is not what might be expected, but is consistent with published viscous drag estimates from tank tests.

7.2.6 Flow visualisation studies clearly demonstrated the presence of cross flow over the hulls, arising from the velocity and pressure changes over the hulls. The rapid decrease in side-force with increase in separation, with the drag remaining sensibly constant, implies that the cross flow was not leading to induced drag of any significance.

7.2.7 Overall, the wind tunnel investigation has demonstrated the ability of such an approach to investigate in some detail the viscous resistance components of multihulls, and to contribute to improving the prediction of viscous drag, form factors and total ship resistance.

7.3 CFD Investigation

7.3.1 The creation of the current geometry models was carried out using CFX-MESHBUILD as it was the only one available for the writer during the time of the research. CFX-MESHBUILD is a structured grid and only accepts exactly four points to create a face, the basic element to create the geometry, and the user must define each point to then develop the expected geometry. It does, therefore, cause problems with curved forms and complex three-dimensional geometry, e.g. leading and trailing edges of an ellipsoid or ship hull. Although the user can solve this problem and create rectangular forms, the obtained cells are not likely in proper square form, which is strongly required by the code. Although the code can accept this kind of geometry input, the final results would be not optimal and the viscous pressure drag could be overestimated.

7.3.2 The command file is another input file for the flow solver and plays an important role for the best quality of results. Under command file or language, the problems are identified, e.g. two- or three-dimensional, laminar or turbulent and steady state or transient flow. Input flow characteristics must be given such as reference temperature, density and viscosity. For turbulent flow cases, the user can choose the appropriate turbulence models, i.e. the standard k-ε and the RNG k-ε models for high Reynolds number flows, to solve the problem. In the current investigation, the RNG k-ε was found to be slightly better than the k-ε model. The user has to set the mass residual as it is the only parameter for the convergence test and it is normally set 10^{-4} to 10^{-6}, where the smaller the given value the more accurate the results but consequently the more CPU time required to complete the solution. To obtain better accuracy, the user can choose whether to use first, second or third order schemes. Theoretically, first order scheme can achieve the same accuracy as third order scheme but it needs much more cells where normally will be limited by the power of the computer. It is found that third order scheme (QUICK) provide more accurate results, for two- and three-dimensional cases, than first order scheme with the same number of cells. The use of the PISO algorithm is further found to reduce the CPU time quite significantly as this algorithm adds an extra correction step to SIMPLE to enhance its performance per iteration.

7.3.3 Early investigation determined that the CFX code is a potential research tool to investigate ship viscous resistance. Comparisons with an analytical solution and other data (from Katz and Plotkin) for the two-dimensional case and with slender body theory and analytical solution for three-dimensional case, supported these findings.

7.3.4 Drag of the twin bodies configuration, for two- and three-dimensional cases, were higher than the corresponding monohull, confirming the existence of viscous drag interaction between two hulls. Form factors for the three-dimensional case, especially, are higher than expected. The reason for this is because the cells at the sharp ends are not properly square and hence cannot properly capture the fast changes of pressure gradient. This has been limited by the grid generator used and also by the form of the body itself.

7.3.5 Distributions of pressure for the three-dimensional ellipsoid cases are in broad agreement with the experimental results. The results at the trailing edge for the three-dimensional ellipsoids, however, are slightly overestimated. This has caused higher viscous pressure drag hence higher total viscous drag. Form factors are subsequently higher than those of the experimental work.

7.3.6 The appearance of side-force and flow separation are shown by the two and three-dimensional CFX models. The side-force decreases quickly whilst the total drag drops slowly. From this, it may be inferred that the total drag does not contain any significant induced drag.

7.3.7 Tests at a higher Reynolds number ($1\text{x}10^8$) indicated that fully turbulent flow has been developed at lower Reynolds number ($2.4\text{x}10^6$). A further test with water, instead of air, on a single ellipsoid supported the theoretical basis that the drag components remain unchanged as long as the Reynolds number is kept the same and the flow is incompressible.

7.3.8 Overall, the CFD investigations have demonstrated that the technique can be suitably employed for the investigation of viscous pressure drag for multihulls. On this basis it should, at least in theory, be also possible to investigate scale effects on viscous drag. It is concluded that the technique should be developed further for these purposes.

7.4 Achievement of the Objectives

7.4.1 It is considered that the objectives of the investigation, outlined on page 3, have been achieved. The experimental and numerical investigations have provided a better understanding and identification of the viscous resistance components for high-speed displacement monohulls and catamarans.

7.4.2 It is well established that a correct breakdown and understanding of resistance components is necessary in order to allow satisfactory scaling from model to ship. The current investigation has improved the understanding and quantification of the viscous components and interactions, thus allowing the development of improved scaling methods.

7.5 Recommendations for Future Work

As a result of the research programme using experimental and CFD techniques, the following recommendations are put forward:

7.5.1 Further wind tunnel tests should be carried out. These should be for reflex ship hulls and should investigate the effects of length/displacement ratio and hull separation on form factor. As well as total drag and surface pressure measurements, a detailed mapping of the flow velocity field should be carried out using Laser Doppler Anemometer (LDA). This will provide velocity measurements for the momentum analysis of drag and for detailed validation of CFD methods.

7.5.2 The CFD results have been found to predict correctly relative viscous changes due to change in hull separation and length/displacement ratio. It is considered that the technique should be used to derive further parameter information on viscous drag components for reflex ship hulls. The method however was not so successful in correctly estimating the actual level of viscous pressure drag. The overestimation of the viscous pressure drag (with such difficult leading and trailing edges of an ellipsoid) is attributed to the quality of the grid produced. The use of CFX-MESHBUILD grid generator has produced rather poor grid quality and consequently overestimates the total viscous drag. The uses of other grid generators, which can produce an efficient volume-meshing algorithm, would provide better grid quality and improve the quality of the absolute levels of the viscous pressure drag predictions.

References

[1] Phillips, S. J. (editor), *Jane's High-Speed Marine Transportation*, 30th Edition, 1997-1998.

[2] Lackenby, H., *An Investigation into the Nature and Interdependence of the Components of Ship Resistance*, Trans. RINA, Vol. 107, 1965.

[3] Pien, P. C., *Catamaran Hull-Form Design*, International Seminar on Wave Resistance, SNAJ, 1976.

[4] Miyazawa, M., *A study on the flow around a catamaran*, JSNAJ, Vol. 145, 1979.

[5] Everest, J. T., *Some Research on the Hydrodynamics of Catamarans and Multi-Hulled Vessels in Calm Water*, Trans. NECIES, Vol. 84, 1967-68.

[6] Everest, J. T., *Some Comments on the Performance in Calm Water of a Single-Hull Trawler Form and Corresponding Catamaran Ship Made up from Symmetrical and Asymmetrical Hulls*, NPL Ship Division, Ship Report No. 129, 1969.

[7] Hsiung, C. C. and Xu, H., *Determining Optimal Forms of a Catamaran for Minimum Resistance by the Mathematical Programming Method*, Schiffstechnik, Bd. 35, 1988.

[8] Doctors, L. J., Renilson, M. R., Parker, G. and Hornsby, N., *Waves and Wave Resistance of a High-Speed River Catamaran*, Proceedings FAST 1991.

[9] Matsui, S., Shao, S-M, Wang, Y-C and Tanaka, K., *The Experimental Investigations on Resistance and Seakeeping Qualities of High-Speed Catamarans*, Proceedings FAST 1993.

[10] Shao, S-M, Wang, Y-C, Bin, C. and Dou, S-X, *The Experimental Investigation of Hull Form of High-Speed Displacement Vessels*, Shipbuilding of China, No. 1, 1985.

[11] Incecik, A., Morrison, B. F. and Rodgers, A. J., *Experimental Investigation of Resistance and Seakeeping Characteristics of a Catamaran Design*, Proceedings FAST 1991.

[12] Insel, M., An Investigation into the resistance components of high speed displacement catamarans, *Ph.D. thesis*, Department of Ship Science, University of Southampton, 1990.

[13] Insel, M. and Molland, A.F. *An investigation into the resistance components of high speed displacement catamarans*, Trans. RINA, Vol. 34, 1992.

[14] Molland, A.F., Wellicome, J.F. and Couser, P.R., *Resistance experiments on a systematic series of high speed displacement catamaran forms: variation of*

length-displacement ratio and breadth-draught ratio, Ship Science Report No. 71, Department of Ship Science, University of Southampton, 1994.

[15] Couser, P.R., An investigation into the performance of high-speed catamarans in calm water and waves, *Ph.D. thesis*, Department of Ship Science, University of Southampton, 1996.

[16] Couser, P.R., Molland, A.F., Armstrong, N.A. and Utama, I.K.A.P., *Calm water powering predictions for high-speed catamarans*, Proceedings FAST 1997, Sydney, July 1997.

[17] Rovere, J. E., *Catamaran Resistance from Tests on a Single Deminull*, Proceedings FAST 1997, Sydney, July 1997.

[18] Eggers, K., *Resistance components of two-body ships*, Jahrbuch der Schiffbautechnischen Gesellschaft, No. 49, 1955.

[19] Telfer, E. V., *Frictional Resistance and Ship Resistance Similarity*, Trans. INA, Vol. 92, No. 1, 1950.

[20] Hughes, G., *Friction and form resistance in turbulent flow, and a proposed formulation for use in model and ship correlation*, Trans. INA, Vol. 96, 1954.

[21] ITTC, *Report of the Powering Performance Committee of the 20th ITTC*, Proceedings, Part I, Madrid, 1990.

[22] Harvald, S. A., *Resistance and Propulsion of Ships*, John Wiley and Sons, Toronto, 1983.

[23] Alan, J. F. and Conn, J. F. C., *Effect of Laminar Flow on Ship Models*, Trans. INA, Vol. 92, 1950.

[24] Hughes, G., *An analysis of ship model resistance into viscous and wave components: Parts I and II*, Trans. RINA, Vol. 109, 1967.

[25] Lewis, E. V. (editor), *Principles of Naval Architecture*, Vol. II: Resistance, Propulsion and Vibration, SNAME, New Jersey, 1988.

[26] Dyne, G., *A Theoretical Scale Effect Study on the Propulsion Coefficient of a Body of Revolution*, DNV Symposium on Hydrodynamics, Oslo, 1977.

[27] Townsin, R. L. and Wynne, J. B., *Viscous Drag Measurements of Ship Models: The Design and Use of an Automated System*, Trans. NECIES, Vol. 96, 1979-1980.

[28] Cordier, S. and Dumez, F. X., *Resistance Components of Displacement and Semi-Displacement Hull Forms*, a contribution to 20th ITTC conference, 1993.

[29] Cordier, S. and Dumez, F. X., *Scale Effects on the Resistance Components of a High-Speed Semi-Displacement Craft*, Proceedings FAST 1993, Yokohama, 1993.

[30] Tanaka, H., Nakato, M., Nakatake, K., Ueda, T. and Araki, S., *Co-operative Resistance Test with Geosim Models of a High-Speed Semi-Displacement Craft*, JSNAJ, Vol. 169, 1990.

[31] Joubert, P. N. and Matheson, N., *Wind Tunnel Tests of Two Lucy Ashton Reflex Geosims*, Journal of Ship Research, Vol. 14, No. 4, 1970.

[32] Joubert, P. N. and Hoffmann, P. H., *An Experimental Study of the Viscous Resistance of a 0.564-C_B Form*, Journal of Ship Research, Vol. 23, No. 2, June 1979.

[33] Joubert, P. N., Sinclair, T. J. and Hoffmann, P. H., *A Further Study of Bodies of Revolution*, Journal of Ship Research, Vol. 22, No. 1, March 1978.

[34] Morgan, W.B., and Lin, W-C., *Computational Fluid Dynamics, Ship Design and Model Evaluation*, 4th International Congress of the International Maritime Association of East Mediterranean, Varna (Bulgaria), 1987.

[35] Versteeg, H.K. and Malalasekera, W., *An Introduction to Computational Fluid Dynamics*, Longman Scientific & Technical, Harlow (England), 1995.

[36] Morgan, W.B. and Lin, W-C., *Ship Performance Prediction Computational Fluid Dynamics and Experiments*, Schiffstechnik, Bd. 36, 1989.

[37] Bull, P., *CFD Validation for Naval Hydrodynamics*, MSc Course Note on CFD, Department of Ship Science, University of Southampton, 1996.

[38] Thomas, J., a note prepared for discussion at the 3rd ITTC RFC Meeting in Lyngby, Denmark, May 1995.

[39] Molland, A. F. and Utama, I. K. A. P., *Wind Tunnel Investigation of a Pair of Ellipsoids in Close Proximity*, Ship Science Report No. 98, Department of Ship Science, University of Southampton, April 1997.

[40] Davies, P. A. O. L., *The New 7ft x 5ft and 15ft x 12ft Low Speed Wind Tunnel at the University of Southampton*, AASU Report No. 202, December 1961.

[41] Houghton, E. L. and Carpenter, P. W., *Aerodynamics for Engineering Students*, 4th Edition, Edward Arnold, London, 1993.

[42] Duncan, W. J., Thom, A. S. and Young, A. D., *Mechanics of Fluid*, Edward Arnold, London, 1970.

[43] Massey, B. S., *Mechanics of Fluid*, 5th Edition, Van Nostrand Reinhold, Wokingham, UK, 1983.

[44] Lamb, Sir H., *Hydrodynamics*, Paperback Edition, Cambridge University Press, Cambridge, UK, 1993.

[45] Roskho, A., *Experiments on the Flow Past a Circular Cylinder at Very High Reynolds Number*, JFM, Vol. 10, 1961.

[46] Melvill-Jones, B., *The Measurement of Profile Drag by the Pitot-Traverse Method*, The Cambridge University Aeronautics Laboratory, ARC R&M No. 1688, 1935-1936.

[47] Merzkirch, W., *Flow Visualization*, Academic Press, London, 1974.

[48] Glauert, H., *The Interference of a Wind Tunnel on a Symmetrical Body*, ARC R&M No. 1544, April 1933.

[49] Durgun, O. and Kafali, K., *Blockage Correction*, Ocean Engineering, Vol. 18, No. 4, 1991.

[50] Pope, A., *Wind Tunnel Testing*, John Wiley and Sons, New York, 1947.

[51] Pankhurst, R. C. and Holder, D. W., *Wind Tunnel Technique*, Sir Isaac Newton Pitman & Sons, London, 1952.

[52] ESDU, *Blockage Corrections for Bluff Bodies in Confined Flows*, Engineering Science Data Unit, Reference No. 80024, 1980.

[53] Young, A.D., *The Calculation of theTotal and Skin Friction drags of bodies of revolution at zero incidence*, Royal Aeronautical Research Council, Reports & Memoranda, No. 1874, 1939.

[54] Dyne, G., *A Streamline Curvature Method for Calculating the Viscous Flow around Bodies of Revolution*, International Symposium on Ship Viscous Resistance, SSPA, Goteborg, 1978.

[55] Lyon, H.M., *The Effect of Turbulence on the Drag of Airship Models*, Royal Aeronautical Research Council, Reports & Memoranda, No. 1511, 1932.

[56] Lyon, H.M., *A Study of the Flow in the Boundary Layer of Streamline Bodies*, Royal Aeronautical Research Council, Reports & Memoranda, No. 1622, 1935.

[57] Schlichting, H., *Boundary Layer Theory*, McGraw-Hill, New York, 1979.

[58] Cebeci, T., Mosinskis, G.J. and Smith, A.M.O., *Calculation of Viscous Drag in Incompressible Flow*, Journal of Aircraft, Vol. 9, No. 10, October 1972.

[59] Crabtree, L.F., *Technical Note: Prediction of Transition in Boundary Layer on an Aerofoil*, Journal of the Royal Aeronautical Society, Vol. 62, July 1958.

[60] Silverstein, A. and Becker, J. V., *Determination of Boundary Layer Transition of Three Symmetrical Airfoils in the NACA Full-Scale Wind-Tunnel*, National Advisory Committee for Aeronautics, Report No. 637.

[61] Calkins, D. E., *Faired Towline Hydrodynamics*, Journal of Hydronautics, Vol. 4, No. 3, 1970.

[62] Squire, H. B., *Note on Boundary Layer Flow*, Royal Aeronautical Research Council, Reports & Memoranda, No. 1664, 1935.

[63] Biermann, D. and Herrnstein, W. H., *The Interference between Struts in Various Combinations*, National Advisory Committee for Aeronautics, Report No. 468.

[64] Meier, H. U. and Kreplin, H-P, *Experimental Investigation of the Boundary Layer Transition and Separation on a Body of Revolution*, Z. Flugwiss. Weltraumforsch. 4, Heft 2, 1980.

[65] Myring, D. F., *The Profile Drag of Bodies of Revolution in Subsonic Axisymmetric Flow*, Royal Aeronautical Establishment, Technical Report No. 72234, May 1973.

[66] Anderson, J. D., *Computational Fluid Dynamics, the Basics with Applications*, McGraw-Hill International Editions, New York, 1995.

[67] Bertram, V., *Economical Aspects of CFD*, 19th WEGEMT School, Nantes, 1993.

[68] ITTC, *Proceedings of the 21st ITTC*, Volume I, Trondheim (Norway), 1996.

[69] Watson, S. J. P. and Bull, P. W., *The Scaling of High Reynolds Number Viscous Flow Predictions using CFD Techniques*, Proceedings of the Third Osaka Colloquium on Advanced CFD Applications to Ship Flow and Hull Form Design, Osaka Prefecture University, Osaka (Japan), 1998.

[70] Aston, J. G. L., A Direct Approach to Computer Modelling of Fluids, *PhD Thesis*, University of College London, July 1990.

[71] AEA Technology, *CFX 4.2: Solver*, 1997.

[72] Boysan, H. F., *Renormalisation Group Theory Based Turbulence Models and Their Applications to Industrial Problems*, Proceedings of the Institute of Mechanical Engineering, C461/035, 1993.

[73] Cook, M. and Lomas, K., *Modelling Buoyancy-Driven Displacement Ventilation*, CFX Update, No. 14, AEA Technology, autumn 1997.

[74] Patankar, S. V. and Spalding, D. B., *A Calculation Procedure for Heat, Mass and Momentum Transfer in Three-dimensional Parabolic Flows*, Int. J. Heat Mass Transfer, Vol. 15, 1972.

[75] AEA Technology, CFDS-FLOW3D Manual, 1994.

[76] Armstrong, N.A., *An Investigation into the Form Factor of High-Speed Light Craft*, in First AMECRC Postgraduate Students Conference, Western Australia, 9-10 October 1995.

[77] AEA Technology, *CFX 4.2: Pre-processing*, 1997.

[78] AEA Technology, *CFX 4.2: Post-processing*, 1997.

[79] Patel, V. C., Chen, H. C. and Ju, S., *Computations of Ship Stern and Wake Flow and Comparisons with Experiment*, Journal of Ship Research, Vol. 34, No. 3, September 1990.

[80] Lin, W-C., Percival, S. and Gotimer, E. H., *Viscous Drag Calculations for Ship Hull Geometry*, David Taylor Model Basin, report number not given, extracted from the internet, website: at http://www50.dt.navy.mil/reports/viscous.

[81] Grotjans, H. and Menter, F., *Latest Development in Wall Function Techniques*, CFX Update, No. 16, AEA Technology, Autumn 1998.

[82] Katz, J. and Plotkin, A., *Low-Speed Aerodynamics: from Wing Theory to Panel Methods*, McGraw-Hill Inc., New York, 1991.

[83] Thwaites, B., *Incompressible Aerodynamics*, Clarendon Press, Oxford, 1960.

[84] Idelshon, S. R., Onate, E. and Sacco, C., *Finite Element Solution of Free Surface Ship-Wave Problems*, International Journal of Numerical Methods in Engineering, Vol. 45, No. 5, 1999.

[85] Nakos, D. E. and Sclavounos, P. D., *Kelvin Wakes and Wave Resistance of Cruiser- and Transom-Stern Ships*, Journal of Ship Research, Vol. 38, No. 1, March 1994.

[86] Date, J. C. and Turnock, S. R., *A Study into the Techniques Needed to Accurately Predict Skin Friction Using RANS Solvers with Validation Against Froude's Historical Flat Plate Experimental Data*, Ship Science Report No. 114, Department of Ship Science, University of Southampton, March 1999.

[87] Couser, P. R. Wellicome, J. F. and Molland, A. F., *Experimental Measurement of Sideforce and Induced Drag on Catamaran Demihulls*, International Shipbuilding Progress, Vol. 45, No. 443, 1998.

Appendix A

A Flow around Slender Bodies of Revolution

(notes provided by Dr. J. F. Wellicome)

A.1 General Case

Assume a slender body of revolution as seen in Figure A.1 with a source distribution about its centre line, m(s).

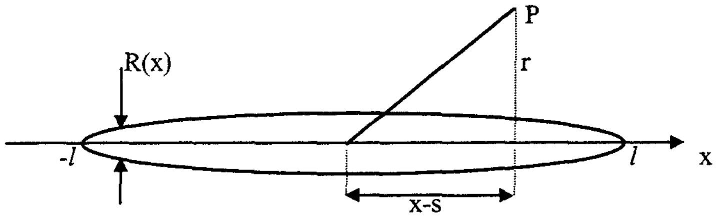

Figure A.1: Slender body of revolution

Velocities (in x- and y-direction) at P are

$$u = U + \int_{-l}^{l} \frac{(x-s)m(s)ds}{\left[(x-s)^2 + r^2\right]^{3/2}} \tag{A.1}$$

and

$$v = \int_{-l}^{l} \frac{r.m(s)ds}{\left[(x-s)^2 + r^2\right]^{3/2}} \tag{A.2}$$

as $r \rightarrow 0$ within body length, therefore

$$v = m(x)\int_{-1}^{1} \frac{r\,ds}{\left[(s-x)^2 + r^2\right]^{3/2}} \tag{A.3}$$

$$v = \frac{m(x)}{r}\left[\frac{s-x}{\sqrt{(s-x)2 + r2}}\right] = \frac{2m(x)}{r} \tag{A.4}$$

Body boundary condition is

$$v = UR'(x) = \frac{2m(x)}{R(x)} \tag{A.5}$$

therefore

$$m(x) = \frac{1}{2}UR(x)R'(x) \tag{A.6}$$

Body cross-sectional area is

$$A(x) = \pi R(x)^2 \tag{A.7}$$

$$A'(x) = 2\pi R(x)R'(x) \tag{A.8}$$

therefore Equation (A.6) becomes

$$m(x) = \frac{1}{4\pi}UA'(x) \tag{A.9}$$

Hence

$$\frac{u}{U} = 1.0 + \frac{1}{4\pi}\int_{-1}^{1} \frac{(x-s)A'(s)}{\left[(x-s)^2 + r^2\right]}ds \tag{A.10}$$

and

$$\frac{v}{U}=\frac{r}{4\pi}\int_{-1}^{1}\frac{A'(s)}{\left[(x-s)^2+r^2\right]^{3/2}}ds \tag{A.11}$$

A.2 The Case of a Slender Ellipsoid

Cross-sectional area at any arbitrary positions of an ellipsoid is

$$A(x)=A_0\left(1-\left(\frac{x}{l}\right)^2\right) \tag{A.12}$$

where A_0 is maximum cross-sectional area.

And,

$$A'(x)=\frac{-2xA_0}{l^2} \tag{A.13}$$

Furthermore, by applying Equation (A.13) into Equations (A.10) and (A.11) two consecutive equations are obtained. They are

$$\frac{u}{U}=1.0+\frac{A_0}{2\pi l^2}\int_{-1}^{1}\frac{s(s-x)ds}{\left[(s-x)^2+r^2\right]^{3/2}} \tag{A.14}$$

and

$$\frac{v}{U}=\frac{-rA_0}{2\pi l^2}\int_{-1}^{1}\frac{sds}{\left[(s-x)^2+r^2\right]^{3/2}} \tag{A.15}$$

By assuming

$$I_0 = \int_{-1}^{1} \frac{ds}{\left[(s-x)^2 + r^2\right]^{3/2}} = \frac{1}{r^2}\left[\frac{(s-x)}{\sqrt{(s-x)^2 + r^2}}\right]_{-1}^{1} \qquad (A.16)$$

$$I_1 = \int_{-1}^{1} \frac{(s-x)ds}{\left[(s-x)^2 + r^2\right]^{3/2}} = \left[\frac{-1}{\sqrt{(s-x)^2 + r^2}}\right]_{-1}^{1} \qquad (A.17)$$

$$I_2 = \int_{-1}^{1} \frac{(s-x)^2 ds}{\left[(s-x)^2 + r^2\right]^{3/2}} = \int_{-1}^{1} \frac{ds}{\sqrt{(s-x)^2 + r^2}} - r^2 I_0 \qquad (A.18)$$

therefore

$$I_2 = \left[\ln\left((s-x) + \sqrt{(s-x)^2 + r^2}\right)\right]_{-1}^{1} - r^2 I_0 \qquad (A.19)$$

then

$$\frac{u}{U} = 1.0 + \frac{A_0}{2\pi l^2}\left(I_2 + xI_1\right) \qquad (A.20)$$

and

$$\frac{v}{U} = \frac{-rA_0}{2\pi l^2}\left(I_1 + xI_0\right) \qquad (A.21)$$

Furthermore, especially when x = 0:

$$I_2 = \ln\left(\frac{\sqrt{l^2 + r^2} + 1}{\sqrt{l^2 + r^2} - 1}\right) - \frac{21}{\sqrt{l^2 + r^2}} \qquad (A.22)$$

and

$$\frac{u}{U} = 1.0 + \frac{A_0}{2\pi l^2} I_2 \tag{A.23}$$

where

$$\frac{A_0}{2\pi l^2} = \frac{R_0^2}{2l^2} = \frac{1}{2}\left(\frac{D_0}{L}\right)^2 \tag{A.24}$$

total body length L = 2l.

Equation (A.23) can be further used to investigate the velocity interference between two ellipsoids placed parallel one to another. These typical values, referred to as u/U, are based on length to maximum diameter ratio (L/D_0) against separation to length ratio (S/L) and are tabulated in Table A.1.

TABLE A.1: Typical values of u/U

	L/D_0	
S/L = r/2l	10.0	5.0
0.05	1.020	1.080
0.20	1.007	1.029
0.50	1.002	1.007

Tests at L/D_0 = 10.0 indicate a relatively small interference between the two bodies. Inspections at L/D_0 = 5.0 exhibit that the body velocities are about 1.08 times the free stream velocity and the interference velocities are about 3% at S/L = 0.20 and about 1% at S/L = 0.50.

Further investigations were extended to L/D_0 = 6.0 and are tabulated in Table A.2.

TABLE A.2: Typical values of u/U at L/D_0 = 6.0

S/L = r/2l	u/U
0.05	1.057
0.10	1.037
0.20	1.020
0.25	1.015
0.30	1.012
0.40	1.007
0.50	1.005
1.00	1.001

It is indicated that the body velocities are quite significant at about 6% of the free stream velocity at small separation. The interference velocities are about 2% to 0.5% between S/L = 0.2 and 0.5 and the interaction effectively disappears when S/L increases beyond 1.0.

Based on these results, it was decided to conduct the current work using slender ellipsoids of revolution of $L/D_0 = 6.0$.

Appendix B

B Calculation of Model Particulars

B.1 Chosen Principal Dimensions

Length	L = 1200 mm
Maximum diameter	D = 200 mm

B.2 Body Volume

Volume is calculated (as shown in Figure B.1) as $\text{Vol} = \frac{4\pi}{3} a.b.c$

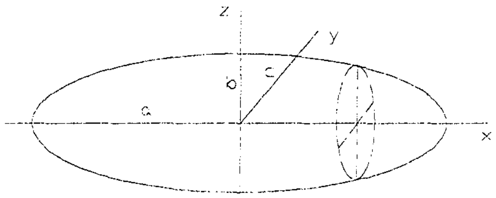

Figure B.1: Ellipsoid body of revolution

Here, Vol. = $(4\pi/3) \times 0.6 \times 0.1 \times 0.1 = 0.0251\ m^3$.

B.3 Wetted Surface Area

A numerical integration using Simpson Rule was applied for this purpose using 65 longitudinal stations. This resulted in the following wetted surface area:

WSA = $0.601\ m^2$.

B.4 Calculation of the Other Particulars

The other main dimensions in ship technology terms, i.e. block coefficient (C_B), midship coefficient (C_M), prismatic coefficient (C_P) and length to displacement ratio $\left(L / \nabla^{1/3}\right)$ can be derived as follows:

Block coefficient:

$$C_B = \frac{\text{Vol.}}{8abc} = \frac{0.025}{8x0.6x0.1x0.1} = 0.521$$

Midship coefficient:

$$C_M = \frac{A_o}{4bc} = \frac{px0.2^2}{4x0.1x0.1} = 0.785$$

Prismatic coefficient:

$$C_P = \frac{C_B}{C_M} = \frac{0.521}{0.785} = 0.664$$

Length to displacement ratio:

$$\frac{L}{\nabla^{1/3}} = \frac{1.2}{(0.5x0.025)^{1/3}} = 5.17$$

Where ∇ is half total ellipsoid volume, i.e. assumes reflection plane at half diameter.

Appendix C

C Data Corrections

C.1 Velocity

The air density (ρ_a) appropriate to ambient temperature and pressure is required in order to obtain actual values of the tunnel speed. The density is obtained using the general gas equation:

$$\rho_a = \frac{p}{RT} \tag{C.1}$$

Where p is atmospheric pressure, T is absolute temperature in °K (°K = °C + 273.15) and R is the gas constant (0.2871 kJ/kg °K) and the specific gravity of mercury is 13.59.

The velocity is then calculated using the following formula:

$$V = \sqrt{\frac{2\rho_w g H}{\rho_a}} \tag{C.2}$$

Where ρ_w is density of water (1000 kg/m^3), g is gravity acceleration (9.81 m/s^2) and H is Betz manometer reading in metres of water.

Equation (C.2) can be written in simple form:

$$V = 140.07\sqrt{\frac{H}{\rho_a}} \tag{C.3}$$

C.2 Reynolds Number

Velocities from section C.1 are used to calculate the Reynolds numbers. The dynamic viscosity of air can be obtained from Table C.1 and the values between the specified temperature are obtained by interpolation.

TABLE C.1: Dynamic viscosity

Temperature (°C)	10^5 (Ns/m^2)
0	1.709
5	1.733
10	1.758
15	1.783
20	1.807
25	1.831
30	1.855
35	1.880

The Reynolds number is:

$$R_L = \frac{\rho_a VL}{\mu} \tag{C.4}$$

C.3 Boundary Corrections

The conditions under which a model is tested in a wind tunnel are not the same as those in free air. Drag forces, obtained from measurements, can be overestimated and therefore must be corrected. It is related to the presence of the model itself in the wind tunnel and reduces the area through which the air must pass, hence increasing the velocity of the air that flows over the model. This effect is referred to as 'blocking'.

Boundary corrections, for the case of ellipsoid body of revolutions, consist of three major parts: wake blockage, longitudinal buoyancy and solid-body blockage [48, 49, and 50]. The wake blockage for three-dimensional arrangements, except for bluff bodies, dive brakes and the like, is very small hence are usually neglected [48]. The longitudinal buoyancy correction is also insignificant [48]. Wake blockage effects give rise to an additional effect on the drag force, resulting in longitudinal buoyancy drag [50]. This equals to [($\Delta V_\infty / V_\infty$) for solid body blockage] x C_D, for fully attached flow. If C_D is about 0.004 the correction will (if the velocity increase is 0.0035) be 0.0014% for single body and (if the velocity increase is 0.007) 0.003% for twin bodies. This correction is very small hence again can be neglected. Boundary corrections therefore can be said to be most likely due to solid-body blockage.

The estimation of the solid body blockage correction is available from a number of references. Three established formulae were given and described in this case [48, 49 and 50]. They are based either on the ratio of body maximum cross-sectional area to tunnel cross-sectional area or the ratio of body volume to tunnel volume.

For the three dimensional case, Ref. [48] indicates that the velocity increase is

$$\frac{\Delta V_\infty}{V_\infty} = \tau\lambda_3\left(\frac{S}{C}\right)^{3/2} \qquad \text{(C.5)}$$

Where, in the case of the wind tunnel tests being described:

τ is tunnel shape factor i.e. 0.809.

λ_3 is body shape factor obtained from a graph i.e. 5.67.

S is body maximum cross-sectional area i.e. 0.0314 m^2 for single body and 0.0628 m^2 for twin bodies.

C is tunnel cross-sectional area i.e. 2.13 m x 1.52 m = 3.2376 m^2.

This formula gives values of 0.0044 for single body and 0.0124 for twin bodies. The solid body velocity blockage correction is then the square of (approximately two times) these values i.e. 0.88% for single body and 2.48% for twin bodies.

Ref. [49] introduced a value of the tunnel shape factor $\left(\frac{\pi}{4}\right)^{1/2}\tau$, which is appropriate to a body of revolution. The velocity increase is indicated as

$$\frac{\Delta V_\infty}{V_\infty}=\left(\frac{\pi}{4}\right)^{1/2}\tau\left(1+0.4\frac{t}{c}\right)\frac{V}{C^{3/2}} \qquad \text{(C.6)}$$

Where,

τ is 0.75 for the octagonal closed tunnel.

V is body volume of the model i.e. 0.025 m^3 for single body and 0.05 m^3 for twin bodies.

This formula gives the values of 0.00304 for single body and 0.00609 for twin bodies. The blockage corrections are therefore 0.61% for single body and 1.22% for twin bodies.

Ref. [50] indicates that the velocity increase for three-dimensional flow in rectangular wind tunnels is given, for axisymmetric bodies, as follows:

$$\Delta V_\infty / V_\infty = 0.36\left[\frac{b_d}{H_d}+\frac{H_d}{b_d}\right]\frac{\text{Vol.}}{A^{1.5}}[1+0.4/f] \qquad \text{(C.7)}$$

Where b_d and H_d are dimensions of tunnel, Vol. is volume of ellipsoids, A is tunnel cross-sectional area and f is fineness ratio (L/D).

This formula results in the values of 0.0035 for single body and 0.007 for twin bodies. The blockage correction is therefore $2\,\Delta V_\infty / V_\infty$ or 0.7% for single body and 1.4% for twin bodies.

Ref. [50] is the latest available reference and the derived corrections are believed to be the most reliable. These corrections are applied to obtain the corrected drag and side-force.

$$C_{D1} = 0.993\, C_D \qquad \text{for single body} \qquad \text{(C.8)}$$

and

$$C_{DI} = 0.986\, C_D \qquad \text{for twin bodies} \qquad (C.9)$$

Similar formulae can be used to calculate the corrected side force i.e. by exchanging C_{DI} with C_{SI} and C_D with C_S. The two formulae are

$$C_{SI} = 0.993\, C_S \qquad \text{for single body} \qquad (C.10)$$

and

$$C_{SI} = 0.986\, C_S \qquad \text{for twin bodies} \qquad (C.11)$$

Reynolds numbers for actual speeds are tabulated in Tables C.2 and C.3.

TABLE C.2: Reynolds numbers (without transition strip)

Model Type	Nominal Speed (m/s)	Atmospheric Temperature (°C)	Atmospheric Pressure (mmHg)	Speed (m/s)	Density of Air (kg/m^3)	Dynamic Viscosity (Ns/m^2)	Reynolds Number
Monohull	20	23.7	767.3	20.22	1.200	1.825E-05	1.60E+06
	30	23.0	767.3	30.22	1.203	1.821E-05	2.40E+06
	40	21.8	767.3	40.30	1.208	1.816E-05	3.22E+06
S/L=0.27	20	25.8	764.0	20.33	1.187	1.835E-05	1.58E+06
	30	26.8	764.0	30.48	1.183	1.840E-05	2.35E+06
	40	26.4	763.5	40.71	1.184	1.838E-05	3.15E+06
S/L=0.37	20	25.8	764.1	20.33	1.187	1.835E-05	1.58E+06
	30	24.7	764.0	30.37	1.191	1.830E-05	2.37E+06
	40	25.2	764.0	40.62	1.189	1.832E-05	3.16E+06
S/L=0.47	20	24.3	764.1	20.28	1.193	1.828E-05	1.59E+06
	30	24.0	764.2	30.33	1.194	1.826E-05	2.38E+06
	40	24.5	764.1	40.57	1.192	1.829E-05	3.17E+06

TABLE C.3: Reynolds numbers (with transition strip)

Model Type	Nominal Speed (m/s)	Atmospheric Temperature (°C)	Atmospheric Pressure (mmHg)	Speed (m/s)	Density of Air (kg/m^3)	Dynamic Viscosity (Ns/m)	Reynolds Number
Monohull	20	21.7	767.5	20.14	1.209	1.815E-05	1.61E+06
	30	22.3	767.4	30.18	1.206	1.818E-05	2.40E+06
	40	22.0	767.4	40.32	1.207	1.817E-05	3.21E+06
S/L=0.27	20	26.5	763.5	20.36	1.183	1.838E-05	1.57E+06
	30	27.0	763.4	30.50	1.181	1.841E-05	2.35E+06
	40	28.0	763.4	40.83	1.177	1.845E-05	3.13E+06
S/L=0.37	20	27.7	763.4	20.41	1.178	1.844E-05	1.56E+06
	30	28.0	763.3	30.55	1.177	1.845E-05	2.34E+06
	40	29.2	763.3	40.91	1.172	1.851E-05	3.11E+06
S/L=0.47	20	28.2	763.2	20.42	1.176	1.846E-05	1.56E+06
	30	28.7	763.2	30.59	1.174	1.849E-05	2.33E+06
	40	29.7	763.1	40.95	1.170	1.854E-05	3.10E+06
S/L=0.57	20	20.3	767.4	20.10	1.214	1.808E-05	1.62E+06
	30	18.0	767.2	29.96	1.224	1.797E-05	2.45E+06
	40	17.5	767.2	40.00	1.226	1.795E-05	3.28E+06

Appendix D

D Parametric Study for the Estimation of Transition Point from Laminar to Turbulent Boundary Layers

A parametric study to estimate skin friction drag based on the predicted transition point has been carried out. The study was conducted at the nominal speeds 20, 30 and 40 m/s by assuming X_Ts (the length when transition point is predicted to occur measured from leading edge) to be 0.05, 0.1, 0.2, 0.3, 0.4 and 0.5 of the total length.

Two mathematically well-defined formulae for the prediction of skin friction drag of a smooth flat plate at zero incidence with partly laminar and partly turbulent boundary layer, described in [42], were applied for the case when there is no transition strip. They are

$$\frac{X_o}{L} = 36.9\left(\frac{X_T}{L}\right)^{5/8} R_L^{-3/8} \tag{D.1}$$

Xo and L are indicated in Figure D.1 where X_0 is length of the plate when there is partly laminar and partly turbulent boundary layer, in m, and L is the total length of the plate, in m.

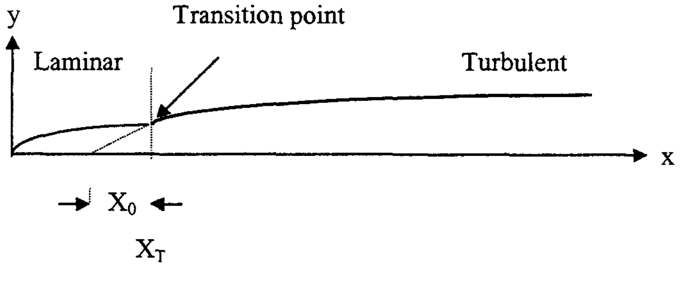

Figure D.1: Location of transition point

and

$$C_F = 0.074 R_L^{-1/5}\left[1-\frac{X_T - X_o}{L}\right]^{4/5} \tag{D.2}$$

where:

R_L is Reynolds number based on length.

C_F is the skin friction coefficient.

TABLE D.1: Test case with nominal speed 20 m/s

X_T/L	Configuration	Actual Speed (m/s)	C_D (x10^3)	C_F (x10^3)	C_D/C_F
0.05	Monohull	20.22	4.358	4.171	1.04
	S/L = 0.27	20.33	4.160	4.182	0.99
	S/L = 0.37	20.33	3.852	4.182	0.92
	S/L = 0.47	20.28	3.376	4.176	0.81
0.10	Monohull	20.22	4.358	4.049	1.08
	S/L = 0.27	20.33	4.160	4.060	1.02
	S/L = 0.37	20.33	3.852	4.060	0.95
	S/L = 0.47	20.28	3.376	4.055	0.83
0.20	Monohull	20.22	4.358	3.780	1.15
	S/L = 0.27	20.33	4.160	3.790	1.10
	S/L = 0.37	20.33	3.852	3.790	1.02
	S/L = 0.47	20.28	3.376	3.785	0.89
0.30	Monohull	20.22	4.358	3.491	1.25
	S/L = 0.27	20.33	4.160	3.501	1.19
	S/L = 0.37	20.33	3.852	3.501	1.10
	S/L = 0.47	20.28	3.376	3.496	0.97
0.40	Monohull	20.22	4.358	3.188	1.37
	S/L = 0.27	20.33	4.160	3.198	1.30
	S/L = 0.37	20.33	3.852	3.198	1.20
	S/L = 0.47	20.28	3.376	3.193	1.06
0.50	Monohull	20.22	4.358	2.873	1.52
	S/L = 0.27	20.33	4.160	2.882	1.44
	S/L = 0.37	20.33	3.852	2.882	1.34
	S/L = 0.47	20.28	3.376	2.877	1.17

TABLE D.2: Test Case with Nominal Speed 30 m/s

X_T/L	Configuration	Actual Speed (m/s)	C_D (x10^3)	C_F (x10^3)	C_D/C_F
0.05	Monohull	30.22	4.043	3.834	1.05
	S/L = 0.27	30.48	4.136	3.851	1.07
	S/L = 0.37	30.37	4.039	3.844	1.05
	S/L = 0.47	30.33	4.052	3.841	1.05
0.10	Monohull	30.22	4.043	3.715	1.09
	S/L = 0.27	30.48	4.136	3.732	1.11
	S/L = 0.37	30.37	4.039	3.725	1.08
	S/L = 0.47	30.33	4.052	3.722	1.09
0.20	Monohull	30.22	4.043	3.456	1.17
	S/L = 0.27	30.48	4.136	3.472	1.19
	S/L = 0.37	30.37	4.039	3.466	1.17
	S/L = 0.47	30.33	4.052	3.463	1.17
0.30	Monohull	30.22	4.043	3.181	1.27
	S/L = 0.27	30.48	4.136	3.196	1.29
	S/L = 0.37	30.37	4.039	3.190	1.27
	S/L = 0.47	30.33	4.052	3.187	1.27
0.40	Monohull	30.22	4.043	2.893	1.40
	S/L = 0.27	30.48	4.136	2.908	1.42
	S/L = 0.37	30.37	4.039	2.902	1.39
	S/L = 0.47	30.33	4.052	2.899	1.40
0.50	Monohull	30.22	4.043	2.594	1.56
	S/L = 0.27	30.48	4.136	2.607	1.59
	S/L = 0.37	30.37	4.039	2.602	1.55
	S/L = 0.47	30.33	4.052	2.599	1.56

TABLE D.3: Test Case with Nominal Speed 40 m/s

X_T/L	Configuration	Actual Speed (m/s)	C_D (x10^3)	C_F (x10^3)	C_D/C_F
0.05	Monohull	40.30	3.993	3.608	1.11
	S/L = 0.27	40.71	4.090	3.624	1.13
	S/L = 0.37	40.62	4.104	3.622	1.13
	S/L = 0.47	40.57	4.084	3.620	1.13
0.10	Monohull	40.30	3.993	3.492	1.14
	S/L = 0.27	40.71	4.090	3.508	1.17
	S/L = 0.37	40.62	4.104	3.506	1.17
	S/L = 0.47	40.57	4.084	3.504	1.17
0.20	Monohull	40.30	3.993	3.242	1.23
	S/L = 0.27	40.71	4.090	3.257	1.26
	S/L = 0.37	40.62	4.104	3.255	1.26
	S/L = 0.47	40.57	4.084	3.253	1.26
0.30	Monohull	40.30	3.993	2.977	1.34
	S/L = 0.27	40.71	4.090	2.991	1.37
	S/L = 0.37	40.62	4.104	2.989	1.37
	S/L = 0.47	40.57	4.084	2.987	1.37
0.40	Monohull	40.30	3.993	2.700	1.48
	S/L = 0.27	40.71	4.090	2.714	1.51
	S/L = 0.37	40.62	4.104	2.712	1.51
	S/L = 0.47	40.57	4.084	2.710	1.51
0.50	Monohull	40.30	3.993	2.412	1.66
	S/L = 0.27	40.71	4.090	2.425	1.69
	S/L = 0.37	40.62	4.104	2.423	1.69
	S/L = 0.47	40.57	4.084	2.422	1.69

Ref. [58] introduced the term 'transition region' as the region in which the boundary layer flow changes from laminar to turbulent. The beginning of this region will be referred to as 'transition point' and will be considered to be the point at which the velocity (and hence the pressure) near the surface begins to show an abnormal fluctuation or an anomaly. The end of the transition region has been taken as the point at which the velocity near the surface has reached a maximum or the pressure has arrived at a minimum value. The anomalies can be seen to occur, as shown in Figures 20a to 31a, between 10% to 30% of the total length when the pressure suddenly goes down and then up.

Based on this information, the transition point is likely to be situated between $X_T/L = 0.20$ and 0.30. This assumption if applied to the data without transition strip leads to the results which are in a good agreement with the results obtained from the test when a transition strip was placed at 0.05L.

This conclusion, drawn from the parametric study, is also in a good agreement with the results shown in [58, 59, and 60]. Ref. [58] indicated that the transition point is shown to occur at X_T/L about 0.26 for R_L from 1.73 to 5.02 x 10^6. Ref. [59], using a graph summarised from [58], indicated that the transition point is located between 0.27 and 0.33L for the same Reynolds number as in the parametric study. Stuper's experiment, using a wing of 17% thickness and moderate camber described in [60], showed that the transition of the boundary layer from laminar to turbulent in the upper surface of the wing, in every case at R_L about 2.8 to 4.8 x 10^6, occurred at a point between 0.27 and 0.3 of the chord from the leading edge. Cuno's experiment, also using a wing of 17% thickness and moderate camber and described in [60], exhibited that the transition occurred at 0.27 of the chord from the leading edge for a Rn of 4.5 x 10^6.

The results from the parametric study in comparison with those with transition strip are further inspected in connection with the form factor values (C_D/C_F). If it is further assumed that no effect on form factors is caused by the attachment of a transition strip, the results could be split into two parts. The first part is when the transition point is estimated to occur at about 0.20L which is available for the single-hull configuration indicating similar form factor values to those with transition strip i.e. 1.17 compared with 1.21 when the nominal speed is 30 m/s and 1.23 compared with 1.22 when it is 40 m/s. This assumption is not suitable for the lowest speed (20 m/s) when low values were obtained.

The second part is when the transition point is predicted to occur at about 0.30 L which is suitable for the twin-hull configuration which exhibits the same values as those with transition strip i.e. respectively 1.29, 1.27 and 1.27 compared with 1.26, 1.21 and 1.21 when the nominal speed is 30 m/s and 1.37, 1.37 and 1.37 compared with 1.33, 1.30 and 1.31 when it is 40 m/s. This assumption, again, is not suitable for the nominal speed 20 m/s.

It is also inferred from the above analysis that the twin-hull configuration is likely to cause the transition point to move slightly backward from the leading edge, from 0.20 L in single-hull case to 0.30 L in twin-hull case. However, the effect of varying S/L is not apparent.

The above analysis for the tests with smooth unstimulated bodies, indicates that the estimation of transition point may be different from case to case. For a more precise and reliable estimate the position of transition should be derived experimentally.

In the case of the current work it is considered that the results for the unstimulated (smooth) bodies at 40 m/s provide useful data although it is likely that the results for the models with turbulence stimulation will be more reliable.

Appendix E

E Estimation of Pressure Drag and Side Force from Pressure Distribution

E.1 Estimation of Pressure Drag

Pressure drag, along with skin friction drag, contributes to the total drag. Pressure drag may be estimated by integrating pressure coefficients over the body. The integration follows the formula:

$$C_{DP} = \int C_P ds \tag{E.1}$$

Where C_P is pressure coefficient, C_{DP} is pressure drag coefficient and ds is distance between two C_ps. In detail, these notations can be seen in Figure E.1.

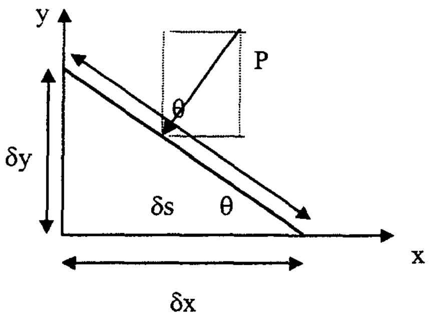

Figure E.1: Load on body surface

From Figure E.1, it can be seen that:

$$\text{Load} = P\delta s \sin\theta \tag{E.2}$$

where

$$\delta s = \frac{\delta y}{\sin\theta} \tag{E.3}$$

therefore

$$C_{DP} = \int C_P \delta y \tag{E.4}$$

Since each percent length (on arbitrary body) possesses its own circumferential pressure, the first stage is to take its average value then to integrate in the y direction. Equation (E.4) can be solved using numerical integration. Since C_P is based on maximum cross-sectional area (whilst C_D is based on wetted surface area), the results must be multiplied by a factor (CSA/WSA) where CSA is maximum cross sectional area (0.0314 m^2) and WSA is wetted surface area (0.6 m^2). The new C_{DP} is then

$$C_{DP1} = 0.0523xC_{DP} \tag{E.5}$$

The results obtained, in addition to skin friction drag, are then compared with the total measured drag and tabulated in Tables E.1 and E.2:

Table E.1: Pressure drag coefficient from integrated pressure (without transition strip)

Model Type	Nominal Speed (m/s)	C_{DP} based on CSA [C_{DP}]	C_{DP} based on WSA [C_{DP1}]	Skin friction drag [C_F]	$C_{DP1} + C_F$	Measured total drag (corrected)
S/L=0.27	20	0.023710	0.001240	0.003501	0.004741	0.004160
	30	0.022099	0.001156	0.003196	0.004352	0.004136
	40	0.021919	0.001148	0.002991	0.004139	0.004090
S/L=0.37	20	0.025458	0.001332	0.003501	0.004833	0.003852
	30	0.022526	0.001178	0.003190	0.004368	0.004039
	40	0.021947	0.001148	0.002989	0.004137	0.004104
S/L=0.47	20	0.024167	0.001264	0.003496	0.004760	0.003376
	30	0.022713	0.001188	0.003187	0.004375	0.004052
	40	0.022006	0.001152	0.002987	0.004139	0.004084

Table E.2: Pressure drag coefficient from integrated pressure (with transition strip)

Model Type	Nominal Speed (m/s)	C_{DP} based on CSA [C_{DP}]	C_{DP} based on WSA [C_{DPI}]	Skin friction drag, ITTC [C_F]	$C_{DPI} + C_F$	Measured total drag (corrected)
S/L=0.27	20	0.023947	0.001254	0.004259	0.005513	0.004973
	30	0.022873	0.001198	0.003926	0.005124	0.004960
	40	0.022904	0.001198	0.003712	0.004910	0.004941
S/L=0.37	20	0.022895	0.001198	0.004263	0.005461	0.004742
	30	0.022905	0.001198	0.003929	0.005127	0.004763
	40	0.022966	0.001202	0.003716	0.004918	0.004824
S/L=0.47	20	0.023196	0.001214	0.004265	0.005479	0.004611
	30	0.023361	0.001222	0.003932	0.005154	0.004775
	40	0.023433	0.001226	0.003718	0.004944	0.004887
S/L=0.57	20	0.022185	0.001160	0.004233	0.005393	0.004744
	30	0.022221	0.001162	0.003893	0.005055	0.004975
	40	0.022724	0.001190	0.003678	0.004868	0.004985

The above results indicate that $C_{DPI} + C_F$ is significantly higher than the measured total drag at low speeds (20 and 30 m/s). This is possibly due to the low measurement values obtained at low speed tests. The difference is about 10% to 40% at 20 m/s and about 2% to 8% at 30 m/s. At higher speed (40 m/s) the difference is not significant i.e. less than 1%.

E.2 Estimation of Side-force

In a similar manner to the interpretation given in Figure E.1 and further explained in Equations (E.2) to (E.4), the same integration technique may be applied to obtain an estimate of side-force. The side-force coefficient is:

$$\text{Local} \quad C_{SF_L} = \int C_P \cos\theta d\theta \qquad \text{(E.6)}$$

$$C_{SF} = \int C_{SF_L} \delta x \qquad \text{(E.7)}$$

Since there is equal spacing, full numerical integration may be applied to the whole length using Simpsons rule. A similar formula to Eq. (E.5) must be applied to give C_{SF} values based on wetted surface area.

The results are compared with the side force measured in the wind tunnel tests and tabulated in Tables E.3 and E.4.

Table E.3: Side-force coefficient from integration of pressures (without transition strip)

Model Type	Nominal speed (m/s)	Calculated C_{SF}	Measured side force, C_{SFI} (corrected)	C_{SFI} when C_{SFI} for monohull is assumed = 0
S/L=0.27	20	0.00303	0.00480	0.00458
	30	0.00311	0.00469	0.00423
	40	0.00346	0.00483	0.00424
S/L=0.37	20	0.00147	0.00212	0.00190
	30	0.00163	0.00234	0.00189
	40	0.00190	0.00246	0.00187
S/L=0.47	20	0.00124	0.00134	0.00112
	30	0.00104	0.00145	0.00099
	40	0.00128	0.00148	0.00089

Table E.4: Side-force coefficient from integration of pressures (with transition strip)

Model Type	Nominal speed (m/s)	Calculated C_{SF}	Measured side force, C_{SFI} (corrected)	C_{SFI} when C_{SFI} for monohull is assumed = 0
S/L=0.27	20	0.00411	0.00447	0.00447
	30	0.00359	0.00429	0.00378
	40	0.00373	0.00455	0.00404
S/L=0.37	20	0.00213	0.00234	0.00234
	30	0.00210	0.00234	0.00184
	40	0.00202	0.00260	0.00209
S/L=0.47	20	0.00109	0.00156	0.00156
	30	0.00127	0.00165	0.00114
	40	0.00146	0.00187	0.00137
S/L=0.57	20	0.00095	0.00101	0.00101
	30	0.00080	0.00085	0.00034
	40	0.00089	0.00120	0.00070

The results indicate that in most cases the calculated side-force is reasonably close to the measured side-force.

Appendix F

F Measured Pressure Coefficients

TABLE F.1: S/L = 0.27, speed = 20 m/s and without transition strip

No.	0%	No.	5%	No.	10%	No.	20%	No.	30%	No.	50%
0	1.028	12	0.083	24	-0.023	36	-0.043	48	-0.101	60	-0.129
1	1.028	13	0.074	25	-0.005	37	-0.035	49	-0.097	61	-0.130
2	1.028	14	0.060	26	-0.041	38	-0.042	50	-0.088	62	-0.113
3	1.028	15	0.042	27	-0.039	39	-0.042	51	-0.081	63	-0.108
4	1.028	16	0.023	28	-0.036	40	-0.042	52	-0.073	64	-0.103
5	1.028	17	0.022	29	-0.044	41	-0.046	53	-0.065	65	-0.103
6	1.028	18	0.014	30	-0.054	42	-0.049	54	-0.063	66	-0.103
7	1.028	19	0.010	31	-0.065	43	-0.048	55	-0.063	67	-0.103
8	1.028	20	0.023	32	-0.073	44	-0.050	56	-0.073	68	-0.081
9	1.028	21	0.015	33	-0.045	45	-0.054	57	-0.084	69	-0.091
10	1.028	22	0.007	34	-0.017	46	-0.058	58	-0.095	70	-0.101
11	1.028	23	0.067	35	-0.021	47	-0.045	59	-0.103	71	-0.128
0	1.028	12	0.083	24	-0.023	36	-0.043	48	-0.101	60	-0.129

No.	70%	No.	80%	No.	90%	No.	95%	No.	100%
72	-0.099	84	-0.073	96	-0.006	108	0.094	120	0.175
73	-0.093	85	-0.087	97	-0.007	109	0.092	121	0.175
74	-0.088	86	-0.131	98	-0.027	110	0.082	122	0.175
75	-0.080	87	-0.108	99	-0.029	111	0.060	123	0.175
76	-0.072	88	-0.085	100	-0.031	112	0.038	124	0.175
77	-0.065	89	-0.091	101	-0.040	113	0.050	125	0.175
78	-0.062	90	-0.085	102	-0.082	114	0.076	126	0.175
79	-0.053	91	-0.089	103	-0.033	115	0.055	127	0.175
80	-0.067	92	-0.083	104	-0.048	116	0.089	128	0.175
81	-0.074	93	-0.093	105	-0.036	117	0.070	129	0.175
82	-0.080	94	-0.102	106	-0.024	118	0.050	130	0.175
83	-0.092	95	-0.090	107	-0.001	119	0.098	131	0.175
72	-0.099	84	-0.073	96	-0.006	108	0.094	120	0.175

TABLE F.2: S/L = 0.27, speed = 30 m/s and without transition strip

No.	0%	No.	5%	No.	10%	No.	20%	No.	30%	No.	50%
0	1.018	12	0.081	24	-0.007	36	-0.084	48	-0.142	60	-0.171
1	1.018	13	0.083	25	-0.003	37	-0.075	49	-0.142	61	-0.174
2	1.018	14	0.063	26	-0.004	38	-0.082	50	-0.128	62	-0.154
3	1.018	15	0.044	27	-0.020	39	-0.082	51	-0.123	63	-0.150
4	1.018	16	0.024	28	-0.036	40	-0.081	52	-0.117	64	-0.145
5	1.018	17	0.019	29	-0.042	41	-0.084	53	-0.108	65	-0.145
6	1.018	18	0.018	30	-0.055	42	-0.089	54	-0.107	66	-0.145
7	1.018	19	0.017	31	-0.065	43	-0.087	55	-0.107	67	-0.145
8	1.018	20	0.017	32	-0.064	44	-0.088	56	-0.115	68	-0.124
9	1.018	21	0.023	33	-0.046	45	-0.095	57	-0.127	69	-0.132
10	1.018	22	0.028	34	-0.027	46	-0.101	58	-0.138	70	-0.140
11	1.018	23	0.068	35	-0.019	47	-0.085	59	-0.148	71	-0.175
0	1.018	12	0.081	24	-0.007	36	-0.084	48	-0.142	60	-0.171

No.	70%	No.	80%	No.	90%	No.	95%	No.	100%
72	-0.142	84	-0.082	96	0.001	108	0.097	120	0.171
73	-0.139	85	-0.085	97	-0.006	109	0.096	121	0.171
74	-0.132	86	-0.111	98	-0.019	110	0.086	122	0.171
75	-0.123	87	-0.101	99	-0.026	111	0.071	123	0.171
76	-0.113	88	-0.091	100	-0.032	112	0.055	124	0.171
77	-0.110	89	-0.092	101	-0.031	113	0.054	125	0.171
78	-0.106	90	-0.085	102	-0.056	114	0.061	126	0.171
79	-0.100	91	-0.085	103	-0.032	115	0.058	127	0.171
80	-0.114	92	-0.080	104	-0.029	116	0.077	128	0.171
81	-0.120	93	-0.087	105	-0.020	117	0.076	129	0.171
82	-0.125	94	-0.094	106	-0.011	118	0.075	130	0.171
83	-0.137	95	-0.099	107	0.001	119	0.101	131	0.171
72	-0.142	84	-0.082	96	0.001	108	0.097	120	0.171

TABLE F.3: S/L = 0.27, speed = 40 m/s and without transition strip

No.	0%	No.	5%	No.	10%	No.	20%	No.	30%	No.	50%
0	1.014	12	0.079	24	-0.006	36	-0.088	48	-0.145	60	-0.173
1	1.014	13	0.083	25	-0.001	37	-0.080	49	-0.144	61	-0.181
2	1.014	14	0.062	26	-0.036	38	-0.087	50	-0.131	62	-0.153
3	1.014	15	0.045	27	-0.035	39	-0.085	51	-0.123	63	-0.152
4	1.014	16	0.027	28	-0.034	40	-0.083	52	-0.114	64	-0.150
5	1.014	17	0.019	29	-0.044	41	-0.090	53	-0.114	65	-0.150
6	1.014	18	0.019	30	-0.054	42	-0.093	54	-0.112	66	-0.150
7	1.014	19	0.021	31	-0.061	43	-0.089	55	-0.111	67	-0.150
8	1.014	20	0.019	32	-0.062	44	-0.094	56	-0.117	68	-0.127
9	1.014	21	0.026	33	-0.046	45	-0.098	57	-0.129	69	-0.135
10	1.014	22	0.033	34	-0.030	46	-0.102	58	-0.141	70	-0.143
11	1.014	23	0.070	35	-0.019	47	-0.087	59	-0.153	71	-0.181
0	1.014	12	0.079	24	-0.006	36	-0.088	48	-0.145	60	-0.173

No.	70%	No.	80%	No.	90%	No.	95%	No.	100%
72	-0.147	84	-0.084	96	0.003	108	0.098	120	0.170
73	-0.146	85	-0.086	97	-0.001	109	0.099	121	0.170
74	-0.139	86	-0.105	98	-0.016	110	0.089	122	0.170
75	-0.127	87	-0.098	99	-0.023	111	0.074	123	0.170
76	-0.115	88	-0.091	100	-0.029	112	0.059	124	0.170
77	-0.111	89	-0.088	101	-0.029	113	0.058	125	0.170
78	-0.106	90	-0.083	102	-0.050	114	0.062	126	0.170
79	-0.104	91	-0.083	103	-0.031	115	0.059	127	0.170
80	-0.117	92	-0.080	104	-0.029	116	0.077	128	0.170
81	-0.123	93	-0.088	105	-0.020	117	0.077	129	0.170
82	-0.128	94	-0.095	106	-0.011	118	0.077	130	0.170
83	-0.140	95	-0.092	107	0.002	119	0.099	131	0.170
72	-0.147	84	-0.084	96	0.003	108	0.098	120	0.170

TABLE F.4: S/L = 0.37, speed = 20 m/s and without transition strip

No.	0%	No.	5%	No.	10%	No.	20%	No.	30%	No.	50%
0	1.016	12	0.067	24	-0.045	36	0.014	48	-0.036	60	-0.049
1	1.016	13	0.039	25	-0.020	37	0.018	49	-0.034	61	-0.058
2	1.016	14	0.045	26	-0.053	38	0.012	50	-0.029	62	-0.048
3	1.016	15	0.032	27	-0.043	39	0.013	51	-0.027	63	-0.051
4	1.016	16	0.018	28	-0.032	40	0.013	52	-0.024	64	-0.054
5	1.016	17	0.017	29	-0.045	41	0.009	53	-0.018	65	-0.054
6	1.016	18	0.018	30	-0.053	42	0.002	54	-0.015	66	-0.054
7	1.016	19	0.026	31	-0.082	43	0.007	55	-0.014	67	-0.054
8	1.016	20	0.030	32	-0.077	44	0.006	56	-0.024	68	-0.033
9	1.016	21	0.035	33	-0.043	45	0.004	57	-0.030	69	-0.037
10	1.016	22	0.040	34	-0.008	46	0.001	58	-0.036	70	-0.041
11	1.016	23	0.045	35	-0.030	47	0.010	59	-0.039	71	-0.056
0	1.016	12	0.067	24	-0.045	36	0.014	48	-0.036	60	-0.049

No.	70%	No.	80%	No.	90%	No.	95%	No.	100%
72	-0.043	84	-0.069	96	-0.026	108	0.080	120	0.179
73	-0.039	85	-0.070	97	-0.024	109	0.076	121	0.179
74	-0.033	86	-0.135	98	-0.032	110	0.072	122	0.179
75	-0.030	87	-0.105	99	-0.028	111	0.053	123	0.179
76	-0.027	88	-0.074	100	-0.023	112	0.034	124	0.179
77	-0.020	89	-0.084	101	-0.041	113	0.049	125	0.179
78	-0.020	90	-0.078	102	-0.091	114	0.083	126	0.179
79	-0.012	91	-0.081	103	-0.036	115	0.056	127	0.179
80	-0.022	92	-0.077	104	-0.051	116	0.094	128	0.179
81	-0.028	93	-0.088	105	-0.043	117	0.064	129	0.179
82	-0.034	94	-0.098	106	-0.035	118	0.033	130	0.179
83	-0.044	95	-0.123	107	-0.024	119	0.105	131	0.179
72	-0.043	84	-0.069	96	-0.026	108	0.080	120	0.179

TABLE F.5: S/L = 0.37, speed = 30 m/s and without transition strip

No.	0%	No.	5%	No.	10%	No.	20%	No.	30%	No.	50%
0	1.017	12	0.059	24	-0.022	36	-0.074	48	-0.110	60	-0.123
1	1.017	13	0.066	25	-0.017	37	-0.069	49	-0.111	61	-0.136
2	1.017	14	0.050	26	-0.041	38	-0.067	50	-0.104	62	-0.120
3	1.017	15	0.037	27	-0.038	39	-0.067	51	-0.102	63	-0.124
4	1.017	16	0.023	28	-0.034	40	-0.066	52	-0.099	64	-0.127
5	1.017	17	0.017	29	-0.043	41	-0.069	53	-0.093	65	-0.127
6	1.017	18	0.019	30	-0.053	42	-0.074	54	-0.090	66	-0.127
7	1.017	19	0.023	31	-0.056	43	-0.070	55	-0.088	67	-0.127
8	1.017	20	0.021	32	-0.053	44	-0.073	56	-0.098	68	-0.105
9	1.017	21	0.033	33	-0.044	45	-0.076	57	-0.104	69	-0.109
10	1.017	22	0.044	34	-0.034	46	-0.078	58	-0.110	70	-0.112
11	1.017	23	0.057	35	-0.028	47	-0.068	59	-0.114	71	-0.137
0	1.017	12	0.059	24	-0.022	36	-0.074	48	-0.110	60	-0.123

No.	70%	No.	80%	No.	90%	No.	95%	No.	100%
72	-0.116	84	-0.092	96	-0.018	108	0.080	120	0.177
73	-0.115	85	-0.086	97	-0.024	109	0.080	121	0.177
74	-0.111	86	-0.091	98	-0.027	110	0.074	122	0.177
75	-0.104	87	-0.089	99	-0.028	111	0.068	123	0.177
76	-0.097	88	-0.087	100	-0.029	112	0.062	124	0.177
77	-0.096	89	-0.084	101	-0.026	113	0.058	125	0.177
78	-0.091	90	-0.081	102	-0.030	114	0.058	126	0.177
79	-0.088	91	-0.079	103	-0.027	115	0.060	127	0.177
80	-0.098	92	-0.080	104	-0.025	116	0.069	128	0.177
81	-0.102	93	-0.087	105	-0.023	117	0.073	129	0.177
82	-0.106	94	-0.094	106	-0.020	118	0.077	130	0.177
83	-0.116	95	-0.094	107	-0.018	119	0.083	131	0.177
72	-0.116	84	-0.092	96	-0.018	108	0.080	120	0.177

TABLE F.6: S/L = 0.37, speed = 40 m/s and without transition strip

No.	0%	No.	5%	No.	10%	No.	20%	No.	30%	No.	50%
0	1.027	12	0.062	24	-0.023	36	-0.097	48	-0.133	60	-0.145
1	1.027	13	0.066	25	-0.015	37	-0.084	49	-0.136	61	-0.160
2	1.027	14	0.050	26	-0.042	38	-0.092	50	-0.126	62	-0.142
3	1.027	15	0.037	27	-0.038	39	-0.093	51	-0.121	63	-0.145
4	1.027	16	0.024	28	-0.034	40	-0.094	52	-0.115	64	-0.148
5	1.027	17	0.020	29	-0.043	41	-0.097	53	-0.115	65	-0.148
6	1.027	18	0.020	30	-0.053	42	-0.097	54	-0.114	66	-0.148
7	1.027	19	0.023	31	-0.056	43	-0.096	55	-0.113	67	-0.148
8	1.027	20	0.022	32	-0.058	44	-0.098	56	-0.114	68	-0.129
9	1.027	21	0.027	33	-0.044	45	-0.102	57	-0.132	69	-0.132
10	1.027	22	0.031	34	-0.029	46	-0.106	58	-0.150	70	-0.135
11	1.027	23	0.057	35	-0.027	47	-0.092	59	-0.136	71	-0.161
0	1.027	12	0.062	24	-0.023	36	-0.097	48	-0.133	60	-0.145

No.	70%	No.	80%	No.	90%	No.	95%	No.	100%
72	-0.141	84	-0.086	96	-0.016	108	0.083	120	0.182
73	-0.138	85	-0.085	97	-0.018	109	0.084	121	0.182
74	-0.137	86	-0.100	98	-0.024	110	0.079	122	0.182
75	-0.130	87	-0.092	99	-0.025	111	0.070	123	0.182
76	-0.122	88	-0.084	100	-0.026	112	0.060	124	0.182
77	-0.121	89	-0.082	101	-0.024	113	0.060	125	0.182
78	-0.113	90	-0.080	102	-0.043	114	0.066	126	0.182
79	-0.112	91	-0.075	103	-0.026	115	0.061	127	0.182
80	-0.123	92	-0.073	104	-0.025	116	0.075	128	0.182
81	-0.127	93	-0.083	105	-0.023	117	0.072	129	0.182
82	-0.131	94	-0.093	106	-0.021	118	0.069	130	0.182
83	-0.141	95	-0.093	107	-0.015	119	0.082	131	0.182
72	-0.141	84	-0.086	96	-0.016	108	0.083	120	0.182

TABLE F.7: S/L = 0.47, speed = 20 m/s and without transition strip

No.	0%	No.	5%	No.	10%	No.	20%	No.	30%	No.	50%
0	1.024	12	0.051	24	-0.075	36	-0.004	48	-0.046	60	-0.063
1	1.024	13	0.048	25	-0.036	37	0.003	49	-0.047	61	-0.074
2	1.024	14	0.046	26	-0.064	38	0.001	50	-0.036	62	-0.071
3	1.024	15	0.034	27	-0.049	39	0.002	51	-0.040	63	-0.077
4	1.024	16	0.022	28	-0.033	40	0.003	52	-0.044	64	-0.083
5	1.024	17	0.016	29	-0.046	41	-0.001	53	-0.039	65	-0.083
6	1.024	18	0.012	30	-0.050	42	-0.008	54	-0.040	66	-0.083
7	1.024	19	0.032	31	-0.090	43	-0.010	55	-0.038	67	-0.083
8	1.024	20	0.033	32	-0.089	44	-0.090	56	-0.049	68	-0.064
9	1.024	21	0.033	33	-0.070	45	-0.055	57	-0.055	69	-0.069
10	1.024	22	0.032	34	-0.055	46	-0.019	58	-0.060	70	-0.073
11	1.024	23	0.036	35	-0.040	47	-0.010	59	-0.059	71	-0.085
0	1.024	12	0.051	24	-0.075	36	-0.004	48	-0.046	60	-0.063

No.	70%	No.	80%	No.	90%	No.	95%	No.	100%
72	-0.077	84	-0.064	96	-0.030	108	0.073	120	0.177
73	-0.074	85	-0.059	97	-0.039	109	0.066	121	0.177
74	-0.069	86	-0.083	98	-0.044	110	0.066	122	0.177
75	-0.065	87	-0.106	99	-0.033	111	0.043	123	0.177
76	-0.062	88	-0.070	100	-0.021	112	0.020	124	0.177
77	-0.059	89	-0.092	101	-0.050	113	0.040	125	0.177
78	-0.057	90	-0.078	102	-0.111	114	0.094	126	0.177
79	-0.054	91	-0.088	103	-0.032	115	0.057	127	0.177
80	-0.063	92	-0.075	104	-0.071	116	0.094	128	0.177
81	-0.066	93	-0.085	105	-0.059	117	0.061	129	0.177
82	-0.068	94	-0.095	106	-0.047	118	0.028	130	0.177
83	-0.079	95	-0.107	107	-0.041	119	0.100	131	0.177
72	-0.077	84	-0.064	96	-0.030	108	0.073	120	0.177

TABLE F.8: S/L = 0.47, speed = 30 m/s and without transition strip

No.	0%	No.	5%	No.	10%	No.	20%	No.	30%	No.	50%
0	1.024	12	0.046	24	-0.046	36	-0.074	48	-0.112	60	-0.104
1	1.024	13	0.053	25	-0.026	37	-0.064	49	-0.112	61	-0.115
2	1.024	14	0.050	26	-0.040	38	-0.066	50	-0.105	62	-0.107
3	1.024	15	0.039	27	-0.034	39	-0.067	51	-0.102	63	-0.111
4	1.024	16	0.028	28	-0.028	40	-0.067	52	-0.099	64	-0.115
5	1.024	17	0.025	29	-0.039	41	-0.076	53	-0.094	65	-0.115
6	1.024	18	0.022	30	-0.048	42	-0.077	54	-0.092	66	-0.115
7	1.024	19	0.028	31	-0.048	43	-0.077	55	-0.084	67	-0.115
8	1.024	20	0.024	32	-0.048	44	-0.078	56	-0.089	68	-0.107
9	1.024	21	0.032	33	-0.046	45	-0.083	57	-0.095	69	-0.101
10	1.024	22	0.039	34	-0.044	46	-0.087	58	-0.101	70	-0.096
11	1.024	23	0.046	35	-0.037	47	-0.076	59	-0.103	71	-0.121
0	1.024	12	0.046	24	-0.046	36	-0.074	48	-0.112	60	-0.104

No.	70%	No.	80%	No.	90%	No.	95%	No.	100%
72	-0.105	84	-0.098	96	-0.021	108	0.077	120	0.178
73	-0.104	85	-0.091	97	-0.026	109	0.074	121	0.178
74	-0.104	86	-0.086	98	-0.033	110	0.070	122	0.178
75	-0.099	87	-0.084	99	-0.030	111	0.065	123	0.178
76	-0.093	88	-0.082	100	-0.027	112	0.060	124	0.178
77	-0.096	89	-0.084	101	-0.022	113	0.058	125	0.178
78	-0.090	90	-0.078	102	-0.026	114	0.055	126	0.178
79	-0.087	91	-0.077	103	-0.023	115	0.061	127	0.178
80	-0.097	92	-0.077	104	-0.037	116	0.066	128	0.178
81	-0.100	93	-0.084	105	-0.029	117	0.071	129	0.178
82	-0.102	94	-0.090	106	-0.020	118	0.076	130	0.178
83	-0.109	95	-0.088	107	-0.021	119	0.072	131	0.178
72	-0.105	84	-0.098	96	-0.021	108	0.077	120	0.178

TABLE F.9: S/L = 0.47, speed = 40 m/s and without transition strip

No.	0%	No.	5%	No.	10%	No.	20%	No.	30%	No.	50%
0	1.020	12	0.049	24	-0.037	36	-0.093	48	-0.121	60	-0.125
1	1.020	13	0.049	25	-0.020	37	-0.083	49	-0.122	61	-0.139
2	1.020	14	0.050	26	-0.048	38	-0.084	50	-0.108	62	-0.124
3	1.020	15	0.039	27	-0.039	39	-0.083	51	-0.106	63	-0.130
4	1.020	16	0.027	28	-0.030	40	-0.081	52	-0.104	64	-0.136
5	1.020	17	0.026	29	-0.037	41	-0.085	53	-0.104	65	-0.136
6	1.020	18	0.026	30	-0.047	42	-0.090	54	-0.104	66	-0.136
7	1.020	19	0.031	31	-0.057	43	-0.088	55	-0.104	67	-0.136
8	1.020	20	0.025	32	-0.059	44	-0.087	56	-0.108	68	-0.117
9	1.020	21	0.019	33	-0.044	45	-0.093	57	-0.115	69	-0.116
10	1.020	22	0.013	34	-0.029	46	-0.098	58	-0.121	70	-0.114
11	1.020	23	0.042	35	-0.035	47	-0.089	59	-0.125	71	-0.139
0	1.020	12	0.049	24	-0.037	36	-0.093	48	-0.121	60	-0.125

No.	70%	No.	80%	No.	90%	No.	95%	No.	100%
72	-0.125	84	-0.079	96	-0.021	108	0.079	120	0.178
73	-0.122	85	-0.077	97	-0.022	109	0.077	121	0.178
74	-0.122	86	-0.102	98	-0.026	110	0.073	122	0.178
75	-0.115	87	-0.090	99	-0.024	111	0.064	123	0.178
76	-0.108	88	-0.077	100	-0.022	112	0.054	124	0.178
77	-0.109	89	-0.079	101	-0.027	113	0.060	125	0.178
78	-0.102	90	-0.078	102	-0.054	114	0.073	126	0.178
79	-0.099	91	-0.073	103	-0.027	115	0.063	127	0.178
80	-0.110	92	-0.073	104	-0.029	116	0.082	128	0.178
81	-0.112	93	-0.083	105	-0.028	117	0.071	129	0.178
82	-0.114	94	-0.092	106	-0.026	118	0.060	130	0.178
83	-0.121	95	-0.093	107	-0.022	119	0.088	131	0.178
72	-0.125	84	-0.079	96	-0.021	108	0.079	120	0.178

TABLE F.10: Cp at S/L = 0.27, speed = 20 m/s and with transition strip

No.	0%	No.	5%	No.	10%	No.	20%	No.	30%	No.	50%
0	1.036	12	0.117	24	-0.019	36	-0.056	48	-0.114	60	-0.133
1	1.036	13	0.078	25	-0.030	37	-0.049	49	-0.110	61	-0.141
2	1.036	14	0.090	26	-0.040	38	-0.059	50	-0.098	62	-0.117
3	1.036	15	0.069	27	-0.035	39	-0.056	51	-0.088	63	-0.114
4	1.036	16	0.047	28	-0.030	40	-0.053	52	-0.078	64	-0.110
5	1.036	17	0.034	29	-0.044	41	-0.062	53	-0.073	65	-0.110
6	1.036	18	0.040	30	-0.054	42	-0.063	54	-0.069	66	-0.110
7	1.036	19	0.045	31	-0.083	43	-0.064	55	-0.069	67	-0.110
8	1.036	20	0.065	32	-0.076	44	-0.061	56	-0.078	68	-0.093
9	1.036	21	0.047	33	-0.042	45	-0.070	57	-0.090	69	-0.102
10	1.036	22	0.028	34	-0.008	46	-0.079	58	-0.101	70	-0.111
11	1.036	23	0.096	35	-0.016	47	-0.059	59	-0.111	71	-0.138
0	1.036	12	0.117	24	-0.019	36	-0.056	48	-0.114	60	-0.133

No.	70%	No.	80%	No.	90%	No.	95%	No.	100%
72	-0.110	84	-0.063	96	-0.004	108	0.096	120	0.165
73	-0.107	85	-0.070	97	-0.007	109	0.090	121	0.165
74	-0.103	86	-0.133	98	-0.020	110	0.083	122	0.165
75	-0.091	87	-0.106	99	-0.021	111	0.058	123	0.165
76	-0.078	88	-0.079	100	-0.021	112	0.033	124	0.165
77	-0.074	89	-0.092	101	-0.047	113	0.047	125	0.165
78	-0.072	90	-0.082	102	-0.103	114	0.088	126	0.165
79	-0.066	91	-0.085	103	-0.042	115	0.057	127	0.165
80	-0.077	92	-0.067	104	-0.048	116	0.097	128	0.165
81	-0.085	93	-0.085	105	-0.037	117	0.069	129	0.165
82	-0.093	94	-0.102	106	-0.026	118	0.040	130	0.165
83	-0.102	95	-0.115	107	-0.015	119	0.068	131	0.165
72	-0.110	84	-0.063	96	-0.004	108	0.096	120	0.165

TABLE F.11: Cp at S/L = 0.27, speed = 30 m/s and with transition strip

No.	0%	No.	5%	No.	10%	No.	20%	No.	30%	No.	50%
0	1.015	12	0.101	24	0.002	36	-0.081	48	-0.140	60	-0.168
1	1.015	13	0.092	25	0.000	37	-0.072	49	-0.145	61	-0.173
2	1.015	14	0.098	26	-0.030	38	-0.084	50	-0.121	62	-0.133
3	1.015	15	0.075	27	-0.031	39	-0.080	51	-0.115	63	-0.138
4	1.015	16	0.052	28	-0.031	40	-0.076	52	-0.109	64	-0.142
5	1.015	17	0.034	29	-0.041	41	-0.081	53	-0.110	65	-0.142
6	1.015	18	0.041	30	-0.057	42	-0.083	54	-0.100	66	-0.142
7	1.015	19	0.041	31	-0.062	43	-0.084	55	-0.099	67	-0.142
8	1.015	20	0.054	32	-0.062	44	-0.078	56	-0.109	68	-0.125
9	1.015	21	0.064	33	-0.045	45	-0.092	57	-0.122	69	-0.132
10	1.015	22	0.073	34	-0.027	46	-0.105	58	-0.135	70	-0.139
11	1.015	23	0.109	35	-0.017	47	-0.080	59	-0.151	71	-0.173
0	1.015	12	0.101	24	0.002	36	-0.081	48	-0.140	60	-0.168

No.	70%	No.	80%	No.	90%	No.	95%	No.	100%
72	-0.138	84	-0.083	96	0.006	108	0.095	120	0.162
73	-0.137	85	-0.080	97	-0.003	109	0.095	121	0.162
74	-0.133	86	-0.102	98	-0.012	110	0.083	122	0.162
75	-0.118	87	-0.096	99	-0.018	111	0.070	123	0.162
76	-0.112	88	-0.090	100	-0.024	112	0.056	124	0.162
77	-0.110	89	-0.091	101	-0.032	113	0.051	125	0.162
78	-0.102	90	-0.088	102	-0.041	114	0.057	126	0.162
79	-0.098	91	-0.082	103	-0.031	115	0.060	127	0.162
80	-0.111	92	-0.084	104	-0.029	116	0.074	128	0.162
81	-0.117	93	-0.087	105	-0.019	117	0.075	129	0.162
82	-0.123	94	-0.090	106	-0.008	118	0.076	130	0.162
83	-0.137	95	-0.095	107	-0.002	119	0.104	131	0.162
72	-0.138	84	-0.083	96	0.006	108	0.095	120	0.162

TABLE F.12: S/L = 0.27, speed = 40 m/s and with transition strip

No.	0%	No.	5%	No.	10%	No.	20%	No.	30%	No.	50%
0	1.015	12	0.106	24	0.011	36	-0.088	48	-0.145	60	-0.173
1	1.015	13	0.113	25	0.012	37	-0.079	49	-0.152	61	-0.177
2	1.015	14	0.101	26	-0.052	38	-0.093	50	-0.124	62	-0.155
3	1.015	15	0.079	27	-0.039	39	-0.087	51	-0.118	63	-0.152
4	1.015	16	0.056	28	-0.026	40	-0.081	52	-0.112	64	-0.149
5	1.015	17	0.038	29	-0.042	41	-0.085	53	-0.114	65	-0.149
6	1.015	18	0.043	30	-0.049	42	-0.086	54	-0.104	66	-0.149
7	1.015	19	0.044	31	-0.052	43	-0.090	55	-0.104	67	-0.149
8	1.015	20	0.059	32	-0.053	44	-0.082	56	-0.117	68	-0.128
9	1.015	21	0.071	33	-0.043	45	-0.098	57	-0.129	69	-0.138
10	1.015	22	0.083	34	-0.033	46	-0.113	58	-0.141	70	-0.147
11	1.015	23	0.114	35	-0.029	47	-0.085	59	-0.158	71	-0.179
0	1.015	12	0.106	24	0.011	36	-0.088	48	-0.145	60	-0.173

No.	70%	No.	80%	No.	90%	No.	95%	No.	100%
72	-0.146	84	-0.085	96	0.008	108	0.098	120	0.162
73	-0.146	85	-0.084	97	0.000	109	0.095	121	0.162
74	-0.137	86	-0.097	98	-0.015	110	0.087	122	0.162
75	-0.127	87	-0.095	99	-0.021	111	0.076	123	0.162
76	-0.116	88	-0.093	100	-0.027	112	0.064	124	0.162
77	-0.116	89	-0.087	101	-0.030	113	0.060	125	0.162
78	-0.106	90	-0.088	102	-0.036	114	0.054	126	0.162
79	-0.107	91	-0.083	103	-0.030	115	0.057	127	0.162
80	-0.118	92	-0.078	104	-0.020	116	0.071	128	0.162
81	-0.124	93	-0.085	105	-0.015	117	0.077	129	0.162
82	-0.130	94	-0.092	106	-0.009	118	0.083	130	0.162
83	-0.140	95	-0.091	107	0.003	119	0.096	131	0.162
72	-0.146	84	-0.085	96	0.008	108	0.098	120	0.162

TABLE F.13: Cp at S/L = 0.37, speed = 20 m/s and with transition strip

No.	0%	No.	5%	No.	10%	No.	20%	No.	30%	No.	50%
0	1.027	12	0.078	24	-0.027	36	-0.074	48	-0.117	60	-0.125
1	1.027	13	0.047	25	-0.019	37	-0.067	49	-0.117	61	-0.134
2	1.027	14	0.072	26	-0.048	38	-0.072	50	-0.104	62	-0.118
3	1.027	15	0.061	27	-0.039	39	-0.066	51	-0.099	63	-0.122
4	1.027	16	0.050	28	-0.029	40	-0.059	52	-0.093	64	-0.125
5	1.027	17	0.041	29	-0.041	41	-0.072	53	-0.092	65	-0.125
6	1.027	18	0.045	30	-0.052	42	-0.070	54	-0.091	66	-0.125
7	1.027	19	0.057	31	-0.077	43	-0.073	55	-0.089	67	-0.125
8	1.027	20	0.069	32	-0.060	44	-0.071	56	-0.095	68	-0.106
9	1.027	21	0.054	33	-0.043	45	-0.080	57	-0.103	69	-0.123
10	1.027	22	0.039	34	-0.025	46	-0.088	58	-0.110	70	-0.139
11	1.027	23	0.077	35	-0.031	47	-0.073	59	-0.117	71	-0.134
0	1.027	12	0.078	24	-0.027	36	-0.074	48	-0.117	60	-0.125

No.	70%	No.	80%	No.	90%	No.	95%	No.	100%
72	-0.113	84	-0.067	96	-0.011	108	0.083	120	0.171
73	-0.112	85	-0.066	97	-0.012	109	0.076	121	0.171
74	-0.107	86	-0.123	98	-0.022	110	0.070	122	0.171
75	-0.103	87	-0.102	99	-0.021	111	0.057	123	0.171
76	-0.099	88	-0.081	100	-0.020	112	0.043	124	0.171
77	-0.094	89	-0.083	101	-0.044	113	0.050	125	0.171
78	-0.088	90	-0.089	102	-0.085	114	0.069	126	0.171
79	-0.085	91	-0.082	103	-0.041	115	0.057	127	0.171
80	-0.096	92	-0.075	104	-0.035	116	0.089	128	0.171
81	-0.100	93	-0.084	105	-0.033	117	0.060	129	0.171
82	-0.104	94	-0.092	106	-0.030	118	0.031	130	0.171
83	-0.112	95	-0.116	107	-0.024	119	0.057	131	0.171
72	-0.113	84	-0.067	96	-0.011	108	0.083	120	0.171

TABLE F.14: Cp at S/L = 0.37, speed = 30 m/s and with transition strip

No.	0%	No.	5%	No.	10%	No.	20%	No.	30%	No.	50%
0	1.021	12	0.075	24	-0.022	36	-0.085	48	-0.123	60	-0.131
1	1.021	13	0.063	25	-0.022	37	-0.077	49	-0.129	61	-0.142
2	1.021	14	0.081	26	-0.043	38	-0.084	50	-0.107	62	-0.127
3	1.021	15	0.067	27	-0.036	39	-0.079	51	-0.105	63	-0.130
4	1.021	16	0.052	28	-0.029	40	-0.073	52	-0.102	64	-0.133
5	1.021	17	0.038	29	-0.036	41	-0.073	53	-0.103	65	-0.133
6	1.021	18	0.050	30	-0.047	42	-0.076	54	-0.092	66	-0.133
7	1.021	19	0.053	31	-0.059	43	-0.077	55	-0.091	67	-0.133
8	1.021	20	0.066	32	-0.053	44	-0.074	56	-0.104	68	-0.114
9	1.021	21	0.063	33	-0.041	45	-0.086	57	-0.111	69	-0.118
10	1.021	22	0.059	34	-0.029	46	-0.098	58	-0.118	70	-0.121
11	1.021	23	0.085	35	-0.031	47	-0.079	59	-0.132	71	-0.142
0	1.021	12	0.075	24	-0.022	36	-0.085	48	-0.123	60	-0.131

No.	70%	No.	80%	No.	90%	No.	95%	No.	100%
72	-0.123	84	-0.080	96	-0.010	108	0.081	120	0.167
73	-0.120	85	-0.072	97	-0.016	109	0.081	121	0.167
74	-0.119	86	-0.101	98	-0.020	110	0.074	122	0.167
75	-0.113	87	-0.094	99	-0.023	111	0.065	123	0.167
76	-0.106	88	-0.087	100	-0.025	112	0.056	124	0.167
77	-0.105	89	-0.087	101	-0.032	113	0.056	125	0.167
78	-0.099	90	-0.082	102	-0.050	114	0.063	126	0.167
79	-0.099	91	-0.082	103	-0.032	115	0.058	127	0.167
80	-0.105	92	-0.078	104	-0.026	116	0.074	128	0.167
81	-0.109	93	-0.084	105	-0.023	117	0.067	129	0.167
82	-0.112	94	-0.090	106	-0.019	118	0.060	130	0.167
83	-0.119	95	-0.096	107	-0.014	119	0.096	131	0.167
72	-0.123	84	-0.080	96	-0.010	108	0.081	120	0.167

TABLE F.15: S/L = 0.37, speed = 40 m/s and with transition strip

No.	0%	No.	5%	No.	10%	No.	20%	No.	30%	No.	50%
0	1.014	12	0.078	24	-0.014	36	-0.088	48	-0.123	60	-0.135
1	1.014	13	0.085	25	-0.009	37	-0.076	49	-0.131	61	-0.143
2	1.014	14	0.085	26	-0.061	38	-0.088	50	-0.108	62	-0.129
3	1.014	15	0.071	27	-0.043	39	-0.080	51	-0.106	63	-0.134
4	1.014	16	0.056	28	-0.025	40	-0.071	52	-0.103	64	-0.138
5	1.014	17	0.042	29	-0.036	41	-0.076	53	-0.106	65	-0.138
6	1.014	18	0.051	30	-0.041	42	-0.077	54	-0.092	66	-0.138
7	1.014	19	0.053	31	-0.047	43	-0.079	55	-0.095	67	-0.138
8	1.014	20	0.066	32	-0.050	44	-0.072	56	-0.105	68	-0.117
9	1.014	21	0.069	33	-0.042	45	-0.086	57	-0.113	69	-0.120
10	1.014	22	0.072	34	-0.033	46	-0.100	58	-0.120	70	-0.122
11	1.014	23	0.094	35	-0.045	47	-0.076	59	-0.134	71	-0.146
0	1.014	12	0.078	24	-0.014	36	-0.088	48	-0.123	60	-0.135

No.	70%	No.	80%	No.	90%	No.	95%	No.	100%
72	-0.124	84	-0.081	96	-0.010	108	0.085	120	0.166
73	-0.122	85	-0.078	97	-0.014	109	0.084	121	0.166
74	-0.121	86	-0.095	98	-0.019	110	0.076	122	0.166
75	-0.115	87	-0.091	99	-0.023	111	0.067	123	0.166
76	-0.108	88	-0.086	100	-0.026	112	0.061	124	0.166
77	-0.106	89	-0.085	101	-0.027	113	0.060	125	0.166
78	-0.100	90	-0.080	102	-0.042	114	0.060	126	0.166
79	-0.101	91	-0.080	103	-0.030	115	0.060	127	0.166
80	-0.108	92	-0.076	104	-0.022	116	0.073	128	0.166
81	-0.111	93	-0.083	105	-0.020	117	0.071	129	0.166
82	-0.114	94	-0.089	106	-0.018	118	0.069	130	0.166
83	-0.119	95	-0.092	107	-0.010	119	0.089	131	0.166
72	-0.124	84	-0.081	96	-0.010	108	0.085	120	0.166

TABLE F.16: Cp at S/L = 0.47, speed = 20 m/s and with transition strip

No.	0%	No.	5%	No.	10%	No.	20%	No.	30%	No.	50%
0	1.017	12	0.068	24	-0.029	36	-0.068	48	-0.099	48	-0.101
1	1.017	13	0.060	25	-0.029	37	-0.061	49	-0.104	49	-0.112
2	1.017	14	0.078	26	-0.036	38	-0.064	50	-0.095	50	-0.101
3	1.017	15	0.065	27	-0.035	39	-0.062	51	-0.090	51	-0.108
4	1.017	16	0.052	28	-0.033	40	-0.059	52	-0.085	52	-0.114
5	1.017	17	0.036	29	-0.036	41	-0.065	53	-0.085	53	-0.114
6	1.017	18	0.046	30	-0.051	42	-0.070	54	-0.084	54	-0.114
7	1.017	19	0.045	31	-0.067	43	-0.064	55	-0.082	55	-0.114
8	1.017	29	0.054	32	-0.051	44	-0.063	56	-0.089	56	-0.100
9	1.017	21	0.058	33	-0.045	45	-0.071	57	-0.094	57	-0.099
10	1.017	22	0.062	34	-0.039	46	-0.079	58	-0.098	58	-0.098
11	1.017	23	0.076	35	-0.038	47	-0.064	59	-0.102	59	-0.114
0	1.017	12	0.068	24	-0.029	36	-0.068	48	-0.099	48	-0.101

No.	70%	No.	80%	No.	90%	No.	95%	No.	100%
72	-0.102	84	-0.090	96	-0.026	108	0.069	120	0.171
73	-0.101	85	-0.075	97	-0.031	109	0.071	121	0.171
74	-0.098	86	-0.096	98	-0.031	110	0.065	122	0.171
75	-0.094	87	-0.092	99	-0.032	111	0.060	123	0.171
76	-0.090	88	-0.088	100	-0.032	112	0.054	124	0.171
77	-0.088	89	-0.089	101	-0.028	113	0.053	125	0.171
78	-0.086	90	-0.083	102	-0.040	114	0.059	126	0.171
79	-0.080	91	-0.081	103	-0.029	115	0.058	127	0.171
80	-0.088	92	-0.074	104	-0.021	116	0.068	128	0.171
81	-0.091	93	-0.082	105	-0.020	117	0.065	129	0.171
82	-0.094	94	-0.090	106	-0.018	118	0.062	130	0.171
83	-0.100	95	-0.105	107	-0.024	119	0.086	131	0.171
72	-0.102	84	-0.090	96	-0.026	108	0.069	120	0.171

TABLE F.17: Cp at S/L = 0.47, speed = 30 m/s and with transition strip

No.	0%	No.	5%	No.	10%	No.	20%	No.	30%	No.	50%
0	1.023	12	0.072	24	-0.026	36	-0.080	48	-0.106	48	-0.112
1	1.023	13	0.057	25	-0.021	37	-0.070	49	-0.115	49	-0.122
2	1.023	14	0.080	26	-0.047	38	-0.079	50	-0.094	50	-0.113
3	1.023	15	0.073	27	-0.036	39	-0.071	51	-0.094	51	-0.118
4	1.023	16	0.056	28	-0.025	40	-0.063	52	-0.093	52	-0.123
5	1.023	17	0.044	29	-0.036	41	-0.068	53	-0.095	53	-0.123
6	1.023	18	0.050	30	-0.046	42	-0.073	54	-0.085	54	-0.123
7	1.023	19	0.052	31	-0.057	43	-0.073	55	-0.087	55	-0.123
8	1.023	29	0.066	32	-0.057	44	-0.070	56	-0.097	56	-0.107
9	1.023	21	0.058	33	-0.042	45	-0.081	57	-0.102	57	-0.107
10	1.023	22	0.050	34	-0.027	46	-0.091	58	-0.107	58	-0.106
11	1.023	23	0.080	35	-0.034	47	-0.071	59	-0.118	59	-0.121
0	1.023	12	0.072	24	-0.026	36	-0.080	48	-0.106	48	-0.112

No.	70%	No.	80%	No.	90%	No.	95%	No.	100%
72	-0.111	84	-0.076	96	-0.023	108	0.076	120	0.173
73	-0.110	85	-0.073	97	-0.023	109	0.073	121	0.173
74	-0.106	86	-0.105	98	-0.026	110	0.070	122	0.173
75	-0.101	87	-0.091	99	-0.023	111	0.061	123	0.173
76	-0.096	88	-0.077	100	-0.020	112	0.051	124	0.173
77	-0.096	89	-0.081	101	-0.031	113	0.058	125	0.173
78	-0.090	90	-0.080	102	-0.056	114	0.075	126	0.173
79	-0.087	91	-0.079	103	-0.029	115	0.061	127	0.173
80	-0.097	92	-0.070	104	-0.026	116	0.084	128	0.173
81	-0.099	93	-0.080	105	-0.026	117	0.067	129	0.173
82	-0.101	94	-0.090	106	-0.025	118	0.050	130	0.173
83	-0.108	95	-0.099	107	-0.023	119	0.093	131	0.173
72	-0.111	84	-0.076	96	-0.023	108	0.076	120	0.173

TABLE F.18: Cp at S/L = 0.47, speed = 40 m/s and with transition strip

No.	0%	No.	5%	No.	10%	No.	20%	No.	30%	No.	50%
0	1.021	12	0.072	24	-0.023	36	-0.083	48	-0.107	48	-0.115
1	1.021	13	0.076	25	-0.013	37	-0.071	49	-0.118	49	-0.113
2	1.021	14	0.083	26	-0.063	38	-0.082	50	-0.095	50	-0.111
3	1.021	15	0.071	27	-0.043	39	-0.074	51	-0.096	51	-0.120
4	1.021	16	0.059	28	-0.022	40	-0.066	52	-0.097	52	-0.128
5	1.021	17	0.044	29	-0.032	41	-0.070	53	-0.100	53	-0.128
6	1.021	18	0.052	30	-0.044	42	-0.072	54	-0.088	54	-0.128
7	1.021	19	0.052	31	-0.046	43	-0.075	55	-0.091	55	-0.128
8	1.021	29	0.067	32	-0.054	44	-0.069	56	-0.098	56	-0.110
9	1.021	21	0.065	33	-0.041	45	-0.081	57	-0.104	57	-0.110
10	1.021	22	0.062	34	-0.028	46	-0.093	58	-0.110	58	-0.110
11	1.021	23	0.087	35	-0.048	47	-0.073	59	-0.120	59	-0.127
0	1.021	12	0.072	24	-0.023	36	-0.083	48	-0.107	48	-0.115

No.	70%	No.	80%	No.	90%	No.	95%	No.	100%
72	-0.115	84	-0.081	96	-0.018	108	0.075	120	0.172
73	-0.113	85	-0.079	97	-0.021	109	0.075	121	0.172
74	-0.111	86	-0.096	98	-0.025	110	0.070	122	0.172
75	-0.106	87	-0.088	99	-0.023	111	0.065	123	0.172
76	-0.100	88	-0.080	100	-0.021	112	0.059	124	0.172
77	-0.101	89	-0.082	101	-0.023	113	0.061	125	0.172
78	-0.094	90	-0.076	102	-0.041	114	0.071	126	0.172
79	-0.093	91	-0.074	103	-0.023	115	0.063	127	0.172
80	-0.101	92	-0.072	104	-0.023	116	0.078	128	0.172
81	-0.103	93	-0.081	105	-0.023	117	0.071	129	0.172
82	-0.104	94	-0.089	106	-0.022	118	0.064	130	0.172
83	-0.112	95	-0.090	107	-0.019	119	0.082	131	0.172
72	-0.115	84	-0.081	96	-0.018	108	0.075	120	0.172

TABLE F.19: Cp at S/L = 0.57, speed = 20 m/s and with transition strip

No.	0%	No.	5%	No.	10%	No.	20%	No.	30%	No.	50%
0	1.025	12	0.072	24	-0.035	36	-0.106	48	-0.142	60	-0.140
1	1.025	13	0.092	25	-0.024	37	-0.097	49	-0.143	61	-0.153
2	1.025	14	0.079	26	-0.035	38	-0.102	50	-0.134	62	-0.145
3	1.025	15	0.067	27	-0.031	39	-0.099	51	-0.132	63	-0.152
4	1.025	16	0.055	28	-0.027	40	-0.096	52	-0.130	64	-0.158
5	1.025	17	0.039	29	-0.036	41	-0.107	53	-0.128	65	-0.158
6	1.025	18	0.045	30	-0.047	42	-0.109	54	-0.126	66	-0.158
7	1.025	19	0.044	31	-0.054	43	-0.107	55	-0.123	67	-0.158
8	1.025	20	0.056	32	-0.050	44	-0.107	56	-0.131	68	-0.143
9	1.025	21	0.064	33	-0.046	45	-0.115	57	-0.137	69	-0.143
10	1.025	22	0.072	34	-0.042	46	-0.122	58	-0.142	70	-0.143
11	1.025	23	0.078	35	-0.031	47	-0.109	59	-0.142	71	-0.157
0	1.025	12	0.072	24	-0.035	36	-0.106	48	-0.142	60	-0.140

No.	70%	No.	80%	No.	90%	No.	95%	No.	100%
72	-0.145	84	-0.094	96	-0.024	108	0.076	120	0.178
73	-0.144	85	-0.078	97	-0.032	109	0.073	121	0.178
74	-0.143	86	-0.082	98	-0.029	110	0.068	122	0.178
75	-0.140	87	-0.083	99	-0.025	111	0.066	123	0.178
76	-0.136	88	-0.084	100	-0.020	112	0.063	124	0.178
77	-0.136	89	-0.082	101	-0.021	113	0.061	125	0.178
78	-0.131	90	-0.078	102	-0.020	114	0.065	126	0.178
79	-0.128	91	-0.077	103	-0.020	115	0.071	127	0.178
80	-0.135	92	-0.066	104	-0.029	116	0.069	128	0.178
81	-0.138	93	-0.077	105	-0.022	117	0.074	129	0.178
82	-0.141	94	-0.087	106	-0.015	118	0.079	130	0.178
83	-0.147	95	-0.096	107	-0.022	119	0.081	131	0.178
72	-0.145	84	-0.094	96	-0.024	108	0.076	120	0.178

TABLE F.20: Cp at S/L = 0.57, speed = 30 m/s and with transition strip

No.	0%	No.	5%	No.	10%	No.	20%	No.	30%	No.	50%
0	1.020	12	0.070	24	-0.023	36	-0.116	48	-0.145	60	-0.145
1	1.020	13	0.083	25	-0.016	37	-0.104	49	-0.150	61	-0.157
2	1.020	14	0.083	26	-0.058	38	-0.115	59	-0.131	62	-0.150
3	1.020	15	0.070	27	-0.042	39	-0.103	51	-0.133	63	-0.157
4	1.020	16	0.057	28	-0.025	40	-0.101	52	-0.135	64	-0.164
5	1.020	17	0.042	29	-0.037	41	-0.110	53	-0.137	65	-0.164
6	1.020	18	0.048	30	-0.044	42	-0.112	54	-0.128	66	-0.164
7	1.020	19	0.050	31	-0.046	43	-0.111	55	-0.127	67	-0.164
8	1.020	20	0.062	32	-0.047	44	-0.108	56	-0.135	68	-0.149
9	1.020	21	0.066	33	-0.043	45	-0.119	57	-0.141	69	-0.147
10	1.020	22	0.070	34	-0.038	46	-0.130	58	-0.147	70	-0.144
11	1.020	23	0.087	35	-0.034	47	-0.111	59	-0.156	71	-0.158
0	1.020	12	0.070	24	-0.023	36	-0.116	48	-0.145	60	-0.145

No.	70%	No.	80%	No.	90%	No.	95%	No.	100%
72	-0.149	84	-0.086	96	-0.023	108	0.076	120	0.181
73	-0.147	85	-0.081	97	-0.023	109	0.074	121	0.181
74	-0.145	86	-0.088	98	-0.025	110	0.073	122	0.181
75	-0.141	87	-0.081	99	-0.021	111	0.071	123	0.181
76	-0.137	88	-0.074	100	-0.017	112	0.069	124	0.181
77	-0.135	89	-0.076	101	-0.016	113	0.069	125	0.181
78	-0.130	90	-0.074	102	-0.024	114	0.071	126	0.181
79	-0.129	91	-0.072	103	-0.014	115	0.071	127	0.181
80	-0.137	92	-0.070	104	-0.016	116	0.077	128	0.181
81	-0.139	93	-0.078	105	-0.017	117	0.076	129	0.181
82	-0.141	94	-0.085	106	-0.017	118	0.074	130	0.181
83	-0.147	95	-0.088	107	-0.017	119	0.076	131	0.181
72	-0.149	84	-0.086	96	-0.023	108	0.076	120	0.181

TABLE F.21: Cp at S/L = 0.57, speed = 40 m/s and with transition strip

No.	0%	No.	5%	No.	10%	No.	20%	No.	30%	No.	50%
0	1.019	12	0.072	24	-0.020	36	-0.105	48	-0.131	60	-0.132
1	1.019	13	0.078	25	-0.040	37	-0.093	49	-0.138	61	-0.145
2	1.019	14	0.085	26	-0.060	38	-0.104	50	-0.119	62	-0.138
3	1.019	15	0.072	27	-0.042	39	-0.097	51	-0.120	63	-0.147
4	1.019	16	0.059	28	-0.023	40	-0.089	52	-0.121	64	-0.155
5	1.019	17	0.043	29	-0.032	41	-0.096	53	-0.123	65	-0.155
6	1.019	18	0.052	30	-0.039	42	-0.096	54	-0.115	66	-0.155
7	1.019	19	0.050	31	-0.046	43	-0.099	55	-0.116	67	-0.155
8	1.019	20	0.062	32	-0.051	44	-0.091	56	-0.121	68	-0.133
9	1.019	21	0.064	33	-0.053	45	-0.105	57	-0.128	69	-0.132
10	1.019	22	0.065	34	-0.035	46	-0.118	58	-0.135	70	-0.131
11	1.019	23	0.088	35	-0.050	47	-0.096	59	-0.142	71	-0.145
0	1.019	12	0.072	24	-0.020	36	-0.105	48	-0.131	60	-0.132

No.	70%	No.	80%	No.	90%	No.	95%	No.	100%
72	-0.137	84	-0.084	96	-0.020	108	0.077	120	0.180
73	-0.134	85	-0.080	97	-0.023	109	0.076	121	0.180
74	-0.135	86	-0.091	98	-0.022	110	0.072	122	0.180
75	-0.129	87	-0.085	99	-0.019	111	0.070	123	0.180
76	-0.123	88	-0.078	100	-0.016	112	0.067	124	0.180
77	-0.127	89	-0.076	101	-0.014	113	0.070	125	0.180
78	-0.118	90	-0.069	102	-0.029	114	0.076	126	0.180
79	-0.120	91	-0.070	103	-0.015	115	0.073	127	0.180
80	-0.124	92	-0.065	104	-0.017	116	0.082	128	0.180
81	-0.126	93	-0.075	105	-0.017	117	0.077	129	0.180
82	-0.128	94	-0.084	106	-0.017	118	0.072	130	0.180
83	-0.134	95	-0.086	107	-0.017	119	0.080	131	0.180
72	-0.137	84	-0.084	96	-0.020	108	0.077	120	0.180

Appendix G

G CFX Presentation

G.1 Grid Generator

The interactive grid generator is an interface to assist the user to create the geometry of his or her model. In CFX, the generation of grids can be conducted in two ways: (1) by use of CFX-MESHBUILD module and (2) by use of CFX-BUILD module.

The interactive pre-processor, CFX-MESHBUILD, creates multi-block meshes for use by CFX-F3D. Blocks are defined by their vertices and edges. The edges are subdivided before the grid generation is performed. Two or three-dimensional patches are created in CFX-MESHBUILD to specify the location of boundary conditions to the flow solvers. This grid generator was fully used for the current work.

CFX-BUILD is a powerful mesh generator, which can create geometry files for CFX-F3D either from scratch or from CAD data e.g. IGES files or Pro/Engineer part files. It can also deal with imperfect CAD data. It has a state-of-the-art graphical user interface and an efficient volume-meshing algorithm.

G.1.1 Geometry Definition

Geometry consists of points and curves. There are two types of points, i.e. free points and curve points. An absolute physical co-ordinate defines the location of a free point. Curve point locations are given with respect to a parent curve. All curves are defined in terms of points.

There are three basic types of curves: line segments, arcs and splines. Arcs are further subdivided into large and small arcs, which are defined using their centre and end points and through arcs, which are constructed to pass through three points.

G.1.2 Block Structure

This part describes how to create, modify and delete mesh objects. Mesh objects are edges, faces and blocks. Mesh objects are used to define the block structure, which defines how the geometry of the flow domain relates to the topology of the mesh.

In general the user needs to generate some geometry before creating the mesh objects. This will minimally consists of the points making up the vertices of the mesh objects. For problems that do not consist solely of regions bounded by straight edges it will also require the necessary boundary vertices.

Patches can be set individually on mesh objects but it is probably easier to use the SET PATCHES menu to set many patches at the same time. Also, edge distributions can be set on individual edges but it is easier to use the SET EDGE DISTRIBUTIONS menu or the SUBDIVISION menu to set a number of edge distributions simultaneously.

The subdivision on edges can be chosen to be: (1) a uniform distribution in which the distribution of the subdivision markers are evenly spaced along the edge; (2) a geometric progression (GP) in which the distribution of the cell width increases or decreases regularly along the edge and; (3) a symmetric geometric propagation (Sym GP) in which the distribution is symmetric about the centre of an edge. It can either have large cells in the middle with the cells decreasing in size towards the ends, or small cells in the middle with increasing in the size as the boundaries are approached.

The aim of the distribution is to let having a clustered grid in location in which the flow needs a precise description (in the immediate vicinity of the body to model the boundary layer) and/or to allow for a smooth grid at the junction of two blocks. By applying a distribution factor to the edge, the optimum distribution can be obtained.

G.1.3 Creating Patches

Patches are labelled regions of the problem geometry on which the user can set the boundary conditions or material properties in the flow solver. Examples might be inlets and outlets (2D) or a porous region (3D). More details on patches and patch types can be found in the appropriate solver manual.

G.1.4 Grid Generation

The overall process of grid generation is controlled from the CREATE GRID menu. The steps involved in generating a grid are as follows:

(1) Propagate the topology. This is always necessary but by default it is done automatically on entry to the menu.

(2) Set the number of subdivisions on each block. If it has not been done, then all edges are assumed to have a minimum number of subdivisions on them.

(3) Set the distribution of grid nodes on each edge. If it has not been set, then all edges are assumed to have a uniform distribution of cells.

(4) Generate the grid, after optionally altering the generation options.

(5) Check the grid is OK using the GRID VISUALISATION menu.

(6) Write the grid to a file.

Grid Quality

A good grid has the properties of smoothness, near orthogonality and sufficient resolution to model the flow. A good grid makes the flow solver more robust and more accurate.

Grid smoothness is a measure of how rapidly cell sizes change. In general, changes in cell size should be kept below 2:1. Grid smoothness is largely controlled by edge distributions.

As far as orthogonality is concerned, ideally grid lines should cross at 90°. In practice, angles between 30° and 120° are usually acceptable and even the occasional 180° angle works satisfactorily.

The block structure chosen may have a significant effect on the resulting grid quality.

Grid Visualisation and Analysis

Having generated a grid, user can immediately find out the grid on block faces. However, this does not tell the user what the grid is like within a block, and the picture is often too cluttered.

There are a number of facilities within CFX-MESHBUILD which allow user to examine the grids that have been created in detail. One of them is the grid statistics menu, which allows user to examine various parameters of the grid including inter-block connections and quality of the grids. This menu is easily customised so that cells and nodes failing certain criteria will be highlighted on the display. It is a very complete display which sometimes known as a weather map because it summarises interesting features of the grid graphically.

Six statistical quantities are calculated in the grid statistics menu. The first four are cell based (calculated for each cell): volume, skew, twist and taper. The last two are vertex based: orthogonality and stretch.

G.2 Flow Solver

CFX is a Navier-Stokes/finite volume code including compressibility, turbulence models, combustion models and multiphase-flow models. The flow solver requires two inputs, (1) a geometry file (geometry and grid data) and (2) a command file (boundary conditions and solver parameter). A user Fortran file may also be applied if necessary.

G.2.1 Command Language

A command file can be generated in two ways (1) using text-editor or (2) directly inside CFX by use of the Interactive Frontend.

The Command Language contains a data file including a set of commands and associated keywords, and routines within CFX-F3D to manipulate these commands and keywords to define the problem to the solver module. There are eight major commands. Most major commands have several subcommands; some of which are optional. The general structure of a Command Language data file (in which should appear in the order) is as follows:

```
>>CFXF3D
        (subcommands and keywords)
>>MODEL TOPOLOGY
        (subcommands and keywords)
>>MODEL DATA
        (subcommands and keywords)
>>SOLVER DATA
        (subcommands and keywords)
>>CREATE GRID
        (subcommands and keywords)
>>MODEL BOUNDARY CONDITIONS
        (subcommands and keywords)
>>OUTPUT OPTIONS
        (subcommands and keywords)
>>STOP
```

G.2.2 Problem Size and Basic Options

Problem Size

CFX-F3D has a large range of options, and because of this the code is structured so that only the storage that is required for a particular selection of options need to be allocated. All arrays are held in three large stack arrays: one for real variables, one for integer variables and one for character variables. The program passes around all arrays as arguments and avoids the use of common blocks for arrays. The size of these arrays is needed by the program for allocation of memory.

Some other information is required to set the overall size of the job. This includes the maximum number of blocks, patches, inter-block boundaries and unmatched grid connections.

In a normal run of the program using a geometry file obtained from a pre-processor, the size of the problem is set automatically from the size of the geometry, although occasionally extra work space will be required.

Type of Flow

The default condition is steady, three-dimensional, incompressible, isothermal, single phase laminar flow without a porous medium. All can be changed using keywords of the >>CFXF3D subcommand >>OPTIONS. In most cases, these keywords simply invoke the setting up of finite difference equations that are either not included, or replace one or more of the equations in the default set.

User Fortran

Fortran routines may be used when there is a need for features that are too complex to be set in the command file, or when an option is required that does not currently have a keyword. Sometimes the Fortran user-defined routines provide a more convenient way of specifying features that are available in the Command Language.

G.2.3 Geometry and Topology

The computational domain in CFX-F3D is a collection of blocks that are connected together across inter-block boundaries. The underlying grid structure of each block is contained in a region, which is topologically a cuboid. This means that each block may be considered conceptually as a rectangular array of ‘bed springs’, which may be distorted to fit the boundary of a desired physical domain. This distortion defines a ‘mapping’ from ‘computational space’, with co-ordinates given by the integer indices (I,J,K) of cell vertices, to the desired region of ‘physical space’. The only restriction to the mapping is the cells do not overlap.

Each block may contain solid or porous blockages, inlets, outlets etc. at arbitrary internal locations. The only restriction is that the structures are composed of complete control cells or complete control cell faces. Thin walls lying on the faces of internal control volumes may also be set. All internal structures are defined using the concept of patches, that is, rectangular sub-arrays of control cells or control cell faces internal to blocks. Patch locations are defined topologically, that is, in terms of their integer locations on each block considered as a rectangular array. The mapping of the block into physical space must be defined so that the internal rectangular arrays of cell faces defining surface patches are mapped onto the required, possibly curved, surfaces in physical space.

G.2.4 Physical Models and Fluid Properties

The physical and numerical models used are specified using subcommands of >>MODEL DATA. Also specified with this command are such things as fluid properties, the manner in which the flow field is initialised, and various other options.

The subcommand of >>FLUID PROPERTIES consists of the following items: isothermal flows, heat transfer, scalar transport parameters, mass transfer parameters, buoyancy-driven flows, rotating co-ordinated flows, utility for calculating physical properties, compressible flows, compressible buoyant flows and user-defined physical properties.

Fluid properties for use in the program can also be read in from a database.

G.2.5 Solution Algorithms

A number of different methods are available for the solution of the linearised transport equations. The methods and the parameters which control them may be set using keywords and subcommand of >>SOLVER DATA. Flexibility is provided in order to cater for the widest possible range of problems, but sensible defaults are set so that, for the majority of problems, the user need take no action in respect of the solver.

The linear equations are derived by integrating transport equations over control volumes (cells), thus each equation may be regarded as 'belonging' to a particular variable and to a particular cell. Such an equation is a formula which describes the influence on that particular variable in that particular cell of:

(a) Other variable in the same cell, and
(b) Values of the same variable in neighbouring cells.
(c) Values of the other variables in neighbouring cells.

There are several reasons why the complete set of equations is not solved simultaneously (in other words by a *direct* method). Quite apart from the excessive computational effort which it would entail, this approach ignores the non-linearity of the underlying differential equations. Therefore iteration is used at 2 levels: an inner iteration to solve for the spatial coupling of each variable and an outer iteration to solve for the coupling between variables. Thus variable is taken in sequence, regarding all other variables as fixed, a discrete transport equation for that variable is formed for every cell in the flow domain and the problem is handed over to a linear equation solver which returns the updated value of the variable. The non-linearity of the original equations is simulated by reforming the coefficients of the discrete equations using the most recently calculated values of the variables, before each inner iteration.

The treatment of pressure is slightly different because it does not obey a transport equation. Instead, simplified versions of the discrete momentum equations are used to derive a functional relationship between a correction to the pressure and corrections to the velocity components in each cell. Substitution of this expression into the continuity equation leads to an equation linking the pressure-correction with the continuity error in the cell. This set of simultaneous equations is passed, as before, to a linear equation solver. The solution is used both to update pressure and to correct the velocity field through the functional relationship in order to enforce mass conservation. The exact implementation of this pressure-correction step can give rise to several different *velocity-pressure coupling* algorithms, of which the SIMPLE algorithm is the best known.

The Outer Iteration

There are a number of ways in which the solution process may be stopped either completely or for the current time step of a transient problem. The convergence criteria used may differ depending on the simulation being carried out.

The maximum number of global (outer) iterations may be reached. The number of iterations required might be between 1 and 40, say, for each time step of a transient calculation, and from a few hundred to several thousands for a steady state calculation, depending on the accuracy desired in the solution and the complexity of the problem. It is a good practice to divide very large (and costly) predictions into a series of runs using the dump and restart facilities. In this way the user may judge whether the problem is converging satisfactorily.

Certain criteria, which determine whether the solution procedure has converged may be satisfied. The default convergence criterion is the same for steady state calculations or for transient calculations using a fixed time step. In these cases the software, by default, only tests the error in continuity –the mass source residual– to see whether it has fallen below some tolerance set by the user (say 10^{-4}).

The basis for updating pressure and correcting velocity components for continuity is the SIMPLE algorithm. This, and alternative algorithms, are selected by means of keywords of the subcommand >>PRESSURE CORRECTION. The default algorithm is SIMPLEC. SIMPLEC is a modification of SIMPLE, which differs in its derivation of a simplified momentum equation. Further details of these algorithms can be found in [38]. A trivial extra amount of work is required for SIMPLEC as compared with SIMPLE, so the cost may be regarded as nearly identical. For a number of model problems, SIMPLEC has proved less sensitive to selection of under-relaxation factors and has required less under-relaxation, so this algorithm is preferred.

Such an alteration to the solution strategy might be useful, for example, in a highly turbulent problem to solve the turbulence model equations more accurately. Because of the structure of the linearised k and ε equations, they are usually solved fairly accurately individually with a minimum of effort. A better joint solution is obtained by alternating between the k equation and ε equation a few times within each outer iteration; so set NTUB to 2 or 3 as desired.

Under-relaxation has several interlinked purposes in the solution process. Firstly and principally, the amount by which a variable would change if its discrete transport equation were solved as its stands is reduced. In this way, difficulties caused by instability due, among other factors, to non-linearity are overcome. Under-relaxation for all the transport equations is implemented by scaling the coefficient of the variable in the current cell by an under-relaxation factor (URF) in the range 0<URF<1. The smaller this factor is chosen, the more under-relaxation is employed. If an URF is set to high, instability may result. The level at which this occurs depends strongly on the algorithm being used to solve the velocity-pressure coupling. At its most serious this instability can cause rapid divergence. A less extreme effect is rapid oscillation of point values as the iteration proceed, which may not cause divergence but will slow the rate of convergence. This effect may generally be observed in the monitoring values and/or the residuals, which are printed out at every iteration. If an URF is chosen to small, the physics of the system evolves at a slow rate and the cost of solving the problem is greater than it need be. However, there is less likelihood of causing failure to converge. The default values will solve most problems reasonably efficiently yet reliably, since optimum values for the under-relaxation factors are not especially sensitive for the default velocity-pressure coupling algorithm.

As an alternative to setting under-relaxation factors, the user may request false time-stepping using keywords of the subcommand >>FALSE TIMESTEPS. In this case, the equations are modified in the same way as if each outer iteration is a time step, with two difference: the 'old' time values used are the most recently calculated values of each convergence rate. This procedure may also be applied at each (true) time step of a transient calculation, in which case the equations are modified twice. A value of zero (the default) means that no false time stepping is applied to that particular equation. It is possible to mix false time steps and under-relaxation factors, and even to use both on the same equations. As with true time stepping, the pressure-correction equation is never modified. Also, it would be inappropriate to apply false time stepping to the calculation of density and viscosity.

The Inner Iteration

The set of linearised difference equations for a particular variable, one equation for each control volume in the flow, is passed to a simultaneous linear equation solver which uses an iterative solution method. An exact solution is not required because this is just one step in the non-linear outer iteration. The alternative methods, available for this purpose, are listed below. The methods are specified as character strings in keywords of the subcommand >>EQUATION SOLVERS.

SOLVER	STRING
Line relaxation	LINE SOLVER
Preconditioned conjugate gradients	ICCG
Full field Stone's method	STONE
Block Stone's method	BLOCK STONE
Algebraic Multi-grid	AMG
General version of Algebraic Multi-grid	GENERAL AMG

The computational effort which may be expected in obtaining a reasonable solution to the set of equations must be specified. Since the various methods are of differing complexities, it does not make sense to talk simply of a number of iterations except in the context of a particular method. The parameters which control the solution process are a minimum number of iterations, a maximum number of iterations and a residual reduction factor. Defaults of these parameters are given in [71]. Values of the residual reduction factors will typically be in the range 0.01 to 0.5. A stopping criterion based on a residual reduction factor is less dependent on problem size and difficulty than one based on fixing the number of iterations and so is preferable for application to general problems.

The algebraic multi-grid method may be used for any of the equations including the pressure correction equation. It solves the discretised equations on a series of coarsening meshes. The meshes are chosen by CFX-F3D algebraically rather than geometrically. The coarse meshes are produced internally by CFX-F3D, so the user does not have to specify anything relating to the AMG meshes.

Convergence Difficulties

The most likely cause of the iterative process failing to converge is that the problem has not been set up as intended. The cause of failure to converge may be an input error, such as conflicting or simply unphysical specifications of the various internal structures and boundary condition types. This can occur when problem dimensions are altered (possibly for grid refinement purposes) and the user's Fortran subroutine have not been written so as to be independent of such changes. Careful checking of the information printed out in the Frontend phase of the program is recommended; check that the information is both correct and complete.

If the problem is physically reasonable with a well-defined stable mathematical solution and has been specified correctly, yet it still fails to converge satisfactorily, then numerical difficulties may be suspected. The parameters governing the solvers have been given default values which are inevitably a compromise between efficiency and reliability for a wide range of problem types. It may simply be that a more conservative selection of the parameters is needed. By this it meant: requesting a more accurate solution of the inner iterations; or selecting a better outer iteration strategy; or employing greater under-relaxation (reducing under-relaxation factors); or a combination of these techniques.

A well-converge inner iteration is important in reliably obtaining solutions to difficult problems. Poor convergence in the pressure-correction iteration, in particular, will lead to loss of mass conservation, and non-physical results. Therefore it is recommended that a fairly large maximum number of iterations for pressure is allowed and a residual reduction factor criterion used to stop the iteration; this strategy will usually guarantee satisfactory mass conservation at all stages of the iteration without being inordinately expensive. If it appears that the mass source residual is not being reduced then the residual reduction factor for the pressure-correction equation should be modestly reduced in order to drive this equation to a more accurate solution, hence enforcing better mass conservation.

If it is thought that the pressure-correction iteration is still not being adequately treated, in particular if the block structure is complex, the AMG solver can be used instead of ICCG for the pressure-correction equation. The Frontend printing contains details of how well-ordered the blocks are. If the percentage of well-ordered blocks is low, then the user should switch to using AMG or BLOCK STONE instead of ICCG. The well-orderedness cannot be altered by the user. When using STONE or ICCG, the software reorders the blocks to make the structure of the matrix as close to a single block structure as possible; the higher the well-orderedness the more successfully this can be done.

Likewise, line relaxation may be inadequate for solving the transport equations in very complex geometries, since it solves along gridlines in one orientation only and thus connections in other directions are less well treated. In this case, a whole field solver such as STONE or AMG may be preferable, again using residual reduction factors to test convergence. Care must be exercised in using one of these other methods for the turbulence equations, because both k and ε must always remain positive. It is possible for these solvers to produce negative values in a partially converge solution, even though the converged solution is strictly positive. Note also that the higher order upwind and QUICK differencing schemes can give rise to converged solutions with negative values of k and ε when, for example, a shear layer is not adequately resolved by the grid. It is recommended, even if using higher order schemes for the velocity components, to use upwind or hybrid schemes for k and ε. These are guaranteed to maintain positivity, and accuracy of convective transport of these variables is less than of an issue as they are strongly dominated by production and dissipation.

It is possible that the solution algorithm is being too ambitious in searching for a solution and is encountering numerical instabilities. In this case a better selection of under-relaxation factors must be made, bearing in mind the choice of velocity-pressure coupling algorithm. Insufficient under-relaxation of the equations will lead to divergence or rapid oscillation of point values, observable in the variables at the monitoring point (assuming it has been chosen sensibly, i.e. centrally to the important parts of the flow). Alternatively, false time stepping can be tried, using small false time steps.

It is likely the case that a steady state calculation is neither converging nor diverging i.e. it is possible that a steady state solution does not exist. This is particularly likely for laminar flows at Reynolds numbers where transition to unsteady flow may be expected, especially if higher order difference scheme are being employed. This is also possible for forms such as ellipse and ellipsoid even in turbulent flow condition. If this is the case, it is sensible to switch to a transient calculation.

The above symptoms are possible even for flows which have steady state solutions. A steady state calculation may be considered as a transient calculation with infinite time step. If a time accurate simulation of the flow from its initial guess to its steady state solution indicates that the flow approaches the steady state solution in a complex manner, then it is quite likely that an attempt to reach the steady state solution in a single huge time step will overshoot the mark and never recover. This is particularly true high speed compressible flow and multi-phase flows, where many complex interacting shock waves may have to pass through the system before a steady state is established. It is also true of flows which are strongly buoyancy driven and internal gravity waves have to dissipate through the system before a steady state is reached.

If such a situation is suspected, the following strategy is recommended:

(1) Try real time stepping towards the steady state. It is worthwhile starting with very small time steps, perhaps close to the Courant limit $(\Delta t / 2\Delta x)$, and gradually increasing these. In this case, the choice of time step is dictated by the size of the grid. A very fine grid would have a relatively small cell size, which will require a relatively small time step if instability is to be avoided. A Courant number close to unity is found to give a stable rate of convergence and the choice of Δt has been dictated by this factor in every grid used. The closer the solution is to the steady state, the larger the time step that can be chosen. If only the steady state solution is of interest, and time accuracy is unimportant, it is not necessary to converge at every time step, so a fixed small number of iterations could be performed at each time step.

(2) The strategy of increasing the time step as the steady state is reached can be automated to a certain extent using the adaptive time stepping option. Set a small initial time step and a large final time step and a very large maximum time.

(3) If the memory overheads of real time stepping are prohibitive, try false time stepping, starting with very small false time steps and restarting with larger false time steps.

The above mentioned problems with steady state calculations can also occur in transient calculations if the time step is too large to resolve complex physics that may be occurring on smaller time scales. This is true in particular for combusting flows, high speed compressible flows and multi phase flows. In this situation, the adaptive time stepping strategy is strongly recommended. In this case the maximum allowed time step should be sufficiently small to give the desired time accuracy, and the minimum allowed time step should be set much smaller in order to cater for those time steps which do not converge with the maximum time step.

For a highly turbulent flow, where solution of the k and ε equations is likely to govern the rate of convergence, increase NTURB from 1 to 2 or even 3, in order that the numerical calculation adheres closely to the k-e model, thus minimising the chance of compounding numerical and modelling errors.

One of the most common causes of lack of convergence of turbulent flow calculations in CFX-F3D is due to the cross-derivative diffusion terms in the k and e equations on non-orthogonal grids. This usually manifests itself as divergence of the calculation, with residuals in each equation only large at a localised set of points and in this region a point with very small value of e and a large value of the turbulence viscosity that is not physically sensible. By choosing these start and end iterations in a sensible manner (e.g. start iteration equal to zero and end iteration equal to half of the maximum number of iterations) convergence can usually be achieved. However occasionally this is not the case and it is necessary to omit these terms in the ε equation for the entire calculation. This is achieved by setting the start value for the ε equation greater than the maximum number of iterations and the end value for the ε equation to be greater than or equal to the start value. This technique will always eliminate convergence problems of this type, but it should be remembered that the analytic e equation is no longer being discretised in full. However the omitted terms should not be too important, as the equation is dominated by the production, dissipation, advection and normal diffusion terms.

Another lack of convergence, or slow convergence, is the numerical precision of the solution procedure. It has been found that on some problems convergence can be improved by running in double precision. If CFX-F3D is being run on one standard work-station platforms, it is straightforward within CFX-ENVIRONMENT to use the double-precision version of the code although this would require more memory and perhaps more CPU time.

G.2.6 Gridding Options

The software provides three alternative methods for specifying the grid:

(1) The grid may be read from a disk file. This allows complex grids to be generated using one of a number of grid generation packages. This is the most common way of setting the grid in the software. When using the CFDS pre-processor, the grid is read in from a geometry file output by the pre-processor.

(2) Simple grids may be defined explicitly in the Command Language data file; either by specifying the location of the node points, or by defining the grid increments.

(3) The grid may be defined in a user-defined Fortran routine.

The second and third methods require the use of the >>CREATE GRID command.

G.2.7 Boundary Conditions

All real information is set using subcommands and keywords of >>MODEL BOUNDARY CONDITIONS. It is assumed that the boundary surfaces have been previously defined either in a pre-processor or using the appropriate subcommands and keywords of >>CREATE PATCH. Note that planes of periodicity and symmetry need no real information. Also, if a solid surface is to take the default conditions of zero velocity and zero heat transfer, then no action need be taken as these are default boundary conditions at walls and conducting boundaries. Real data must always be supplied for any inlets, or pressure boundaries.

G.2.8 Output Options

The output options available allow the user to control the contents of the output file produced by CFX-F3D and also the contents and format of the dump file produced. In addition it is possible to produce the data for line graphs of variables at particular points in the domain as the simulation progresses, and to produce the data for animated shaded contour plots. >>OUTPUT OPTIONS and all its subcommands are optional.

The output file stores all the relevant information of each run i.e. type of flow and solution procedure options as in the command file; topology structure i.e. a list of block names and sizes followed by a list of the patches and their locations; each wall and conducting boundary listed together with real information of the patches unless it has a default boundary conditions; grid vertex co-ordinates for each block; residual and monitoring values for each iteration; values of relevant variables at cell centres at the end of the run and; the list of the walls and conducting boundaries with the integration results over each surface which gives the force on it. A careful check is required to ensure the problem was properly defined and the convergence has been successfully obtained.

The dump file contains the results of the following variables: velocity components, pressure, turbulence kinetic energy, k and ε which allows the post-processor program (CFX-VIEW) to plot different pictures such as vector, contour and shaded contour for each variable.

Appendix H

H Mathematical Models

H.1 Governing Equations

The basic set of equations solved by the program for laminar flow comprise equations for the conservation of mass, momentum and, in a non-isothermal flow, energy. They are called the Navier-Stokes equations. It should be emphasised that the equations for 'laminar flow' are also valid for turbulent flow. Turbulent flows are just very unsteady laminar flows. The equations, assuming isothermal flow as in the present investigation, are as follows:

$$\frac{\partial \rho}{\partial t} + \nabla.(\rho U) = 0 \qquad \text{(H.1)}$$

the momentum equation:

$$\frac{\partial \rho U}{\partial t} + \nabla.(\rho U \otimes U) = \mathbf{B} + \nabla.\sigma \qquad \text{(H.2)}$$

where σ is the stress tensor:

$$\sigma = -p\delta + \mu\left(\nabla U + (\nabla U)^T\right) \qquad \text{(H.3)}$$

and, the energy equation:

$$\frac{\partial \rho H}{\partial t} + \nabla.(\rho U H) - \nabla.(\lambda \nabla T) = \frac{\partial p}{\partial t} \qquad \text{(H.4)}$$

Where ρ is the fluid density, $U=(U,V,W)$ the fluid velocity, p the pressure, T the temperature, t the time, H the total enthalpy, **B** the body force, μ the molecular viscosity and λ the thermal conductivity.

Furthermore, the complete main transport equations in index notations using a Cartesian co-ordinate system are:

$$\frac{\partial \rho}{\partial t}+\frac{\partial}{\partial x^i}\left(\rho U_i\right)=0 \tag{H.5}$$

$$\frac{\partial \rho U^k}{\partial t}+\frac{\partial}{\partial x^i}\left(\rho U^i U^k\right)=-B^k+\frac{\partial \sigma^{ik}}{\partial x^i} \tag{H.6}$$

$$\sigma_{ij}=-p\delta^{ij}+\mu\left(\frac{\partial U^j}{\partial x^i}+\frac{\partial U^i}{\partial x^j}\right) \tag{H.7}$$

$$\frac{\partial \rho H}{\partial t}+\frac{\partial}{\partial x^i}\left(\rho U^i H-\lambda\frac{\partial T}{\partial x^i}\right)=\frac{\partial p}{\partial t} \tag{H.8}$$

H.2 Turbulence k-ε Model

The k-ε model uses an eddy-viscosity hypothesis for the turbulence. The continuity and momentum equations are then:

$$\frac{\partial \rho}{\partial t}+\nabla.\left(\rho \mathbf{U}\right)=0 \tag{H.9}$$

and

$$\frac{\partial \rho \mathbf{U}}{\partial t}+\nabla.\left(\rho \mathbf{U}\otimes\mathbf{U}\right)-\nabla.\left(\mu_{eff}\nabla\mathbf{U}\right)=-\nabla p'+\nabla.\left(\mu_{eff}\left(\nabla\mathbf{U}\right)^T\right)+\mathbf{B} \tag{H.10}$$

ρ is the mean fluid density, **U** the velocity and μ_{eff} the effective viscosity defined by:

$$\mu_{eff} = \mu + \mu_T \tag{H.11}$$

where μ_T is the turbulence viscosity.

In the k-ε model arguments of dimensional analysis suggest that μ_T may be represented by:

$$\mu_T = C_\mu \rho \frac{k^2}{\varepsilon} \tag{H.12}$$

The transport equations for the turbulence kinetic energy k and turbulence dissipation rate ε are:

$$\frac{\partial \rho k}{\partial t} + \nabla.(\rho \mathbf{U} k) - \nabla.\left(\left(\mu + \frac{\mu_T}{\sigma_k}\right)\nabla k\right) = P + G - \rho\varepsilon \tag{H.13}$$

and

$$\frac{\partial \rho \varepsilon}{\partial t} + \nabla.(\rho \mathbf{U} \varepsilon) - \nabla.\left(\left(\mu + \frac{\mu_T}{\sigma_\varepsilon}\right)\nabla \varepsilon\right) = C_1 \frac{\varepsilon}{k}(P + C_3 \max(G,0)) - C_2 \rho \frac{\varepsilon^2}{k} \tag{H.14}$$

respectively, where P is the shear production defined by:

$$P = \mu_{eff} \nabla \mathbf{U}.\left(\nabla \mathbf{U} + (\nabla \mathbf{U})^T\right) - \frac{2}{3}\nabla.\mathbf{U}\left(\mu_{eff}\nabla.\mathbf{U} + \rho k\right) \tag{H.15}$$

and G is production due to the body force defined by:

$$G = G_{buoy} + G_{rot} + G_{res} \tag{H.16}$$

where G_{buoy}, G_{rot} and G_{res} are terms representing production due to buoyancy, rotation and resistances respectively. However $G_{rot}=0$ and only G_{buoy} is included in the code. Therefor $G = G_{buoy}$ and is defined by:

$$G = -\frac{\mu_{eff}}{\rho\sigma_T}\mathbf{g}.\nabla\rho \tag{H.17}$$

which with the Boussinesq buoyancy approximation, can be written as:

$$G = \frac{\mu_{eff}}{\sigma_T}\beta\mathbf{g}.\nabla T - \frac{\mu_{eff}}{\sigma_Y}\alpha\mathbf{g}.\nabla Y \tag{H.18}$$

The modified pressure p' is related to the true pressure p by

$$p' = p + \frac{2}{3}\rho k + \left(\frac{2}{3}\mu_{eff} - \zeta\right)\nabla.\mathbf{U} - \rho_0\phi \tag{H.19}$$

where ζ is the bulk viscosity, and ϕ is a gravitational quantity with

$$\nabla\phi = \mathbf{g} \tag{H.20}$$

H.3 Turbulence RNG k-ε Model

The RNG k-e model is an alternative to standard k-ε model for high Reynolds number flows. The model, which derived from a renormalisation group analysis of the Navier-Stokes equations, differs from the standard model only through a modification to the equation for ε, except for using a different set of model constants.

The equations describing the turbulence model, equations (H.13) and (H.14) become:

$$\frac{\partial \rho k}{\partial t} + \nabla.(\rho \mathbf{U} k) - \nabla.\left(\left(\mu + \frac{\mu_T}{\sigma_k}\right)\nabla k\right) = P + G - \rho\varepsilon \tag{H.21}$$

and

$$\frac{\partial \rho \varepsilon}{\partial t} + \nabla.(\rho \mathbf{U} \varepsilon) - \nabla.\left(\left(\mu + \frac{\mu_T}{\sigma_\varepsilon}\right)\nabla \varepsilon\right) = (C_1 - C_{1RNG})\frac{\varepsilon}{k}(P + C_3 \max(G,0)) - C_2 \rho \frac{\varepsilon^2}{k} \tag{H.22}$$

Where C_{1RNG} is given through the equations:

$$C_{1RNG} = \frac{\eta\left(1 - \frac{\eta}{\eta_0}\right)}{\left(1 + \beta\eta^3\right)} \tag{H.23}$$

and

$$\eta = \left(\frac{P}{\mu}\right)^{0.5} \frac{k}{\varepsilon} \tag{H.24}$$

H.4 Boundary Conditions

H.4.1 Wall Boundary Conditions

Velocity boundary conditions may be specified by the user in the mixed form:

$$AU_i + B\tau_i = C_i, \qquad i = 1,2,3 \tag{H.25}$$

where $\tau_i = \left(\mu \frac{\partial U_i}{\partial y}\right)_w$ is the wall shear stress. The default is no slip, that is, $A_i=1$, $B_i=0$ and $C_i=0$.

If Bi=0 and Ci$\neq$0a moving wall is specified. If Ai=0 then the shear stress is specified. In this way the shear stress may be set to zero for solving the Euler equations.

H.4.2 Wall Boundary Conditions for Turbulent Flow

Many of the variables vary rapidly in the near-wall region of the flow and, instead of using extremely fine grids in these regions, their behaviour is specified with wall functions. A more fundamental problem is that the model equations, as defined, do not accurately represent the turbulence in the near-wall region. The wall function concept is illustrated below by considering the flow in a fully developed boundary layer over a stationary wall. Near the wall (say at y=d), it is found that the wall shear stress τ is related to the turbulence kinetic energy by

$$\tau^2 = C_\mu \rho^2 k^2 \tag{H.26}$$

A new quantity τ_k is defined such that

$$\tau_k = \rho C_\mu{}^{1/2} k \tag{H.27}$$

This may be used to define scaled variables

$$u^+ = -\frac{(\rho\tau_k)^{1/2}}{\tau} u \tag{H.28}$$

and,

$$y^+ = \frac{(\rho\tau_k)^{1/2}}{\mu}(d-y) \tag{H.29}$$

For a fully developed boundary layer, these non-dimensionalisations are quite standard but are found to be superior to non-dimensioning with respect to τ in other cases.

The scaled velocity component parallel to the wall and in the x direction is

$$u^+ = y^+ \qquad \text{for } y^+ < y_0^+ \tag{H.30a}$$

or,

$$u^+ = \frac{1}{\kappa}\log\left(Ey^+\right) \qquad \text{for } y^+ > y_0^+ \tag{H.30b}$$

where log is a natural logarithm.

The cross-over point y_0^+ between the viscous sub-layer and the logarithmic region is the upper root of

$$y_0^+ = \frac{1}{\kappa}\log\left(Ey_0^+\right) \tag{H.31}$$

This is given in the array XYPLUS in the program and is set using the command >>SUBLAYER THICKNESS. The constant E may be set in the command language using the >>LOGLAYER CONSTANT command.

The equation for the turbulence kinetic energy k is solved in the control volume immediately adjacent to the wall. From this the value of the wall shear stress may be obtained. Note that a special treatment of the production terms in the k equation is necessary in order to use only quantities to the flow and the specified boundary conditions on the velocities and temperature.

The turbulence dissipation is obtained from the turbulence kinetic energy through the relation

$$\varepsilon = \frac{C_\mu^{3/4} k^{3/2}}{\kappa (d - y)} \tag{H.32}$$

H.4 Flow Boundaries

A flow boundary is (by definition) a boundary where fluid can enter or leave the domain. These are split into three types: inlets, mass flow boundaries and pressure boundaries.

H.4.1 Inlets

It is assumed that if the inflow is supersonic then all variables must be specified upstream and if the flow is subsonic, all variables except pressure are specified upstream, and pressure is extrapolated from downstream.

H.4.2 Mass Flow Boundary

It is assumed that all three velocity components are extrapolated and then adjusted to fix desired mass flow rates; temperature and scalars are fixed if flow is in or if flow is out and subsonic or extrapolated if flow is out and supersonic, and pressure is always extrapolated.

H.4.3 Pressure Boundaries

It is assumed that pressure is fixed if flow is in or if flow is out and subsonic or extrapolated if flow is out and supersonic; temperature and scalars are fixed if flow is in or flow is out and subsonic or extrapolated if flow is out and supersonic, and all velocity components are extrapolated if flow is out or extrapolated in this way: min(|U|, speed of sound) if flow is in.

Appendix I

I Examples of Command File used in CFX

I.1 Command File for Two-dimensional Cases

```
>>CFX4
  >>OPTIONS {setting the flow type}
    TWO DIMENSIONS {two-dimensional problem indicator}
    BODY FITTED GRID
    CARTESIAN COORDINATES
    TURBULENT FLOW
    ISOTHERMAL FLOW
    INCOMPRESSIBLE FLOW
    STEADY STATE
>>MODEL DATA
  >>DIFFERENCING SCHEME {setting the finite differencing scheme
used}
    ALL EQUATIONS 'QUICK'
  >>TITLE
    PROBLEM TITLE 'FLOW OVER AN ELLIPSE FORM (UNBOUNDED)'
  >>PHYSICAL PROPERTIES
    >>STANDARD FLUID
      FLUID 'AIR'
      STANDARD FLUID REFERENCE TEMPERATURE 2.8800E+02
    >>FLUID PARAMETERS
      VISCOSITY 1.7880E-05
      DENSITY 1.2300E+00
    >>TURBULENCE PARAMETERS
      >>TURBULENCE MODEL {setting the turbulence model}
        TURBULENCE MODEL 'K-EPSILON'
>>SOLVER DATA
  >>PROGRAM CONTROL
    MAXIMUM NUMBER OF ITERATIONS 4000
    MASS SOURCE TOLERANCE 1.0000E-06
  >>EQUATION SOLVERS
    U VELOCITY 'AMG'
    V VELOCITY 'AMG'
    PRESSURE 'AMG'
    K 'AMG'
    EPSILON 'AMG'
>>CREATE GRID
  >>INPUT GRID
    READ GRID FILE
    FORMATTED
>>MODEL BOUNDARY CONDITIONS {setting the boundary conditions}
  >>WALL BOUNDARIES
    PATCH NAME 'FACE-NUMBER-18'
  >>WALL BOUNDARIES
    PATCH NAME 'FACE-NUMBER-15'
  >>SET VARIABLES
    PATCH NAME 'INLET'
    U VELOCITY 3.0000E+01
    V VELOCITY 0.0000E+00
    K 1.8000E+00
    EPSILON 7.3790E+00
  >>SET VARIABLES
    PATCH NAME 'SIDES'
    U VELOCITY 3.0000E+01
>>OUTPUT OPTIONS
  >>FRONTEND PRINTING
    NO FRONTEND PRINTING
  >>LINE GRAPH DATA
```

```
      XYZ -6.000001E-01 0.000000E+00 0.000000E+00
      EACH ITERATION
      FILE NAME 'A'
      U VELOCITY
      PRESSURE
    >>LINE GRAPH DATA
      XYZ 0.000000E+00 -1.000000E-01 0.000000E+00
      EACH ITERATION
      FILE NAME 'B'
      U VELOCITY
      PRESSURE
    >>LINE GRAPH DATA
      XYZ 6.000001E-01 0.000000E+00 0.000000E+00
      EACH ITERATION
      FILE NAME 'C'
      U VELOCITY
      PRESSURE
>>STOP
```

II.2 Command File for Three-dimensional Cases

```
>>CFX4
  >>OPTIONS {setting the flow type}
    THREE DIMENSIONS {three-dimensional problem indicator}
    BODY FITTED GRID
    CARTESIAN COORDINATES
    TURBULENT FLOW
    ISOTHERMAL FLOW
    INCOMPRESSIBLE FLOW
    STEADY STATE
>>MODEL DATA
  >>DIFFERENCING SCHEME {setting the finite differencing scheme
used}
    ALL EQUATIONS 'QUICK'
  >>TITLE
    PROBLEM TITLE 'FLOW OVER NPL 5B SHIPHULL MODEL'
  >>WALL TREATMENTS
    WALL PROFILE 'LOGARITHMIC'
    NO SLIP
  >>PHYSICAL PROPERTIES
    >>STANDARD FLUID
      FLUID 'AIR'
      STANDARD FLUID REFERENCE TEMPERATURE 2.8800E+02
    >>FLUID PARAMETERS
      VISCOSITY 1.7880E-05
      DENSITY 1.2300E+00
    >>TURBULENCE PARAMETERS
      >>TURBULENCE MODEL (setting the turbulence model)
        TURBULENCE MODEL 'K-EPSILON'
>>SOLVER DATA
  >>PROGRAM CONTROL
    MAXIMUM NUMBER OF ITERATIONS 3000
    MASS SOURCE TOLERANCE 1.0000E-06
  >>ALGEBRAIC MULTIGRID PARAMETERS
    CONNECTIVITY TOLERANCE 1.0000E-14
    SINGULARITY TOLERANCE 1.0000E-03
    WORK SPACE FACTOR 3.0000E+00
  >>DEFERRED CORRECTION {setting virtual/dummy correction values}
    K START 3001
    K END 3001
    EPSILON START 3001
    EPSILON END 3001
  >>EQUATION SOLVERS
    U VELOCITY 'AMG'
```

```
      V VELOCITY 'AMG'
      W VELOCITY 'AMG'
      PRESSURE 'AMG'
  >>CREATE GRID
    >>INPUT GRID
      READ GRID FILE
      FORMATTED
  >>MODEL BOUNDARY CONDITIONS {setting boundary conditions)
    >>SET VARIABLES
      PATCH NAME 'FACE-NUMBER-135'
      U VELOCITY -2.1800E+01
      V VELOCITY 0.0000E+00
      W VELOCITY 0.0000E+00
      K 9.5000E-01
      EPSILON 1.3300E+00
    >>SET VARIABLES
      PATCH NAME 'FACE-NUMBER-139'
      U VELOCITY -2.1800E+01
      V VELOCITY 0.0000E+00
      W VELOCITY 0.0000E+00
      K 9.5000E-01
      EPSILON 1.3300E+00
    >>SET VARIABLES
      PATCH NAME 'FACE-NUMBER-143'
      U VELOCITY -2.1800E+01
      V VELOCITY 0.0000E+00
      W VELOCITY 0.0000E+00
      K 9.5000E-01
      EPSILON 1.3300E+00
    >>SET VARIABLES
      PATCH NAME 'FACE-NUMBER-147'
      U VELOCITY -2.1800E+01
      V VELOCITY 0.0000E+00
      W VELOCITY 0.0000E+00
      K 9.5000E-01
      EPSILON 1.3300E+00
    >>SET VARIABLES
      PATCH NAME 'OUTSIDES'
      U VELOCITY -2.1800E+01
    >>SET VARIABLES
      PATCH NAME 'TOPSIDES'
      U VELOCITY -2.1800E+01
  >>OUTPUT OPTIONS
    >>FRONTEND PRINTING
      NO FRONTEND PRINTING
      NO TOPOLOGY STRUCTURE
    >>LINE GRAPH DATA
      XYZ -6.000001E-01 1.000000E-06 1.000000E-06
      EACH ITERATION
      FILE NAME ‘A’
      U VELOCITY
      PRESSURE
    >>LINE GRAPH DATA
      XYZ -4.800001E-01 0.000000E+00 6.000000E-02
      EACH ITERATION
      FILE NAME ‘B’
      U VELOCITY
      PRESSURE
    >>LINE GRAPH DATA
      XYZ -3.600001E-01 0.000000E+00 8.000000E-02
      EACH ITERATION
      FILE NAME ‘C’
      U VELOCITY
      PRESSURE
    >>LINE GRAPH DATA
      XYZ -2.100001E-01 0.000000E+00 9.400000E-02
```

```
    EACH ITERATION
    FILE NAME ‘D’
    U VELOCITY
    PRESSURE
  >>LINE GRAPH DATA
    XYZ 0.000001E+00 0.000000E+00 1.000000E-01
    EACH ITERATION
    FILE NAME ‘E’
    U VELOCITY
    PRESSURE
  >>LINE GRAPH DATA
    XYZ 2.100001E-01 0.000000E+00 9.400000E-02
    EACH ITERATION
    FILE NAME ‘F’
    U VELOCITY
    PRESSURE
  >>LINE GRAPH DATA
    XYZ 3.600001E-01 0.000000E+00 8.000000E-02
    EACH ITERATION
    FILE NAME ‘G’
    U VELOCITY
    PRESSURE
  >>LINE GRAPH DATA
    XYZ 4.800001E-01 0.000000E+00 6.000000E-02
    EACH ITERATION
    FILE NAME ‘H’
    U VELOCITY
    PRESSURE
  >>LINE GRAPH DATA
    XYZ 6.000001E-01 1.000000E-06 1.000000E-06
    EACH ITERATION
    FILE NAME ‘I’
    U VELOCITY
    PRESSURE
>>STOP
```

Appendix J

J Flow past Two-dimensional Ellipse

(Provided by Dr. J. F. Wellicome)

Consider a circle:

$$\varsigma = e^{i\theta} \tag{J.1}$$

Using Z plane mapping:

$$Z = a\varsigma + \frac{b}{\varsigma} = x + iy \tag{J.2}$$

Where, x=(a+b) cos θ and y=(a-b) sin θ

Flow past a circle:

$$W = aU\left(\varsigma + \frac{1}{\varsigma}\right) \tag{J.3}$$

This give W→UZ at infinity hence equals the free stream velocity (U).

Furthermore:

$$\frac{dW}{d\varsigma} = aU\left(1 - \frac{1}{\varsigma^2}\right) \tag{J.4}$$

Flow past an ellipse in Z plane:

$$\bar{q} = \frac{dW}{dZ} = \frac{dW}{d\varsigma} : \frac{dZ}{d\varsigma} \tag{J.5}$$

Hence:

$$\bar{q} = \frac{aU\left(1 - \frac{1}{\varsigma^2}\right)}{a - \frac{b}{\varsigma^2}} \qquad \text{(J.6)}$$

$$\frac{\bar{q}}{U} = \frac{\varsigma - \frac{1}{\varsigma}}{\varsigma - \left(\frac{1-\tau}{1+\tau}\right)\frac{1}{\varsigma}} \qquad \text{(J.7)}$$

On the ellipse:

$$\frac{\bar{q}}{U} = \frac{e^{i\theta} - e^{-i\theta}}{e^{i\theta} - \left(\frac{1-\tau}{1+\tau}\right)e^{-i\theta}} = \frac{i(1+\tau)\sin\theta}{\tau\cos\theta + i\sin\theta} \qquad \text{(J.8)}$$

Using its conjugate, hence:

$$\frac{\bar{q}q}{U^2} = \frac{(1+\tau)^2\sin^2\theta}{\tau^2\cos^2\theta + \sin^2\theta} = \left(\frac{u}{U}\right)^2 \qquad \text{(J.9)}$$

Finally,

$$C_P = 1 - \left(\frac{u}{U}\right)^2 = 1 - \frac{(1+\tau)^2\sin^2\theta}{\tau^2\cos^2\theta + \sin^2\theta} \qquad \text{(J.10)}$$

TABLE 1: Wind tunnel data – drag coefficients (without transition strip)

Model Type	Actual Speed (m/s)	Reynolds Number	Measured Drag (N)	Drag Coefficient $[C_D]$	Corrected Drag Coefficient $[C_{D1}]$	Skin Friction Coefficient $[C_F]$	C_{D1}/C_F	$C_D$cat / $C_D$mono
Monohull	20.22	1.60E+06	0.646	4.389E-03	4.358E-03	3.780E-03	1.15	-
	30.22	2.40E+06	1.342	4.072E-03	4.043E-03	3.456E-03	1.17	-
	40.30	3.22E+06	2.367	4.022E-03	3.993E-03	3.242E-03	1.23	-
S/L=0.27	20.33	1.58E+06	0.621	4.219E-03	4.160E-03	3.501E-03	1.19	0.95
	30.48	2.35E+06	1.383	4.195E-03	4.136E-03	3.196E-03	1.29	1.02
	40.71	3.15E+06	2.442	4.148E-03	4.090E-03	2.991E-03	1.37	1.02
S/L=0.37	20.33	1.58E+06	0.575	3.907E-03	3.852E-03	3.501E-03	1.10	0.88
	30.37	2.37E+06	1.350	4.096E-03	4.039E-03	3.190E-03	1.27	1.00
	40.62	3.16E+06	2.450	4.163E-03	4.104E-03	2.989E-03	1.37	1.03
S/L=0.47	20.28	1.59E+06	0.504	3.424E-03	3.376E-03	3.496E-03	0.97	0.77
	30.33	2.38E+06	1.354	4.109E-03	4.052E-03	3.187E-03	1.27	1.00
	40.57	3.17E+06	2.438	4.142E-03	4.084E-03	2.987E-03	1.37	1.02

Note: values of C_F (for case without transition strip) are obtained from the parametric study of transition point prediction explained in Appendix D.

TABLE 2: Wind tunnel data – drag coefficients (with transition strip)

Model Type	Actual Speed (m/s)	Reynolds Number	Drag (N)	Drag Coefficient $[C_D]$	Corrected Drag Coefficient $[C_{D1}]$	Skin Friction Coefficient, ITTC $[C_F]$	C_{D1}/C_F	$C_D$cat / $C_D$mono
Monohull	20.14	1.61E+06	0.658	4.473E-03	4.441E-03	4.238E-03	1.05	-
	30.18	2.40E+06	1.571	4.767E-03	4.734E-03	3.908E-03	1.21	-
	40.32	3.21E+06	2.675	4.544E-03	4.512E-03	3.692E-03	1.22	-
S/L=0.27	20.36	1.57E+06	0.742	5.044E-03	4.973E-03	4.259E-03	1.17	1.12
	30.50	2.35E+06	1.658	5.031E-03	4.960E-03	3.926E-03	1.26	1.05
	40.83	3.13E+06	2.950	5.011E-03	4.941E-03	3.712E-03	1.33	1.10
S/L=0.37	20.41	1.56E+06	0.708	4.809E-03	4.742E-03	4.263E-03	1.11	1.07
	30.55	2.34E+06	1.592	4.831E-03	4.763E-03	3.929E-03	1.21	1.01
	40.91	3.11E+06	2.879	4.893E-03	4.824E-03	3.716E-03	1.30	1.07
S/L=0.47	20.42	1.56E+06	0.688	4.677E-03	4.611E-03	4.265E-03	1.08	1.04
	30.59	2.33E+06	1.596	4.843E-03	4.775E-03	3.932E-03	1.21	1.01
	40.95	3.10E+06	2.917	4.956E-03	4.887E-03	3.718E-03	1.31	1.08
S/L=0.57	20.10	1.62E+06	0.708	4.812E-03	4.744E-03	4.233E-03	1.12	1.07
	29.96	2.45E+06	1.663	5.046E-03	4.975E-03	3.893E-03	1.28	1.05
	40.00	3.28E+06	2.975	5.055E-03	4.985E-03	3.678E-03	1.36	1.10

TABLE 3: Wind tunnel data – side-force coefficients (without transition strip)

Model Type	Actual Speed (m/s)	Reynolds number	Side-force (N)	Side-force Coefficient [C_{SF}]	Corrected Side Force Coefficient [C_{SFI}]	C_{SF} when C_{SFI} for monohull assumed = 0
Monohull	20.22	1.60E+06	0.033	0.00022	0.00022	0.00000
	30.22	2.40E+06	0.150	0.00046	0.00045	0.00000
	40.30	3.22E+06	0.350	0.00059	0.00059	0.00000
S/L=0.27	20.33	1.58E+06	0.717	0.00487	0.00480	0.00458
	30.48	2.35E+06	1.567	0.00475	0.00469	0.00423
	40.71	3.15E+06	2.883	0.00490	0.00483	0.00424
S/L=0.37	20.33	1.58E+06	0.317	0.00215	0.00212	0.00190
	30.37	2.37E+06	0.783	0.00238	0.00234	0.00189
	40.62	3.16E+06	1.467	0.00249	0.00246	0.00187
S/L=0.47	20.28	1.59E+06	0.200	0.00136	0.00134	0.00112
	30.33	2.38E+06	0.483	0.00147	0.00145	0.00099
	40.57	3.17E+06	0.883	0.00150	0.00148	0.00089

TABLE 4: Wind tunnel data – side-force coefficients (with transition strip)

Model Type	Actual Speed (m/s)	Reynolds number	Side Force (N)	Side Force Coefficient [C_{SF}]	Corrected Side Force Coefficient [C_{SFI}]	C_{SF} when C_{SFI} for monohull assumed = 0
Monohull	20.14	1.60E+06	0.000	0.00000	0.00000	0.00000
	30.18	2.39E+06	0.167	0.00051	0.00050	0.00000
	40.32	3.19E+06	0.300	0.00051	0.00051	0.00000
S/L=0.27	20.36	1.54E+06	0.667	0.00453	0.00447	0.00447
	30.50	2.31E+06	1.433	0.00435	0.00429	0.00378
	40.83	3.06E+06	2.717	0.00462	0.00455	0.00404
S/L=0.37	20.41	1.53E+06	0.350	0.00238	0.00234	0.00234
	30.55	2.30E+06	0.783	0.00238	0.00234	0.00184
	40.91	3.04E+06	1.550	0.00263	0.00260	0.00209
S/L=0.47	20.42	1.53E+06	0.233	0.00158	0.00156	0.00156
	30.59	2.29E+06	0.550	0.00167	0.00165	0.00114
	40.95	3.03E+06	1.117	0.00190	0.00187	0.00137
S/L=0.57	20.10	1.61E+06	0.150	0.00102	0.00101	0.00101
	29.96	2.45E+06	0.283	0.00086	0.00085	0.00034
	40.00	3.28E+06	0.717	0.00122	0.00120	0.00070

TABLE 5: Wind tunnel data – coefficients of viscous resistance interference (β), without transition strip

Model Type	Actual Speed (m/s)	Reynolds Number	1+k	(1+βk)	β
Monohull	20.22	1.60E+06	1.15	-	-
	30.22	2.40E+06	1.17	-	-
	40.30	3.22E+06	1.23	-	-
S/L=0.27	20.33	1.58E+06	-	1.19	1.27
	30.48	2.35E+06	-	1.29	1.71
	40.71	3.15E+06	-	1.37	1.61
S/L=0.37	20.33	1.58E+06	-	1.10	0.67
	30.37	2.37E+06	-	1.27	1.59
	40.62	3.16E+06	-	1.37	1.61
S/L=0.47	20.28	1.59E+06	-	0.97	-0.20
	30.33	2.38E+06	-	1.27	1.59
	40.57	3.17E+06	-	1.37	1.61

TABLE 6: Wind tunnel data – coefficients of viscous resistance interference (β), with transition strip

Model Type	Actual Speed (m/s)	Reynolds Number	1+k	(1+βk)	β
Monohull	20.14	1.61E+06	1.05	-	-
	30.18	2.40E+06	1.21	-	-
	40.32	3.21E+06	1.22	-	-
S/L=0.27	20.36	1.57E+06	-	1.17	3.40
	30.50	2.35E+06	-	1.26	1.24
	40.83	3.13E+06	-	1.33	1.50
S/L=0.37	20.41	1.56E+06	-	1.11	2.20
	30.55	2.34E+06	-	1.21	1.00
	40.91	3.11E+06	-	1.30	1.36
S/L=0.47	20.42	1.56E+06	-	1.08	1.60
	30.59	2.33E+06	-	1.21	1.00
	40.95	3.10E+06	-	1.31	1.41
S/L=0.57	20.10	1.62E+06	-	1.12	2.40
	29.96	2.45E+06	-	1.28	1.33
	40.00	3.28E+06	-	1.36	1.64

TABLE 7: CFD data – investigation of optimal distance (two-dimensional case)

Inlet	Outlet	Upper Inlet	C_T	Y+	Number of Iterations	CPU Time (seconds)	Number of Cells
1L	1L	1L	0.07910	101-204	719	591	4,200
1L	1.5L	1L	0.07917	88-193	573	501	4,300
1L	2L	1L	0.07920	63-175	554	498	4.440
1L	3L	1L	0.07920	63-175	560	504	4,530
1L	2L	0.5L	0.10139	110-274	1213	1005	4,000
1L	2L	1L	0.07920	63-175	554	498	4,440
1L	2L	1.5L	0.07920	63-175	650	743	4,550
1L	2L	2L	0.07920	63-175	656	747	4,700
1L	2L	1L	0.07920	63-175	554	498	4,440
1.5L	2L	1L	0.07920	63-175	551	601	5,050
2L	2L	1L	0.07920	63-175	522	578	5,550
3L	2L	1L	0.07920	63-175	524	580	6,120

TABLE 8: CFD data – grid independence study (two-dimensional ellipse)

Number of cells	Drag coefficient
4,500	0.0792
7,000	0.0775
12,000	0.0729
16,000	0.0723

TABLE 9: CFD data – total drag, skin friction, form factors and side-force (two-dimensional case)

Configuration	Total Drag	Skin Friction	Form Factor	Side-force	Side-force as % of total drag
One ellipse	0.073	0.057	1.28	-	-
S/L=0.27	0.096	0.060	1.60	0.077	80.2
S/L=0.37	0.088	0.059	1.49	0.046	52.3
S/L=0.47	0.081	0.058	1.40	0.026	32.1
S/L=0.57	0.075	0.058	1.29	0.009	12.0

TABLE 10: CFD data – grid independence study (three-dimensional ellipsoid)

Number of cells	Drag coefficient
50,000	0.00658
100,000	0.00631
200,000	0.00610
300,000	0.00594
400,000	0.00581
600,000	0.00576

TABLE 11: CFD data – total drag, skin friction, viscous pressure drag, and form factor (three-dimensional ellipsoid, L/D=6.0)

Configuration	Total Drag (x1000)	Skin Friction (x1000)	Pressure Drag (x1000)	Form Factor
One ellipsoid	5.581	4.046	1.535	1.379
S/L=0.27, G/L=0.103	5.740	4.105	1.635	1.398
S/L=0.37	5.663	4.074	1.589	1.390
S/L=0.47	5.623	4.063	1.560	1.383
S/L=0.57	5.589	4.049	1.540	1.380

TABLE 12: CFD data – side-force as percentage of total drag (three-dimensional ellipsoid, L/D=6.0)

Configuration	Total Drag (x1000)	Side Force (x1000)	Side Force as % of Total Drag
One ellipsoid	5.581	-	-
S/L=0.27, G/L=0.103	5.740	3.078	53.7
S/L=0.37	5.663	1.571	27.7
S/L=0.47	5.623	0.910	16.2
S/L=0.57	5.589	0.535	9.6

TABLE 13: CFD data – total drag, skin friction, viscous pressure drag, and form factor (three-dimensional ellipsoid, L/D=10.0)

Configuration	Total Drag (x1000)	Skin Friction (x1000)	Pressure Drag (x1000)	Form Factor
One ellipsoid	4.866	4.011	0.855	1.213
S/L=0.203, G/L=0.103	4.921	4.046	0.875	1.216
S/L=0.27, G/L=0.170	4.890	4.029	0.861	1.214

TABLE 14: CFD data – side-force as percentage of total drag (three-dimensional ellipsoid, L/D=10.0)

Configuration	Total Drag (x1000)	Side Force (x1000)	Side Force as % of Total Drag
One ellipsoid	4.866	-	-
S/L=0.203, G/L=0.103	4.921	0.559	11.4
S/L=0.27, G/L=0.170	4.890	0.331	6.8

TABLE 15: CFD data – grid independence study (ship hull models)

Number of cells	Drag coefficients	
	Model 4b	Model 5b
100,000	0.006534	0.006107
200,000	0.006318	0.005701
300,000	0.006157	0.005532
400,000	0.006101	0.005431
600,000	0.006079	0.005407

TABLE 16: CFD data – total drag, skin friction, viscous pressure drag, and form factor (ship hull models)

Configuration	Total Drag (x1000)	Skin Friction (x1000)	Pressure Drag (x1000)	Form Factor
Model 4b				
One body	6.101	4.199	1.902	1.45
S/L=0.20	6.985	4.467	2.518	1.56
S/L=0.40	6.484	4.357	2.127	1.49
Model 5b				
One body	5.431	4.093	1.338	1.33
S/L=0.20	5.911	4.212	1.699	1.40
S/L=0.40	5.672	4.149	1.523	1.37

TABLE 17: CFD data – transom stern drag (ship hull models)

Configuration	Total Drag (x1000)	Skin Friction (x1000)	Pressure Drag (x1000)	Transom Drag (x1000)
Model 4b				
One body	6.101	4.199	1.902	1.510
S/L=0.20	6.985	4.467	2.518	2.130
S/L=0.40	6.484	4.357	2.127	1.734
Model 5b				
One body	5.431	4.093	1.338	1.170
S/L=0.20	5.911	4.212	1.699	1.630
S/L=0.40	5.672	4.149	1.523	1.240

TABLE 18: CFD data – form factor without transom stern effect (ship hull models)

Configuration	Total Drag (x1000)	Skin Friction (x1000)	Form Factor
Model 4b			
One body	4.591	4.199	1.09
S/L=0.20	4.855	4.467	1.09
S/L=0.40	4.750	4.357	1.09
Model 5b			
One body	4.261	4.093	1.04
S/L=0.20	4.485	4.212	1.06
S/L=0.40	4.358	4.149	1.05

TABLE 19: CFD data – side-force as percentage of total drag (ship·hull models)

Configuration	Total Drag (x1000)	Side Force (x1000)	Side Force as % of Total Drag
Model 4b			
One body	6.101	-	-
S/L=0.20	6.985	0.728	10.4
S/L=0.40	6.484	0.138	2.1
Model 5b			
One body	5.431	-	-
S/L=0.20	5.911	0.125	2.1
S/L=0.40	5.672	0.067	1.2

TABLE 20: CFD data – levels of viscous interaction (ellipsoid body of revolution, L/D=6.0, $L/\nabla^{1/3}=5.17$)

Configuration	Pressure Drag (x1000)	Skin Friction (x1000)	C_{VP2}/C_{VP1}	C_{F2}/C_{F1}	β
One ellipsoid	1.535	4.046	-	-	-
S/L=0.27, G/L=0.103	1.635	4.105	1.065	1.015	1.050
S/L=0.37	1.589	4.074	1.035	1.007	1.029
S/L=0.47	1.560	4.063	1.016	1.004	1.011
S/L=0.57	1.540	4.049	1.003	1.001	1.003

TABLE 21: CFD data – levels of viscous interaction (ellipsoid body of revolution, L/D=10.0, $L/\nabla^{1/3}=7.26$)

Configuration	Pressure Drag (x1000)	Skin Friction (x1000)	C_{VP2}/C_{VP1}	C_{F2}/C_{F1}	β
One ellipsoid	0.855	4.011	-	-	-
S/L=0.203, G/L=0.103	0.875	4.046	1.023	1.009	1.014
S/L=0.27, G/L=0.170	0.861	4.029	1.007	1.004	1.005

TABLE 22: CFD data - levels of viscous interaction (ship hull model, Model 4b)

Configuration	Pressure Drag (x1000)	Skin Friction (x1000)	C_{VP2}/C_{VP1}	C_{F2}/C_{F1}	β
One body	1.902	4.199	-	-	-
S/L=0.20	2.518	4.467	1.324	1.064	1.245
S/L=0.40	2.127	4.357	1.118	1.038	1.077

TABLE 23: CFD data – levels of viscous interaction (ship hull model, model 5b)

Configuration	Pressure Drag (x1000)	Skin Friction (x1000)	C_{VP2}/C_{VP1}	C_{F2}/C_{F1}	β
One body	1.338	4.093	-	-	-
S/L=0.20	1.699	4.212	1.270	1.029	1.212
S/L=0.40	1.523	4.149	1.138	1.014	1.121

TABLE 24: Proportions of total drag of two bodies upon total drag of one body

Configuration	Total Drag, CFX (x1000)	C_V twin / C_V mono	
		Wind tunnel or test tank	CFX
Ellipsoid, L/D=6.0			
One ellipsoid	5.581	-	-
S/L=0.27, G/L=0.103	5.740	1.09	1.028
S/L=0.37	5.663	1.05	1.015
S/L=0.47	5.623	1.04	1.008
S/L=0.57	5.589	-	1.001
Ellipsoid, L/D=10.0			
One ellipsoid	4.866	-	-
S/L=0.203, G/L=0.103	4.921	-	1.011
S/L=0.27, G/L=0.170	4.890	-	1.005
Model 4b (with transom)			
One body	6.101	-	-
S/L=0.20	6.985	1.13	1.145
S/L=0.40	6.484	1.11	1.063
Model 5b (with transom)			
One body	5.431	-	-
S/L=0.20	5.911	1.12	1.088
S/L=0.40	5.672	1.11	1.044
Model 4b (without transom)			
One body	4.591	-	-
S/L=0.20	4.855	-	1.058
S/L=0.40	4.750	-	1.035
Model 5b (without transom)			
One body	4.261	-	-
S/L=0.20	4.485	-	1.052
S/L=0.40	4.358	-	1.023

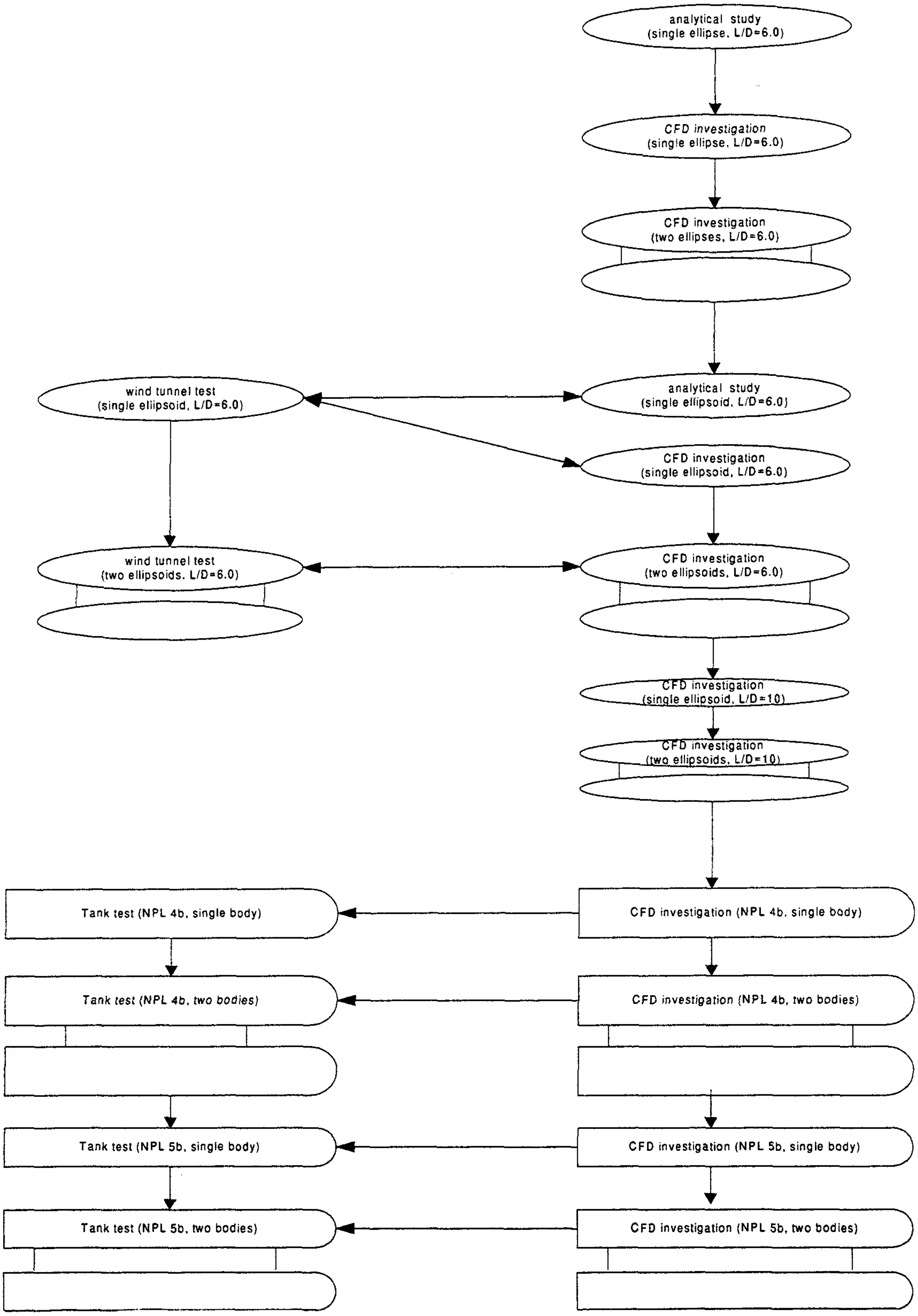

Figure 1: Overall outline of the investigations

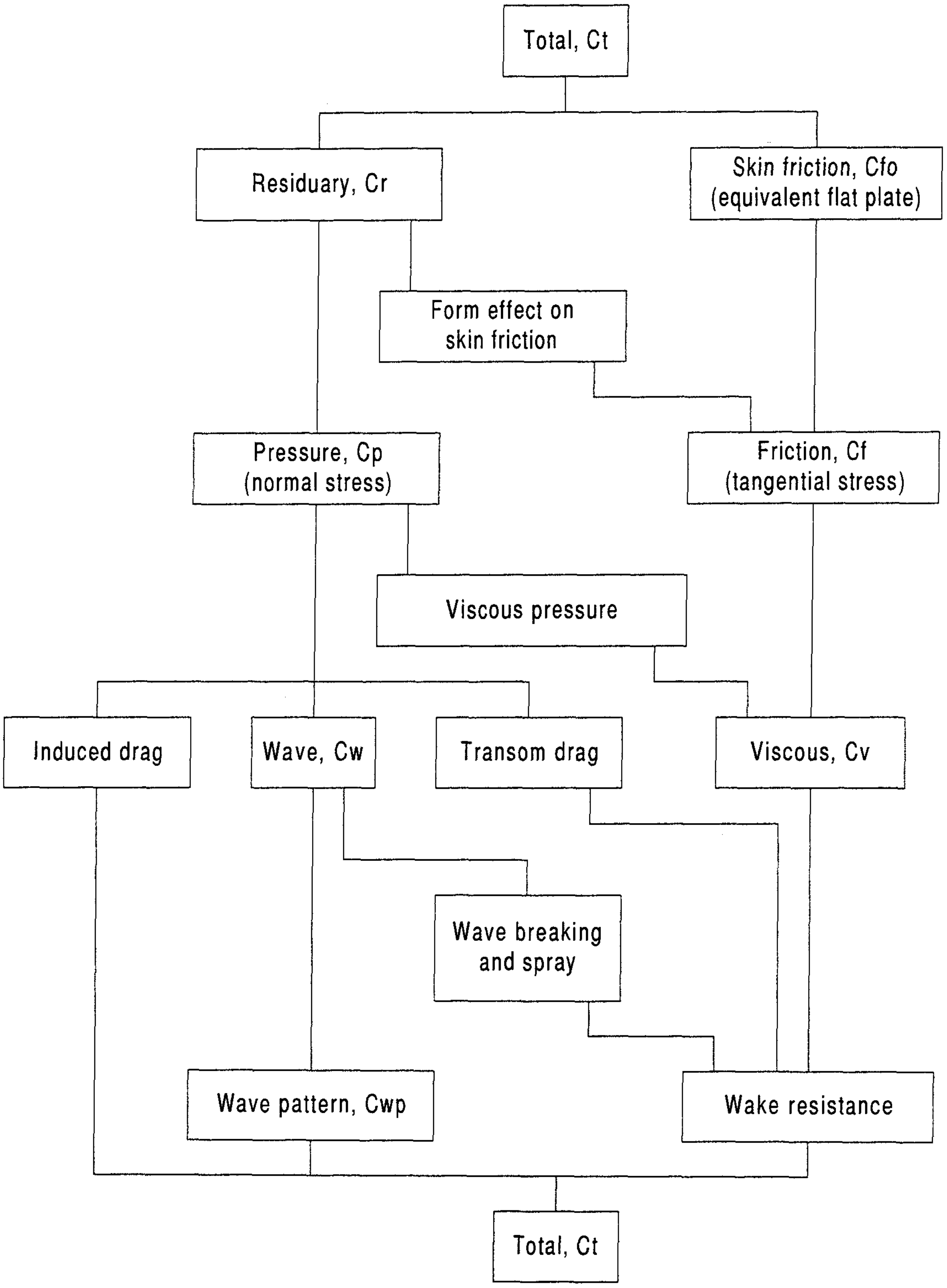

Figure 2: Breakdown of the resistance components, Ref. [16]

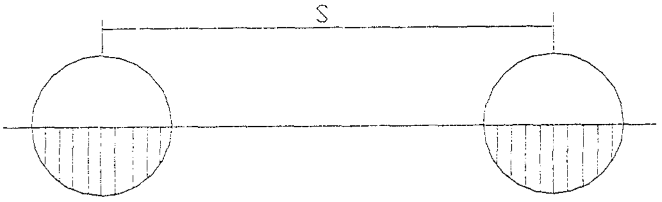

Figure 3a: Two ellipsoids in proximity, cross sectional view

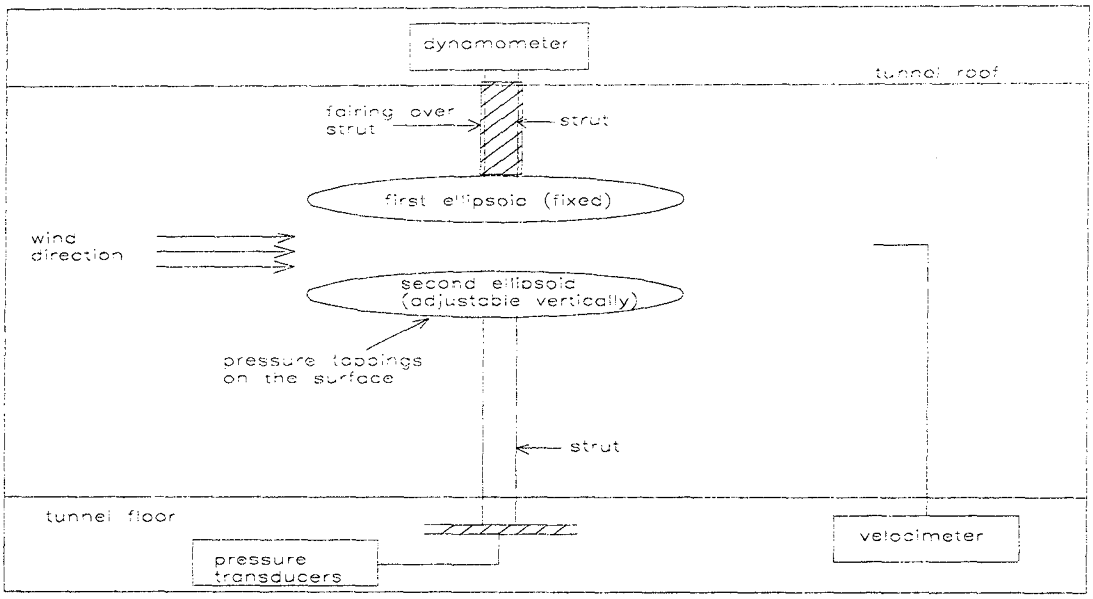

Figure 3b: Set-up of the models in the wind tunnel (schematic)

Figure 3c: Set-up of the models in the wind tunnel (photograph)

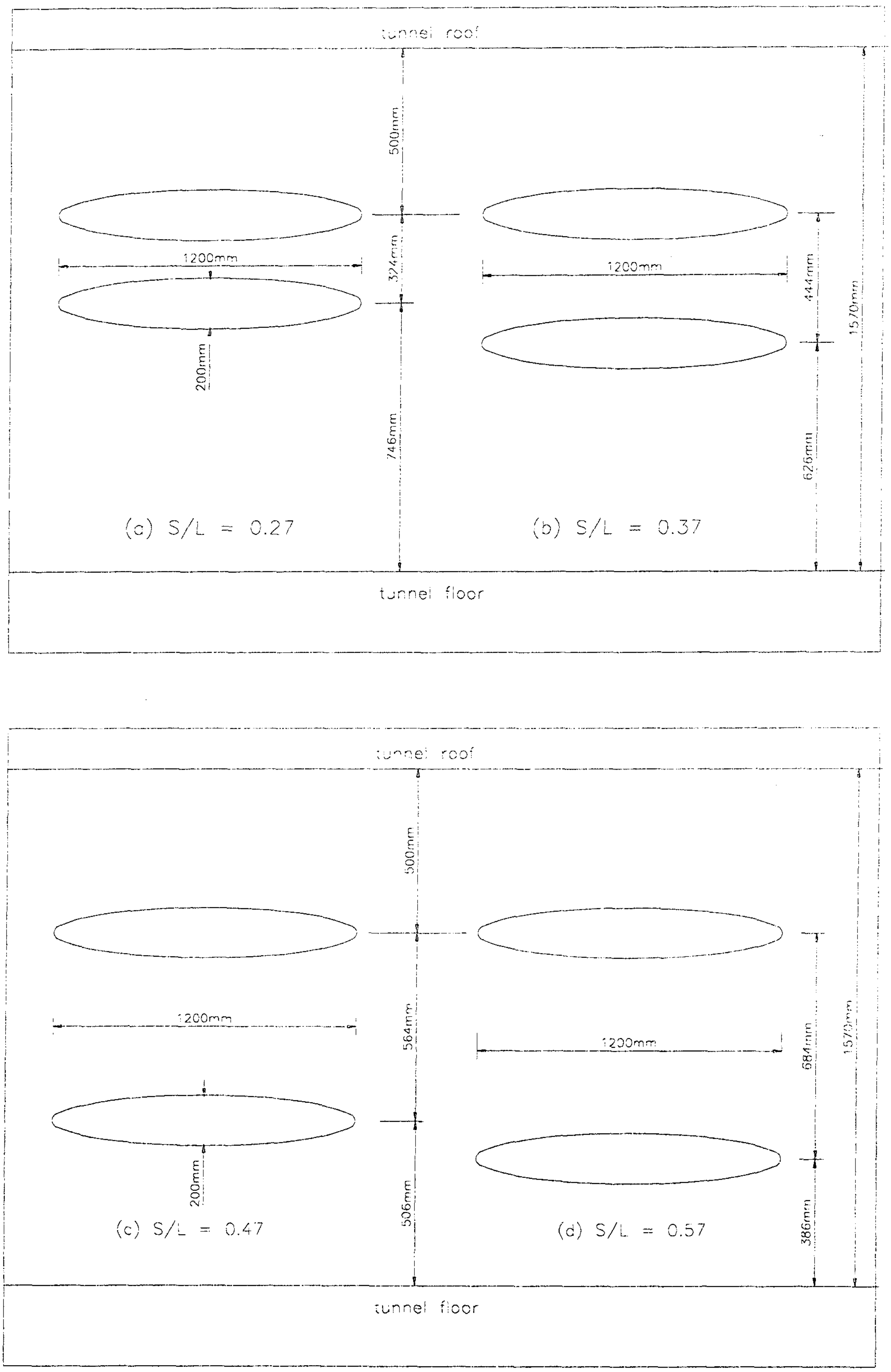

Figure 4: Model dimensions and position relative to tunnel walls

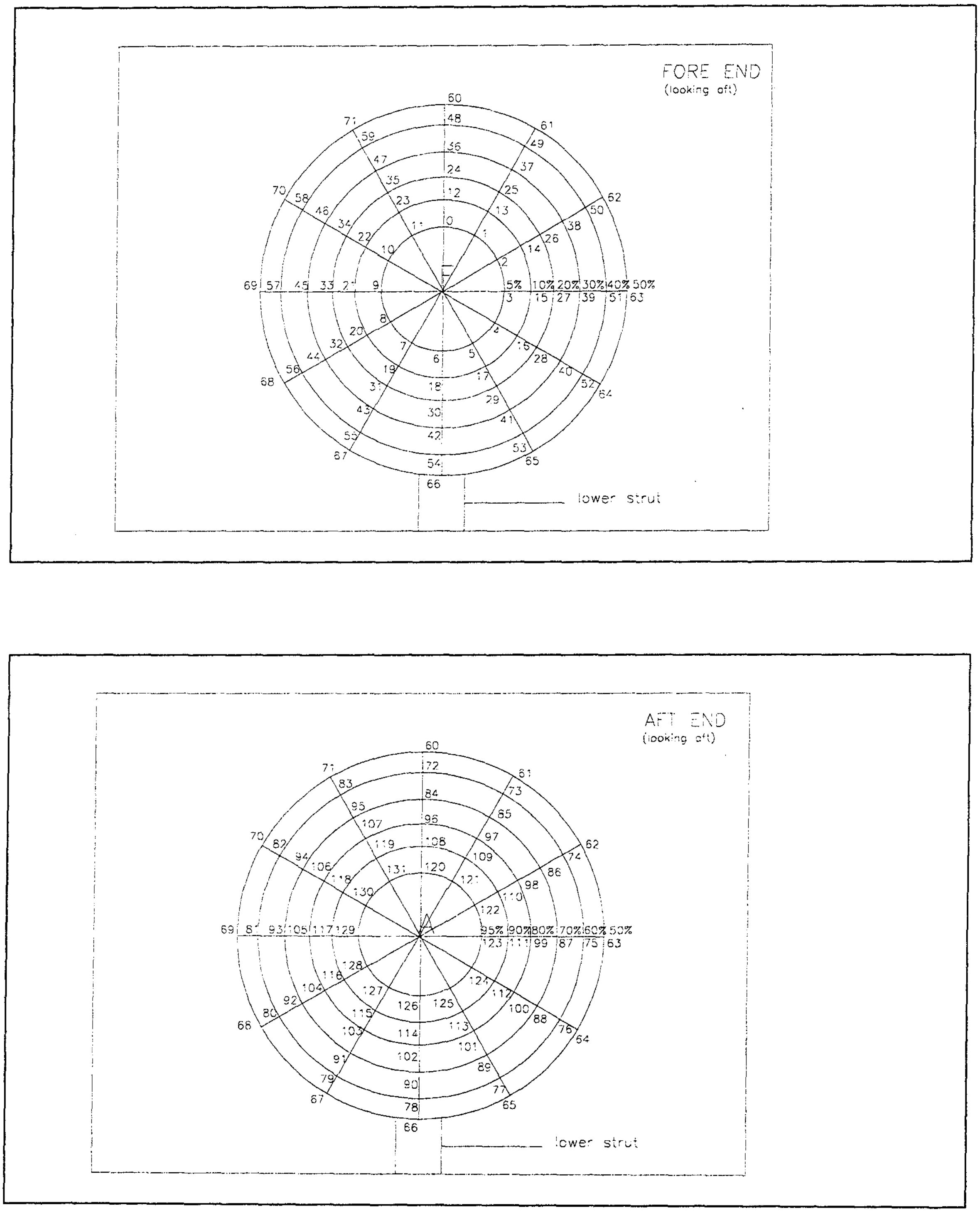

Figure 5a: Circumferential location of the pressure tappings

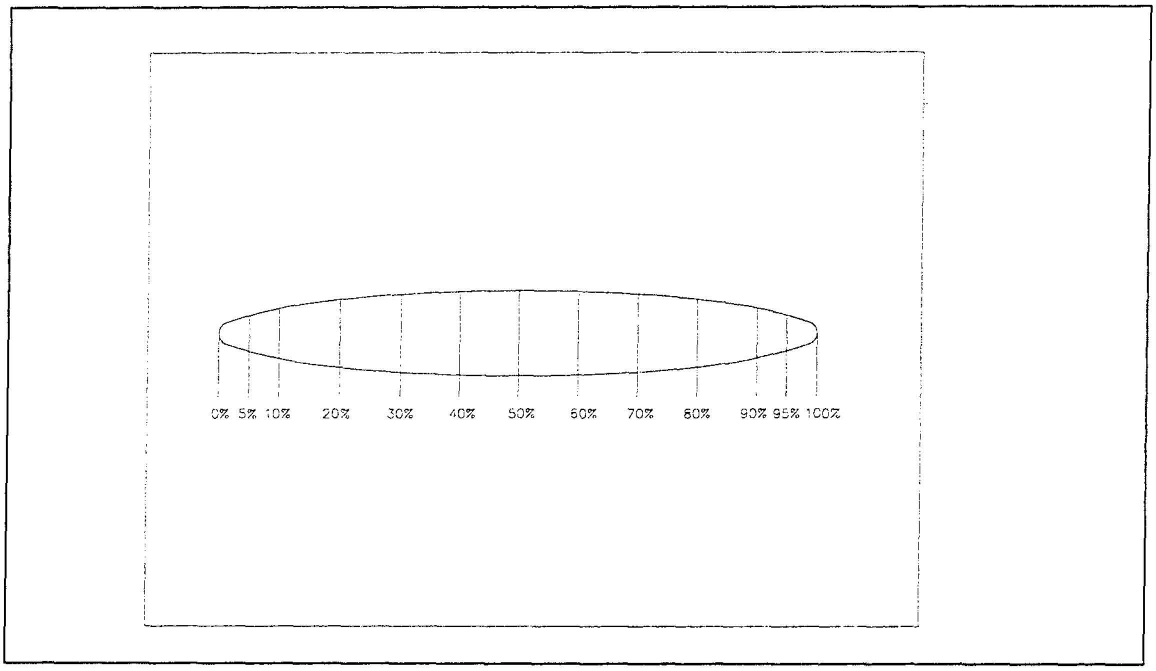

Figure 5b: Longitudinal location of the pressure tappings

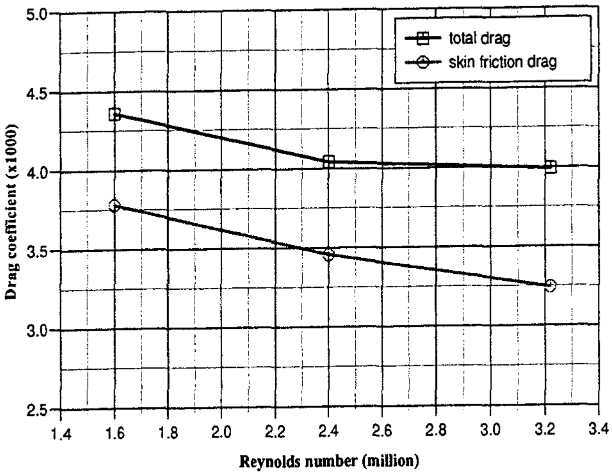

Figure 6a: Monohull, without transition strip

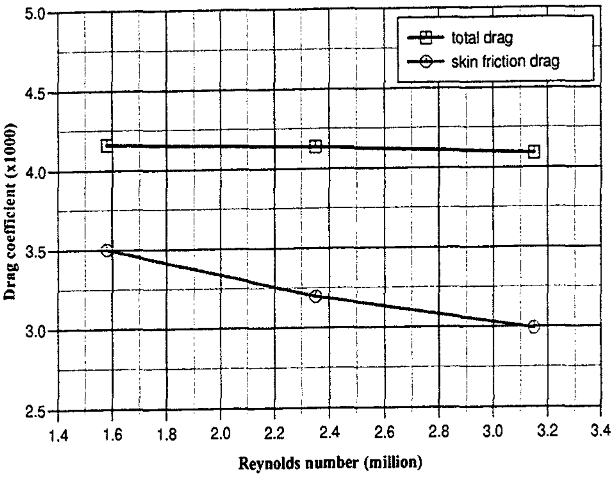

Figure 6b: S/L=0.27, without transition strip

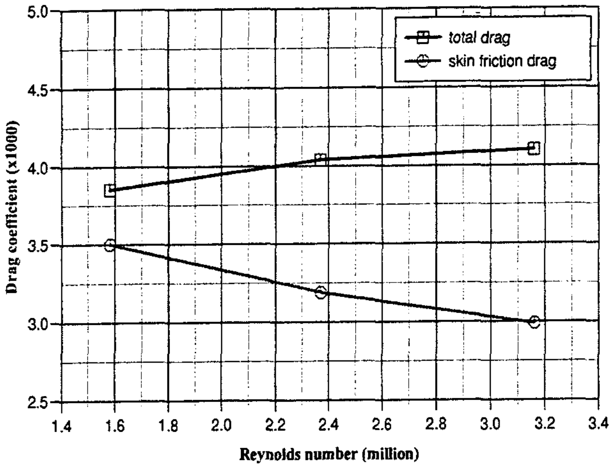

Figure 6c: S/L=0.37, without transition strip

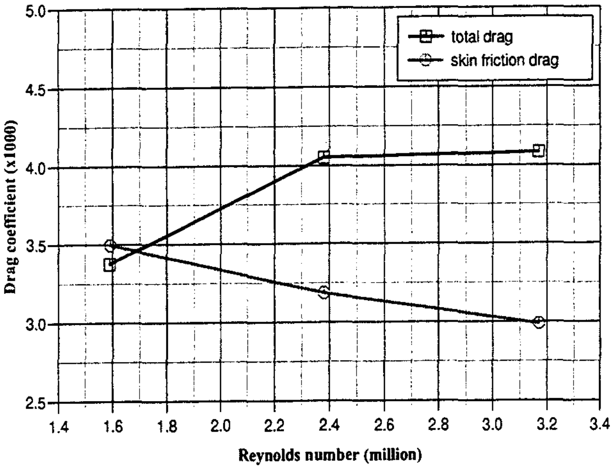

Figure 6d: S/L=0.47, without transition strip

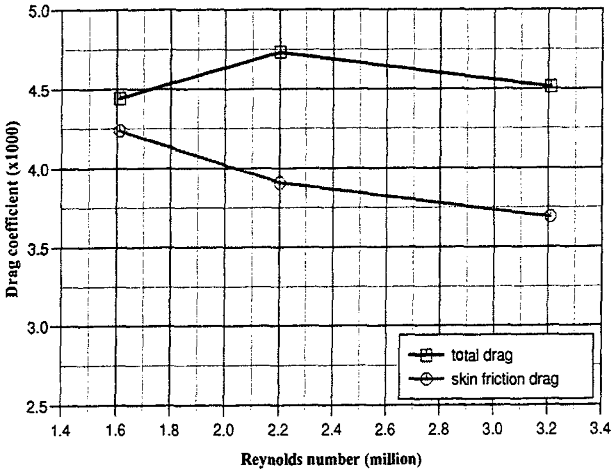

Figure 7a: Monohull, with transition strip

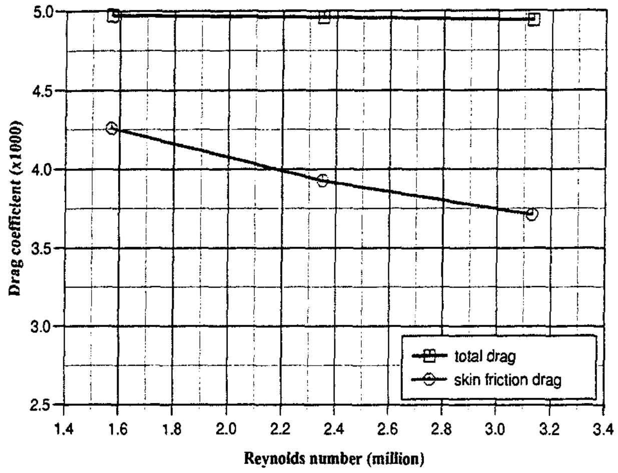

Figure 7b: S/L=0.27, with transition strip

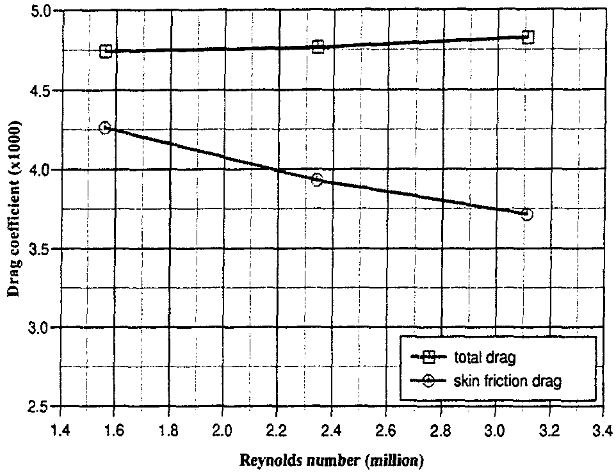

Figure 7c: S/L=0.37, with transition strip

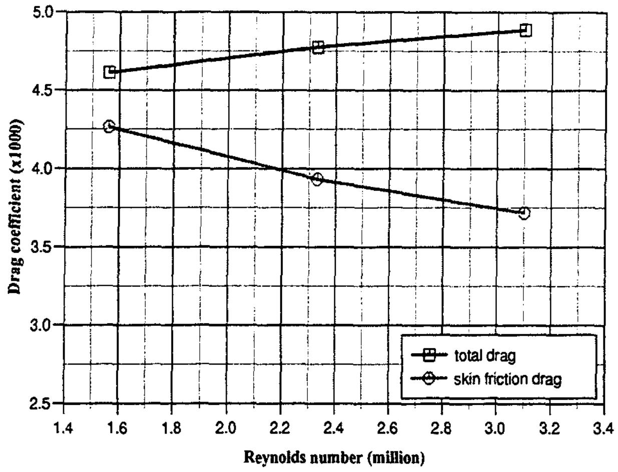

Figure 7d: S/L=0.47, with transition strip

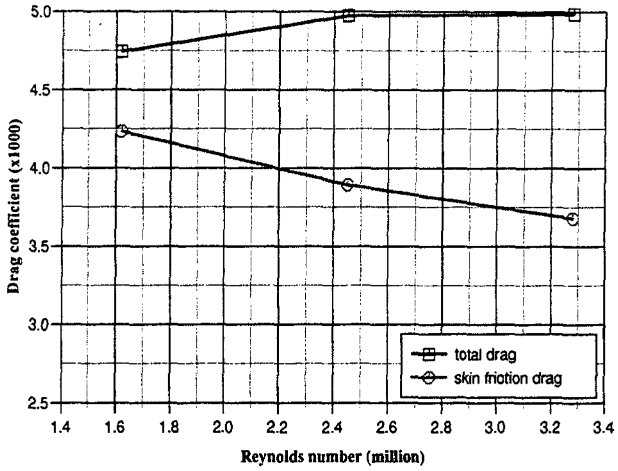

Figure 7e: S/L=0.57, with transition strip

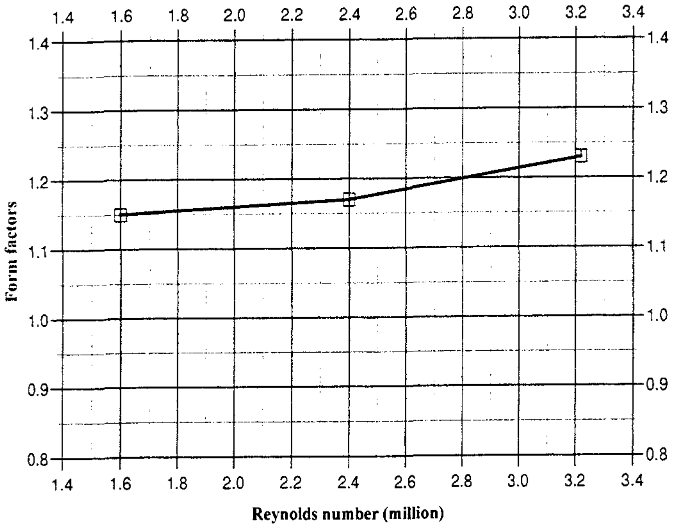

Figure 8a: Monohull, without transition strip

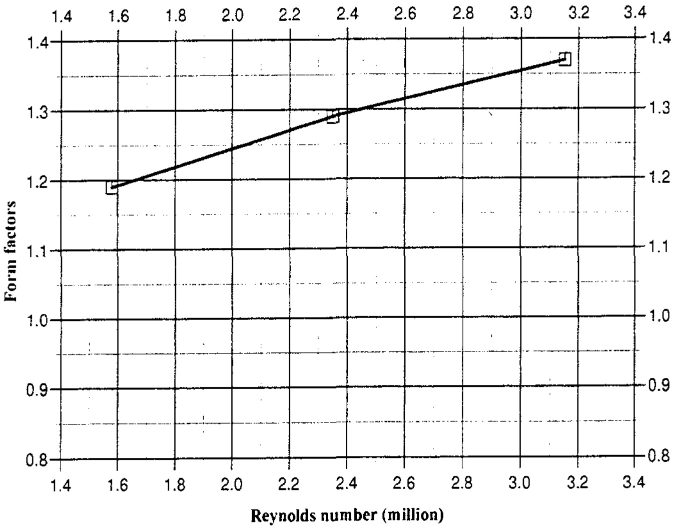

Figure 8b: S/L=0.27, without transition strip

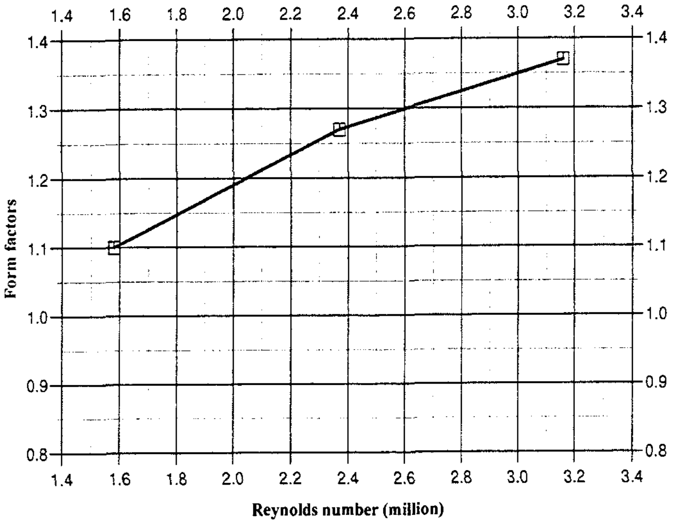

Figure 8c: S/L=0.37, without transition strip

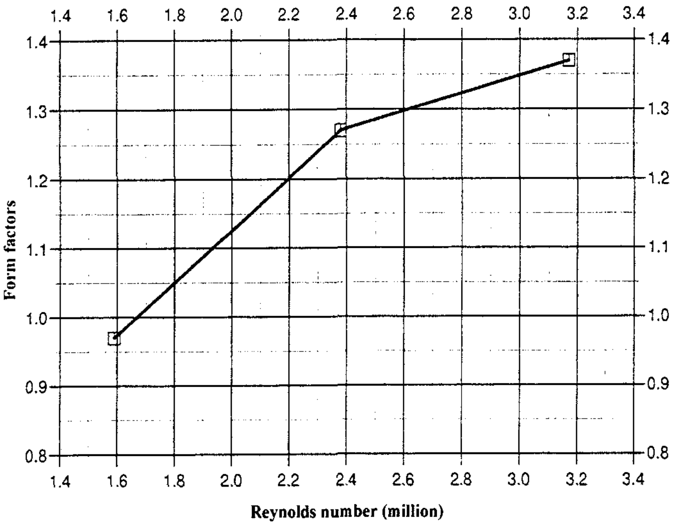

Figure 8d: S/L=0.47, without transition strip

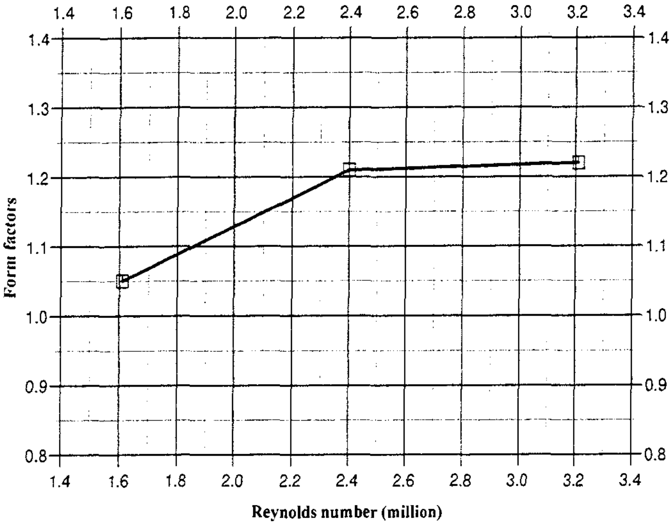

Figure 9a: Monohull, with transition strip

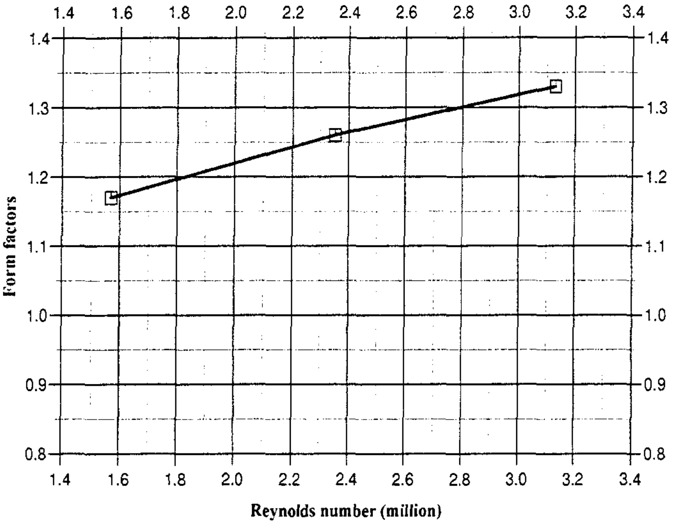

Figure 9b: S/L=0.27, with transition strip

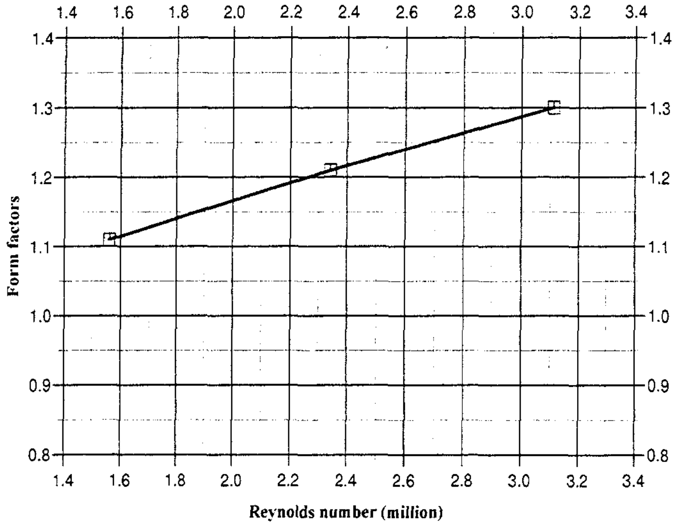

Figure 9c: S/L=0.37, with transition strip

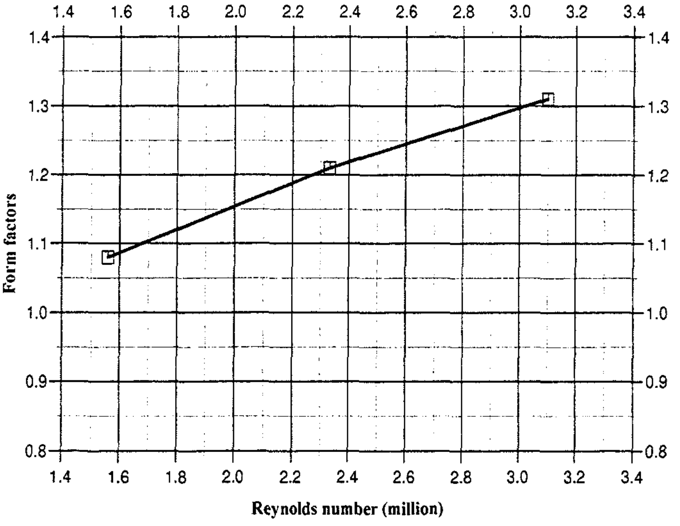

Figure 9d: S/L=0.47, with transition strip

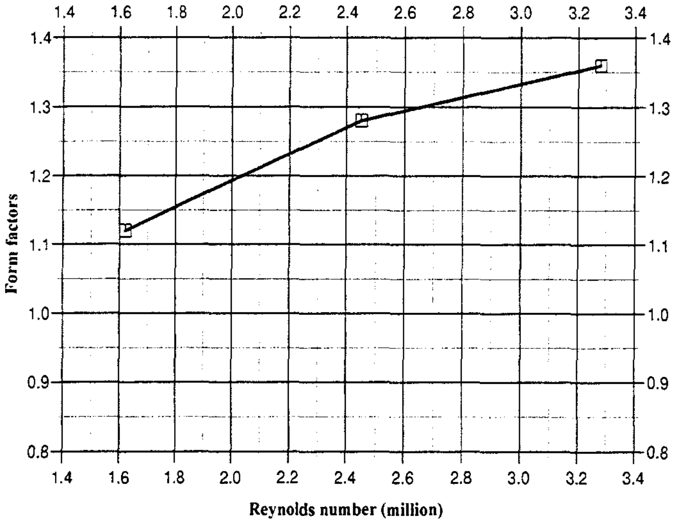

Figure 9e: S/L=0.57, with transition strip

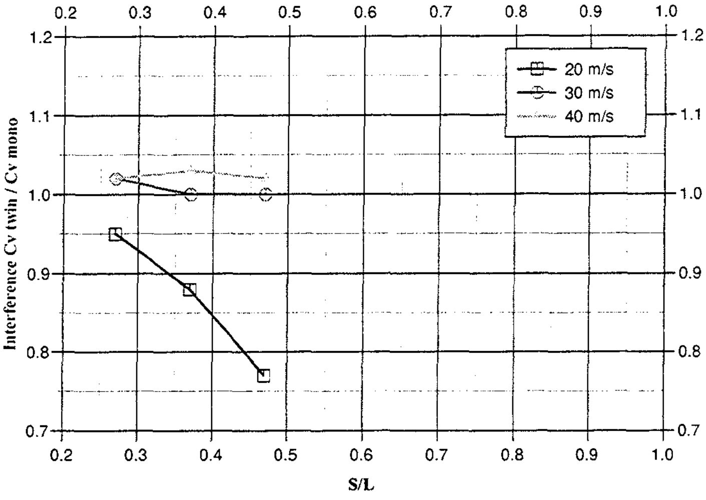

Figure 10a: Viscous interaction, without transition strip

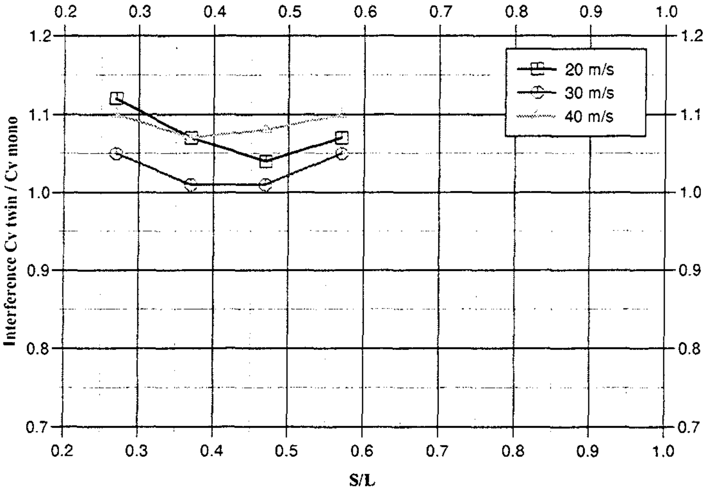

Figure 10b: Viscous interaction, with transition strip

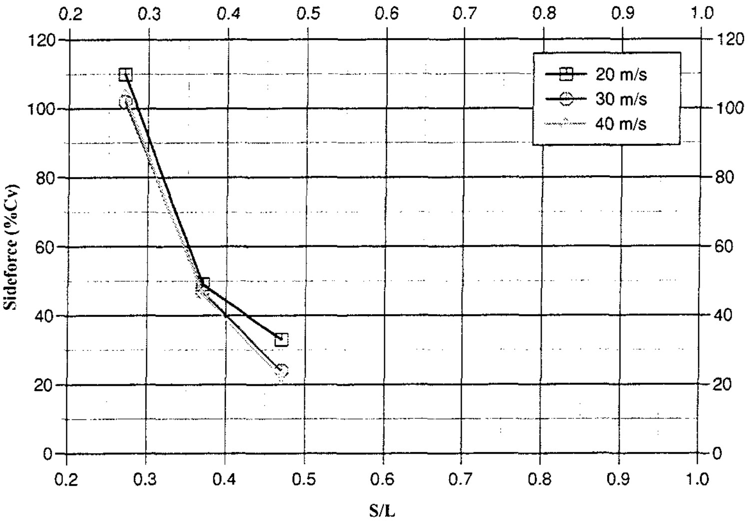

Figure 11a: Sideforce as percentage of Cv, without transition strip

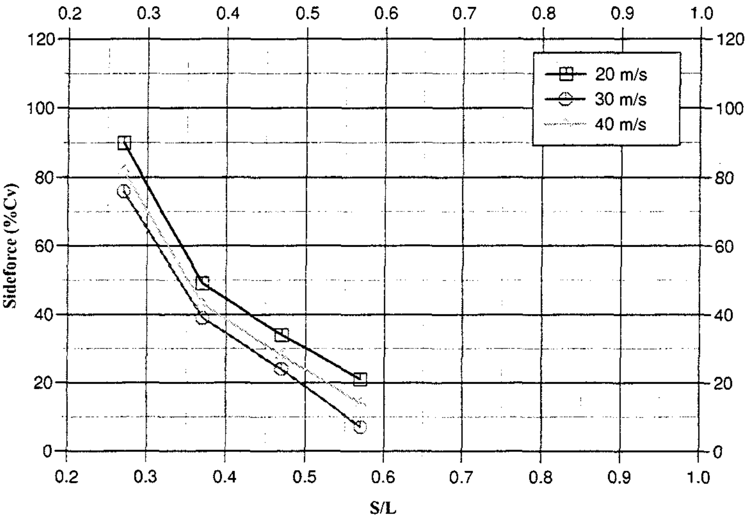

Figure 11b: Sideforce as percentage of Cv, with transition strip

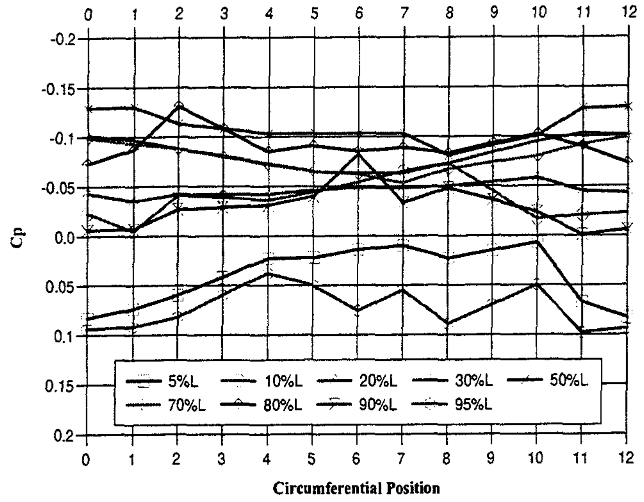

Figure 12a: S/L=0.27, 20m/s, without transition strip

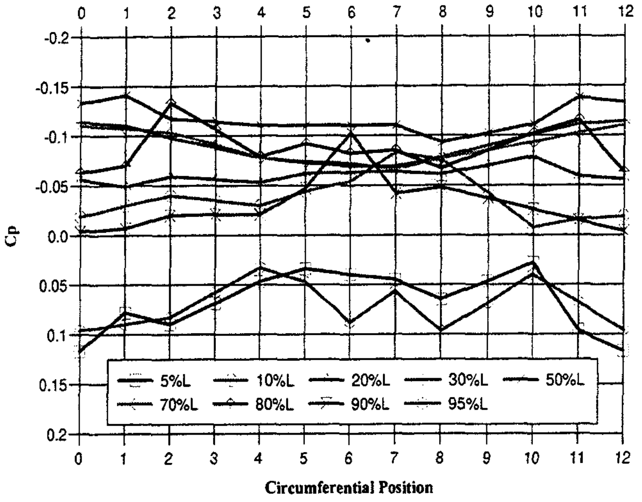

Figure 12b: S/L=0.27, 20m/s, with transition strip

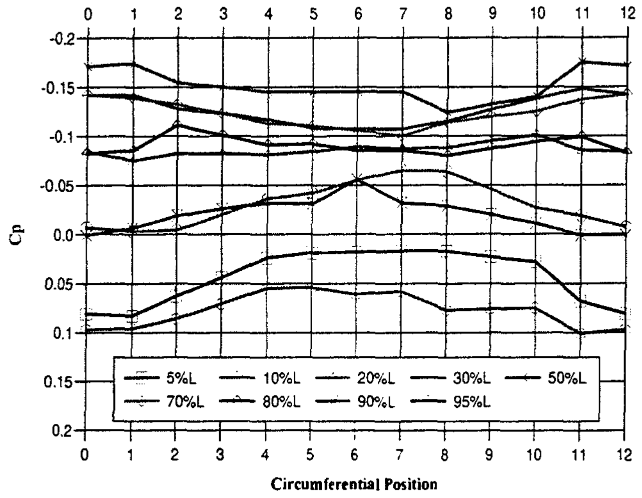

Figure 13a: S/L=0.27, 30m/s, without transition strip

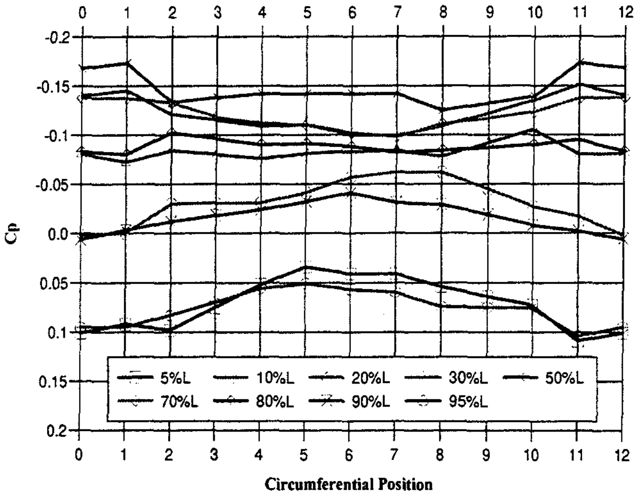

Figure 13b: S/L=0.27, 30m/s, with transition strip

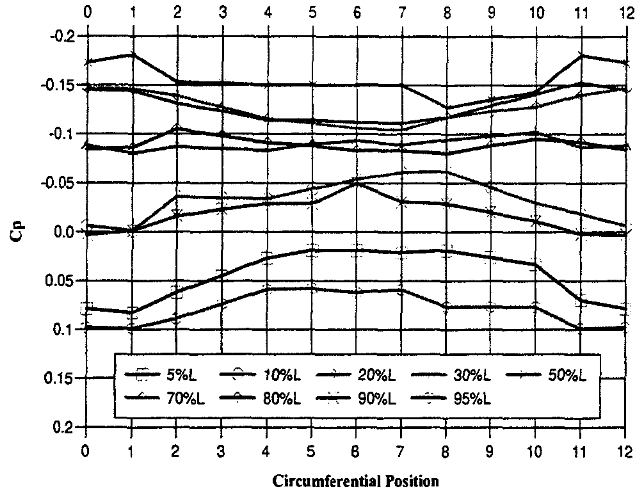

Figure 14a: S/L=0.27, 40m/s, without transition strip

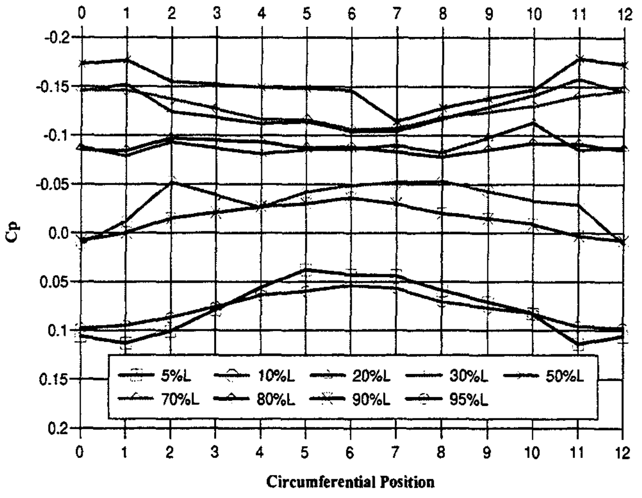

Figure 14b: S/L=0.27, 40m/s, with transition strip

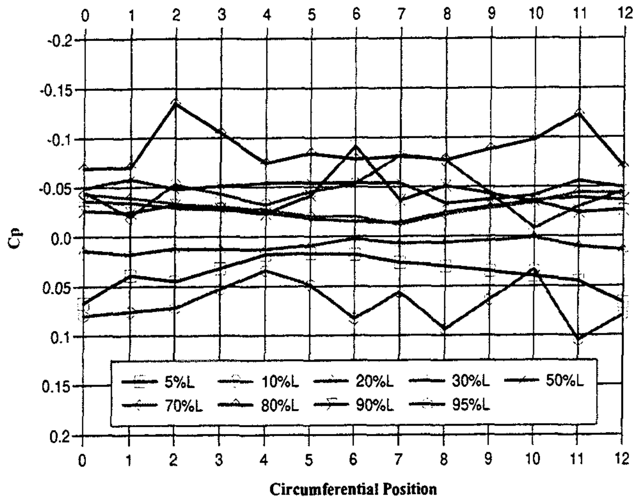

Figure 15a: S/L=0.37, 20m/s, without transition strip

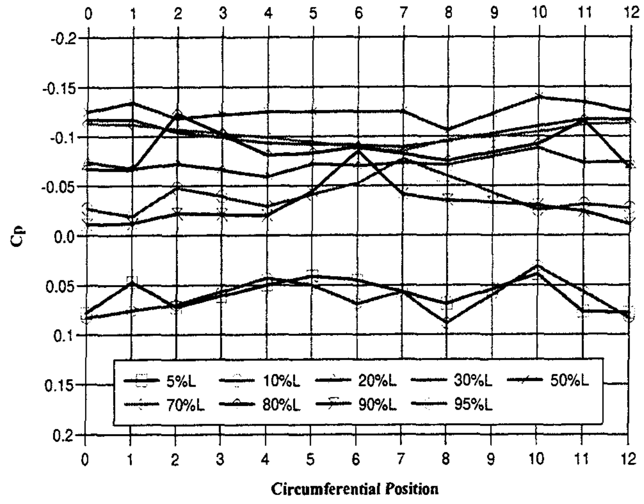

Figure 15b: S/L=0.37, 20m/s, with transition strip

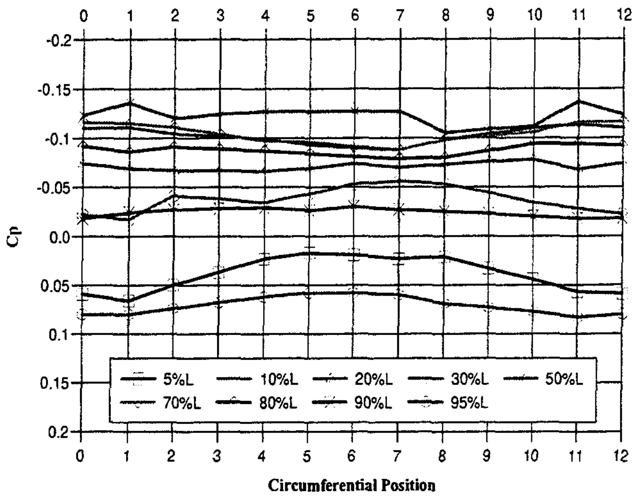

Figure 16a: S/L=0.37, 30m/s, without transition strip

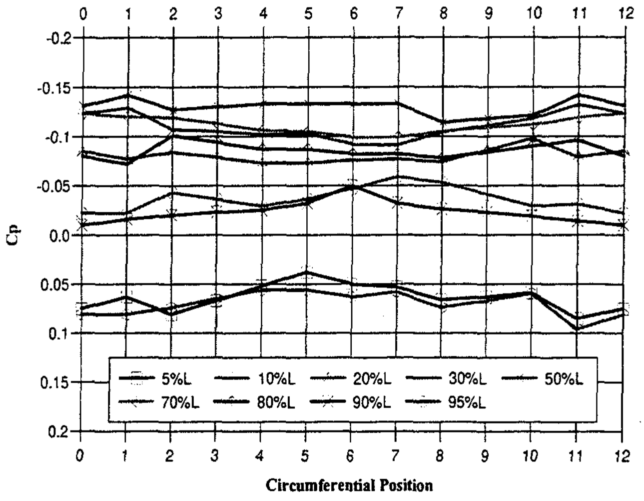

Figure 16b: S/L=0.37, 30m/s, with transition strip

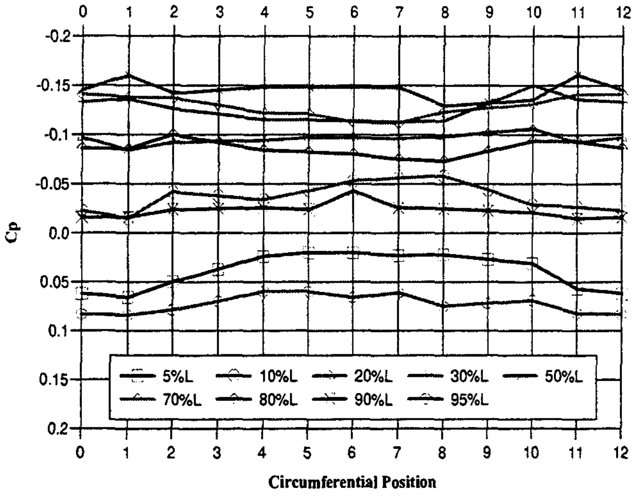

Figure 17a: S/L=0.37, 40m/s, without transition strip

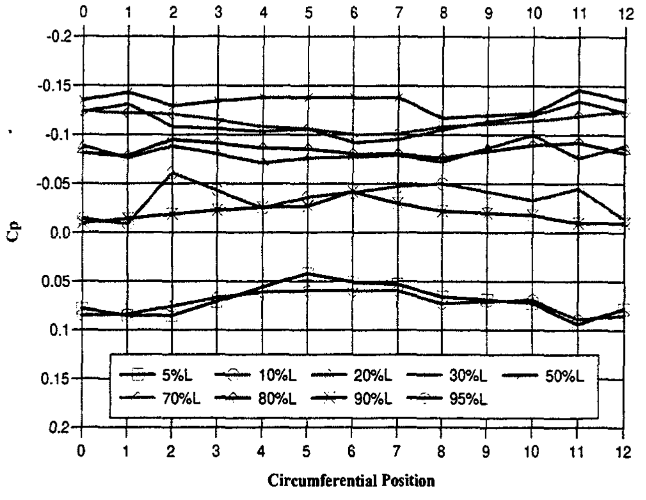

Figure 17b: S/L=0.37, 40m/s, with transition strip

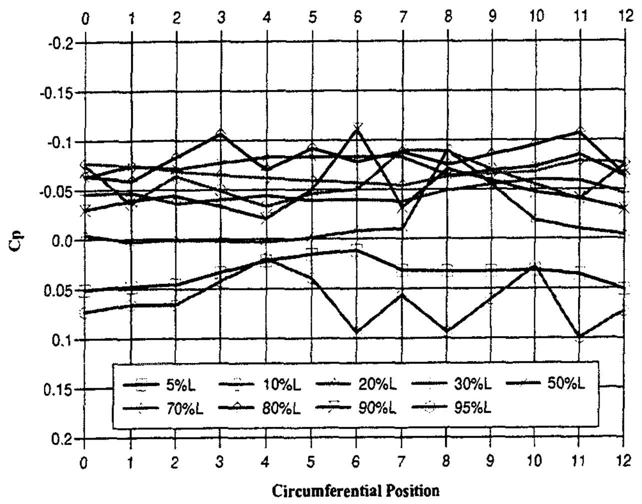

Figure 18a: S/L=0.47, 20m/s, without transition strip

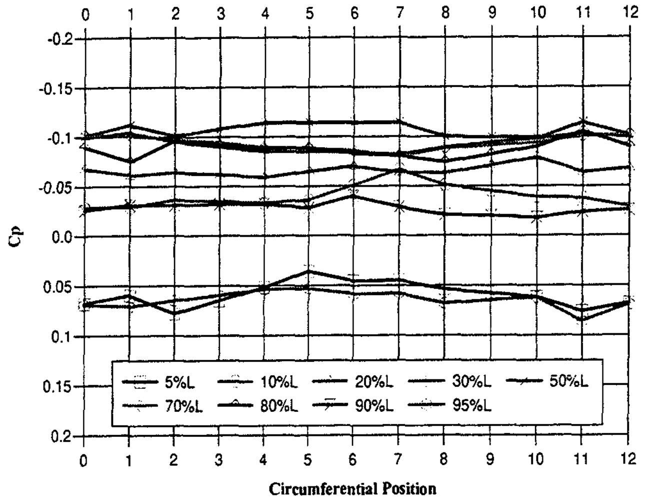

Figure 18b: S/L=0.47, 20m/s, with transition strip

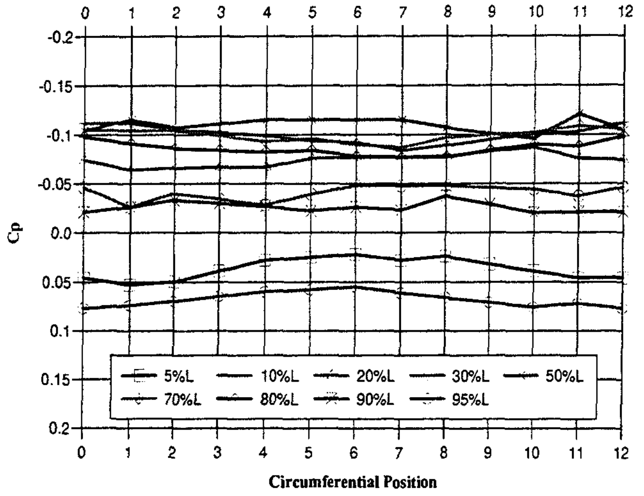

Figure 19a: S/L=0.47, 30m/s, without transition strip

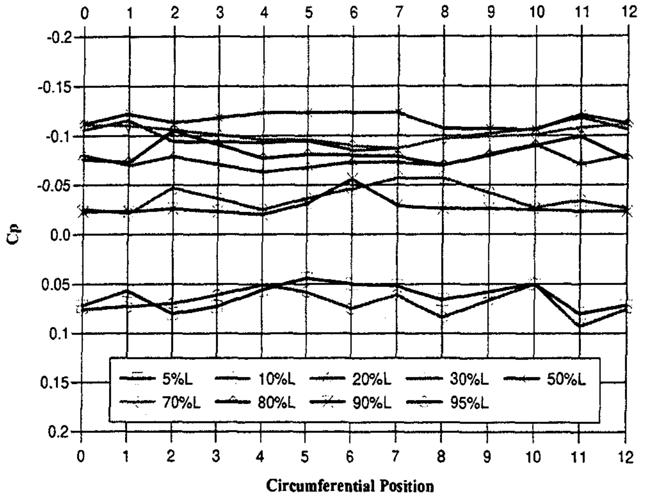

Figure 19b: S/L=0.47, 30m/s, with transition strip

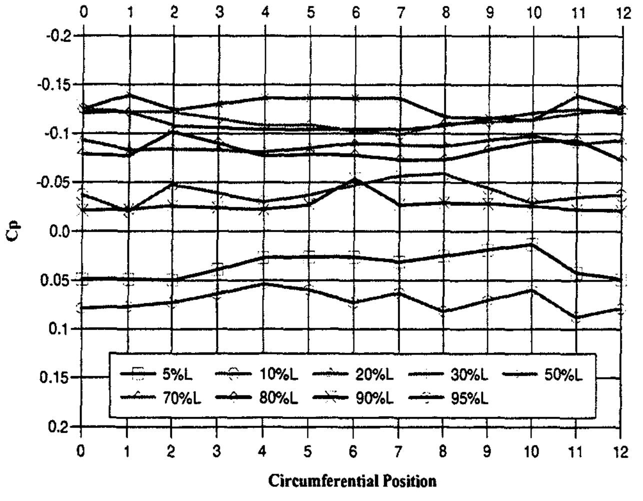

Figure 20a: S/L=0.47, 40m/s, without transition strip

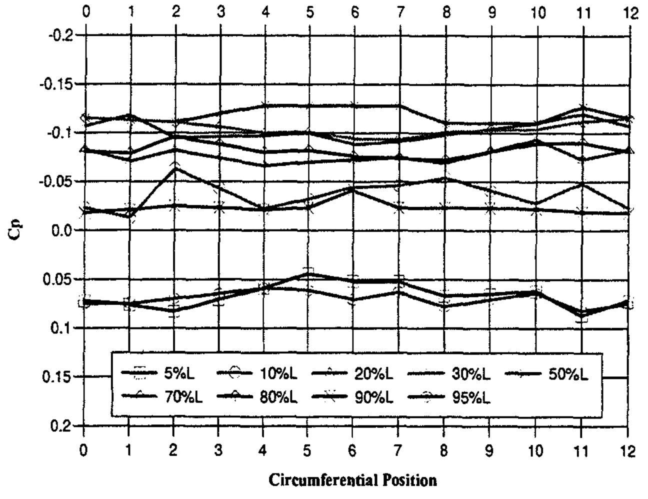

Figure 20b: S/L=0.47, 40m/s, with transition strip

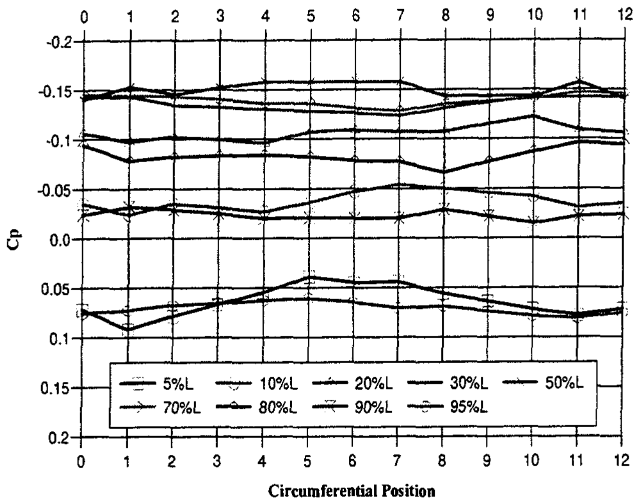

Figure 21a: S/L=0.57, 20m/s, with transition strip

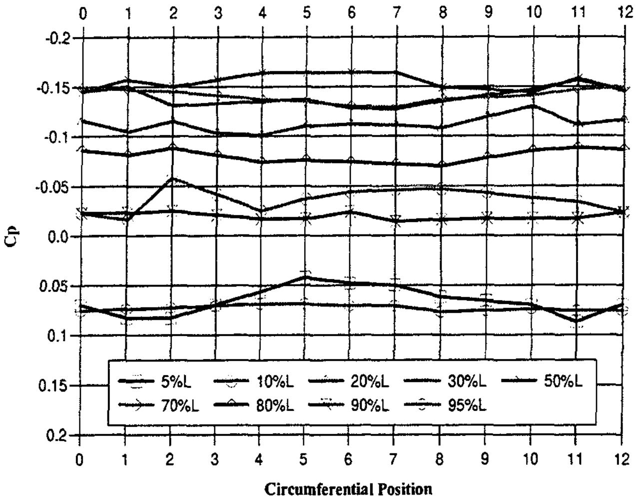

Figure 21b: S/L=0.57, 30m/s, with transition strip

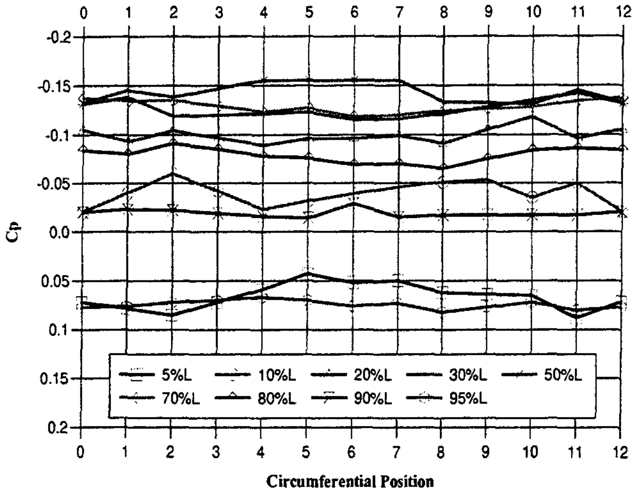

Figure 21c: S/L=0.57, 40m/s, with transition strip

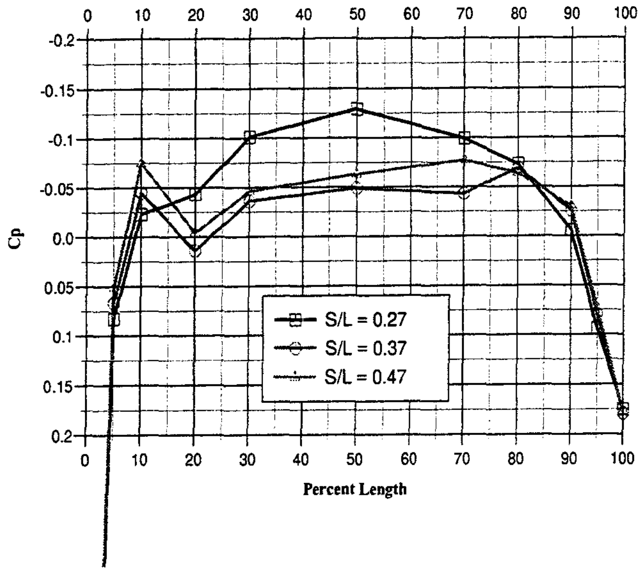

Figure 22a: Position 0, 20m/s, without transition strip

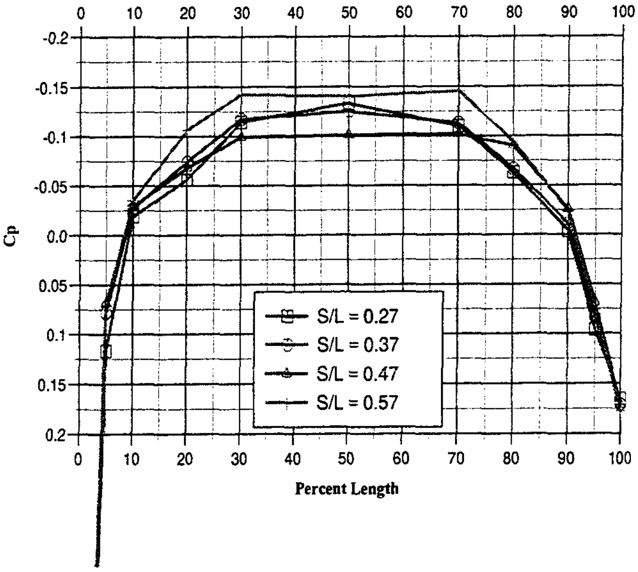

Figure 22b: Position 0, 20m/s, with transition strip

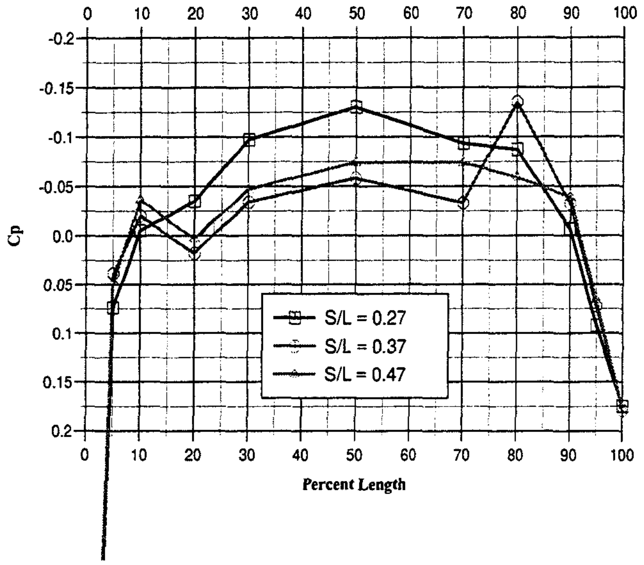

Figure 23a: Position 1, 20m/s, without transition strip

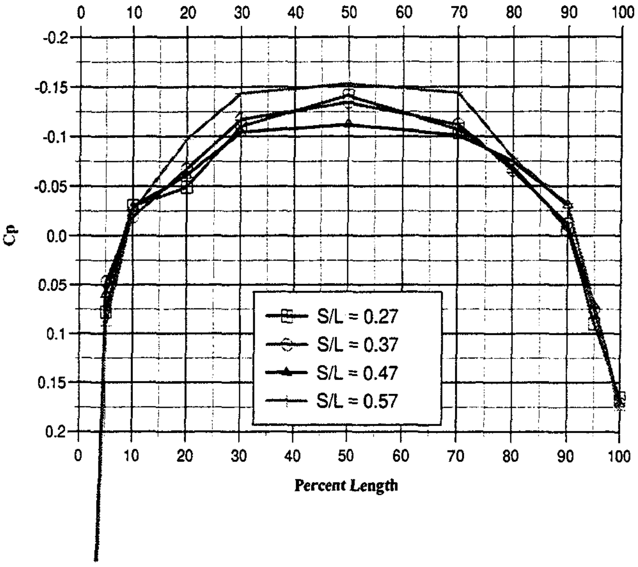

Figure 23b: Position 1, 20m/s, with transition strip

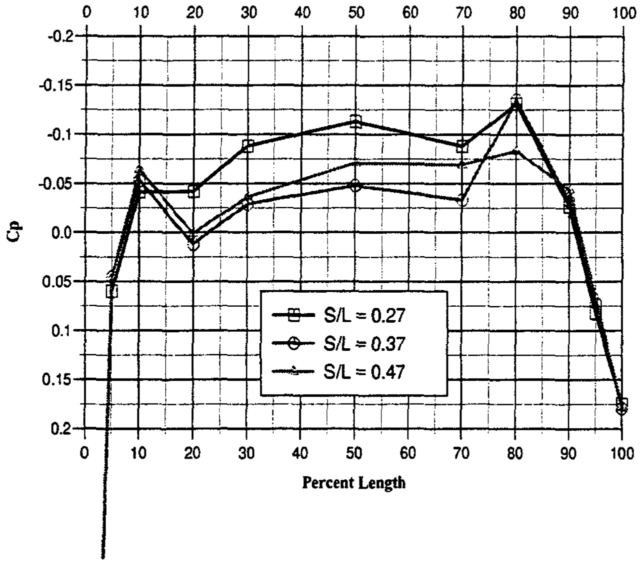

Figure 24a: Position 2, 20m/s, without transition strip

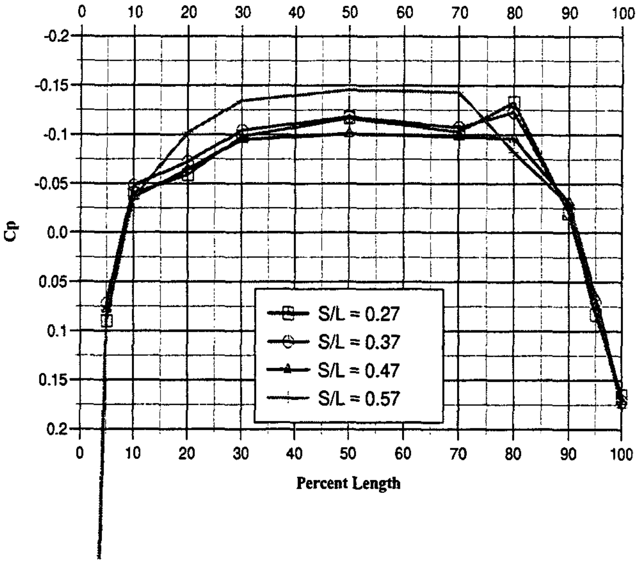

Figure 24b: Position 2, 20m/s, with transition strip

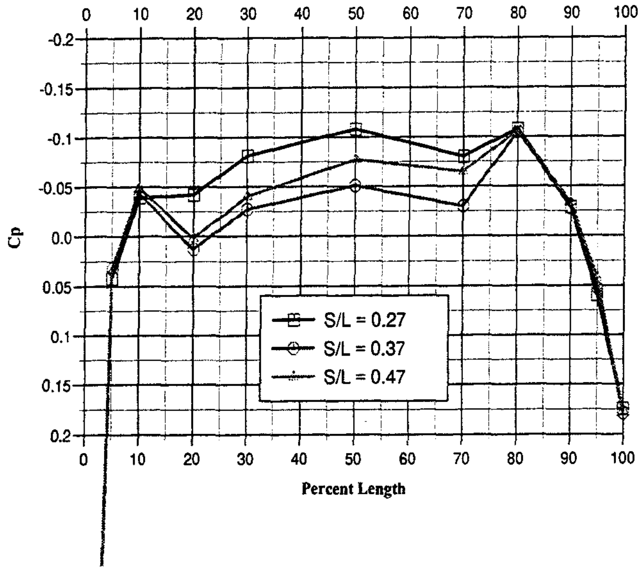

Figure 25a: Position 3, 20m/s, without transition strip

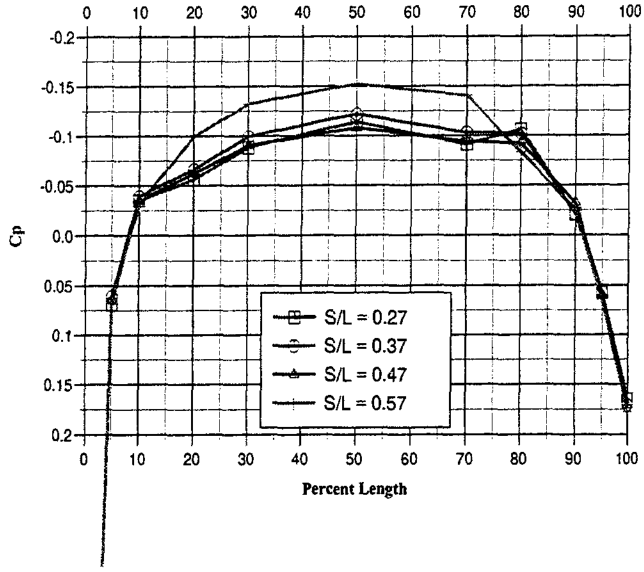

Figure 25b: Position 3, 20m/s, with transition strip

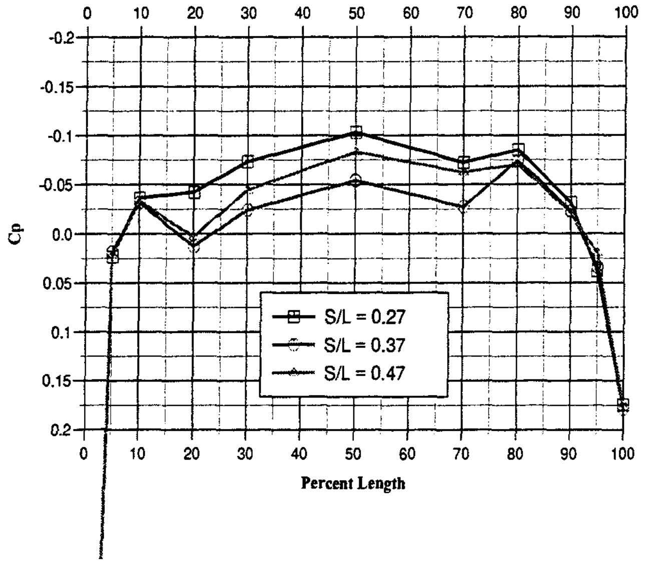

Figure 26a: Position 4, 20m/s, without transition strip

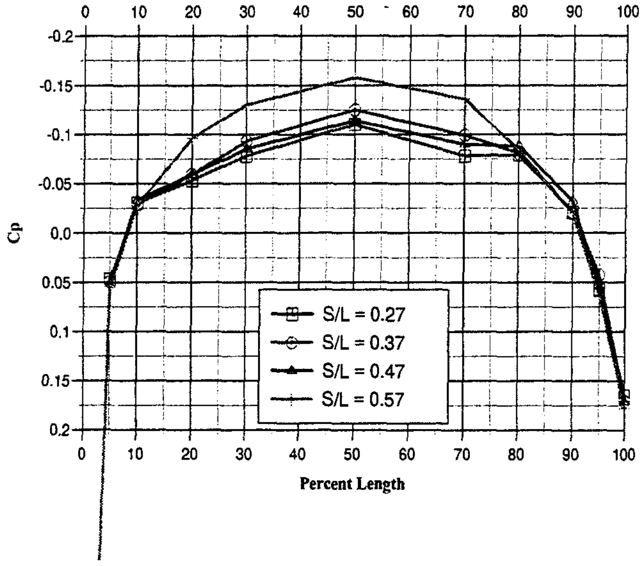

Figure 26b: Position 4, 20m/s, with transition strip

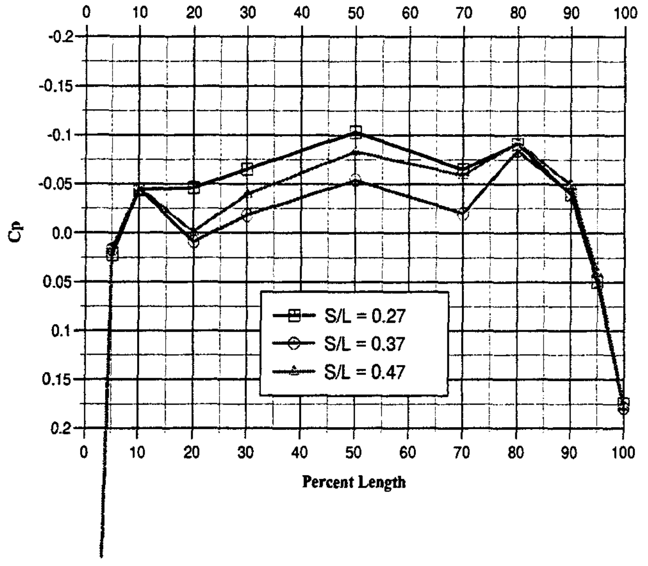

Figure 27a: Position 5, 20m/s, without transition strip

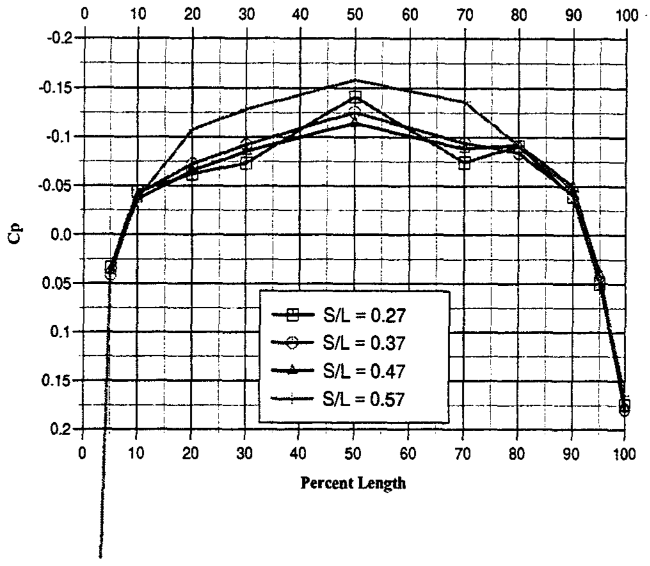

Figure 27b: Position 5, 20m/s, with transition strip

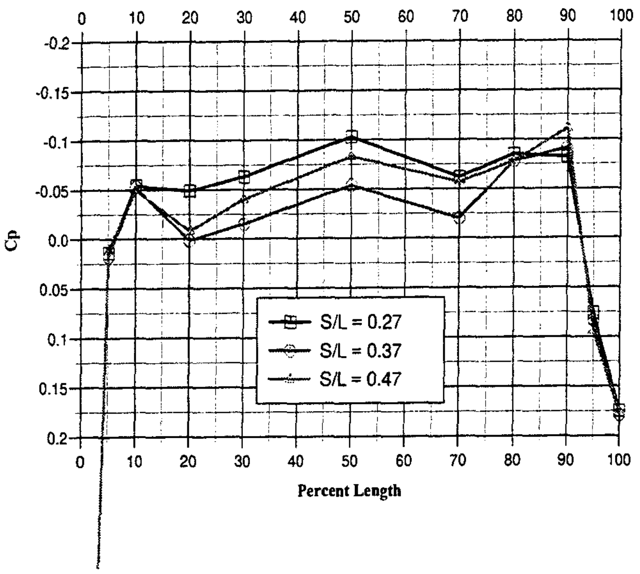

Figure 28a: Position 6, 20m/s, without transition strip

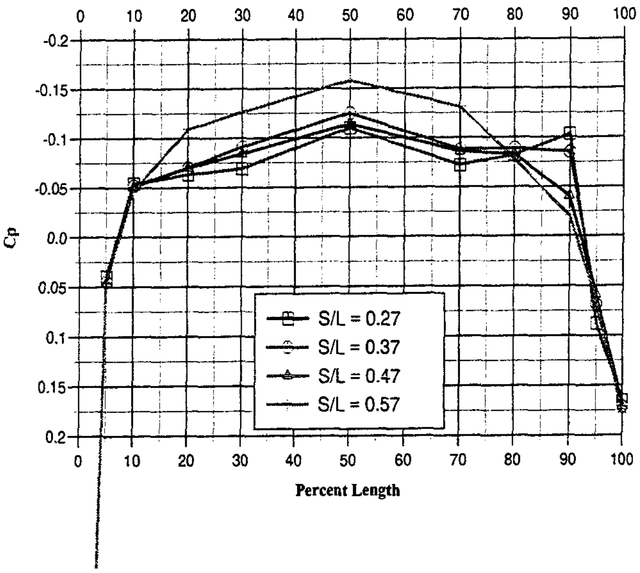

Figure 28b: Position 6, 20m/s, with transition strip

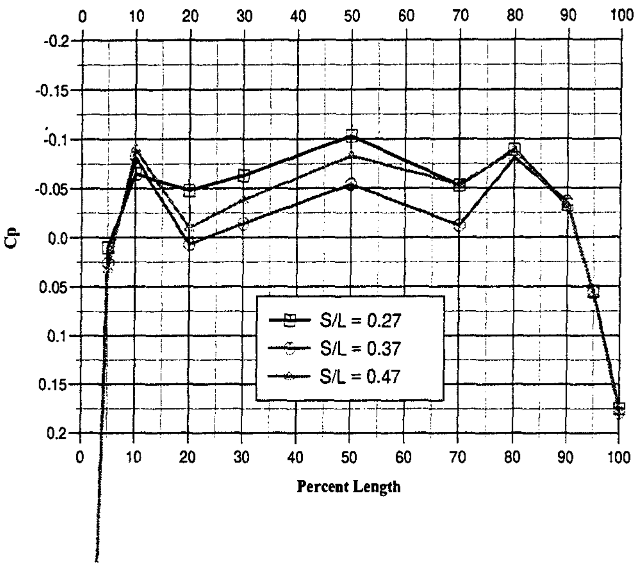

Figure 29a: Position 7, 20m/s, without transition strip

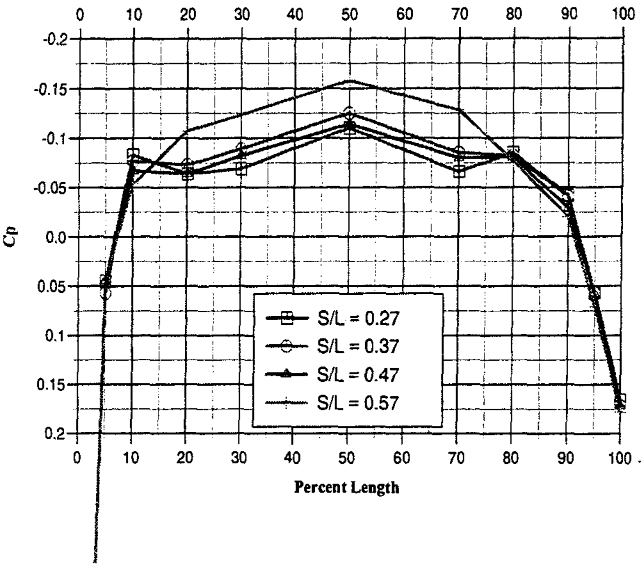

Figure 29b: Position 7, 20m/s, with transition strip

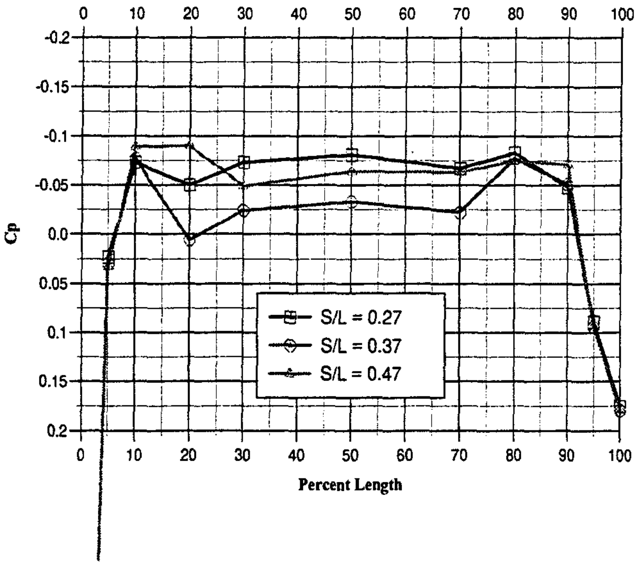

Figure 30a: Position 8, 20m/s, without transition strip

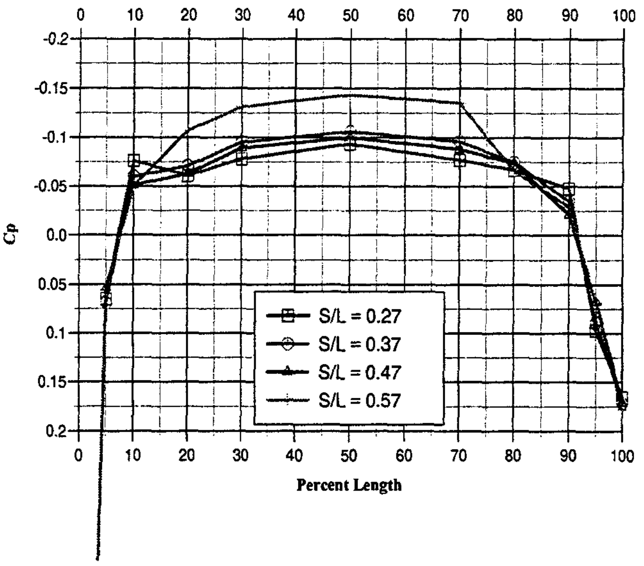

Figure 30b: Position 8, 20m/s, with transition strip

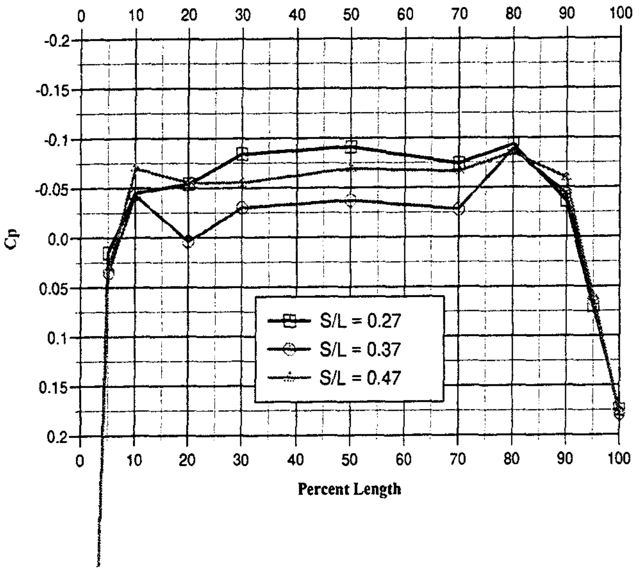

Figure 31a: Position 9, 20m/s, without transition strip

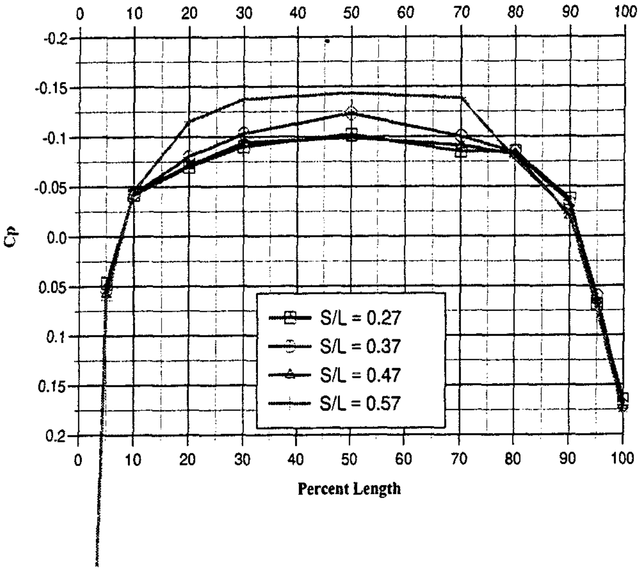

Figure 31b: Position 9, 20m/s, with transition strip

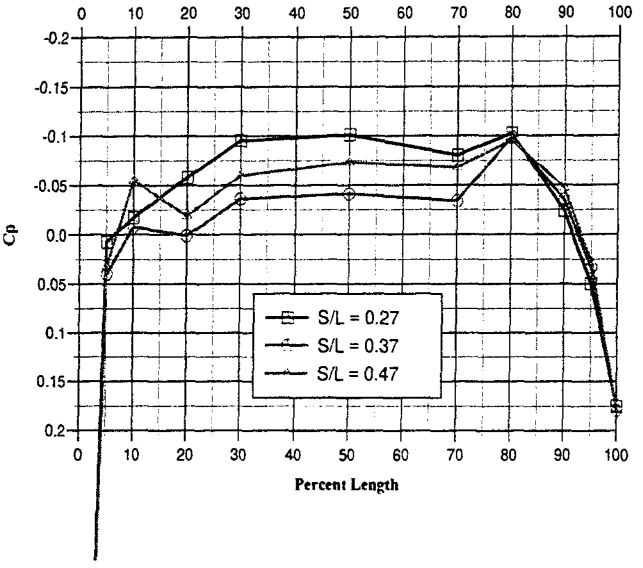

Figure 32a: Position 10, 20m/s, without transition strip

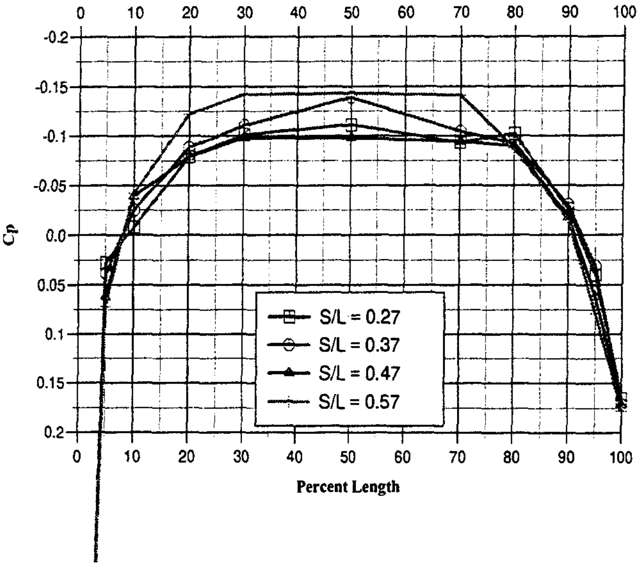

Figure 32b: Position 10, 20m/s, with transition strip

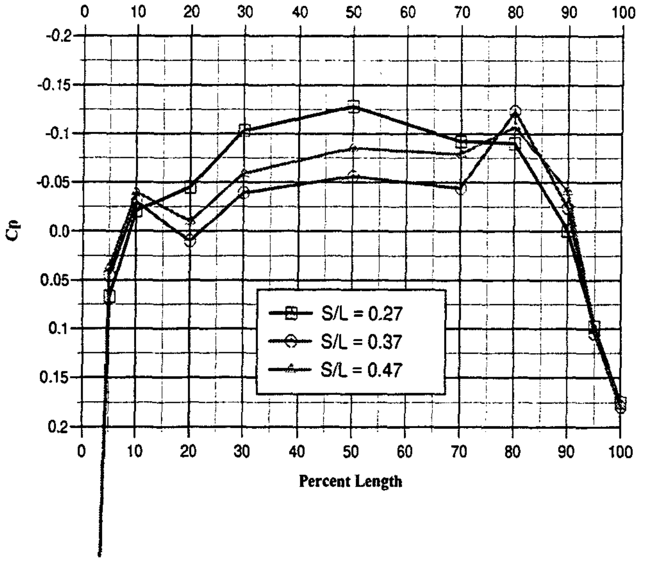

Figure 33a: Position 11, 20m/s, without transition strip

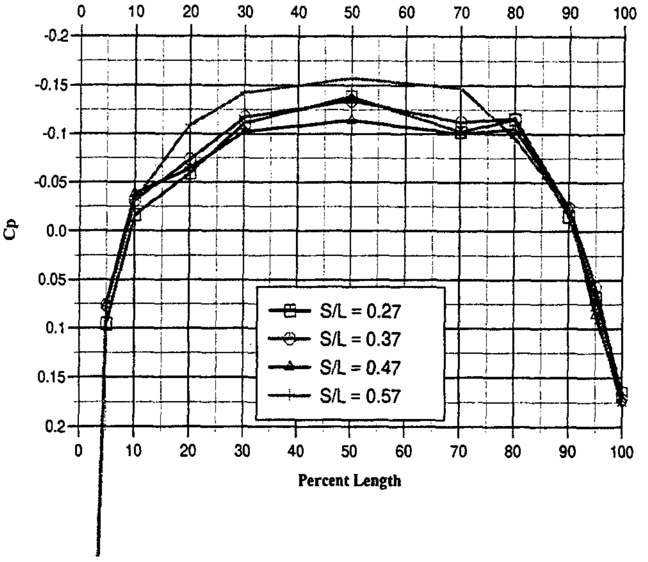

Figure 33b: Position 11, 20m/s, with transition strip

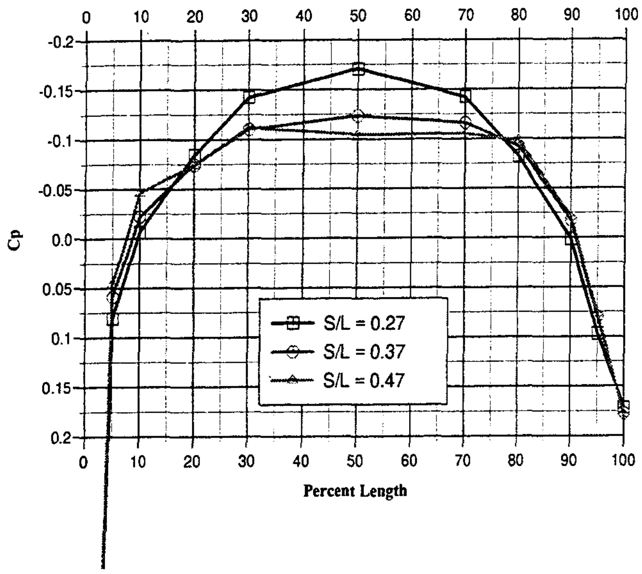

Figure 34a: Position 0, 30m/s, without transition strip

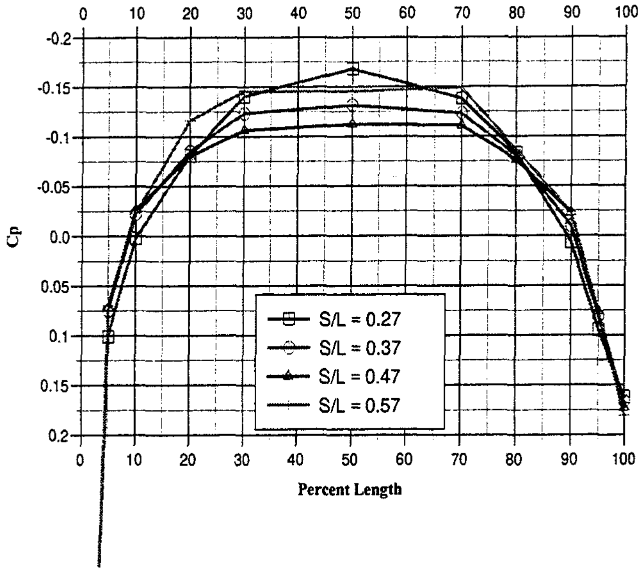

Figure 34b: Position 0, 30m/s, with transition strip

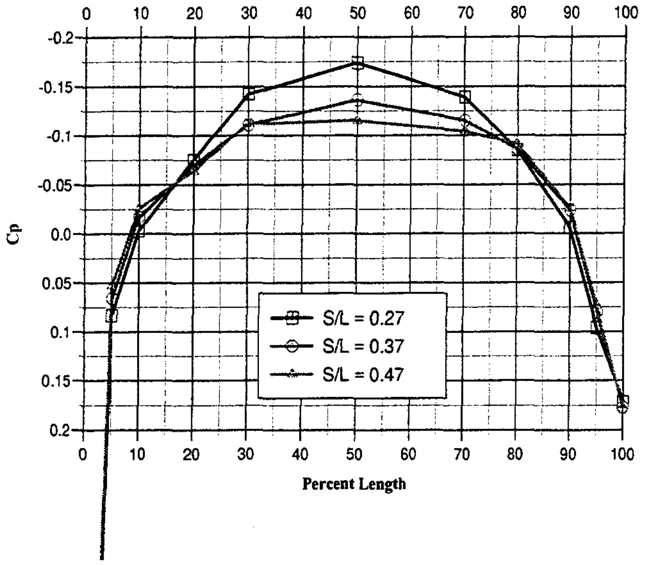

Figure 35a: Position 1, 30m/s, without transition strip

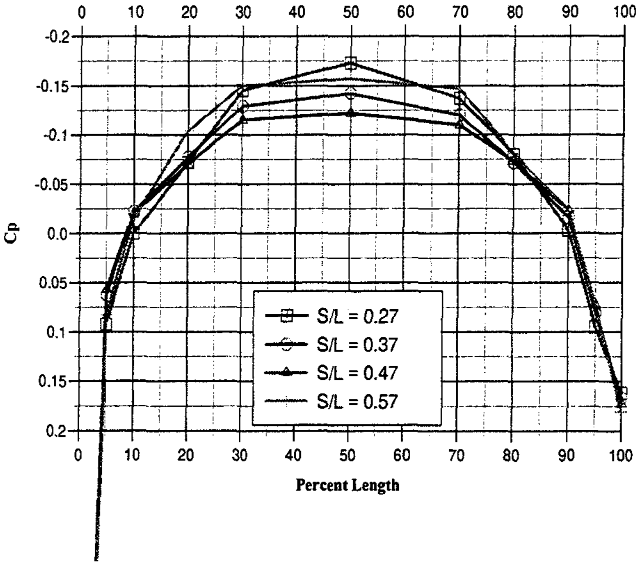

Figure 35b: Position 1, 30m/s, with transition strip

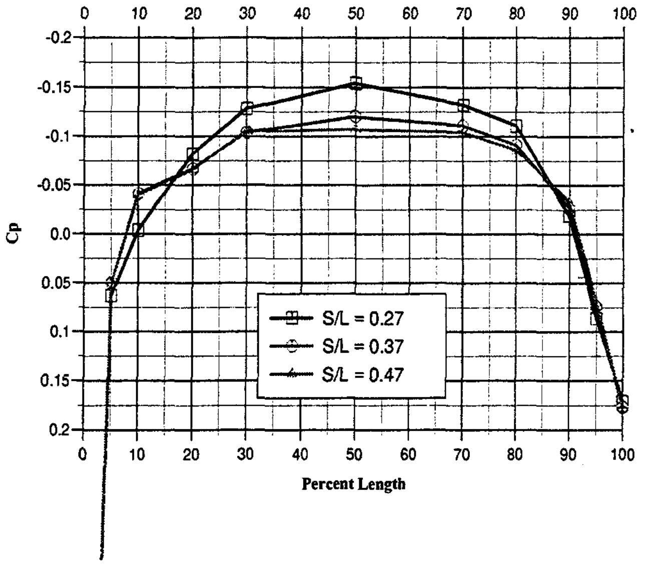

Figure 36a: Position 2, 30m/s, without transition strip

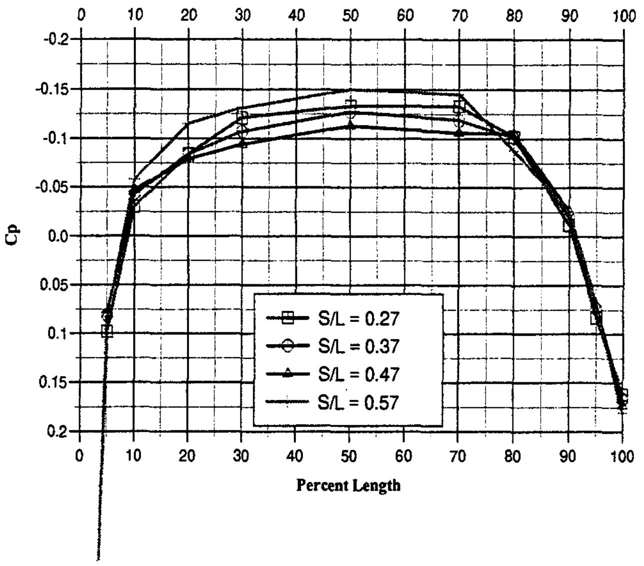

Figure 36b: Position 2, 30m/s, with transition strip

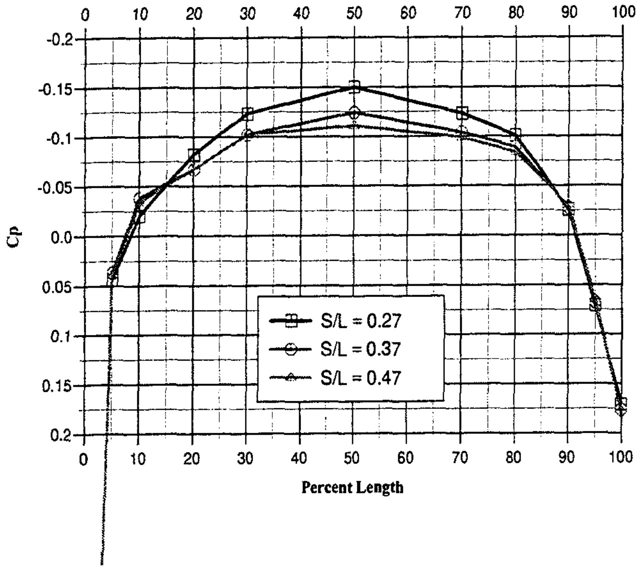

Figure 37a: Position 3, 30m/s, without transition strip

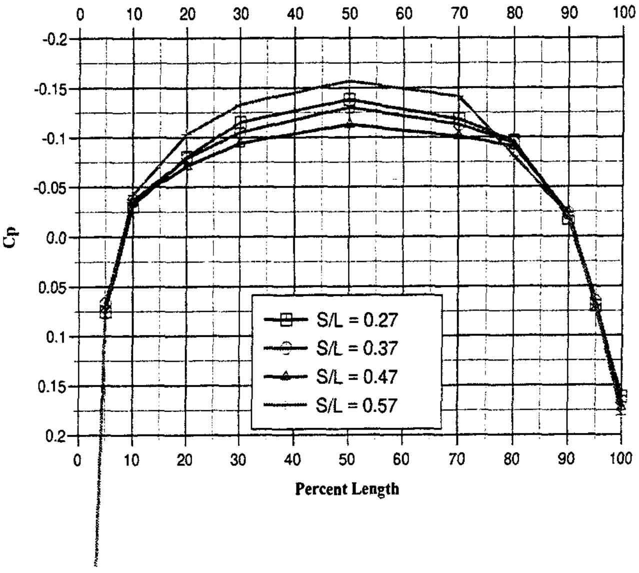

Figure 37b: Position 3, 30m/s, with transition strip

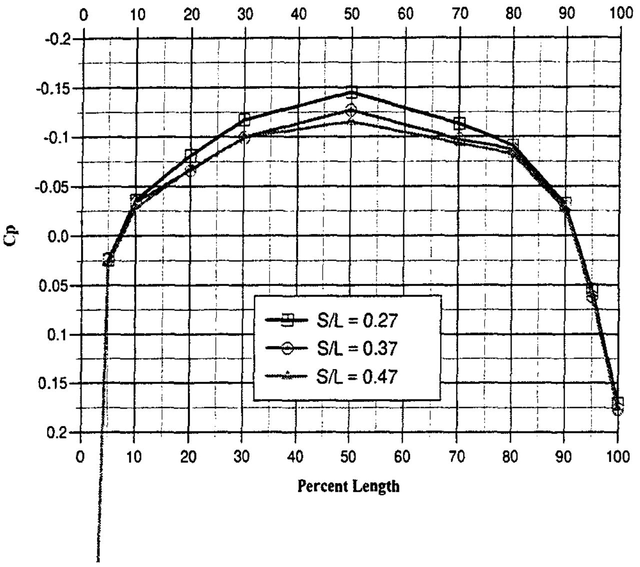

Figure 38a: Position 4, 30m/s, without transition strip

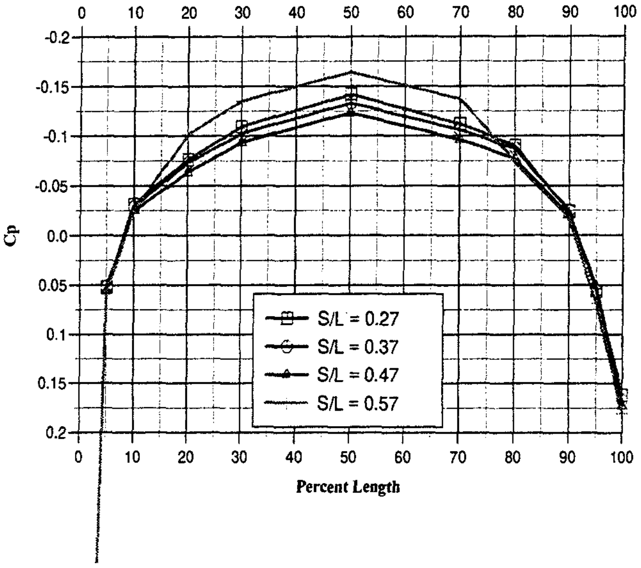

Figure 38b: Position 4, 30m/s, with transition strip

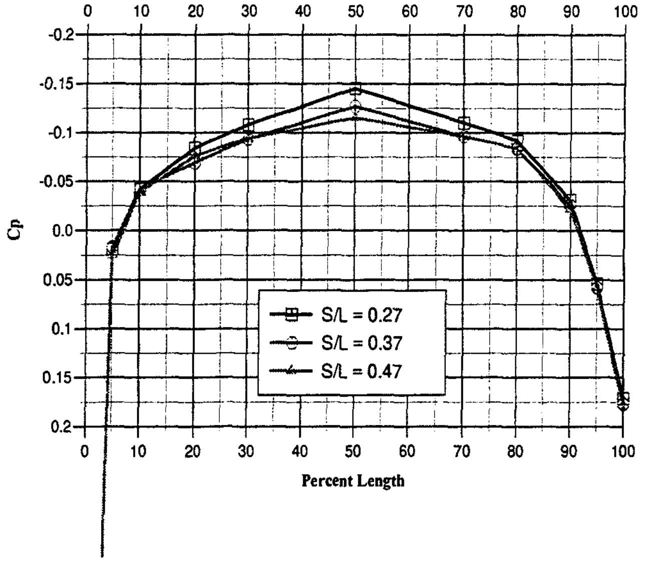

Figure 39a: Position 5, 30m/s, without transition strip

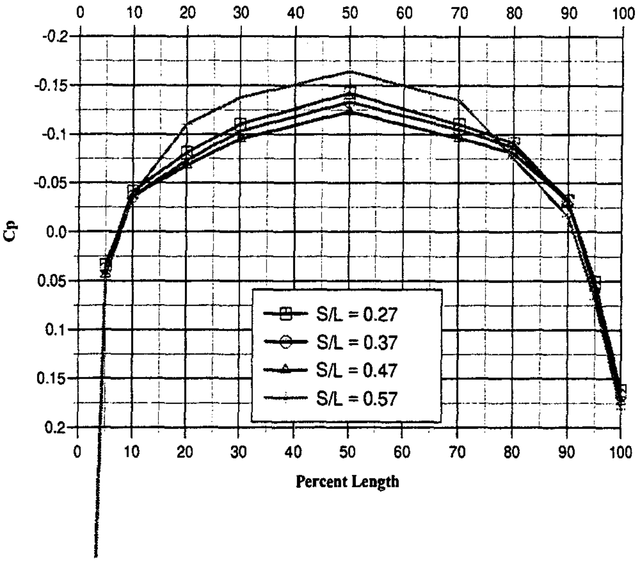

Figure 39b: Position 5, 30m/s, with transition strip

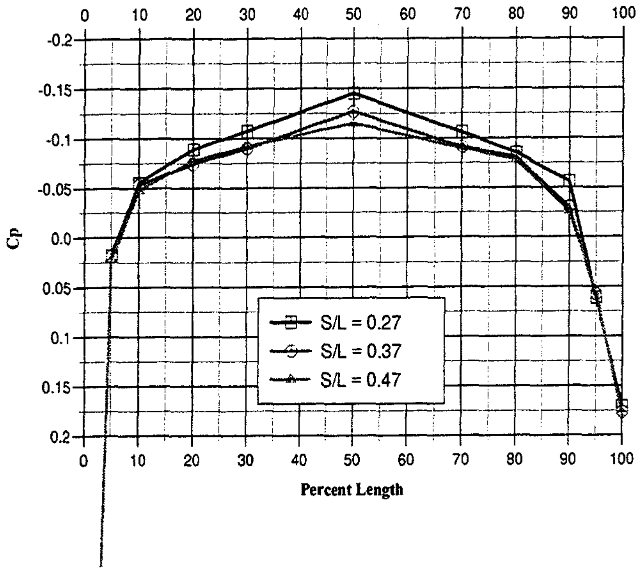

Figure 40a: Position 6, 30m/s, without transition strip

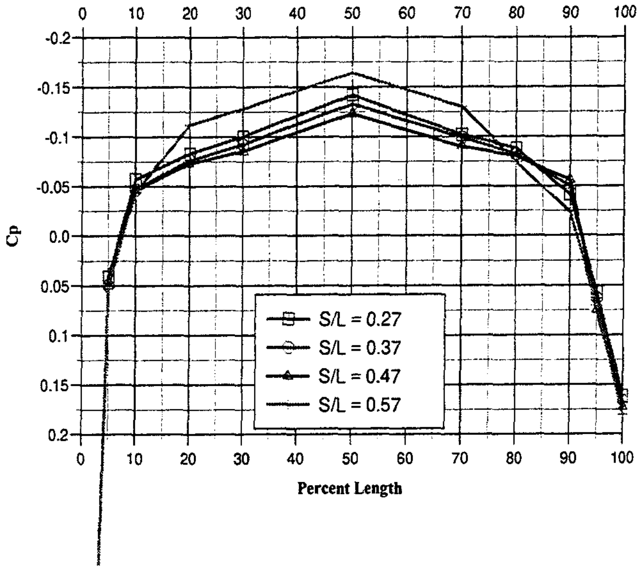

Figure 40b: Position 6, 30m/s, with transition strip

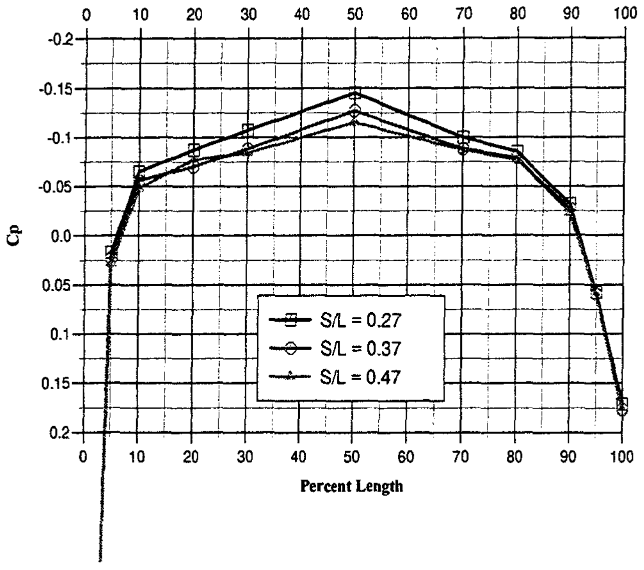

Figure 41a: Position 7, 30m/s, without transition strip

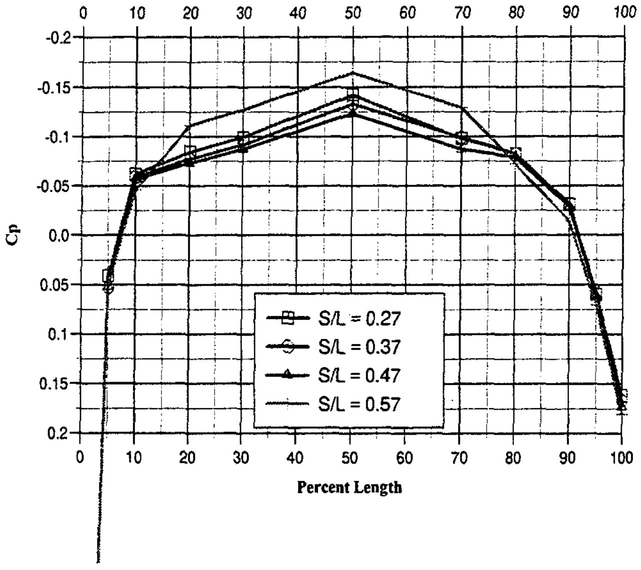

Figure 41b: Position 7, 30m/s, with transition strip

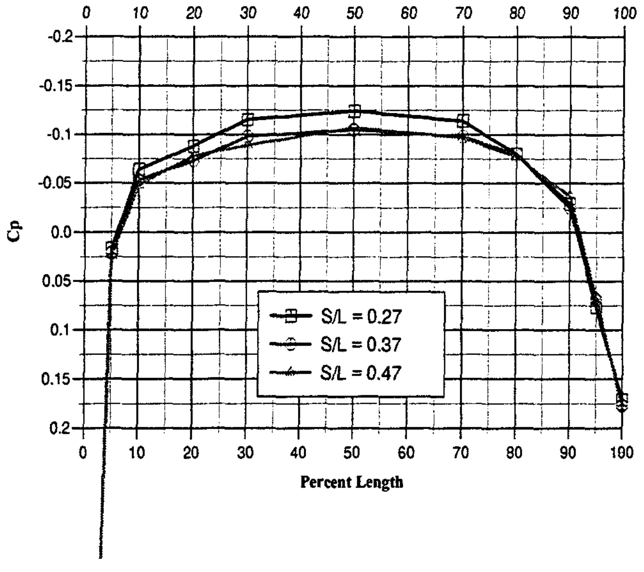

Figure 42a: Position 8, 30m/s, without transition strip

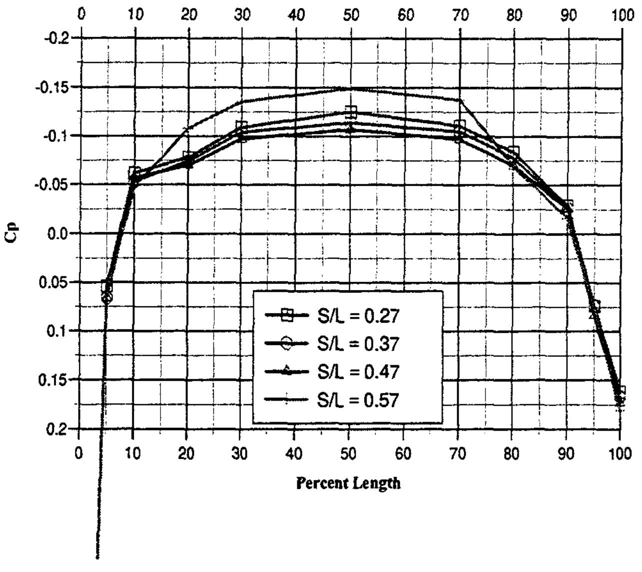

Figure 42b: Position 8, 30m/s, with transition strip

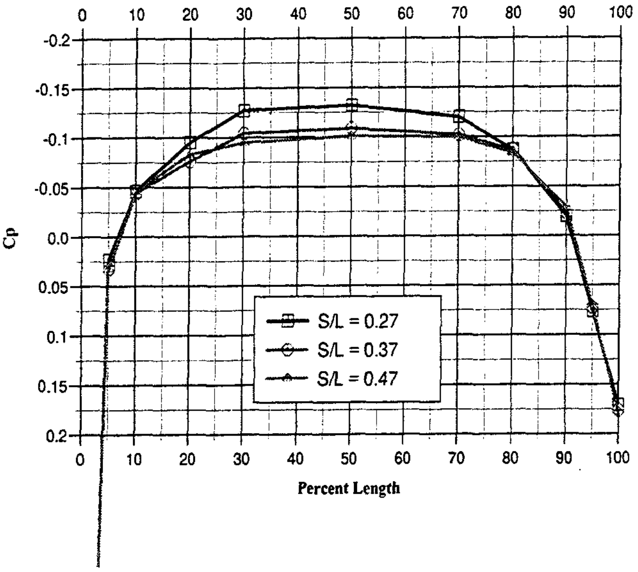

Figure 43a: Position 9, 30m/s, without transition strip

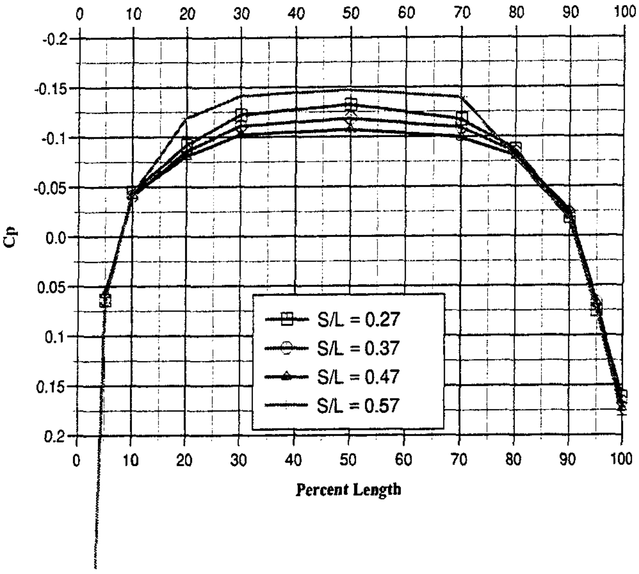

Figure 43b: Position 9, 30m/s, with transition strip

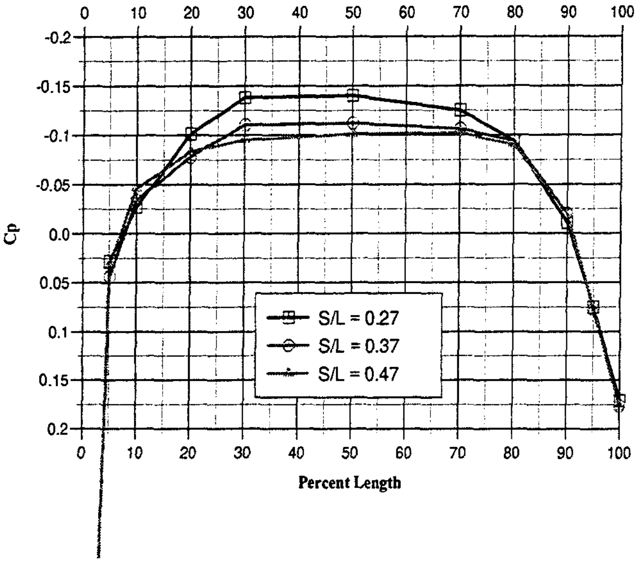

Figure 44a: Position 10, 30m/s, without transition strip

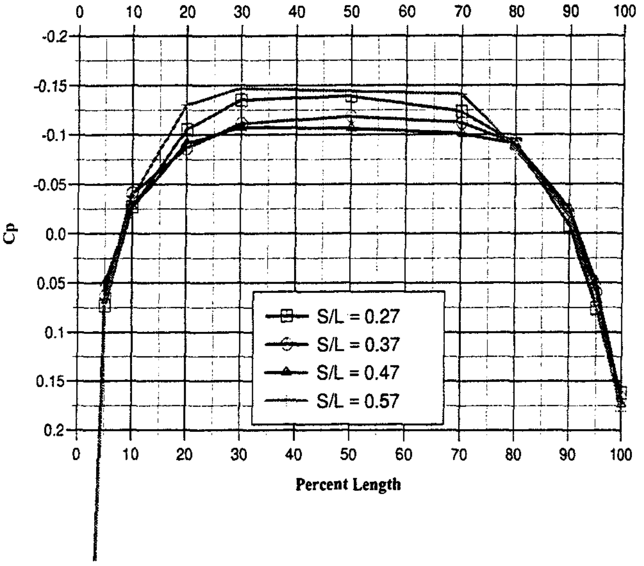

Figure 44b: Position 10, 30m/s, with transition strip

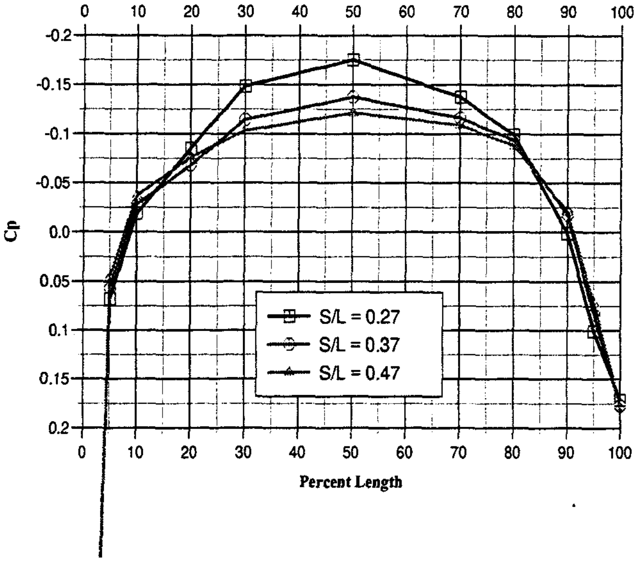

Figure 45a: Position 11, 30m/s, without transition strip

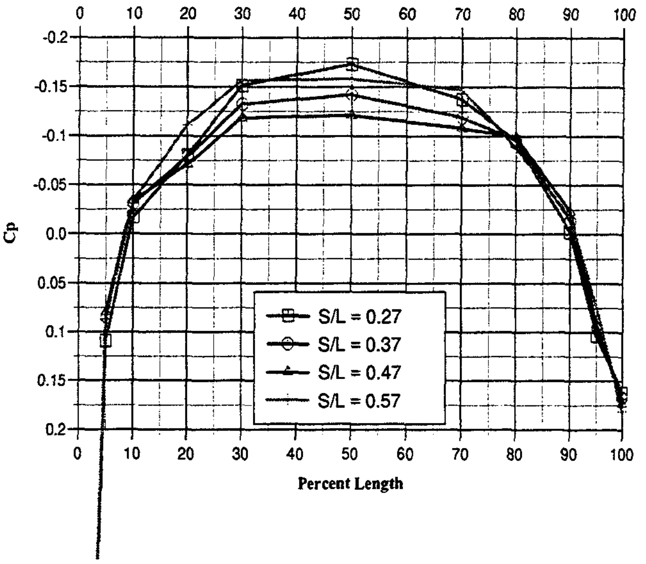

Figure 45b: Position 11, 30m/s, with transition strip

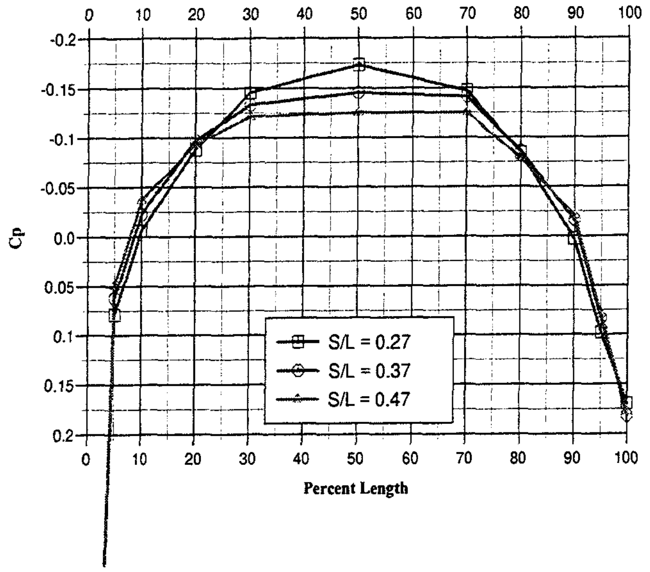

Figure 46a: Position 0, 40m/s, without transition strip

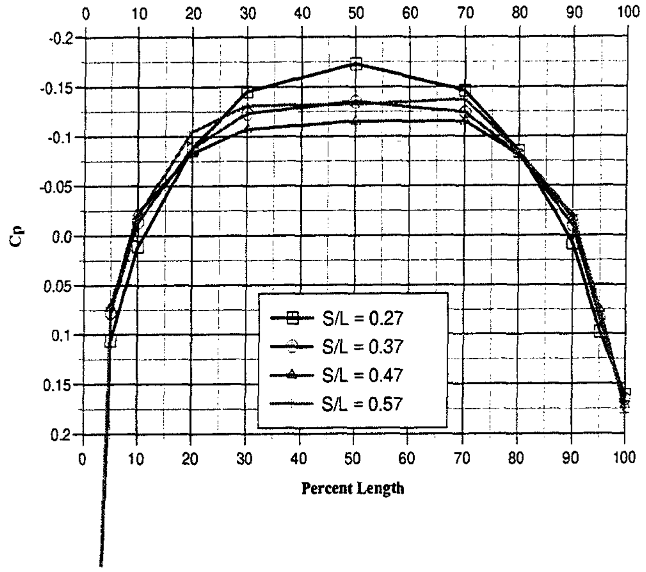

Figure 46b: Position 0, 40m/s, with transition strip

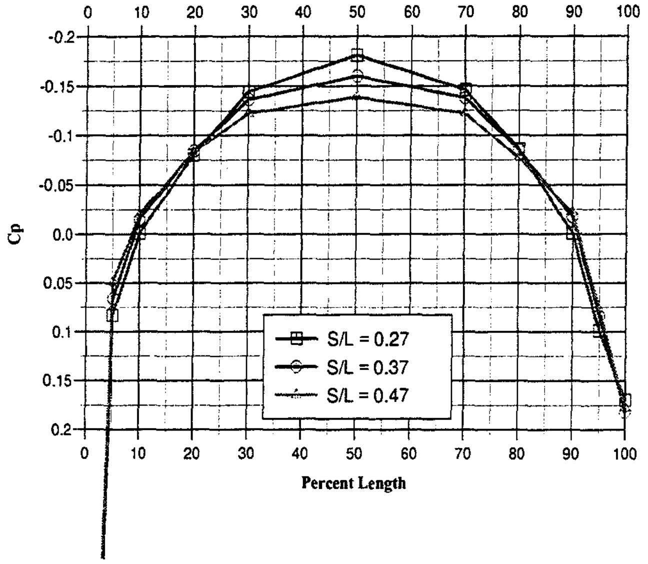

Figure 47a: Position 1, 40m/s, without transition strip

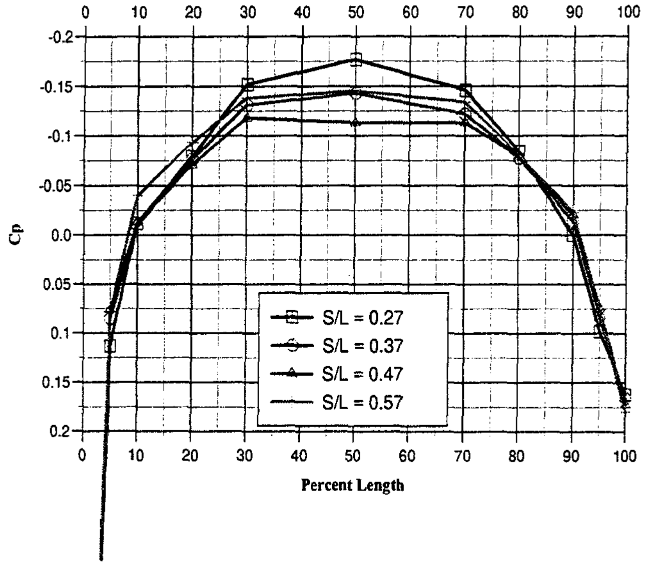

Figure 47b: Position 1, 40m/s, with transition strip

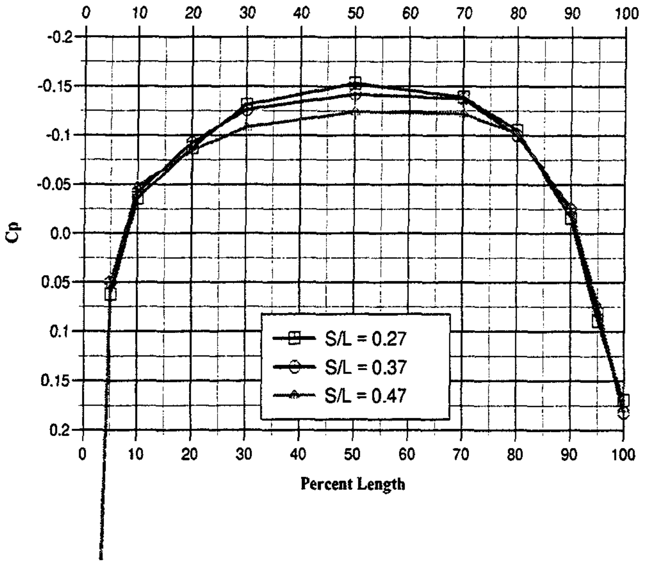

Figure 48a: Position 2, 40m/s, without transition strip

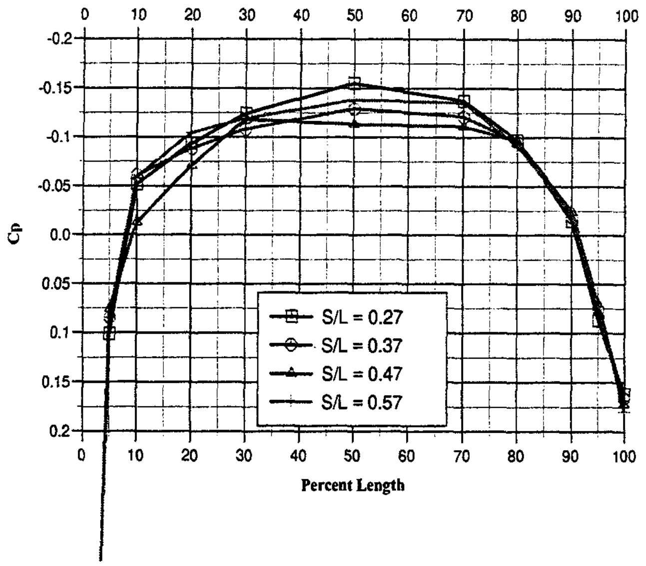

Figure 48b: Position 2, 40m/s, with transition strip

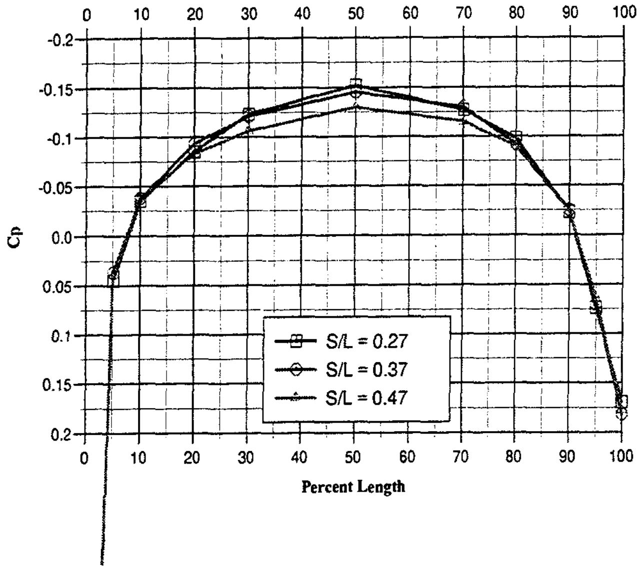

Figure 49a: Position 3, 40m/s, without transition strip

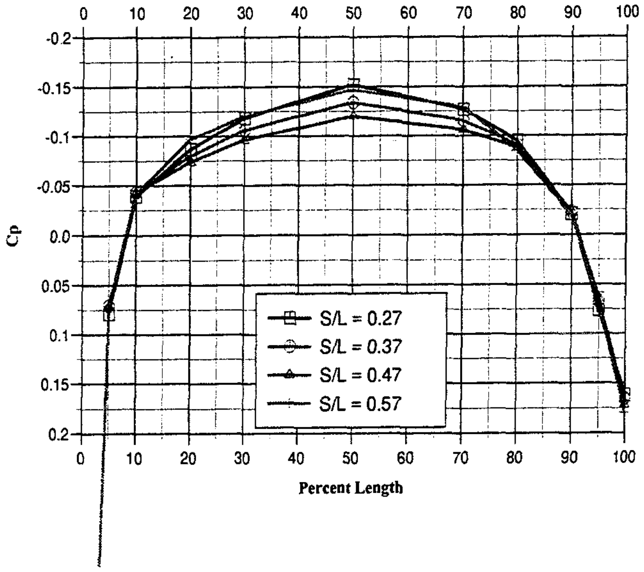

Figure 49b: Position 3, 40m/s, with transition strip

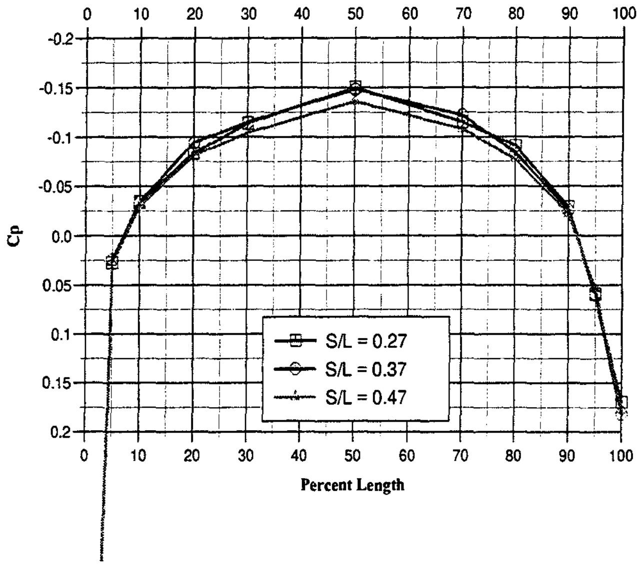

Figure 50a: Position 4, 40m/s, without transition strip

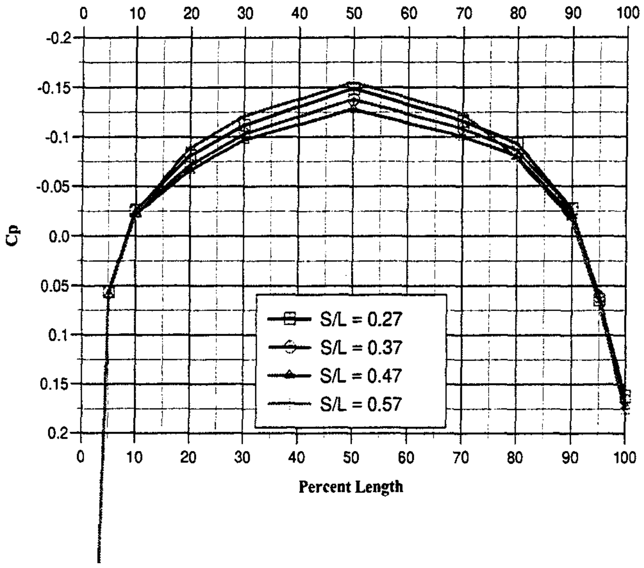

Figure 50b: Position 4, 40m/s, with transition strip

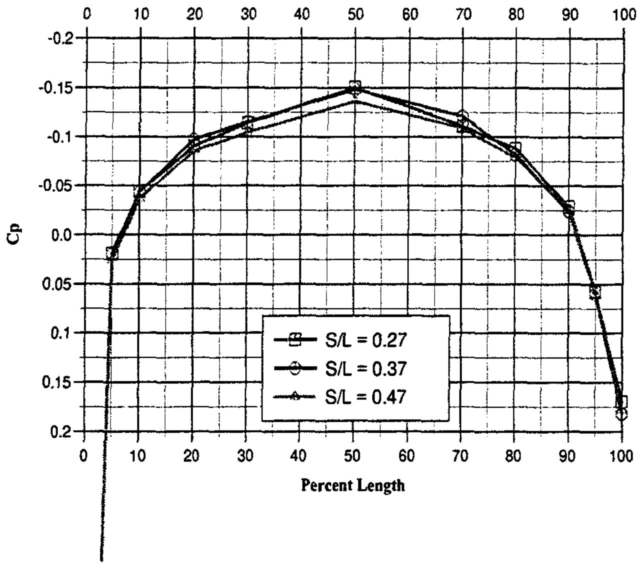

Figure 51a: Position 5, 40m/s, without transition strip

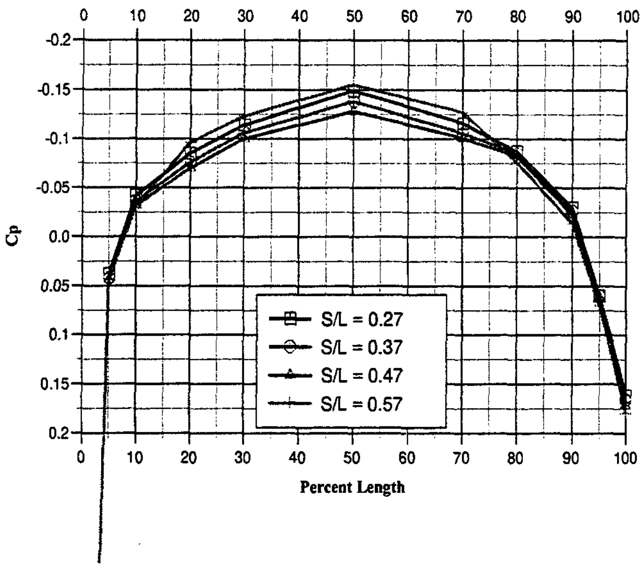

Figure 51b: Position 5, 40m/s, with transition strip

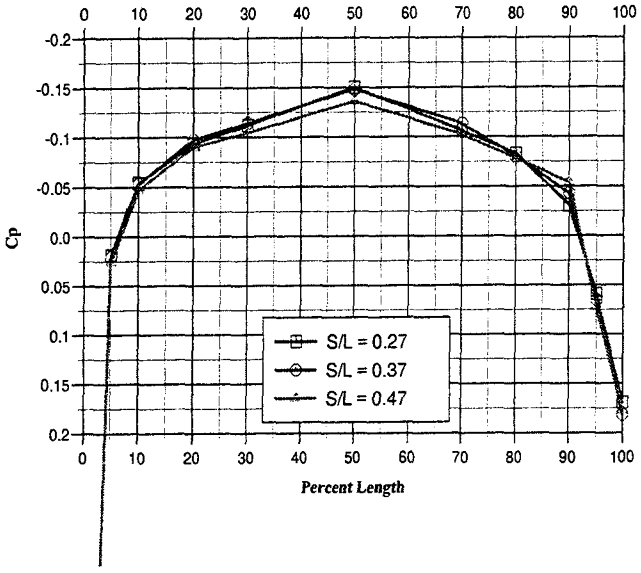

Figure 52a: Position 6, 40m/s, without transition strip

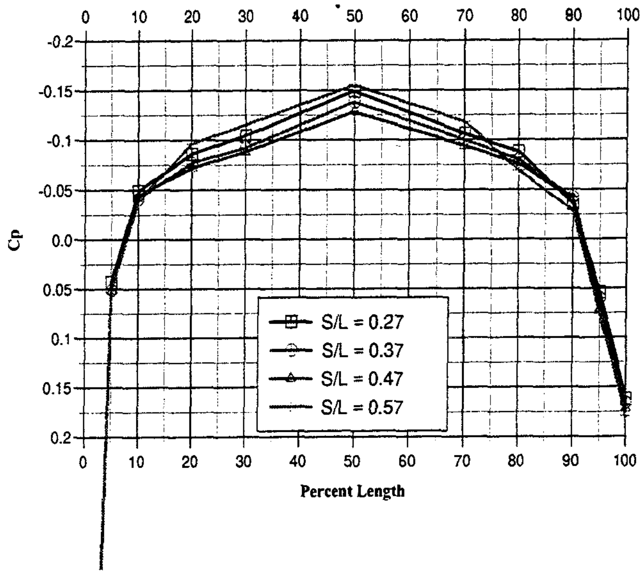

Figure 52b: Position 6, 40m/s, with transition strip

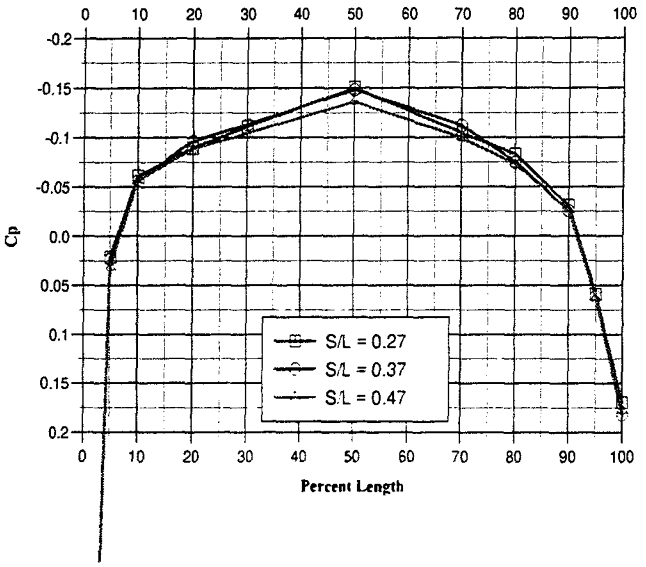

Figure 53a: Position 7, 40m/s, without transition strip

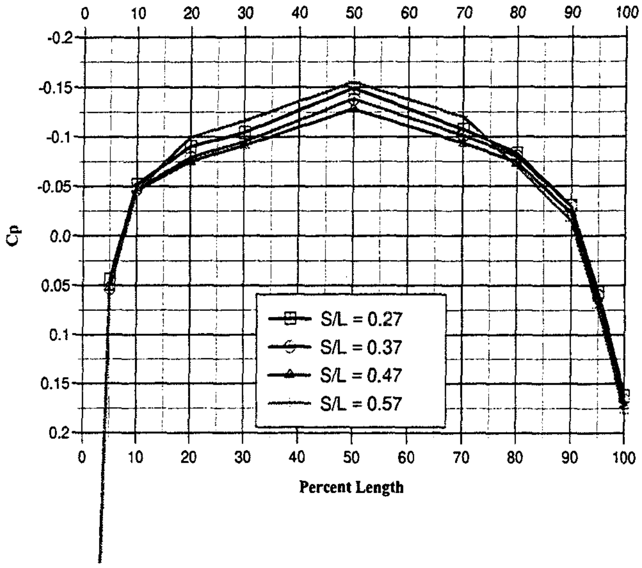

Figure 53b: Position 7, 40m/s, with transition strip

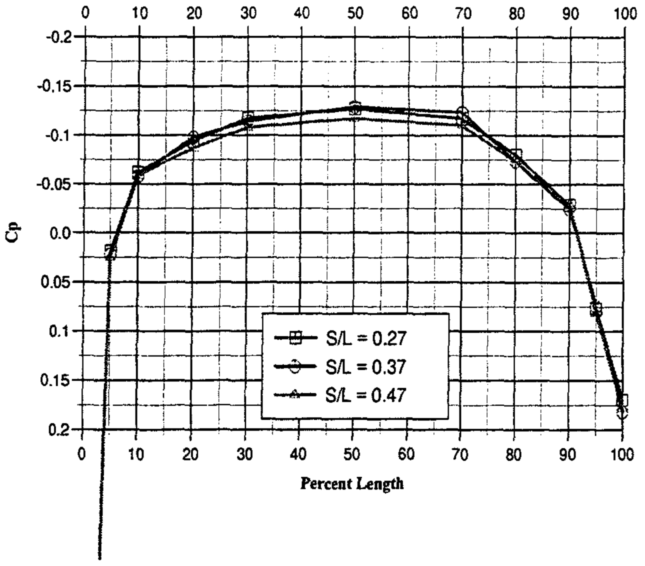

Figure 54a: Position 8, 40m/s, without transition strip

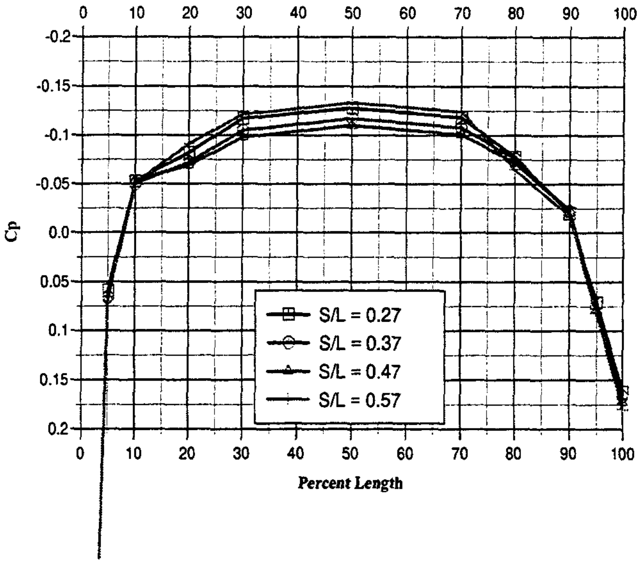

Figure 54b: Position 8, 40m/s, with transition strip

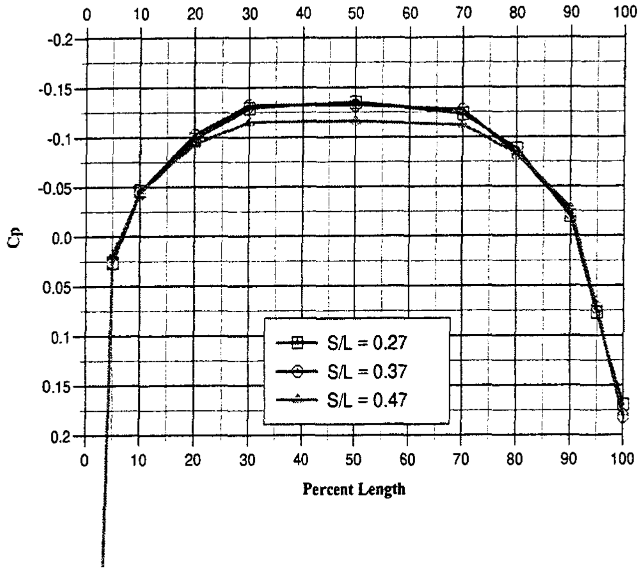

Figure 55a: Position 9, 40m/s, without transition strip

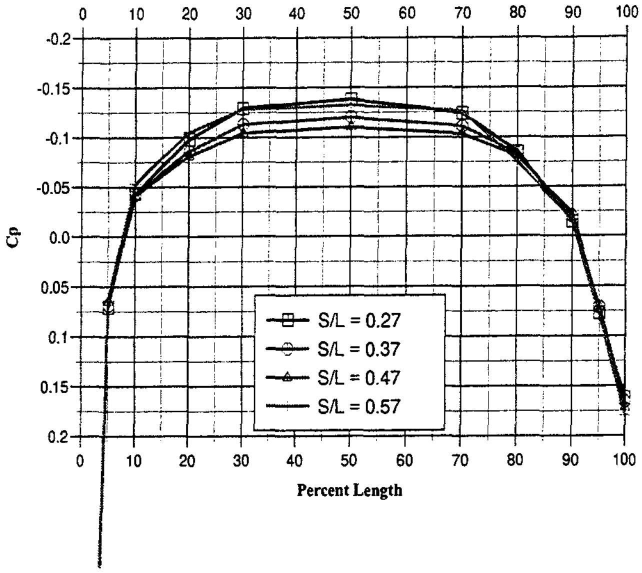

Figure 55b: Position 9, 40m/s, with transition strip

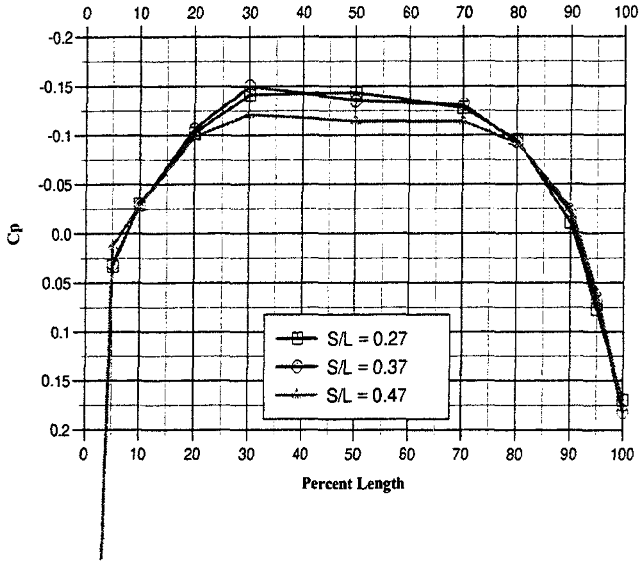

Figure 56a: Position 10, 40m/s, without transition strip

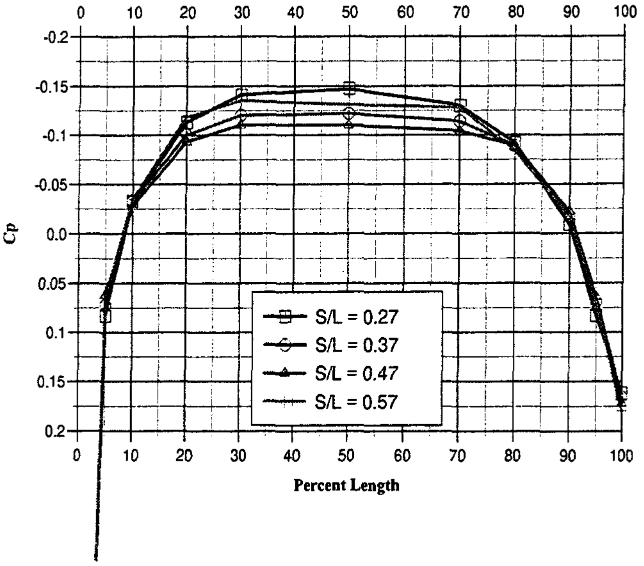

Figure 56b: Position 10, 40m/s, with transition strip

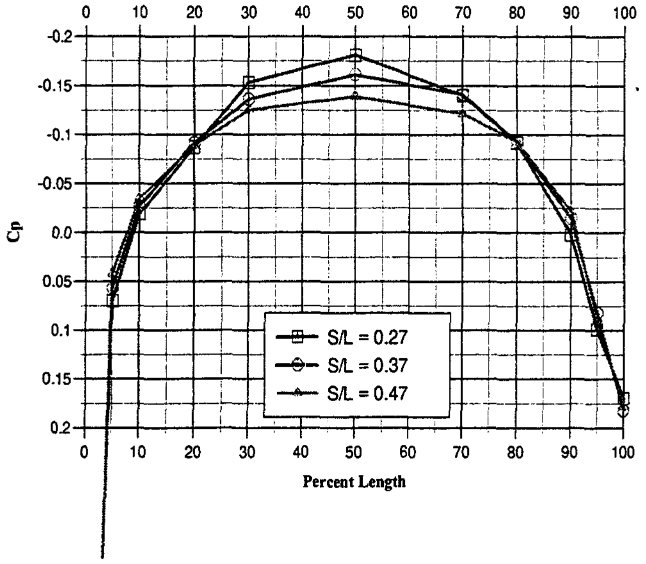

Figure 57a: Position 11, 40m/s, without transition strip

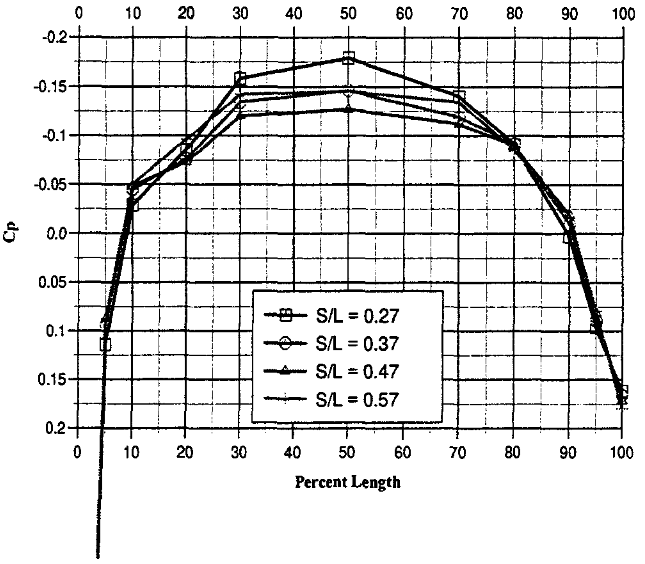

Figure 57b: Position 11, 40m/s, with transition strip

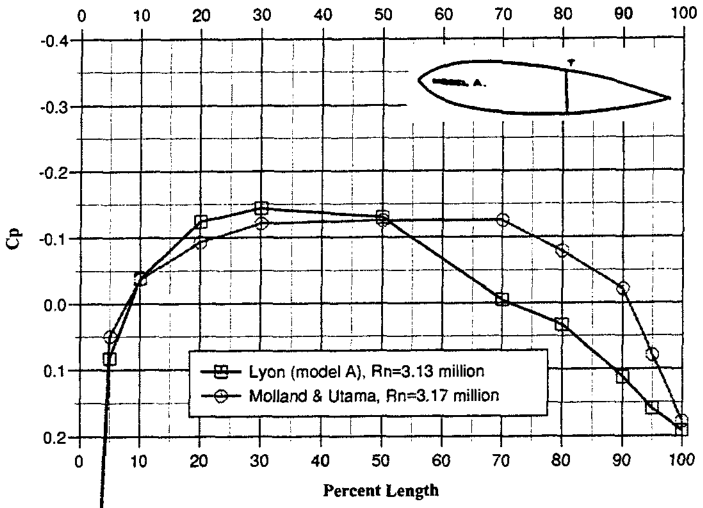

Figure 58a: Lyon Model A vs Molland and Utama

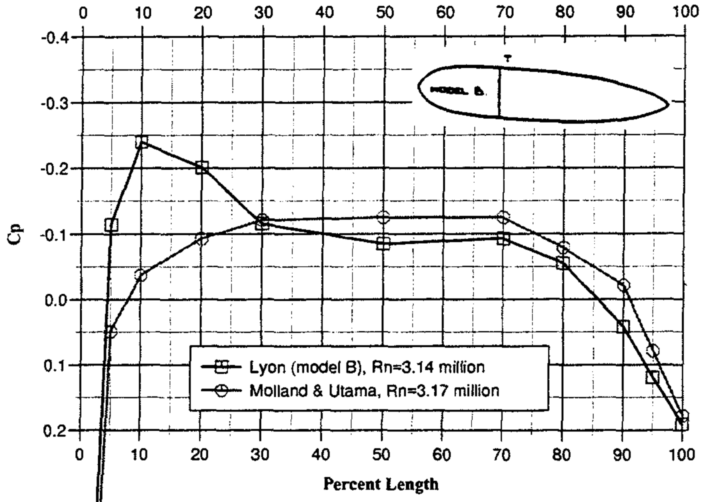

Figure 58b: Lyon Model A vs Molland and Utama

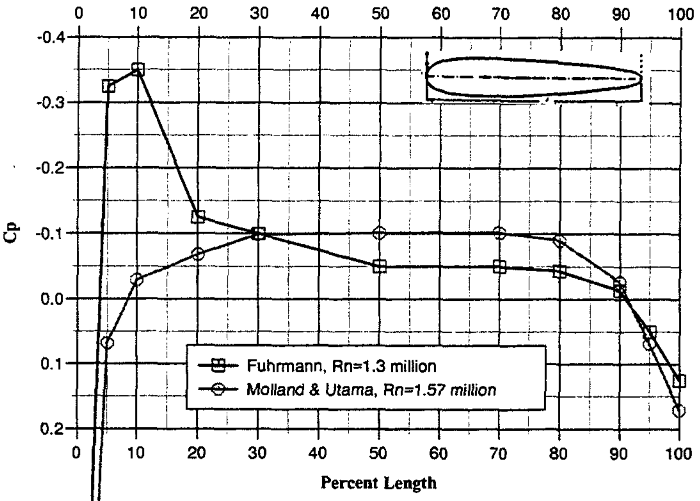

Figure 58c: Fuhrmann vs Molland and Utama

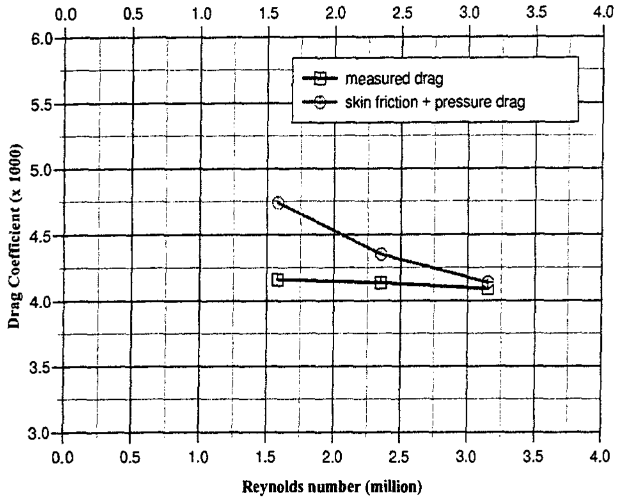

Figure 59a: S/L=0.27, without transition strip

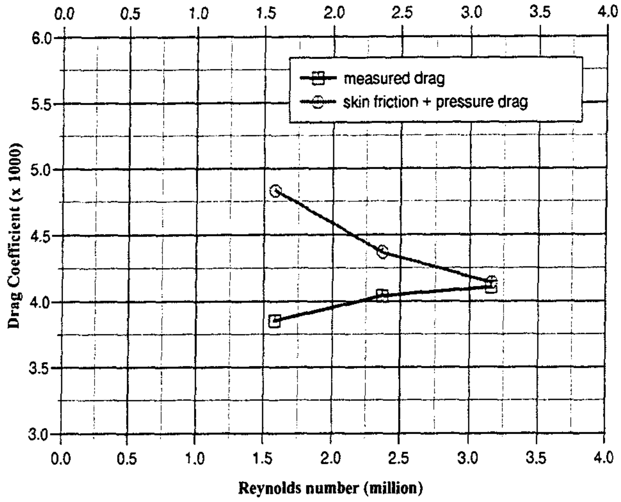

Figure 59b: S/L=0.37, without transition strip

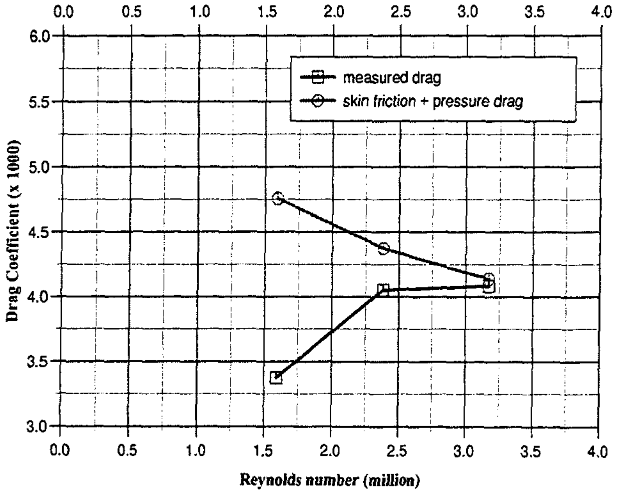

Figure 59c: S/L=0.47, without transition strip

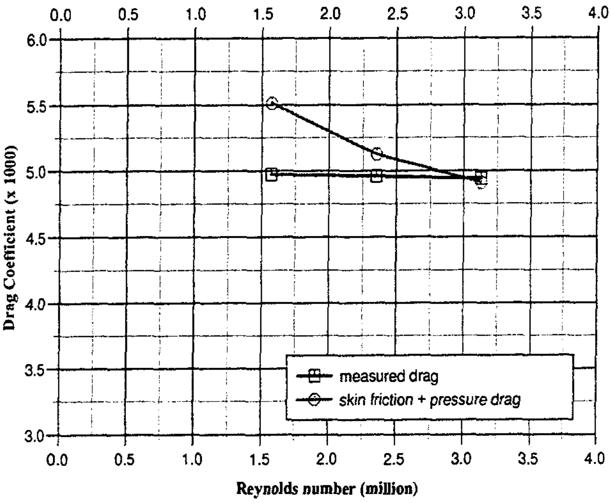

Figure 59d: S/L=0.27, with transition strip

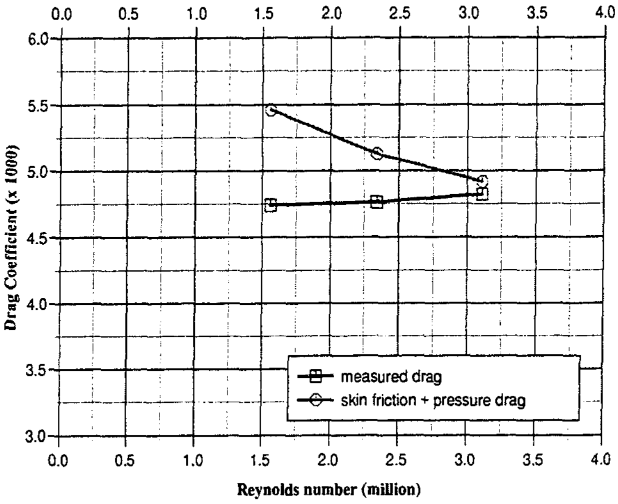

Figure 59e: S/L=0.37, with transition strip

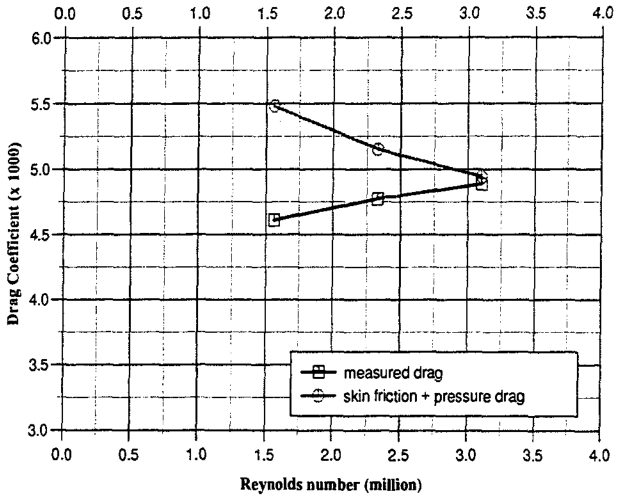

Figure 59f: S/L=0.47, with transition strip

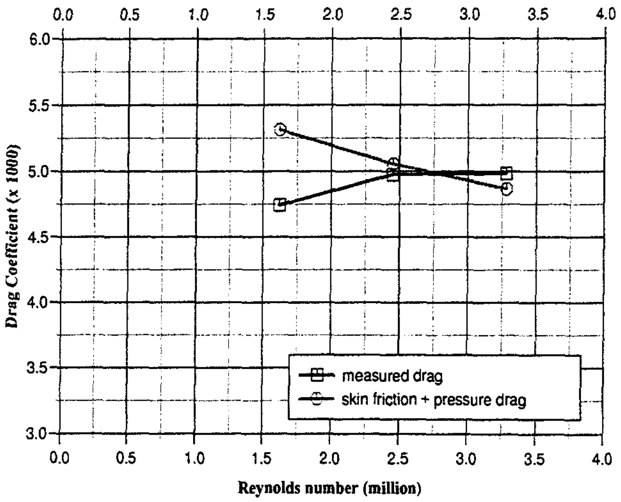

Figure 59g: S/L=0.57, with transition strip

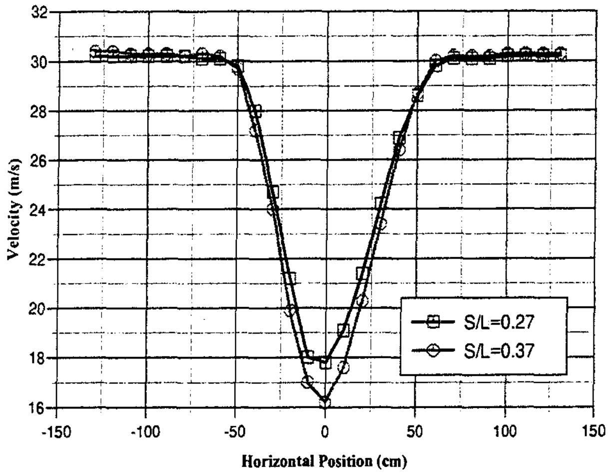

Figure 60: Horizontal velocity distribution

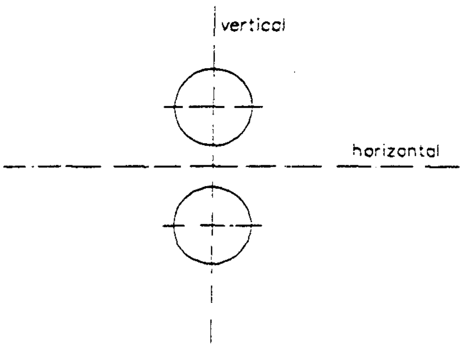

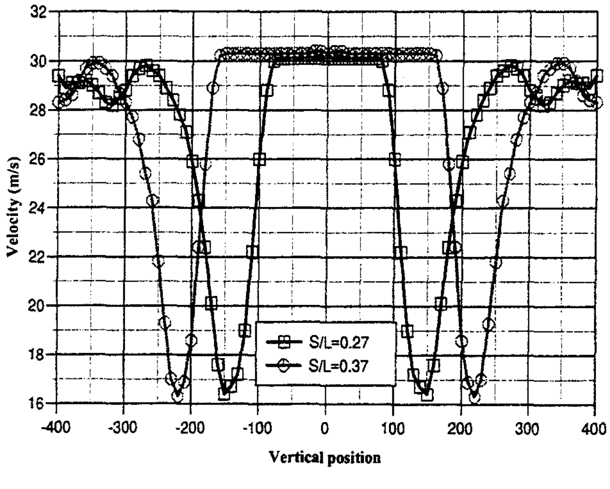

Figure 61: Vertical velocity distribution

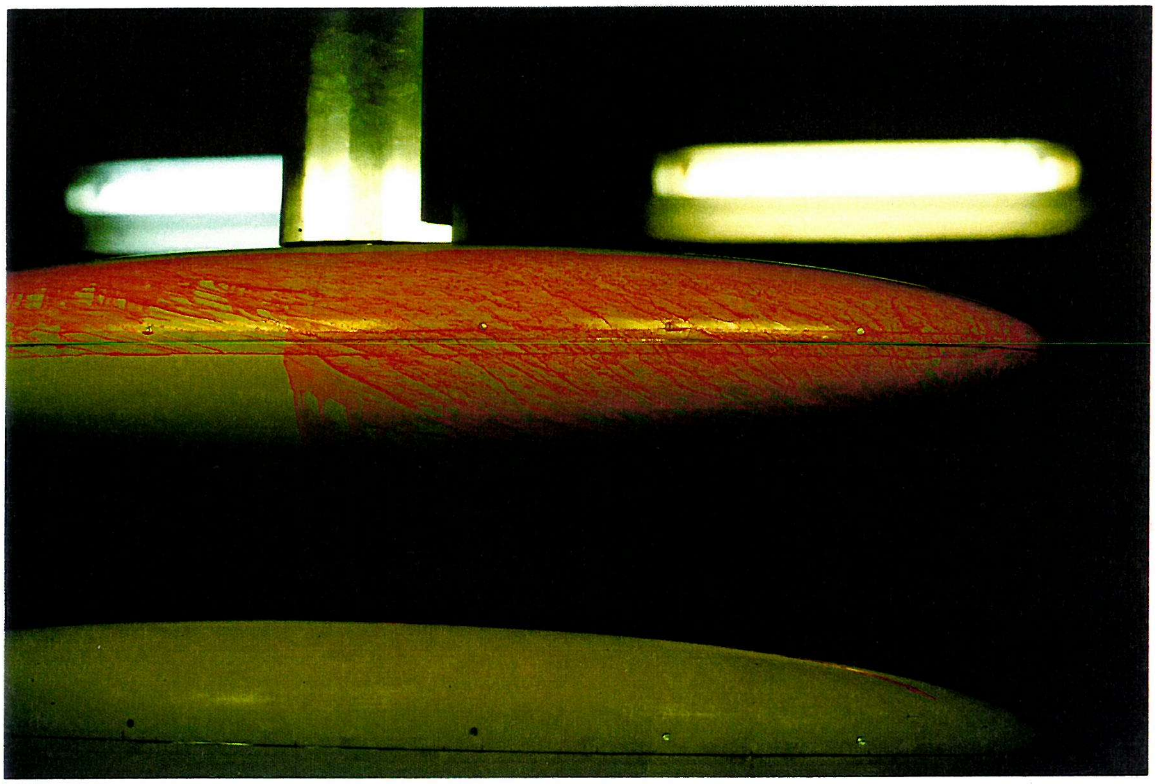

Figure 62: Flow visualisation using red paint

Figure 63: Flow visualisation using white cotton threads

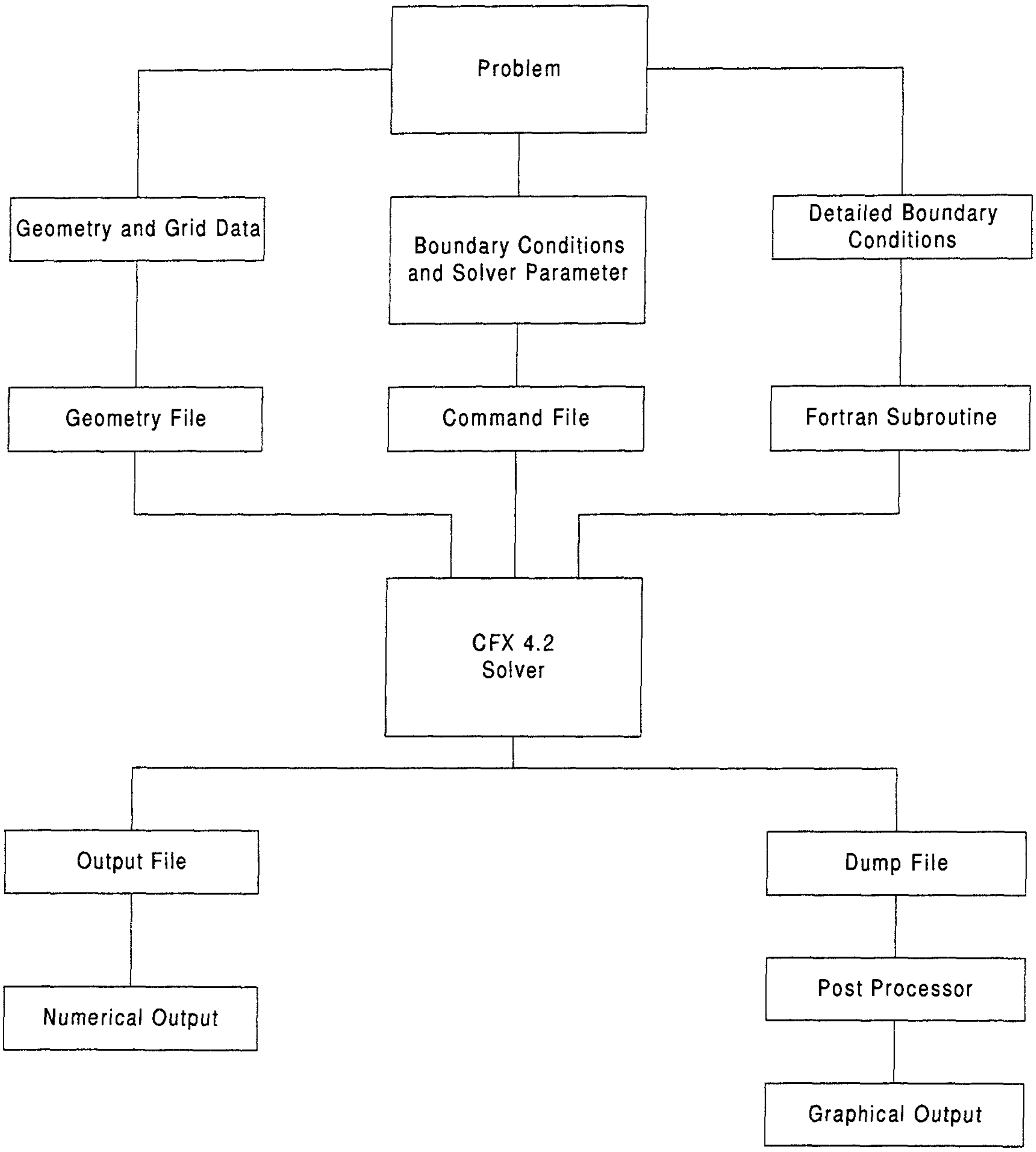

Figure 64: Flowchart of the CFX solution

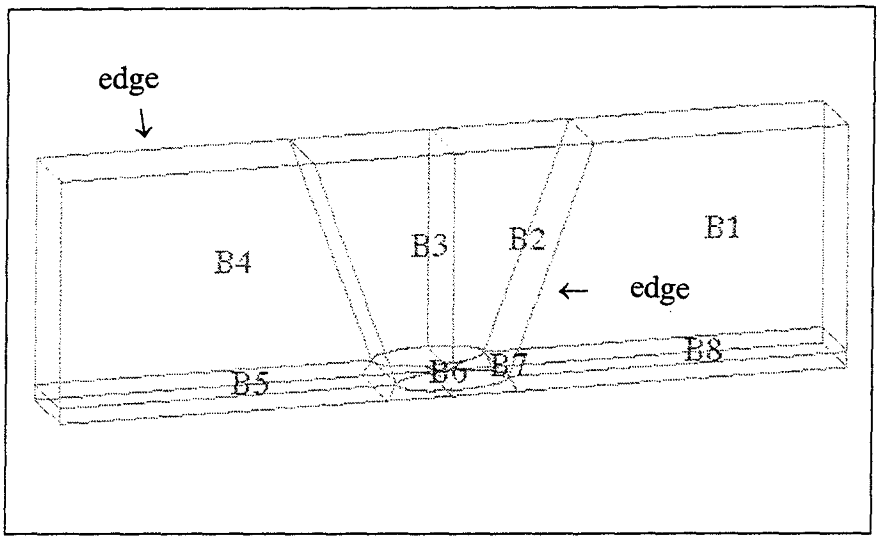

Figure 65: Definition of blocks by vertices and edges

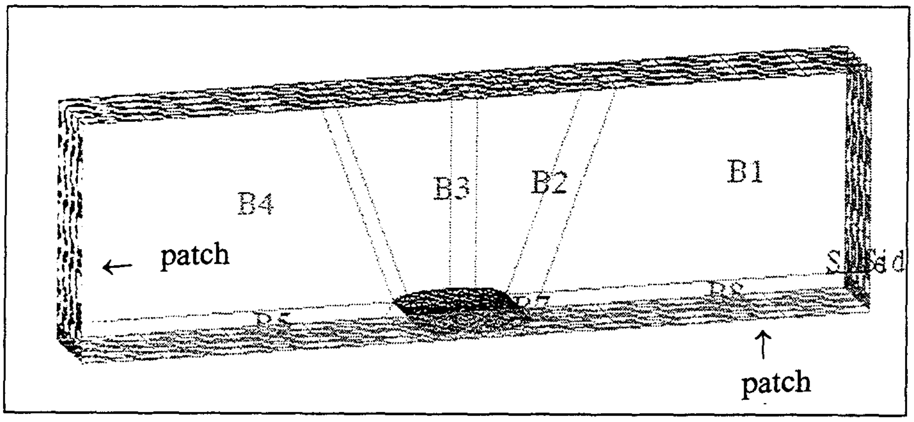

Figure 66: Patches and the boundary conditions

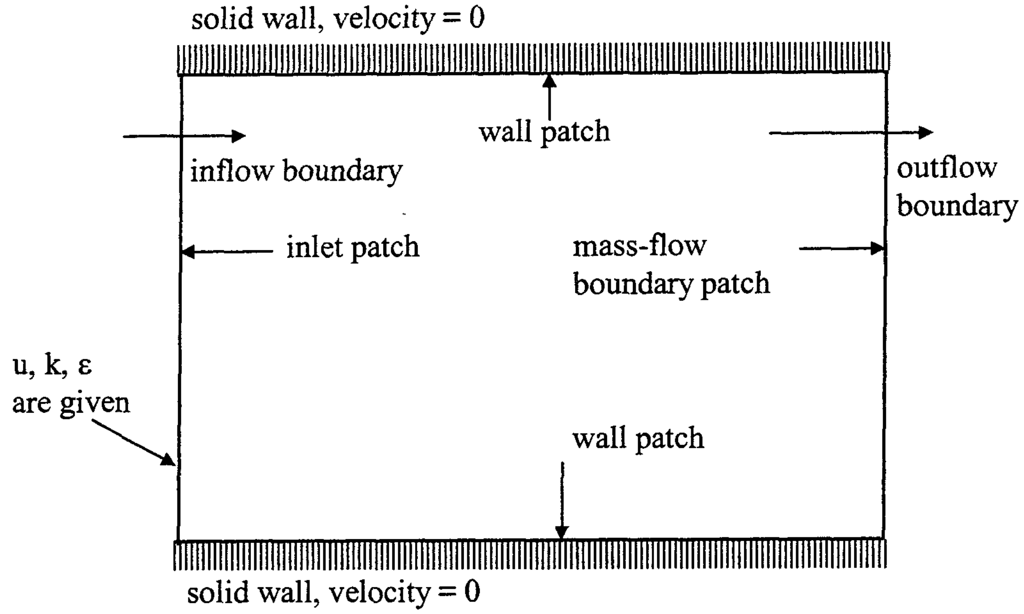

Figure 67: Internal flow condition

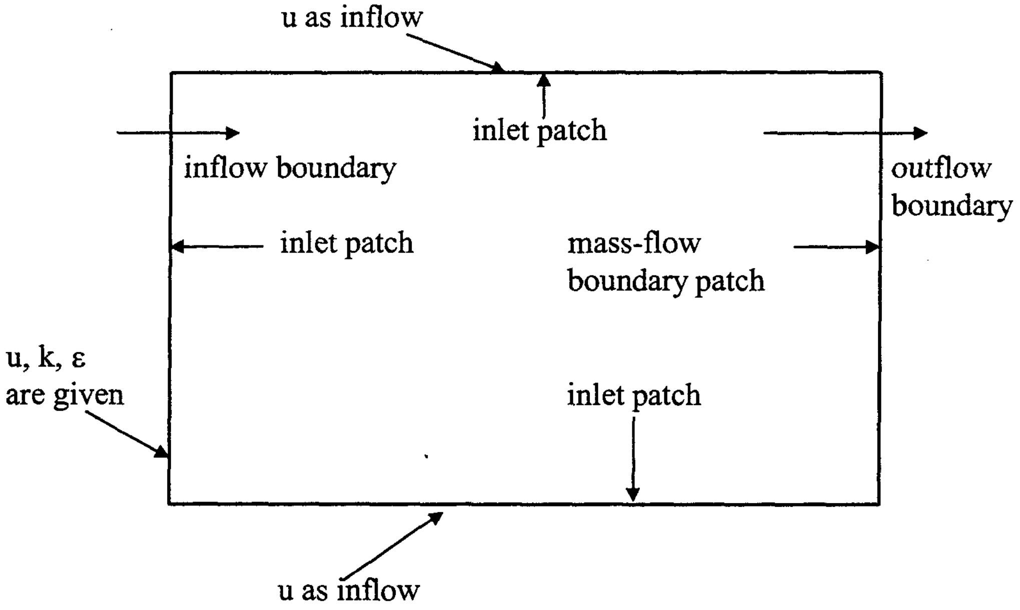

Figure 68: External flow condition

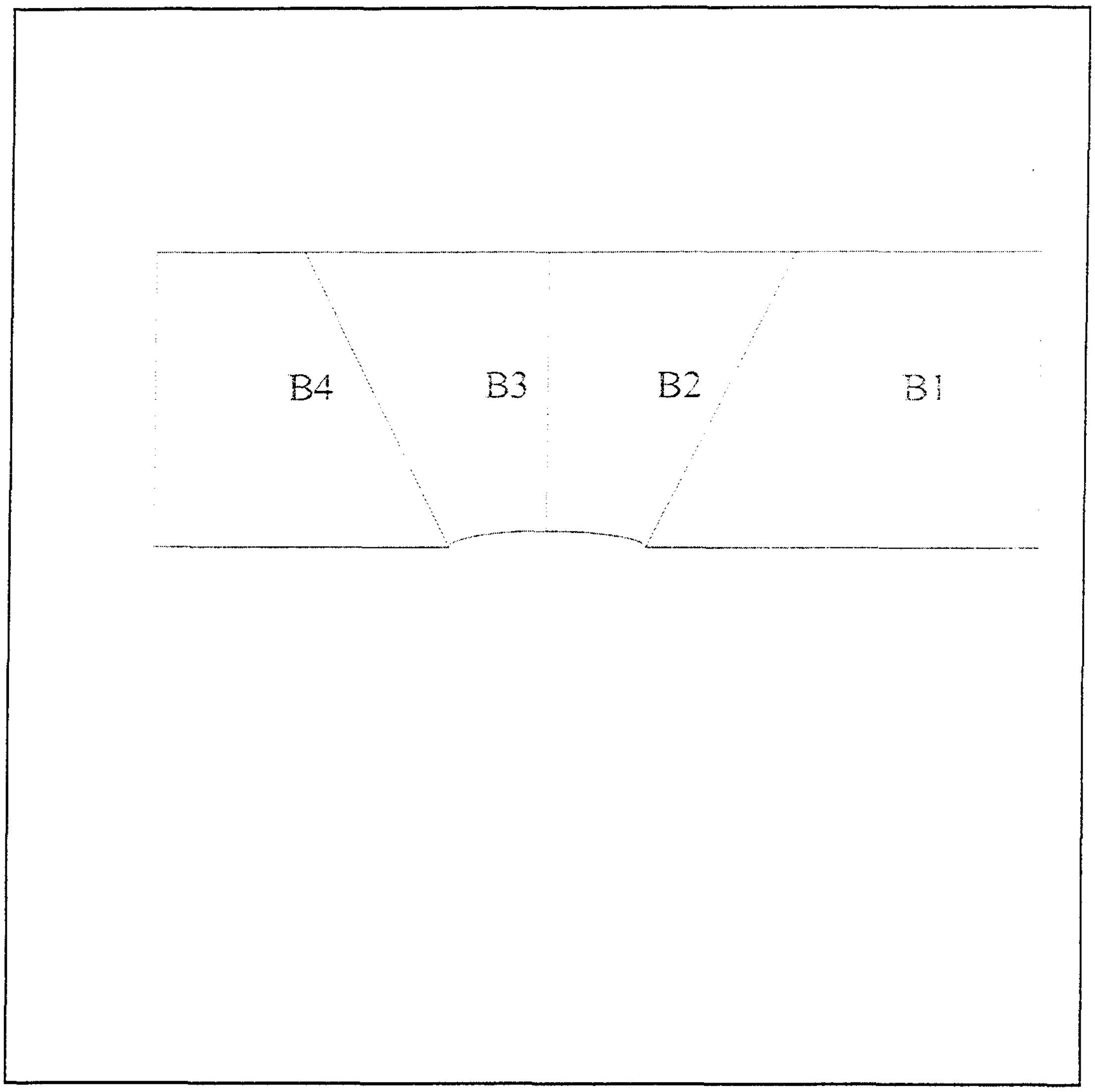

Figure 69: Two-dimensional ellipse model

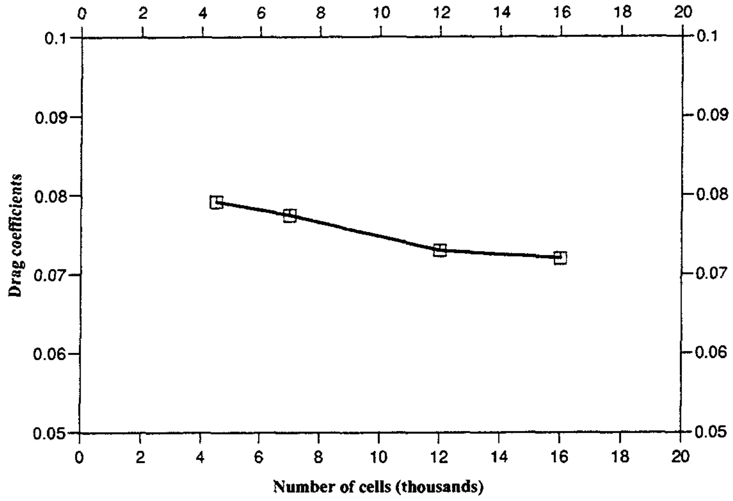

Figure 70: Grid independence study of two-dimensional ellipse

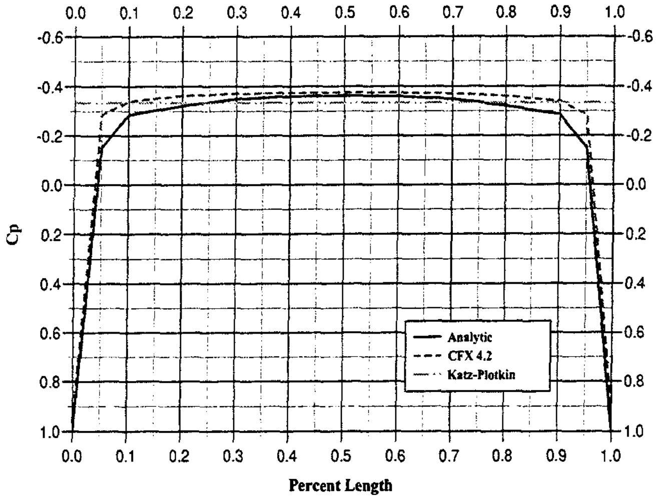

Figure 71: Comparison of Cp, two-dimensional

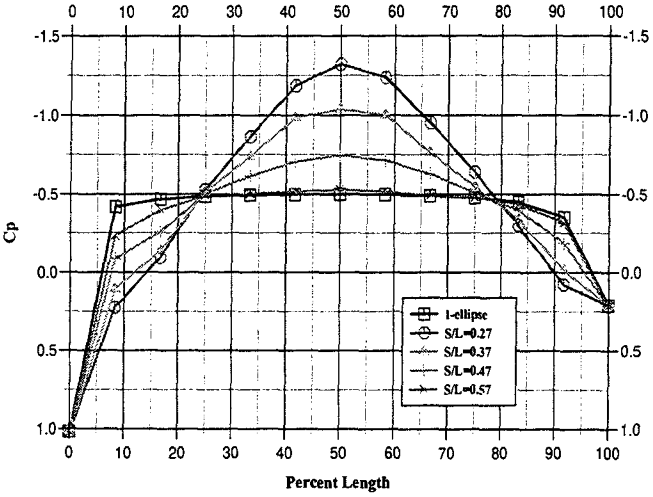

Figure 72: Pressure Distributions, two-dimensional

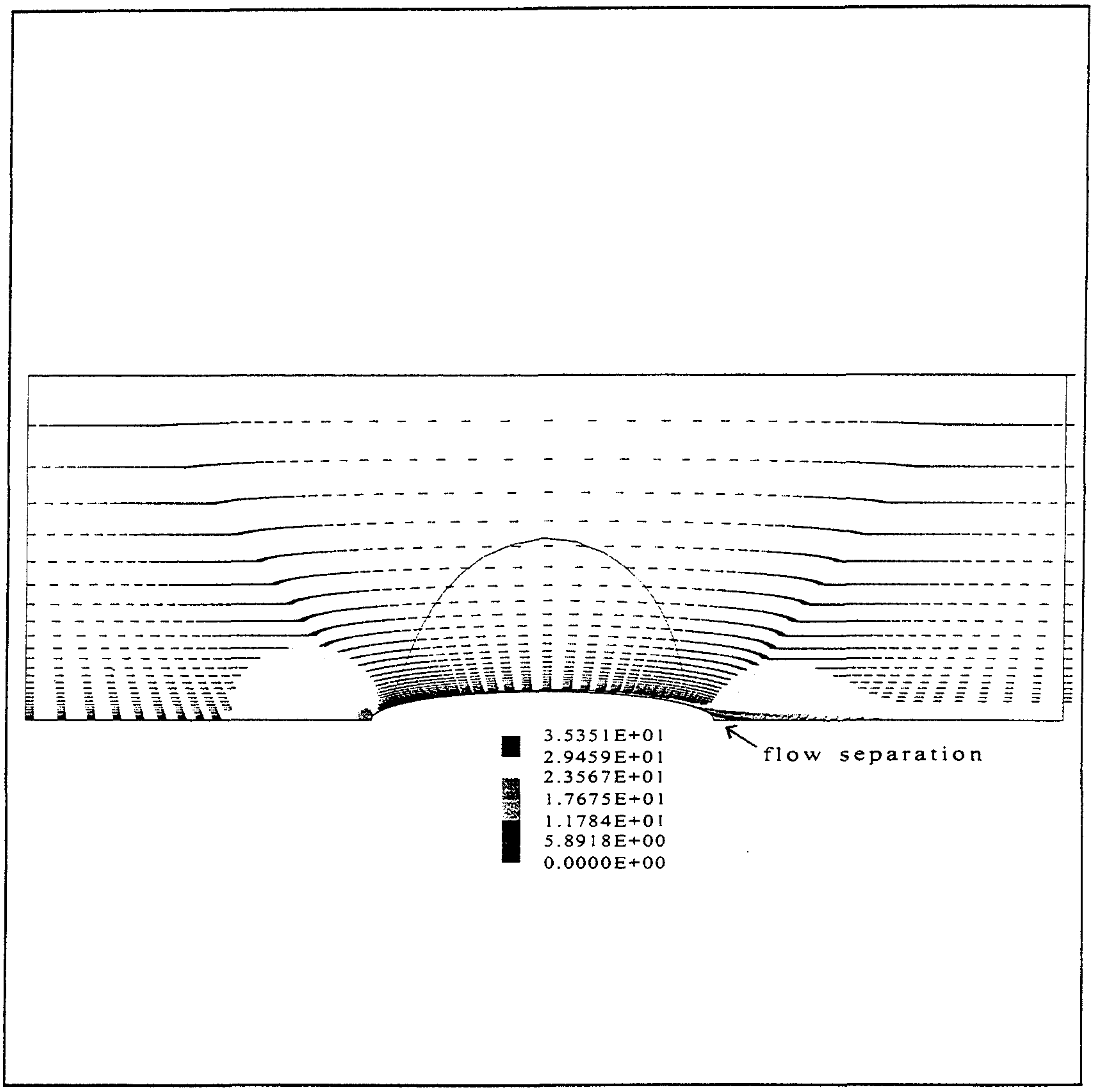

Figure 73: Flow separation on two-dimensional ellipse

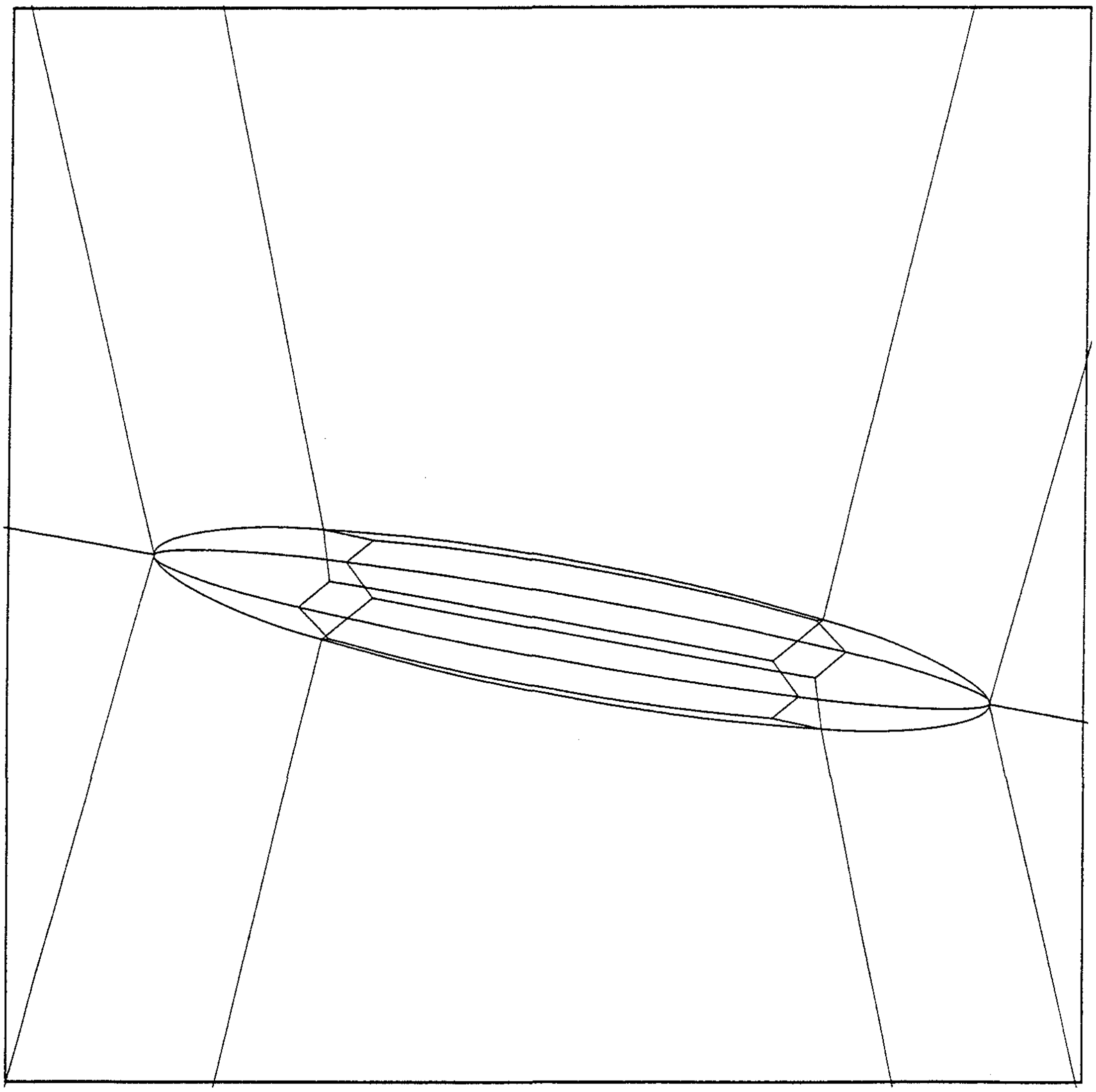

Figure 74: Three-dimensional ellipsoid model

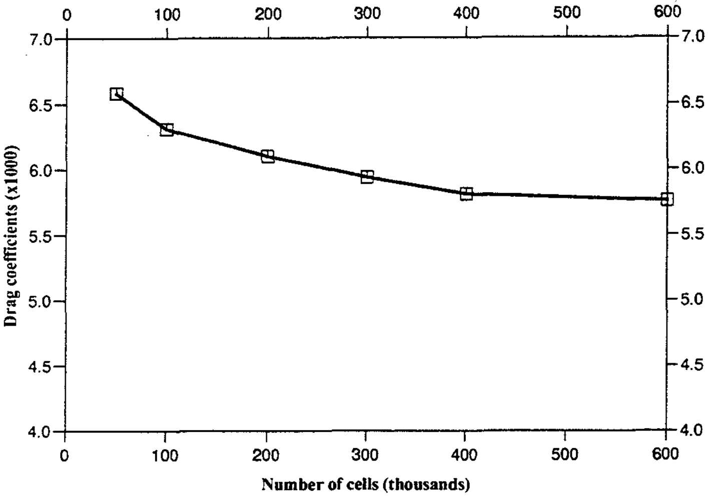

Figure 75: Grid independence study of three-dimensional ellipsoids

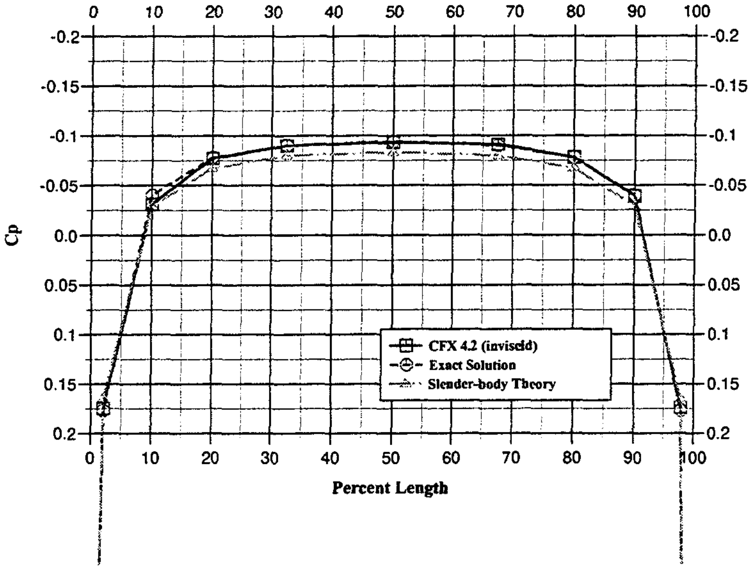

Figure 76: Comparison of Cp from CFX, three-dimensional

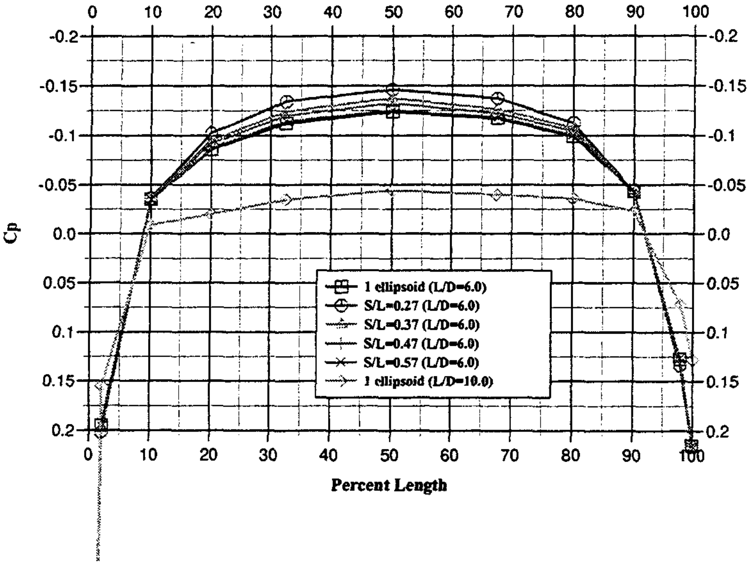

Figure 77: Pressure Distributions from CFX, three-dimensional

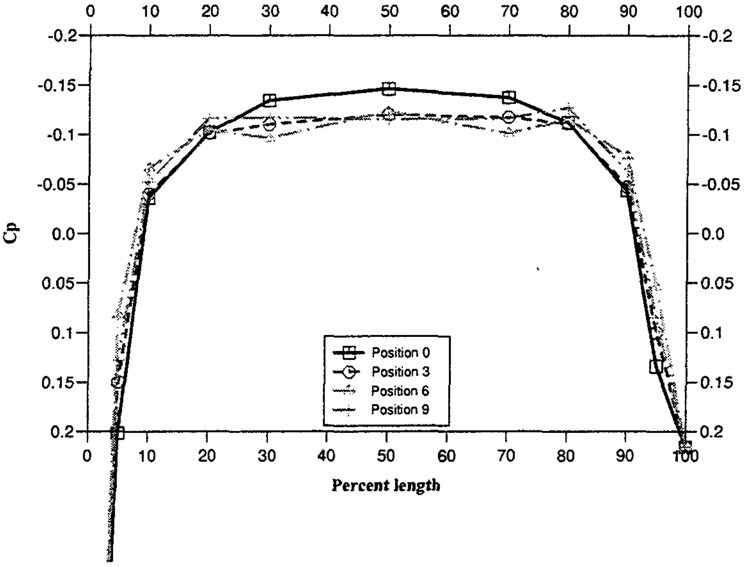

Figure 78: Pressure changes on ellipsoid at S/L=0.27

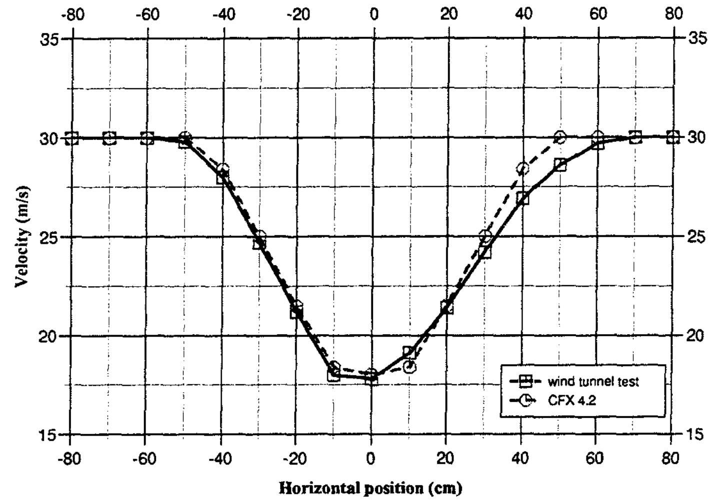

Figure 79: Horizontal velocity at 0.25L behind stern, S/L=0.27

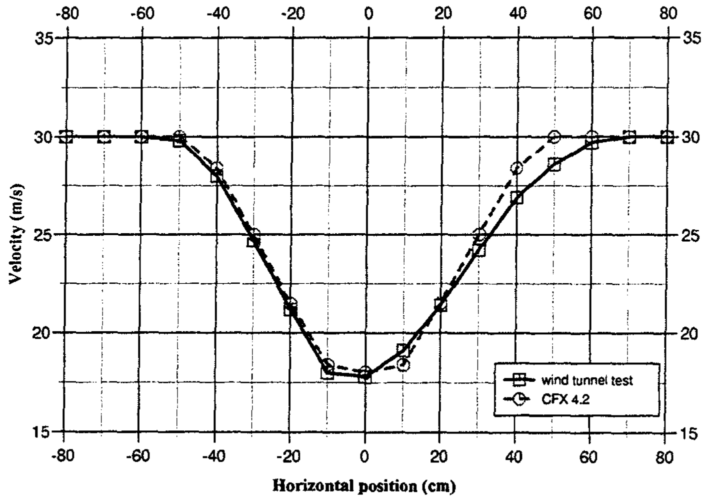

Figure 80: Horizontal velocity at 0.25L behind stern, S/L=0.37

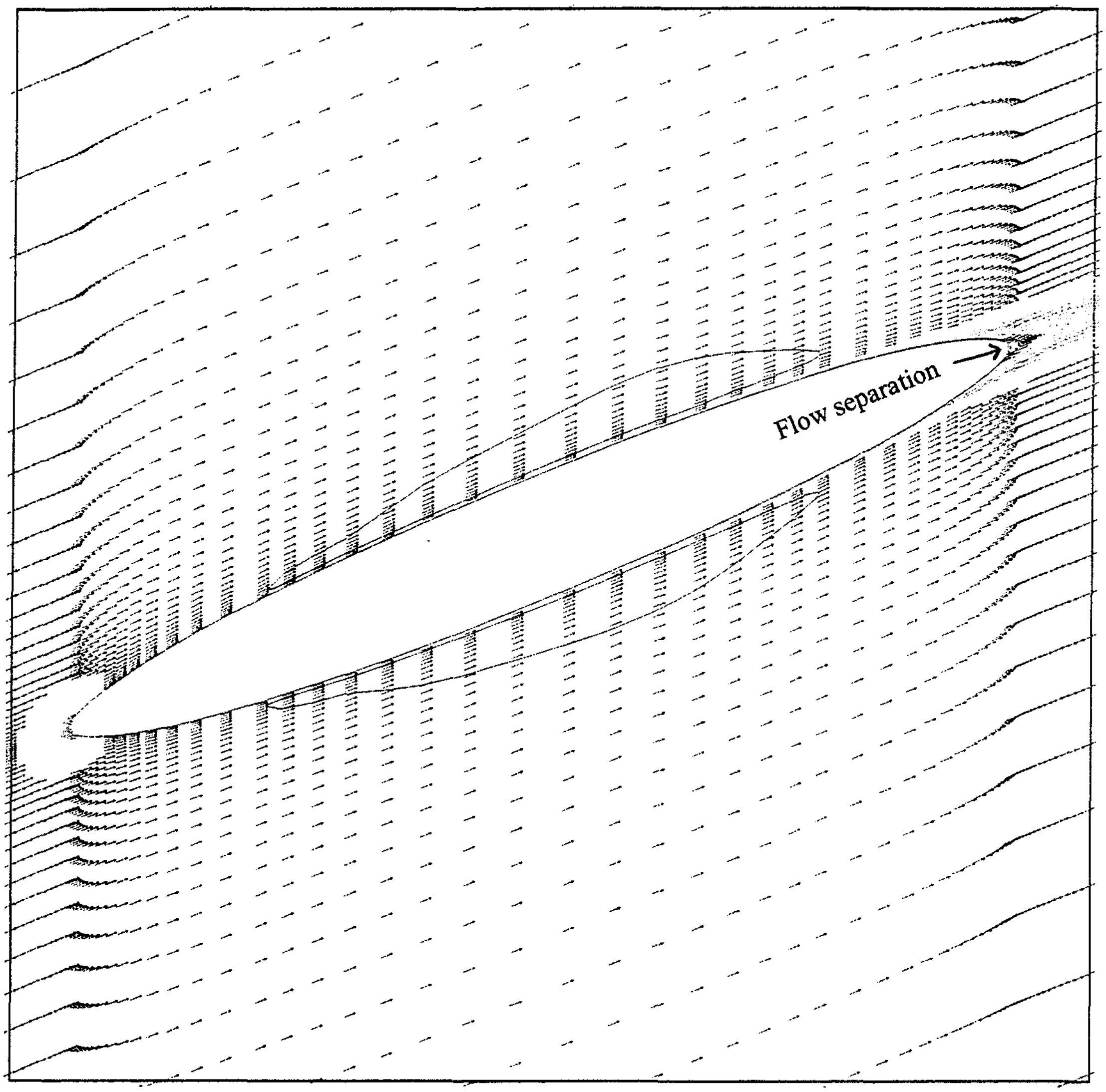

Figure 81: Flow separation on three-dimensional ellipsoid

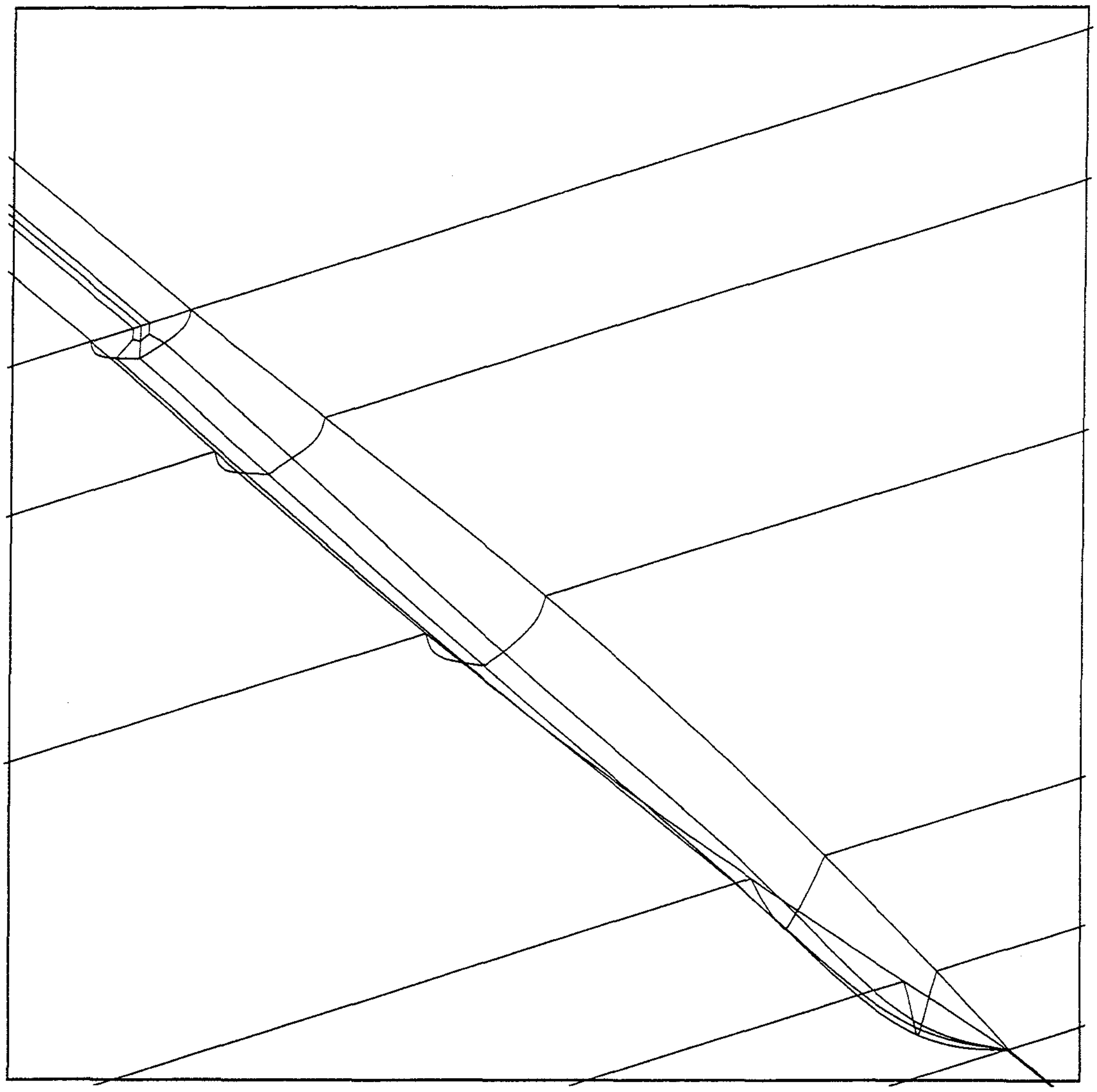

Figure 82: Three-dimensional ship hull model

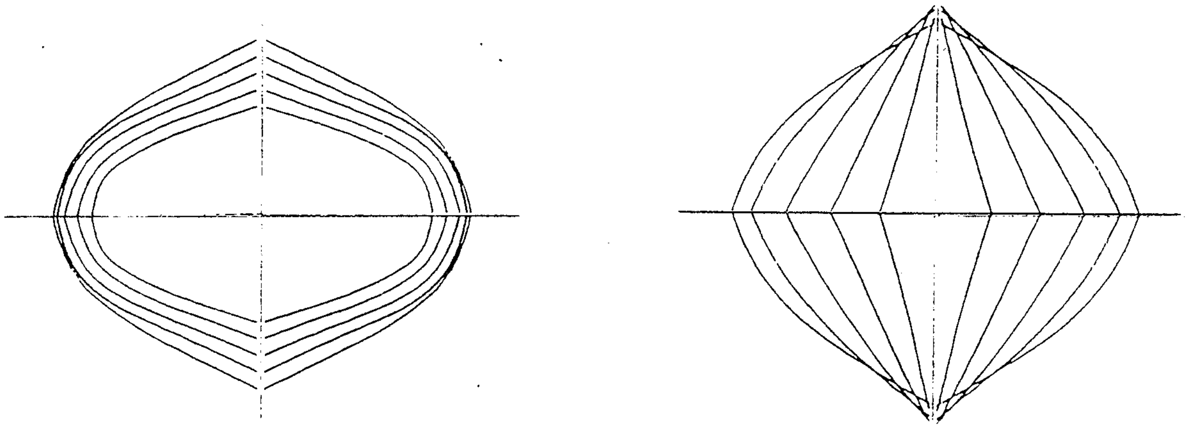

Aft end

Fore end

Figure 83: Body plan of the ship hull model

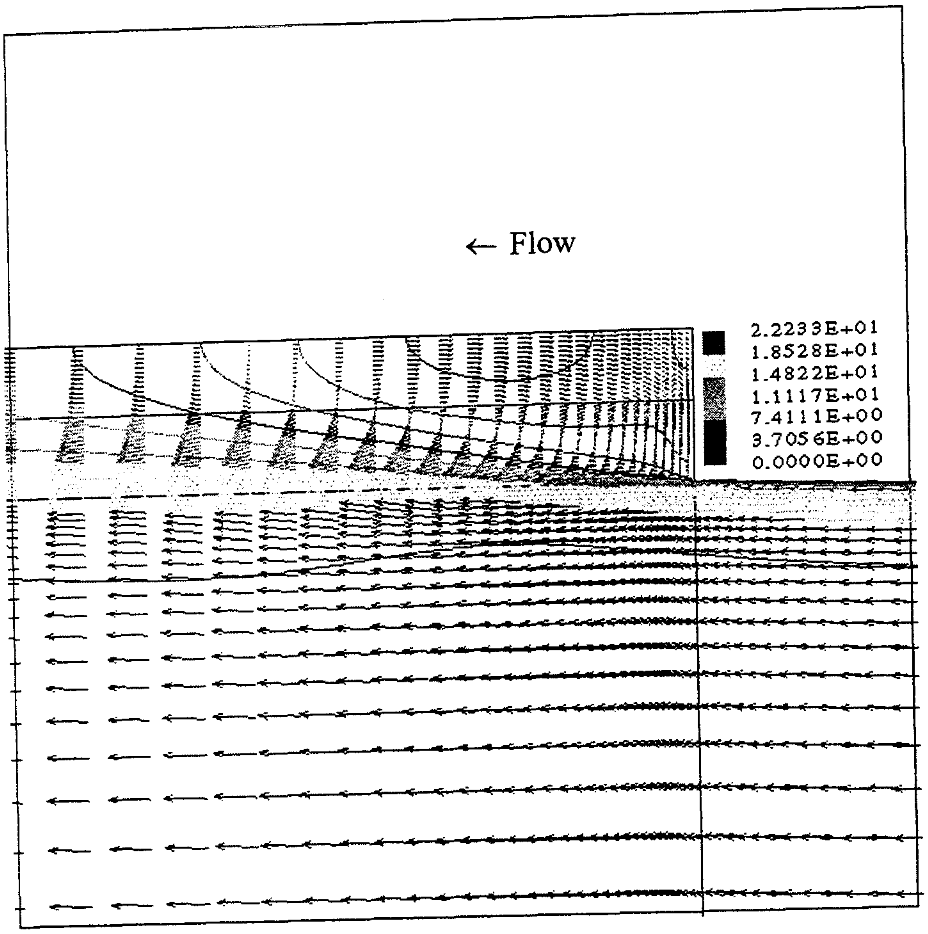

Figure 84: Flow behind transom stern of ship hull model at high Rn

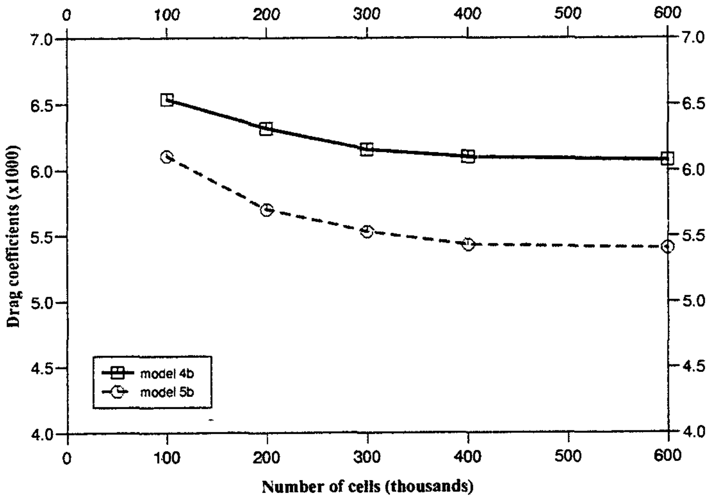

Figure 85: Grid independence study of ship hull models

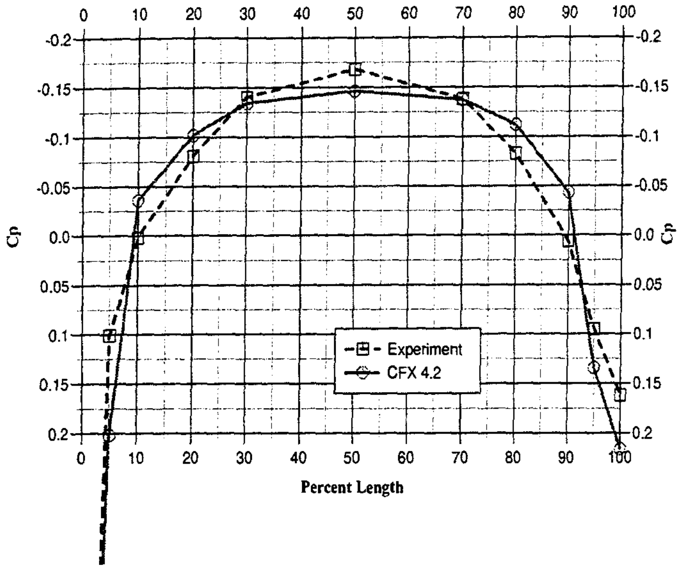

Figure 86a: Comparison of Cp at the closest line, S/L=0.27

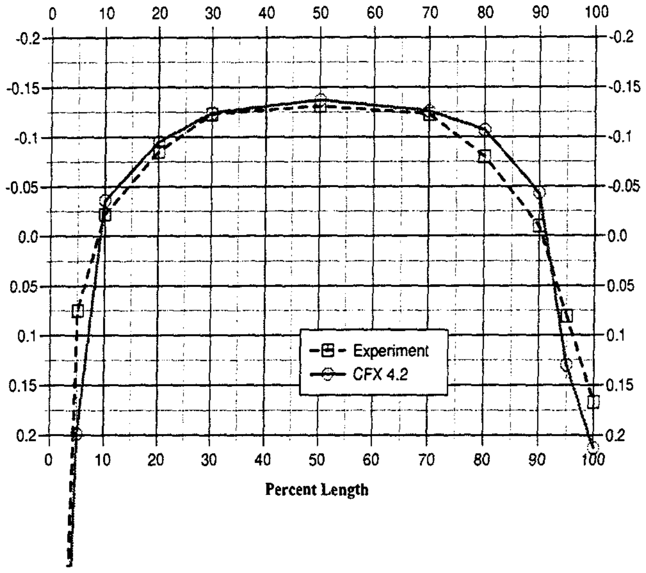

Figure 86b: Comparison of Cp at the closest line, S/L=0.37

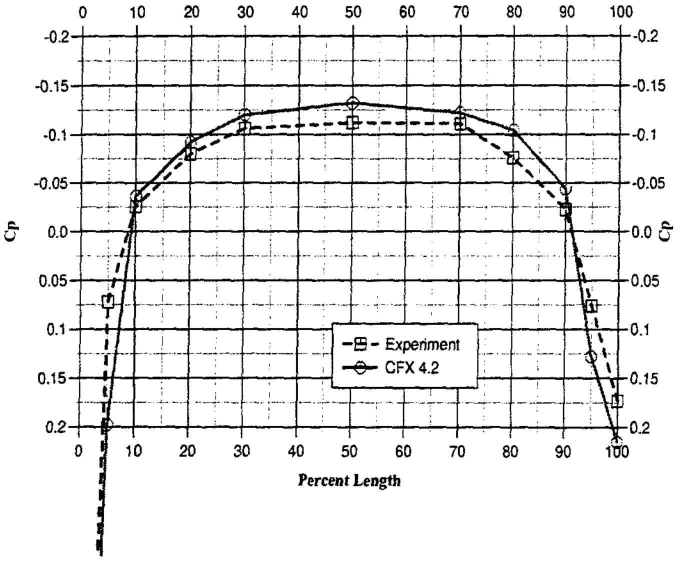

Figure 86c: Comparison of Cp at the closest line, S/L=0.47

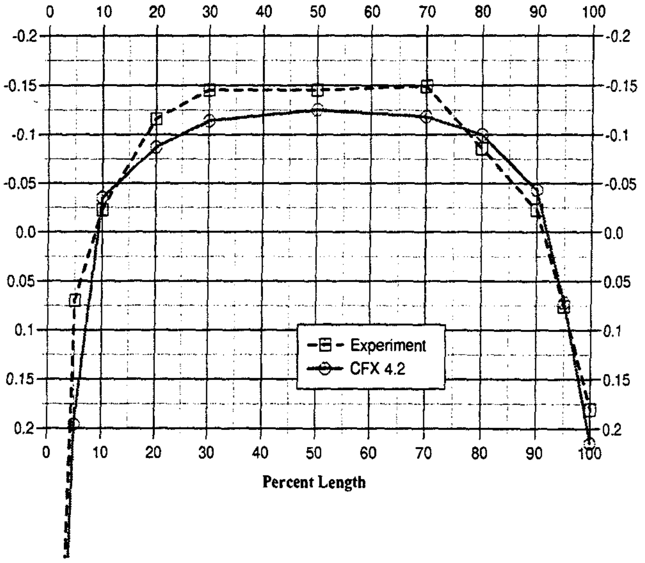

Figure 86d: Comparison of Cp at the closest line, S/L=0.57

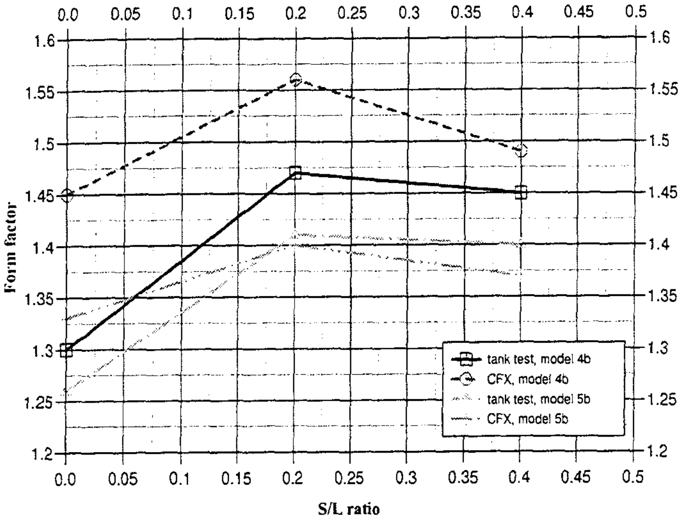

Figure 87: Form factors of ship hull models

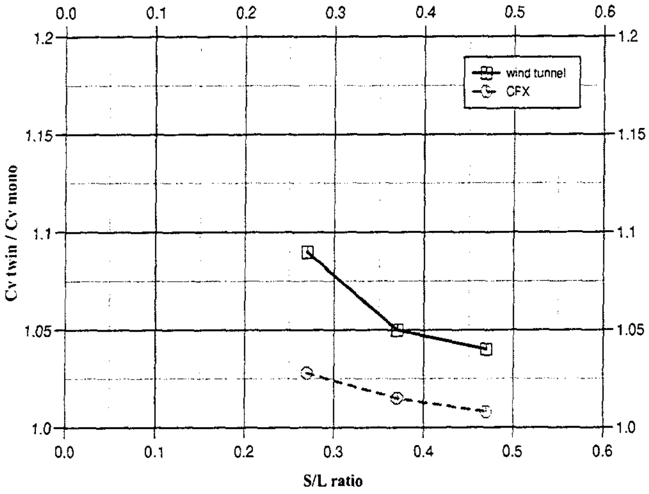

Figure 88: Total viscous interference of ellipsoids

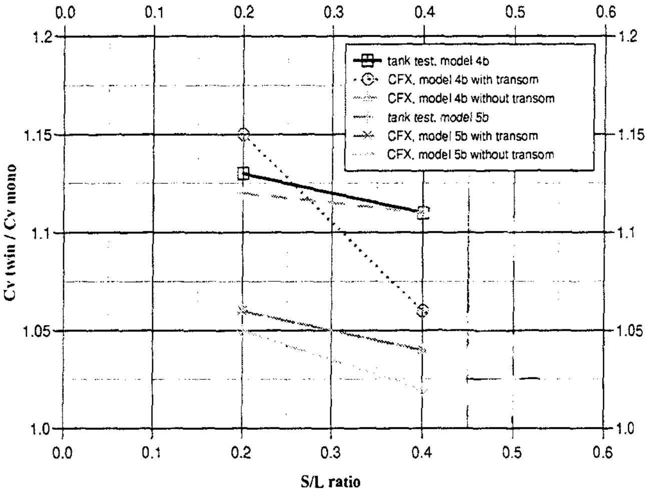

Figure 89: Total viscous interference of ship hull models

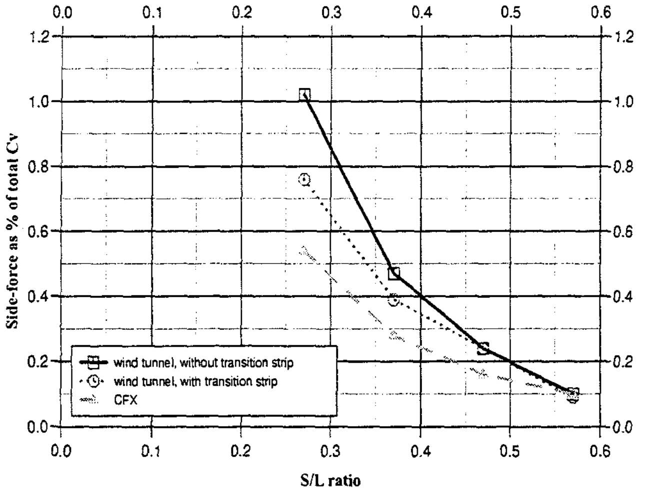

Figure 90: Side-force as % of total Cv for ellipsoids

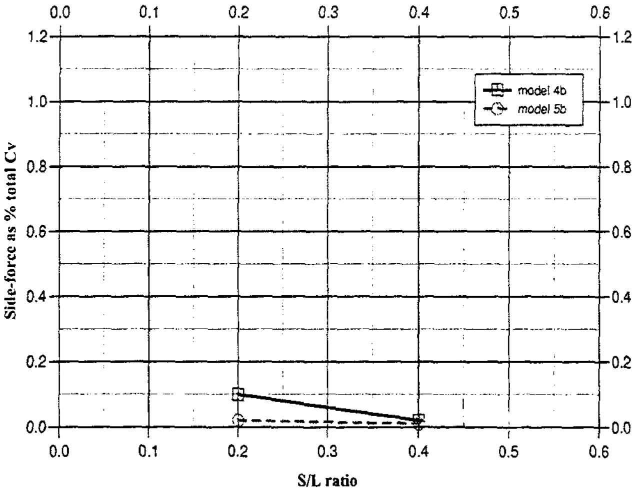

Figure 91: Side-force as % of total Cv for ship hulls (CFX)